DISSERTATION | DOCTORAL THESIS

Titel | Title

Proteomics-based discovery platforms to unravel modes of action of metal-based drug candidates

verfasst von | submitted by

Lukas Skos BSc MSc

angestrebter akademischer Grad | in partial fulfilment of the requirements for the degree of

Doktor der Naturwissenschaften (Dr.rer.nat.)

Wien | Vienna, 2026

Studienkennzahl lt. Studienblatt | Degree programme code as it appears on the student record sheet:	UA 796 605 419
Dissertationsgebiet lt. Studienblatt | Field of study as it appears on the student record sheet:	Chemie
Betreut von | Supervisor:	Univ.-Prof. Dr. Christopher Gerner Assoz. Prof. Dr. Samuel Meier-Menches

Acknowledgements

Firstly, I would like to thank my patient and supportive supervisor, Samuel Meier-Menches, for giving me the opportunity to work in this fascinating research field. He always made time for me, proving valuable feedback and gave me a chance to grow as an early scientist. Sam encouraged me to look for the bigger picture and he made my international research stay possible. Secondly, I would like to thank Christopher Gerner for his co-supervision, for always having an open ear and giving valuable input on finding the missing links in biochemical processes throughout my PhD.

Many thanks go to Andrea Bileck for her assistance on all projects, for always having an answer to scientific questions and the numerous conversations beyond research. I want to express my gratitude to Astrid Slany and Thomas Mohr for helping in one way or another and providing expert advice and support. Big thank you to Jessica Walker for always having the teaching sessions in the practical course prepared in a way which made this aspect of the PhD a breeze and a fun experience. I thank my fellow PhD colleagues for entertaining lunch and coffee breaks and making even the more challenging days enjoyable. Special thanks to Patricia Janker-Bortel for becoming a true friend and sharing the same humor, thus brightening even grey days.

I also wish to thank Günter Plessl-Walder, Johanna Mader and Peter Frühauf for organizing new things and unearthing others from times long gone. A very special thank you to Andrea Hilbert for always knowing the way through bureaucratic madness and supporting everyone in a way only she can.

Many thanks go to all our collaboration partners like Wolfgang Kandioller, Alexander Rosner and Dina Baier, and those from the Berger and Heffeter labs for their excellent contributions. Further, I would like to express my gratitude to Angela Casini at the Technical University of Munich for her valuable insights and for welcoming me in her research group. A big thank you to Claudia Schmidt, Julia Stebani and Darren Wragg for the fond memories in Munich and becoming close friends.

Yasmin, my muse: our constructive discussions, your support and you motivating me, all had a great impact on this thesis. I am grateful to have you in my life, and I am looking forward to our journey ahead.

And finally, my parents, for their never-ending encouragement and love, giving me the strength to fulfill my dreams.

This doctoral thesis is based on the following publications and manuscripts:

Selectivity for TP53 signalling drives the mode of action of a highly potent *N*,*O*,*O*-tridentate naphthoquinone-based organo-ruthenium anticancer drug candidate

Rosner A.*, Skos L.*, Mendrina T., Baier D., Hejl M., Borutzki Y., Gradl M., Geisler H., Mohr T., Legin A., Jakupec M., Bileck A., Gerner C., Koellensperger G., Heffeter P., Berger W., Keppler B.K., Kandioller W., Meier-Menches S.M.

* These authors contributed equally

Chemical Science, 2025, 16, 15652-15665

DOI: 10.1039/d5sc00735f

Gold-templated covalent targeting of the CysSec-dyad of thioredoxin reductase 1 in cancer cells

Skos L.*, Schmidt C.*, Thomas S.R., Park M., Geiger V., Wenisch D., Bonsignore R., Del Favero G., Mohr T., Bileck A., Gerner C., Casini A., Meier-Menches S.M.

* These authors contributed equally

Cell Reports Physical Science, 2024, 5(7), 102072

DOI: 10.1016/j.xcrp.2024.102072

Methods to identify protein targets of metal-based drugs

Skos L., Borutzki Y., Gerner C., Meier-Menches S.M.

Current Opinion in Chemical Biology, 2023, 73, 102257

DOI: 10.1016/j.cbpa.2022.102257

Zusammenfassung

Das zufällig entdeckte Chemotherapeutikum Cisplatin ist zu einem unersetzlichen Teil unseres Behandlungsrepertoires gegen Krebserkrankungen geworden. Angetrieben durch dessen klinischen Erfolg und den anhaltenden Bedarf an neuen Medikamenten, rückten zunehmend auch andere metallorganische Verbindungen in den Fokus der medizinisch-chemischen Forschung. Ihre strukturelle Vielfalt, beruhend auf deren Metall- und Liganden-Systemen, verspricht die Entwicklung von maßgeschneiderten Molekülen für spezifische Anwendungen in der Krebsbehandlung. Nachdem das Paradigma der DNS-Bindung überwunden wurde, zeigte sich, dass diese Substanzklasse in der Lage ist, Proteine als Ziel zu erkennen. Chemoproteomische Techniken haben sich bei der Identifizierung direkter Interaktionspartner als wirksam erwiesen und ermöglichen, in Kombination mit Proteom-Profilanalysen, die unvoreingenommene Hypothesen-Generierung potenzieller Wirkmechanismen der Testsubstanzen. Ziel dieser Dissertation ist es, eine proteomische Plattform auf Grundlage von Proteomprofilierung und Chemoproteomik zu entwickeln, um metallbasierte Wirkstoffkandidaten zu untersuchen, die in phänotypischen Wirkstoffforschungsmodellen identifiziert wurden, und deren zugrundeliegenden Wirkmechanismus aufzuklären. Hierzu wurde in der ersten Studie eine dosis-abhängige chemoproteomische Technik entwickelt, die auf einer neuartigen Immobilisierungsstrategie basiert, um einen C^N zyklometallierten Gold(III)-Komplex in Kolorektalkrebszellen zu erforschen. Mittels Affinitäts-Pulldown-Experimenten, Analysen des Proteomprofils und weiteren Validierungsexperimenten konnte gezeigt werden, dass der Au-Komplex über einen zweistufigen Mechanismus reagiert, der zur selektiven TXNRD1-Inhibition führt. Parallel dazu wurden weitere Selenoproteine herunterreguliert, und der NRF2-Keap1 Signalweg ohne begleitende ROS-Bildung induziert, der sich als wichtig für das Überleben der Krebszellen erwies. Die zweite Studie untersuchte den Wirkmechanismus eines hoch-zytotoxischen N,O,O-tridentaten Ruthenium(Aren)-Komplexes auf Basis eines Naphtochinon-Liganden sowie dreier Analoga, die sich in Ligandenstruktur und Metallzentrum (Ru, Os) unterscheiden. Diese Komplexe verhielten sich über einen längeren Zeitraum kinetisch inert, behielten jedoch ihre Reaktivität bei und banden bevorzugt an Aminosäuren statt Nukleotiden. Es erwies sich, dass Löslichkeit, antiproliferative Aktivität und Interaktionsverhalten mit Proteinen stärker vom Liganden als vom Metallzentrum bestimmt wurden. Diese Studie verdeutlicht somit, wie strukturelle Variationen die Effekte auf Proteinebene in Struktur-Wirkungs-Beziehungen beeinflussen. Die beiden 3-Ethylnaphthochinon-Derivate wirkten sich hauptsächlich auf das TP53-Signalnetzwerk aus, wobei die Ruthenium-Hauptverbindung die TP53-DDX3X-p21 Achse vermutlich über eine

direkte DDX3X-Wechselwirkung stark störte und dadurch die p21-Expression minimierte. Diese direkte Wechselwirkung wurde durch eine neuartige chemoproteomische Technik auf der Grundlage einer Limitierten Proteolyse nachgewiesen. Die Ruthenium-Leitverbindung zeigte zudem in einem Mausmodell die stärkste krebshemmende Wirkung, indem sie die CT26-Tumorgröße signifikant reduzierte und EGFR im Tumorgewebe als direkten Behandlungseffekt herunterregulierte. Dies bestätigte die *in vitro* Ergebnisse bezüglich der TP53-DDX3X-p21 Achse, von der gezeigt wurde, dass sie die EGFR-Level modulieren kann. Insgesamt wurde im Rahmen der hier vorgestellten Projekte eine proteomische Forschungsplattform geschaffen, die von speziellen Zellkultur-Workflows begleitet wird und zur Untersuchung neuidentifizierter, metallbasierter Wirkstoffkandidaten genutzt werden kann. Diese duale proteomische Plattform ermöglicht es, deren Interaktionspartner zu identifizieren und mögliche Wirkmechanismen aufzudecken. Die gewonnenen Erkenntnisse können für die Weiterentwicklung der Wirkstoffe herangezogen werden und so die Identifizierung potenzieller metallbasierter, klinischer Kandidaten erleichtern.

Abstract

The serendipitously discovered chemotherapeutic agent cisplatin has become an indispensable part of our cancer treatment arsenal. Driven by its clinical success and the ongoing need for new medication, other metal-based compounds have increasingly become the focus of medicinal chemical research. Their structural diversity, based on their metal and ligand systems, promises the development of tailor-made molecules for specific anticancer applications. After overcoming the DNA-targeting paradigm, this compound class was shown capable of targeting proteins. Chemoproteomic techniques have proven effective for identifying direct interaction partners and, when combined with proteome profiling analyses, enable the unbiased generation of hypotheses regarding the potential mechanism of action (MoA) of the tested substance. The aim of this dissertation is to develop a proteomic platform based on proteome profiling and chemoproteomics to investigate metal-based candidate drugs identified in phenotypic drug discovery models and to elucidate their underlying MoA. To this end, a dose-dependent chemoproteomic technique was developed in the first study based on a novel immobilization strategy to investigate a C^N cyclometallated gold(III) complex in colorectal cancer cells. Using affinity pulldown experiments, proteome profiling analyses, and further validation experiments, it was demonstrated that the Au-complex reacts *via* a two-step mechanism, leading to selective inhibition of TXNRD1. In parallel, other selenoproteins were downregulated and without concomitant ROS formation the Nrf2-Keap1 pathway was induced, which was found to be important for cancer cell survival. The second study investigated the MoA of a highly cytotoxic N,O,O-tridentate ruthenium(arene) complex based on a naphthoquinone ligand, and three analogues differing in ligand structure and metal center (Ru, Os). These complexes were kinetically inert over an extended time period but retained their reactivity, and preferred binding to amino acids rather than nucleotides. The solubility, antiproliferative activity, and protein interaction behavior were shown to be determined more strongly by the ligand compared to the metal center. This study then highlighted how structural variations influenced protein-level effects in structure-activity relationships. The two 3-ethyl naphthoquinone derivatives primarily influenced the TP53 signaling network, with the ruthenium lead compound strongly disrupting the TP53-DDX3X-p21 axis presumably *via* direct DDX3X interaction, thereby reducing p21 expression. The direct interaction was proven by a novel chemoproteomic technique based on Limited Proteolysis. The ruthenium lead compound also exhibited the strongest anticancer effect in a mouse model, significantly reducing CT26 tumor size and downregulating EGFR in tumor tissue as direct treatment effect, confirming the *in vitro* findings regarding the TP53-DDX3X-p21 axis, which has been shown to modulate EGFR levels. Overall, the projects

presented here established a proteomic discovery platform, accompanied by dedicated cell culture workflows, that can be used to investigate newly identified metal-based drug candidates. This dual proteomic platform allows to identify their interaction partners and uncover their potential MoA. The information obtained can be used for compound maturation to facilitate the identification of potential metal-based clinical candidates.

Table of Contents

Abbreviations

3PM	Predictive, preventive and personalized medicine
AA	Amino acid
AcBPP	Activity-based protein profiling
ADME	Absorption, Distribution, Metabolism, Excretion
AfBPP	Affinity-based protein profiling
AI	Artificial intelligence
CuAAC	Copper(I)-catalyzed azide–alkyne cycloaddition
DC	Direct current
DDA	Data-dependent acquisition
DIA	Data-independent acquisition
ER	Endoplasmic reticulum
ESI	Electrospray ionization
FDR	False discovery rate
GPCR	G-protein coupled receptors
HPLC	High-performance liquid chromatography
HR	High resolution
HSAB	Hard-soft acid-base
iPSC	Induced pluripotent stem cells
LC	Liquid chromatography
LC-MS/MS	Liquid chromatography tandem mass spectrometry
LFQ	Label-free quantification
LINCS	Library of integrated network-based cellular signatures
m/z	Mass-to-charge
ML	Machine learning
MoA	Mode of action
MS	Mass spectrometry
MS/MS	Tandem mass spectrometry
NGS	Next generation sequencing
NSAID	Nonsteroidal anti-inflammatory drug
NSCLC	Non-small cell lung cancer
PDD	Phenotypic drug discovery
PTM	Post-translational modification

QqQ	Triple quadrupole
RF	Radio frequency
ROS	Reactive oxygen species
RPLC	Reversed-phased liquid chromatography
SAR	Structure-activity relationships
SILAC	Stable isotope labelling by amino acids in cell culture
TDD	Target-based drug discovery
TIMS	Trapped ion mobility spectrometry
TMT	Tandem mass tags
TOF	Time-of-flight
TPP	Thermal proteome profiling
WCL	Whole cell lysate

1 Introduction and Theoretical Background

Almost 15 years ago, while investigating how new approved drugs were discovered, it was realized that many first-in-class compounds were identified by phenotypic drug discovery (PDD) and not by target-based drug discovery (TDD).[1] Since then, the interest in PDD has reignited as a powerful strategy for identifying novel therapeutic agents by screening compounds in biologically relevant systems without prior knowledge of specific molecular targets.[2,3] This approach is especially helpful to investigate the overlapping chemical space of covalently binding compounds and metal-based drug candidates to find new remedies for complex medical conditions like cancer and targets deemed hard-to-drug or undruggable. Liquid chromatography tandem mass spectrometry (LC-MS/MS) plays a pivotal role as an analytical technique throughout this discovery process, enabling target identification, profiling of drug-induced changes at the proteome level and thus, elucidation of mechanisms of action (MoA).[4,5] The following chapters will elaborate how the integration of advanced (chemo-)proteomic techniques in PDD with viable model systems can enable the identification and validation of targets of covalent drug candidates. Especially in the field of metal-based anticancer agents, these methods provide deep insights into compound mode of action and off-target effects.[4,6]

1.1 Drug discovery

Looking into the past, there was always a pursuit of medication to treat the ailments of people. Historically, the early apothecaries can be regarded as the first people who tried to discover new medicines by administering their concoctions containing herbs and mineral powders to observe the effects on their patients. These rudimentary approaches laid the groundwork for the emerging field of pharmaceutical science as a discipline with Jöns Jacob Berzelius (1779–1848) as one of the first chemists, who greatly contributed to this field and also wrote the first book on the physiological chemistry of animals.[7] With the rapid advancements during that period in chemistry, metal salts containing mercury, arsenic and gold started to find their way into the repertoire of possible components for treatment.[8] It was not until the 20th century, however, that a change from a trial-and-error screening approach happened to a more systematic one where active compounds were examined for their medicinal properties.[9] But still, some of the most impactful medical findings during that era such as the antibiotic penicillin (Alexander Fleming, 1928) or the metal complex cisplatin in cancer therapy (Barnett Rosenberg, 1969) were

discovered serendipitously and not by rational design.[10,11] With the advent of technologies like mass spectrometry and its later hyphenation to high pressure liquid chromatography as well as the establishment of structural and molecular biology, scientists were able to thoroughly examine the effects of compounds on multiple levels. This progress in drug development was further fueled by omics platforms, the addition of computational tools and bioinformatics allowing for high-throughput screening methods that paved the way for rational drug discovery and design (Figure 1).[2,4,12]

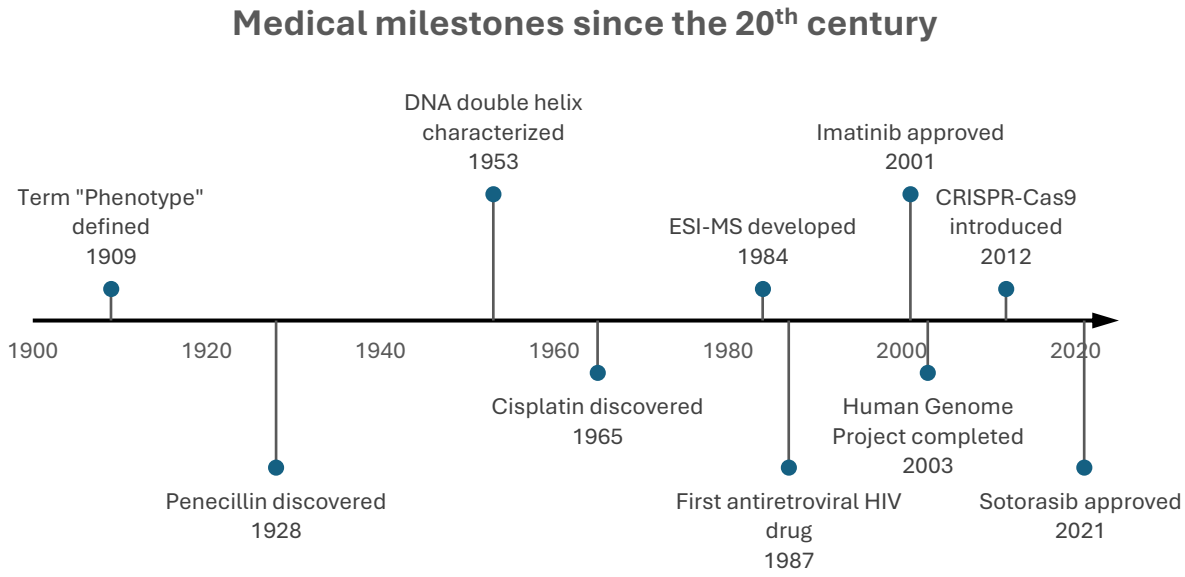

Figure 1: Timeline with significant medical milestones since the 20th century, including serendipitous discoveries like penicillin and cisplatin as antibiotic and anticancer agent respectively, technical developments that enabled new levels of investigation (e.g. introduction of the electrospray ionization) and examples of approved drugs for medical conditions previously believed to be undruggable.[13–20]

Nowadays, the process to find new small molecule therapeutics can be predominantly categorized into two approaches: target-based drug discovery and phenotypic drug discovery. Both approaches have their respective starting points but converge into a similar compound optimization path after initial findings and are described in detail in the following sections.[2,5]

1.2 Target-based drug discovery

After the establishment of molecular biology and genomics in the 1980s, scientific disciplines that made it possible to identify and validate molecular targets, followed by the approval of the

first successfully developed candidate, TDD became the dominant drug discovery approach ever since.[12] As the name implies, target-based drug discovery (sometimes abbreviated as TBDD) focusses on the modulation of a specific molecular target within the pathophysiology of a disease. Such targets can be cellular components, mutated genes, RNA, and proteins like kinases, enzymes or receptors. The resulting development of active agents can then include small molecules as well as biologics like antibodies or short peptides.[21,22]

1.2.1 Process of target-based drug discovery

In brief, the first step in target-based drug discovery is to gain a deeper understanding of the disease and its underlying molecular mechanism. A suitable target with a therapeutic effect and ideally without any adverse effects is identified by investigating the deviations from pathomechanisms of diseases compared to the healthy state *via* various techniques. The selected target is then validated systematically through biochemical assays, gene editing and screening against compound libraries to further optimize the lead structure in regard to improve efficacy, selectivity, and their pharmacokinetic properties.[22] Recent technological and methodological advances that significantly transformed TDD, were the continuous improvements of biochemical assays and the establishment of fragment-based and focused libraries to screen large quantities of active agents against targets of interest enhancing throughput rates even more.[23] Further, gene editing with the CRISPR-Cas9 technology and RNA interference (RNAi) deeply improved the systematic examination of gene functions and the validation of target molecules.[4,24] Additionally, the establishment of mass spectrometry-based omics techniques (metabomics, proteomics, lipidomics, etc.) and the implementation of bioinformatical tools enabled the identification of off-targets and the investigation of drug-target interactions in complex biological samples.[25] After the release of ChatGPT by the company OpenAI to the public in November 2022, many have rediscovered the numerous applications of artificial intelligence (AI) and machine learning (ML), also in science.[26] Since then, great expectations have been placed on machine learning and network analysis to study large data sets for drug discovery and potentially unveil new targets.

Advantages of this drug discovery method are its simplicity and specificity once a suitable target has been identified, as it operates with prior knowledge of the molecular targets and can be scaled industrially. However, the identification of a suitable target can be difficult as most diseases do not depend on a single protein.[12,27] This method enables rational drug design and optimization based on the structure and biological function of the target. Additionally, this

approach can also be utilized for precision medicine through the development of targeted therapies, especially in cancer therapy, chronic conditions and infectious diseases.[22]

1.2.2 FDA-approved drugs discovered through TDD

Successful examples of target-based drug discovery are the selective tyrosine kinase inhibitor imatinib (Gleevec®), for the treatment of various forms of leukemia, as well as the identification and targeting of the HER2 receptor with trastuzumab (Herceptin®) in breast cancer therapy.[28,29] Further, the discovery of reverse transcriptase and integrase as key enzymes in the pathomechanism of HIV/AIDS led to the treatment with their respective inhibitors zidovudine and lamivudine (Combivir®) as well as raltegravir (Isentress®).[30,31] The chemical structures of the mentioned drugs are displayed in figure 2.

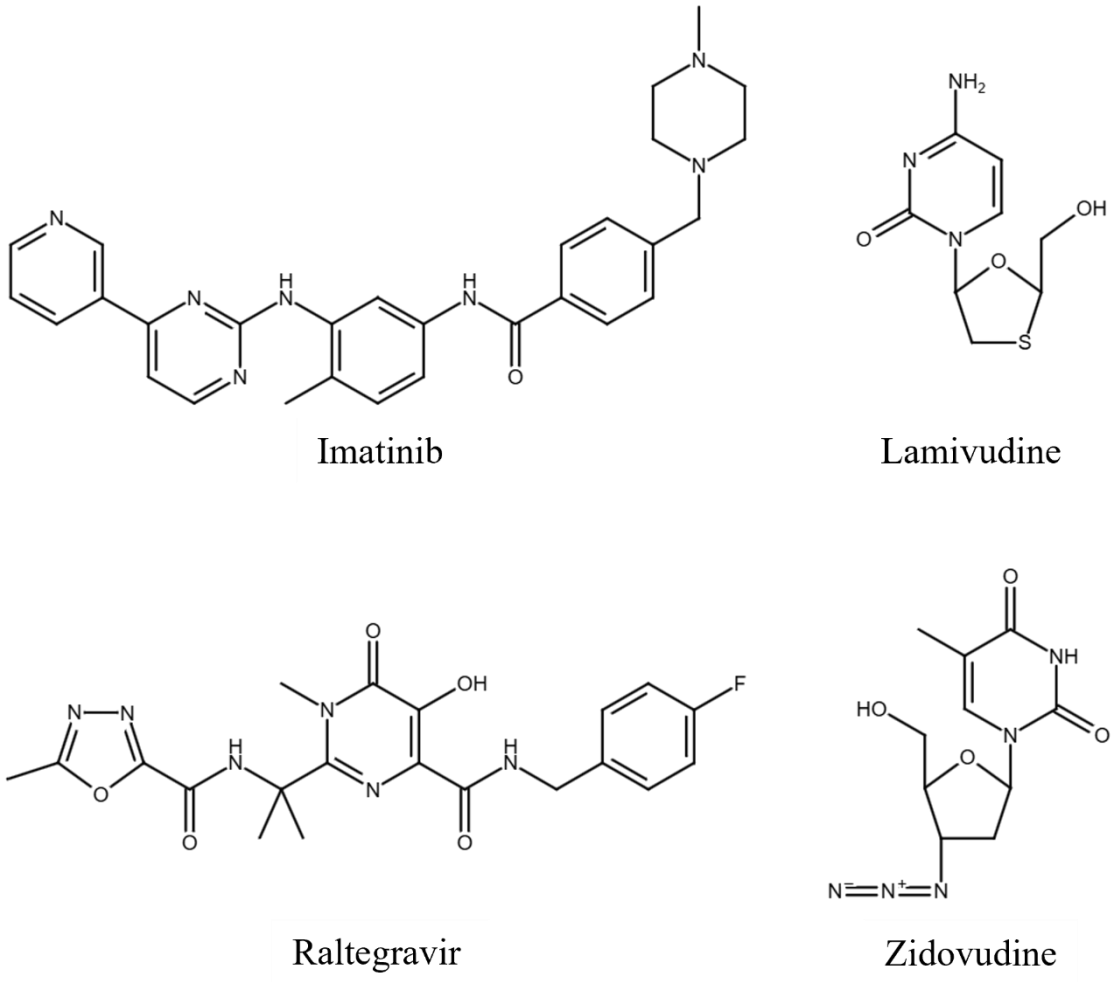

Figure 2: Molecular structures of FDA-approved active agents discovered through the target-based drug discovery approach.

Yet, TDD comes with its own limitations and challenges. As with many drug discovery approaches, the experimental validation of potential targets can be its time-consuming and

costly bottleneck. Another drawback is that not all targets validated *in vitro* or in animal models translate into effective human therapies illustrating translational gaps.[32] Additionally, many promising targets such as KRAS, TP53, STAT3, etc. that are commonly mutated in many cancer types were labelled as hard-to-drug or even undruggable due to a lack of suitable drug binding sites (*vide infra*).[33–36] However, some experts see the biggest issue for TDD in its reductionist approach, focusing on a single target and not accounting for the complexity of biological systems and disease networks, potentially leading to limited efficacy or unforeseen side effects. Moreover, critics of this drug discovery method even attribute the therapeutic properties of many approved drugs found through this approach to off-target effects.[12]

To summarize, target-based drug discovery remains a pivotal part of modern pharmaceutical research due to its rational and systematic approach. While this method has its own challenges related to biological complexity and translatability into clinical studies, ongoing developments in molecular biology, computational analyses, and high-throughput technologies continue to improve its efficiency and success rate, leading to more targeted and effective treatments.

1.3 Phenotypic drug discovery

Phenotypic drug discovery can be considered as the first drug discovery approach and always coexisted with TDD but was relegated to the background after the inception of the target-based approach.[2] However, one aspect that reignited the interest in phenotypic drug discovery was a review from Swinney and Anthony in 2011. This work compared the success rates of both drug discovery methods to identify first-in-class medication and had shown that the PDD approach managed to yield 50% more (18 vs. 27) compounds with FDA approval during the observed time period from 1999 to 2008.[1] The investigational strategy of PDD allows for the examination of a broader biological aspect and focusses on the modulation of (patho-)physiological relevant model systems by probing these empirically in an agnostic fashion were neither the target nor the mechanism are known.[2,5] With this concept it is possible to uncover molecules which can act as previously unknown or unexpected molecular targets or impact on novel signaling pathways, MoA or polypharmacological effects, thereby expanding the druggable space.[37] In this context, for the unbiased screenings the phenotype of each condition is examined very thoroughly with the modern definition of a phenotype including morphological changes of cells or tissue, expression of specific patterns of biomarkers, proteins, metabolites, other biomolecules, post-translational modifications (PTM) and/or behavioral traits.[13] These (molecular) signatures can then further be used to define states that represent a diseased, healthy

or cured condition. Additionally, great attention must be paid to the selection of suitable *in vitro* and *in vivo* models for PDD, as they must meet specific criteria which are detailed in the next chapter (*1.4 Model systems in phenotypic drug discovery*).

1.3.1 Process of phenotypic drug discovery

The underlaying process of phenotypic drug discovery starts with the testing of compounds on model systems, closely mimicking the investigated pathology aiming to discover active agents that induce a therapeutic effect. Following this is the examination of the mode of action and the molecular target(s) of the identified candidates. With the gained knowledge from the target deconvolution, the investigated drug candidates are then optimized in regard to their efficacy, potency, selectivity, and drug safety before they advance to clinical testing.[3] Due to the broader approach and its focus on physiological relevance, this method is well suited to find first-in-class drug candidates with novel MoAs or previously unknown molecular targets, making it especially valuable for conditions with multiple contributing factors.[2,37] Additionally, because of the functional readouts of this strategy, the hit compounds are more likely to show therapeutic effects in whole organisms, potentially reducing late-stage clinical failures.[37] However, phenotypic drug discovery also comes with disadvantages. The developed testing assays are highly complex and do not always enable high-throughput screening compared to TDD. Further, the subsequent target deconvolution step to determine the mode of action for a hit compound can be challenging and time-consuming and, in some cases, mechanistic uncertainty or a not fully identified target can remain, making the drug optimization step more difficult.[37,38]

To mitigate some of those drawbacks, PDD is continuously improved and expanded. Such improvements include high-content screenings to enhance throughput, as well as the integration of various omics techniques: Through the combination of the results from genomics, transcriptomics, proteomics, lipidomics, metabolomics and many more, in a multiomic investigation it is possible not only to obtain a comprehensive image of the pathomechanism of the investigated disease but also to interlink the findings on various levels through bioinformatics.[4,25] However, this strategy generates large amounts of data that require comprehensive analysis, for which machine learning and artificial intelligence can be used, potentially accelerating data processing and evaluation.[39–41] Another application for AI in the drug discovery space is drug repurposing with the goal of finding new uses for already approved medication, reducing costs and development time.[42,43] Further, an advanced computational program called Library of Integrated Network-Based Cellular Signatures (LINCS) was developed that converts drug-induced perturbation profiles into graphical representations such

as heat maps, networks, or display morphological features in a Cell Painting.[44] The Cell Painting assay is a fully automated high-content imaging method that incorporates different fluorescent dyes to label cellular components like the DNA, RNA, actin, endoplasmic reticulum (ER), mitochondria, Golgi apparatus and the plasma membrane, respectively. By taking high-resolution images and monitoring the cells over two weeks, it is possible to visualize the effect of the treatment on a morphological level thus define the phenotypic profile of the cells.[45] With these molecular signatures, a model condition can be defined. By comparing the respective end points of each state to the effects of the investigated hit compound, the molecule can then be fine-tuned to deliver the desired therapeutic outcome through modulating the diseased phenotype back into a healthy state (Figure 3).[2,5,46] A medication that manages to restore the healthy phenotype is arsenic trioxide (As_2O_3) in the treatment of acute promyelocytic leukemia (APL). This cancer form expresses a fusion protein encoded by the PML-RARα gene which arrests the myeloid cells in their promyelocytic stage. Even though not fully elucidated, part of the mechanism of action of the metallodrug involves the degradation of the fusion protein, fully differentiating the abnormal cells and therefore restoring their function again.[47] However, the computational profiling approach involving LINCS is currently limited to known molecular mechanisms at the pathway level and is utilized in the so-called mechanism-informed phenotypic drug discovery approach.[2,44]

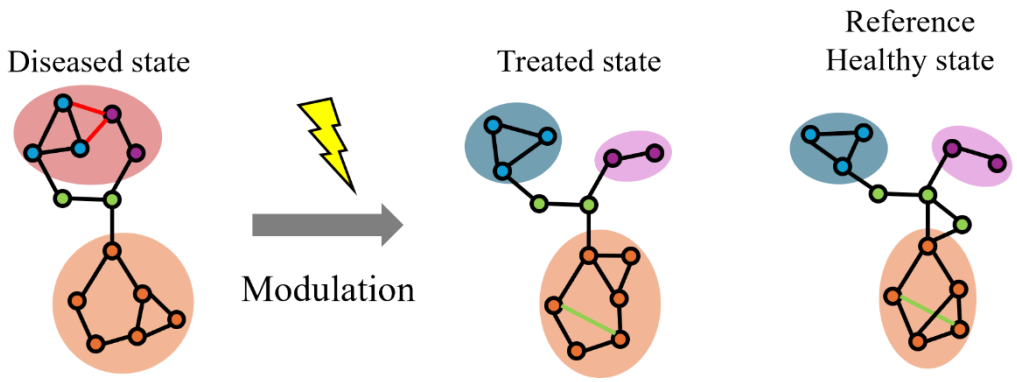

Figure 3: A schematic illustration of simple networks depicting the alteration of a diseased phenotype towards treated state resembling a healthy reference network after modulation. Each node represents a biomolecule that interacts with its directly connected neighbors. The colors of the nodes represent the affiliation to a functional group whereas the colored circles around multiple nodes group the biomolecules according to biological processes.

1.3.2 FDA-approved drugs discovered through PDD

The modern execution of phenotypic drug discovery successfully enabled novel therapies with approved drugs covering a broad scope of diseases, ranging from genetic disorders over infectious diseases to cancer treatment: risdiplam (Evrysdi®) was approved for the spinal muscular atrophy therapy, where inherited genetic disorders lead to progressive muscle weakness and wasting caused by degeneration and loss of motor neurons. The underlying mechanism is based on the absence of the survival of motor neuron 1 (SMN1) gene, whereby the homologous SMN2 gene can produce truncated analogues of the SMN protein. Administration of initial hit compounds led to the inclusion of exon 7 in the SMN2 pre-splicing process, resulting in the expression of the complete protein. This was detected in firefly luciferase transfected human embryonal kidney cells (HEK293H), confirmed by RT-PCR and luminescence measurement, and validated in patient-derived induced pluripotent stem cells.[48,49] Another example is the hepatitis C treatment daclatasvir (Daklinza®), which inhibits the non-enzymatic viral protein NS5A, thus blocking virus reproduction. This drug was discovered in a screening for the inhibition of virus replicons in Huh-7 hepatocellular carcinoma cells monitored through the replicon's respective reporter tags. In the end, over a million drug candidates were investigated until daclatasvir was found.[50] PDD proved the success of a combinatory treatment with ivacaftor and lumacaftor (Orkambi®) in cystic fibrosis by improving protein folding and reinstating the function of an affected chlorine channel in this disease's pathomechanism. The initial hit compound for the development of ivacaftor was revealed in a screening of gene edited Fischer rat thyroid cells with a specific mutation (p.Phe508del) responsible for cystic fibrosis, looking for an active agent that generated a signal in an apical membrane chloride current measurement. Lumacaftor, however, was revealed in another compound screening of a small molecule library against the mutated cystic fibrosis transmembrane conductance regulator protein. Later, the co-administration of both compounds was evaluated in patient derived cells.[51,52] Further, a new mechanism was discovered through the anti-cancer agent vorinostat (Zolinza®) for cutaneous T-cell lymphoma that modulates the histone acetylation process. In this instance, the drug was discovered during the optimization process of a hybrid polar compound intended for the induction of differentiation in transformed murine erythroleukemia cells. However, further investigation revealed that this small molecule strongly inhibits the activity of several histone deacetylases (HDACs), thus reopening the chromatin structure and activating transcription factors like p21.[53,54] The above mentioned examples are presented in figure 4.

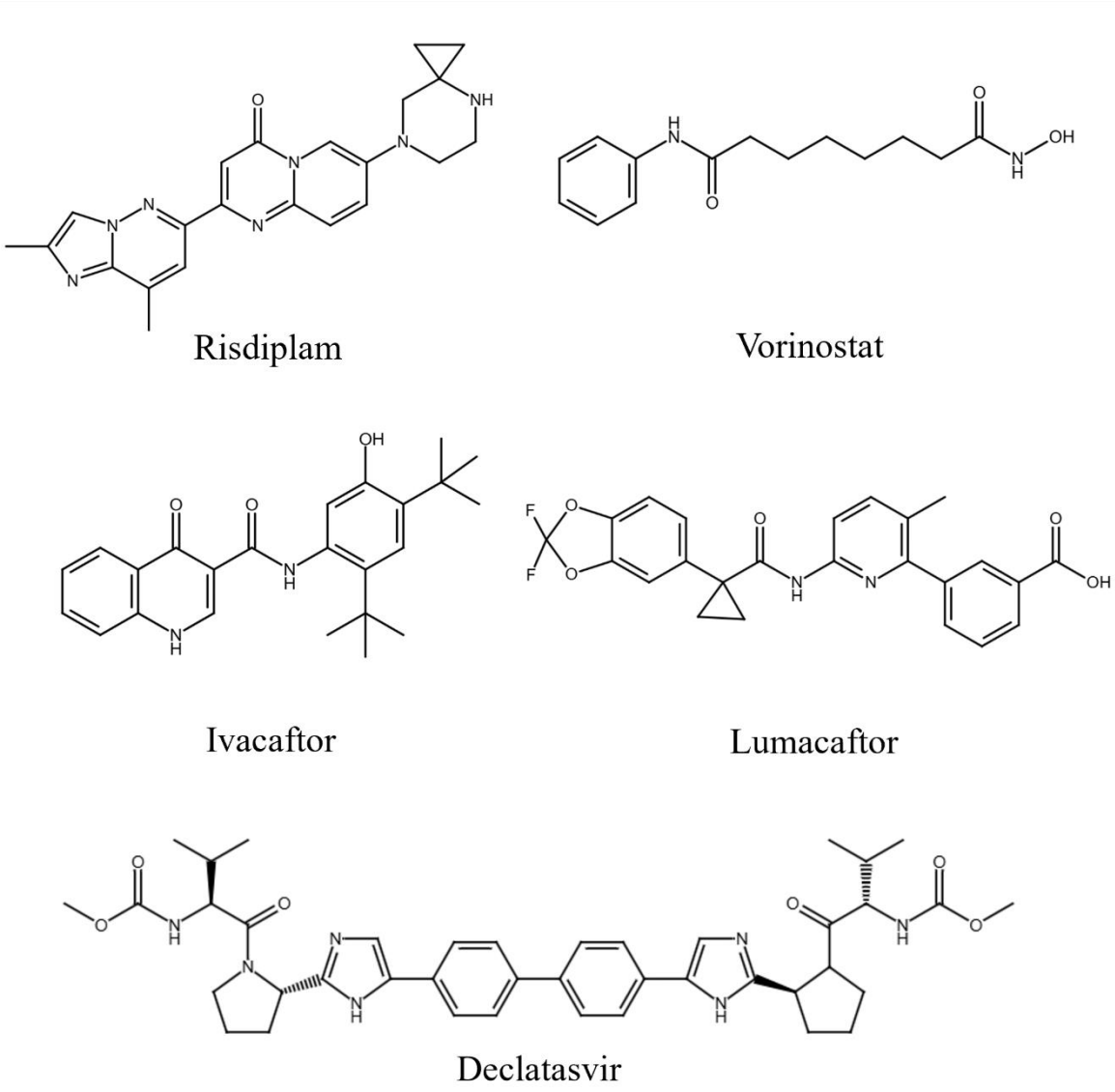

Figure 4: Molecular structures of FDA-approved compounds discovered through the phenotypic drug discovery approach.

1.3.3 Comparison of the TDD and PDD approaches

Comparing phenotypic drug discovery and target-based drug discovery shows that each approach has a very different starting point (Figure 5). In TDD the molecular target and its involvement in the diseases' mechanism are known from the beginning, whereas in PDD neither the target nor the underlying mechanism of the test substance is identified. Therefore, in phenotypic drug discovery the identification of the molecular target and the inherent MoA happens after a hit compound was obtained. Both strategies have different discovery focuses: PDD aims to identify functional biological effects and TDD emphasizes the interaction between the compound and the molecular target of interest. This aspect is also reflected in regards of throughput. As complex biological assays are used in PDD for their readout, the number of

substances analyzed is lower than in TDD, where work can be carried out in high throughput due to the simpler screening readouts. Taking each concept's approach into account, PDD is capable to yield a hit compound that can be a first-in-class drug candidate, whereas TDD owed to its methodology will give the best-in-class lead structure. Due to its complex nature and low throughput, PDD is an approach that currently is more feasible in an academic setting while TDD is successfully implemented in industry with its possibility to highly automize its streamlined strategy and efficiency in cost and time.[2,37,55]

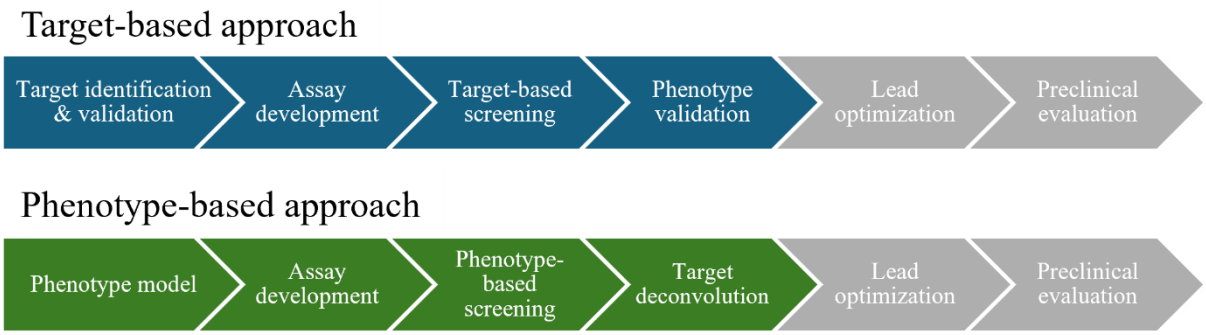

Figure 5: Comparison of the workflows of both drug discovery approaches with target-based on top starting with the identification of the molecular target and at the bottom PDD starting with the selection of a physiologically relevant model system.

In conclusion, through the implementation of omics techniques, improved assay designs and recent technological advancements in bioinformatics, PDD was able to attenuate its limitations in target identification and mode of action deconvolution. Thus, this approach provides a discovery platform based on representative disease models that reveals relevant targets, which in some cases are deemed hard-to-drug or even undruggable. Nonetheless a trend emerged in recent years, which uses a hybridized concept, where the broad exploration approach of PDD screening is followed by the subsequent target-based optimization strategy of TDD to further improve its success rate and biological relevance for active agents in drug discovery.[37]

1.4 Model systems in phenotypic drug discovery

Model systems are an indispensable tool in drug discovery, bridging the gap between a hypothesis and observable biological outcomes. They provide a controlled environment and display relevant disease mechanisms, thus enabling the investigation of modes of action, the identification and evaluation of molecular targets, as well as the assessment of safety aspects

and therapeutic efficacy.[2,37,56] Model systems can range from biochemical assays with simple readouts like enzyme inhibition, over 2D or 3D grown cells in culture for a more complex environment up to vertebrates that fully display systemic biological functions in an organism (Figure 6).[57,58] The following section will focus on 2D cell culture, what to consider when working with them in a PDD setting and what limitations they face in translational cancer research.

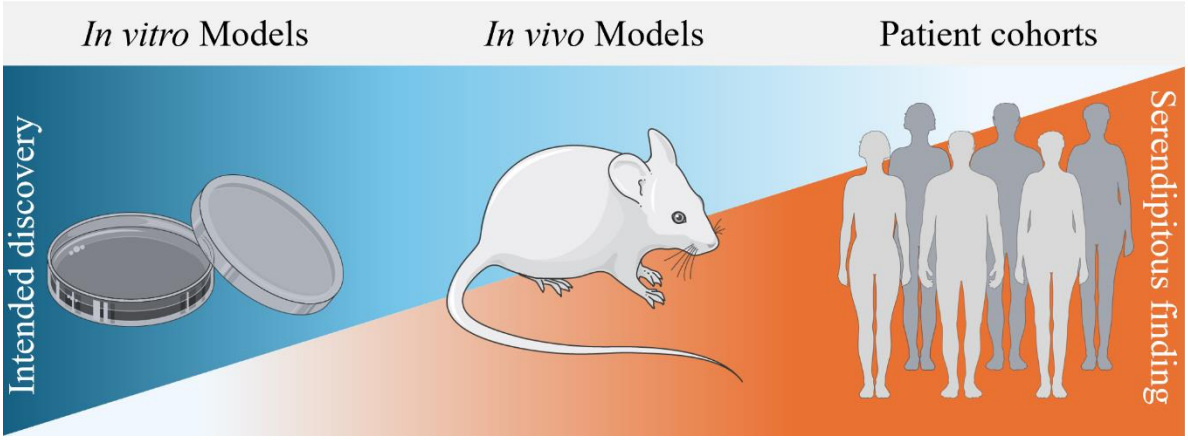

Figure 6: Various model systems used in drug discovery processes placed on a colored gradient that represents the likelihood for either planned discovery or serendipitous finding. Adapted from Vincent F. et al. This figure contains images from Servier Medical Art (https://smart.servier.com), licensed under CC BY 4.0 (https://creativecommons.org/licenses/by/4.0/).[2,59]

For the use in PDD, cellular models must meet certain requirements to be eligible: they should mimic the pathomechanism as closely as possible leading to better capturing of mechanistic and toxicity aspects as well as improving the odds to translate the initial findings into *in vivo* experiments and lastly the clinic. Further, the model systems need to be robust and reproducible providing measurable and quantifiable endpoints that can facilitate unbiased investigations. Finally, the obtained results should enable mode of action deconvolution, target identification and validation through various techniques such as integrated multiomic experiments or gene editing (e.g. CRISPR-Cas9), which also are used to assess potential off-target effects of the active agent.[25,32,55,60]

1.4.1 *In vitro* model systems

The most commonly used *in vitro* models for such investigations are cultures of a single cell type grown in a two-dimensional monolayer, providing a platform in a simplified biological environment. Building on the 2D monolayer setup, more complex models can be constructed that incorporate different cells in co-culture to examine potential disease-relevant interaction in

a heterogeneous tumor microenvironment.[60] Transwell inserts in cell plates can mimic cellular walls as in the gastrointestinal tract to investigate cell migration and invasion of certain tissue types or their molecular resorption.[61] Another source for cell samples is patient-derived material which can be used as primary cells conserving the phenotypic characteristics of the disease making this the ideal starting point for predictive, preventive and personalized medicine (3PM). But due to the limited lifespan of primary cells, they can also be immortalized or transformed into induced pluripotent stem cells (iPSC) to preserve a unique genetic composition for further drug screening and validation.[57,62]

Traditional 2D cell cultures have many benefits based on their ease of handling and maintenance leading to lower costs and a rapid turnover, thus making them especially suitable for pilot studies and high throughput screenings. Many assay protocols, reagents and analytical tool kits are optimized for this artificial cell platform allowing routine workflows, increasing reproducibility across experiments and laboratories, and thereby enabling basic mechanistic studies of cellular processes and signaling pathways. As Bortel *et al*. demonstrated in 2024, maintaining a highly homogenous cell population within an experiment significantly enhances the information density of multiomic readouts and therefore supporting a more comprehensive elucidation of the perturbation.[63] For target validation or additional mechanistic investigations cell lines can be genetically manipulated to express reporter molecules or to represent a model with knocked out or knocked down genetic function which is more challenging in complex organisms.[64] However, this reductionist setup has its drawbacks as the 2D model system is incapable of fully displaying organ-specific interactions or systemic responses like immune reactions thus providing weak predictive power for the translation of the investigated compound into clinical evaluation. To overcome the obstacle of cellular simplicity, more advanced platforms like the three-dimensional spheroids and organoids are employed to reproduce tissue structures and cell-cell interactions. An even higher degree of physiological relevance can be achieved with organ-on-a-chip models that combine growing cells on microfluidic devices mimicking a dynamic environmental flow.[57]

1.4.2 *In vivo* model systems

After the initial discovery phase using *in vitro* models, investigations are continued in more complex biological organisms using animal models to test the findings and their translatability into *in vivo* and lastly in human settings.[65] *In vivo* models display systemic effects of whole living organisms that the previously described *in vitro* models lack, by encompassing multiple layers of biological complexity. To gain insight into the organisms' responses to active agents,

the animal models are examined with samples from tissue or tumor showing local effects, whereby liver samples and body fluids like blood plasma display systemic effects.[66–69] These characteristics enable thorough investigations of multi-organ interactions and pharmacokinetics, thus providing information on absorption, distribution, metabolism, excretion (ADME) and toxicity of the tested small molecule, which can be extended to long-term effect screenings as well as examinations of immune responses or microbiome involvement.[58,65] Interestingly, those advantages are also considered responsible for the *in vitro – in vivo* discrepancy leading to translational gaps preventing drug candidates from entering the clinical phase.[65] Further aspects to consider when choosing an *in vivo* model are how a tumor was grown in the organism (xenograft VS allograft VS orthotopic VS induced) since for example the immune system is compromised within a xenograft.[70–73] Also, the way of administration (per oral (p. o.), intravenously (iv.), intraperitoneal (ip.), etc.) can influence the pharmacokinetic properties as effects like the liver-first-pass can be triggered, when a drug candidate is injected into the peritoneum.[74]

Even though traditional 2D cell cultures are simplified models to investigate the effects of drug candidates, they are essential for the initial discovery phase by providing a platform that is cost-effective, robust, suitable for high-throughput applications, and deliver first mechanistic insights. With the incorporation of the PDD approach, optimized pharmacokinetic and toxicological assays in physiological relevant cell models allow for an improved predictive power on the small molecule's behavior. To further increase biological contextualization and test for translatability, these *in vitro* findings are verified in animal models. However, the translation of such an *in vitro* result to an *in vivo* mode of action can be challenging. But with the implementation of sophisticated analytic methods like integrated multiomics they can provide a more complete image combining inter-organ relations, immune responses and metabolic activities, therefore leading to a global understanding of the drug candidate's mode of action thus increasing safety and success rates in drug development.

1.5 Covalent drug discovery

Covalent drugs exist already for over a century in our medicinal arsenal and comprise of small molecules which covalently bind to targets of interest.[75] The two most prominent active agents of this category are the nonsteroidal anti-inflammatory drug (NSAID) aspirin (acetylsalicylic acid) and the antibiotic penicillin. Aspirin inhibits the cyclooxygenase 1 (COX1) enzyme through acetylation of serine in its active site and thereby alleviating fever, inflammation and

pain symptoms.[76] Penicillin on the other hand binds to the enzyme D-alanine peptidase in gram-positive bacteria thus interfering in the formation of the bacteria's cell membrane.[77] In general, this class of medication has a two-step mechanism in which the active agent first is reversibly positioned in the protein's binding pocket as it resembles the targets' substrate in its transition state. During this phase, it is possible that through conformational changes of the protein a cryptic pocket might be revealed. Subsequently, a permanent or highly stable covalent bond is established with a nucleophilic amino acid within an active center or in its close proximity.[78,79] Responsible for the covalent bonds are reactive electrophilic functional groups of the compound, often referred to as "warheads". Ideally, these moieties have the properties of being biorthogonal, meaning that their reaction happens highly selectively in an organism without the interference from native biochemical processes. Examples of such warheads are acrylamide or β-lactam ring structures targeting the amino acids cysteine (Cys) and serine (Ser) respectively and are presented in table 1.

Table 1: Table with selected functional groups used in covalent drug design, including their molecular structure and the specific amino acid targets. Table adapted from Bhole R. P. et al.[80]

Name	Structure	Targets
Acrylamide	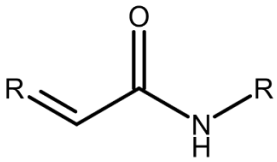	Cys
Aldehyde	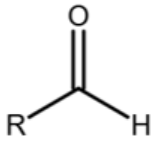	Lys, Thr, Tyr
Boronic acid	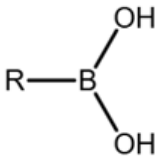	Asp, Ser, Thr
β-Lactam ring	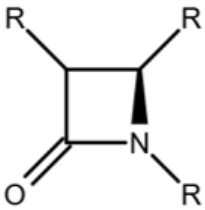	Ser
Nitrile	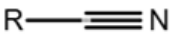	Asn, Gln, Trp

For more information on warheads and their selective targeting, the interested reader is referred to the following publications.[81–84] Compared to conventional medication, the covalent nature of the drug alters pharmacodynamic and pharmacokinetic properties considerably. However, exactly this reactivity also raises concerns about toxicity and possible off-target effects.[75,76] Nonetheless, developments in medicinal chemistry, structural biology, computational methods, and (chemo-)proteomic platforms have enabled new approaches of rational design strategies for selective covalent drug candidates.

1.5.1 Process of covalent drug discovery

The discovery process of covalent drug candidates can be accomplished by two different strategies. The ligand-first approach, with its design philosophy rooted in TDD, integrates mild electrophilic moieties into known bioactive structures with reversible properties to extend the effect duration through the covalent bond.[75] Successful drugs obtained through this method were osimertinib (Tagrisso®), a treatment for non-small cell lung cancer (NSCLC) selectively targeting the epidermal growth factor receptor (EGFR) with T790M mutation, and ibrutinib (Imbruvica®), which inhibits Bruton's tyrosine kinase (BTK) in chronic lymphocytic lymphoma (CLL) therapy.[85,86] In the electrophile-first approach, which takes techniques from both TDD and PDD, the emphasis lies on the discovery of covalent bonds through the screening of electrophilic agents or fragments against libraries comprising of proteins of interest.[75] Recent accomplishments achieved through the electrophile-first approach were the inhibitors nirmatrelvir, utilized as one component in the treatment of SARS-CoV-2 targeting the virus' main protease M^{pro}, and sotorasib (Lumakras®), which was FDA-approved in 2021 for the therapy of NSCLC with the specific mutation of KRAS(G12C), which was previously deemed as undruggable.[87,88] The molecular structures of these electrophilic covalent drugs are depicted in figure 7. The possibility to use nucleophilic covalent ligands had also been explored, but due to fewer available electrophilic reaction partners like cofactors and post-translational modifications currently only hydrazine containing compounds have been presented that inhibit the enzymes monoamine oxidase (MAO) A and B.[89]

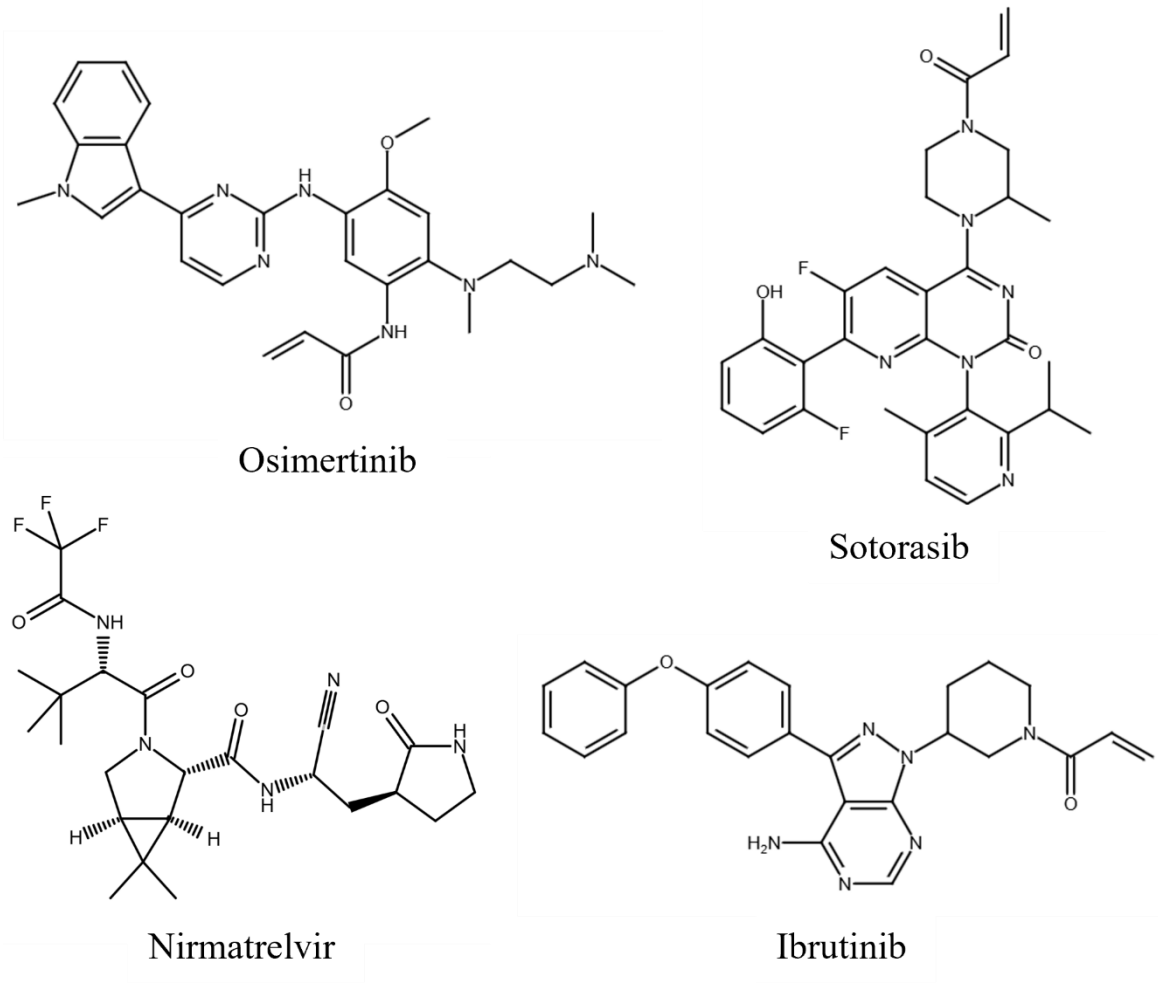

Figure 7: Molecular structures of FDA-approved covalent drugs. Osimertinib and ibrutinib are candidates discovered through the ligand-first approach, while nirmatrelvir and sotorasib were discovered through the electrophile-first approach.

Fragments of the electrophile-first approach have the properties of being simple molecule building blocks with a molecular weight usually under 300 Da and exhibit a strong ligand efficiency for the binding pocket driving the initial reversible interaction.[90,91] This simplification, compared to the screening of complete molecules, facilitates high-throughput screenings of the chemical space for key interaction hotspots and provides a solid starting point for the drug design process.[75,90,91] Screening libraries consist of a large collection of curated molecules and can have a theme or focus which ranges from biological targets such as specific kinases, g-protein coupled receptors (GPCR) or ion channel libraries over panels of cell lines and products from natural extracts to fragments with druglike characteristics to investigate for antitumor, antimicrobial or antiviral properties.[92–95] These platforms are distinguished into two types which are used in different phases of the drug discovery process. The first category of library assembles structurally diverse molecules and is used in the hit discovery phase to

increase the chances of discovering novel interactions whereas the second type is comprised of structurally similar agents which enable target validation, drug optimization and potentially the derivation of structure-activity relationships (SAR).[75,90,91] It was also reported that a technique from Next Generation Sequencing (NGS) was leveraged to highly increase the throughput rate by addition of DNA barcodes to compounds to screen thousands of molecules in parallel.[96] However, to obtain meaningful results from these screening approaches the quality of the created libraires is essential.

1.5.2 Chemoproteomic discovery platforms

Mass spectrometry-based methods that enable the discovery of protein targets and covalent compounds as well as their binding sites in complex biological systems are summarized under the umbrella term chemoproteomic platforms. These methods can be used to screen both covalent and non-covalent interactions, but the focus here will be on covalent interactions. The three main strategies behind this technology can be classified into affinity-based or activity-based interactions and label-free approaches.[5,75,97] Affinity-based protein profiling (AfBPP) is commonly used in the discovery of conventional drugs and utilizes a strong reversible interaction between a compound and its target(s). In this discovery concept the molecule is required to be functionalized *via* at least one reactive handle so it can be immobilized on a solid support in a later step during sample preparation for pulldown experiments. These affinity probes are then exposed to lysates from cells or tissue to create a non-covalent bond which must be strong enough to withstand multiple washing steps. Following this, the proteins are digested with tryptic enzymes into peptides which are then measured in a mass spectrometer and bioinformatically evaluated. However, the deconvolution of such datasets can be difficult due to the enrichment of both specific and non-specific interactors. Therefore, a competitive pulldown setup in which one half of the samples are pretreated with the investigated compound in its free form can provide results that can identify the selectivity of the drug candidate (Figure 8). Through the addition of further handles to the bioactive small molecule more functionalities can be exploited including fluorophores for colocalization studies, azide or alkyne moieties for Click Chemistry and photoactivatable groups that can form covalent crosslinks to proteins in proximity.[5,98,99]

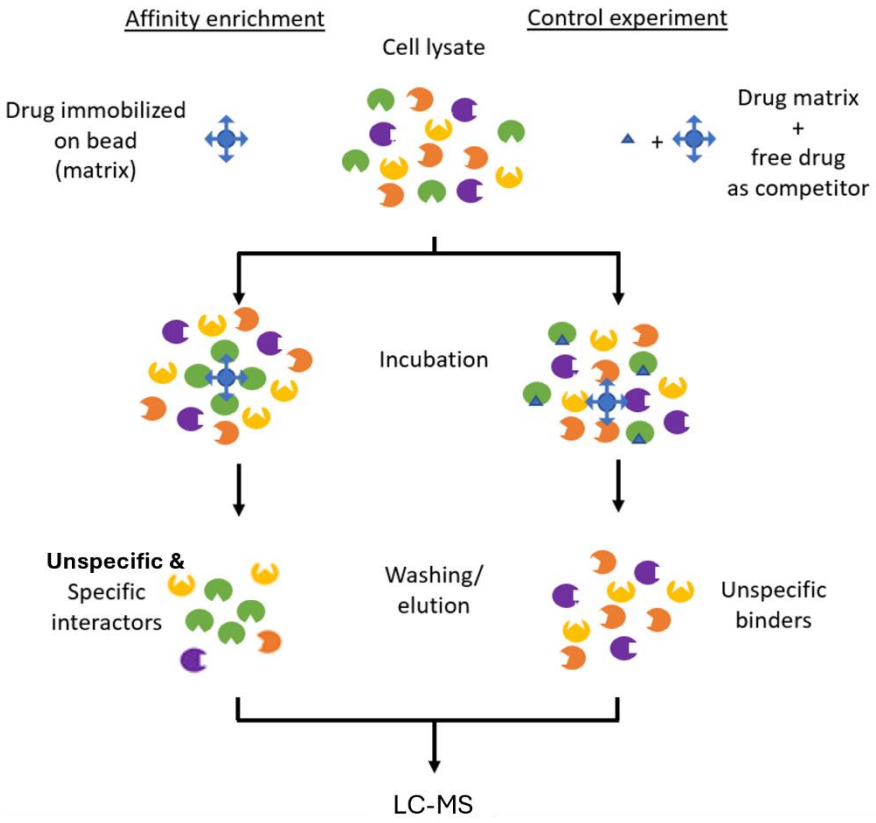

Figure 8: Illustration of a competitive affinity enrichment pull-down assay where in one sample set the immobilized compound of interest is immediately exposed to the whole cell lysate to let the specific as well as unspecific binding partner interact with the probe. The other sample set is pretreated with the free compound to saturate the specific binding sites before the affinity probe is exposed to this whole cell lysate to facilitate that only unspecific binding partners remain. After washing, elution and measurement of both sample sets, the results are compared differentially to obtain a list where only the specific interactors are presented.

The probes for activity-based protein profiling (AcBPP) are small molecules based on a parent drug, natural product or fragment, containing two functionalized handles with one of them being an electrophilic warhead designed to specifically interact with proteins that have active functions such as enzymes and the other handle acting as a reporter tag. Through the selection of the reactive groups the agent can be directed towards specific enzyme classes and again the reporter handle can be functionalized for copper(I)-catalyzed azide–alkyne cycloaddition (CuAAC) or imaging studies. However, in some situations the modification of the investigated drug candidate should be carefully considered since any addition to the lead structure will have an impact on the interaction between the compound and the targeted protein as well as on its general pharmacological aspects.[5,100,101] To circumvent this problem of structural modification of the hit compound and the subsequent changes in biological activity, label-free strategies can be applied. In this approach, target identification occurs through the observation of compound induced stability changes to target proteins measured *via* a chemical, proteolytic or thermal stimulus.[5,102] For instance, Limited Proteolysis (LiP) is a method that monitors how well treated

proteins can resist proteases resulting from changes in their conformation after compound-induced perturbations.[103] Building on that concept, Drug Affinity Response Target Stability (DARTS) was developed in which living cells or whole cell lysates are treated followed by either gel electrophoresis or MS measurement.[104] One of the latest entries in this category is the Peptide-Centric Local Stability Assay (PELSA), in which the samples are digested with protease solution in excess to quickly generate peptides after treatment, that are subsequently subjected to target identification studies.[105] An evolution from the proteolytic approaches are the techniques where the investigated sample sets are exposed to denaturing or oxidizing agents after the treatment with the examined compound to observe a shift in stability.[106] The thermal strategy Cellular Thermal Shift Assay (CETSA) examines the changes of protein melting points recorded as a curve from which the difference to the control sample is calculated. But this method requires validation of the findings through specific antibodies in a Western Blot which led to the development of an unbiased technique called Thermal Proteome Profiling (TPP).[107] This procedure incorporates Tandem Mass Tags (TMT) where each of the mass tags represents a different temperature point. Before measurement the samples are combined and yield a graph which is computed from all measuring points, however this approach needs mass spectrometers with high resolution (HR) MS2 capabilities.[108,109] The evolved iterations of the presented label-free approaches facilitate examinations on a proteome wide level for unbiased target identification, with each one being technically a stand-alone tool but cross verification through other approaches can greatly strengthen the identification of the target proteins. It also needs to be kept in mind that these methods cannot account for stability shifts stemming from post-translational or other modifications on affected proteins.[110,111] Nonetheless, for covalent drug discovery the activity-based protein profiling and label-free approach have proven to be very effective. In addition, technical developments and increasingly powerful computational methods are being used in conjunction with all of the above-described approaches. *In silico* tools like molecular modelling and docking studies are capable of simulating the protein of interest in its three-dimensional conformation revealing potential binding pockets or show drug-target interactions, guiding the rational design to next generation covalent drug candidates.[112]

1.5.3 Covalent drug candidate optimization

With a suitable hit compound identified after the screening and discovery process, the subsequent rational design strategies enhance the molecule in several key aspects: Firstly, the selectivity is improved through directing the compound at non-conserved motifs exclusive in disease relevant protein(s), reducing off-target interactions. This is followed by carefully

adjusting the reactivity of the warhead towards the aimed nucleophilic residue for the covalent bond. In this step moderately reactive functional moieties are preferred, to minimize off-target binding. Furthermore, the initial non-covalent interaction, which positions the active agent in the targeted binding pocket, is optimized to ensure that the covalent bond is only formed at the intended position to even further enhance the selectivity of the active agent.[75,113,114]

Strengths of covalent drugs derive from the covalent bond resulting in prolonged target engagement thus potentially enabling lower or fewer dosages. Strategies of this compound class also allow for the targeting of proteins with challenging binding sites and might be employed to overcome acquired resistances to conventional reversable drugs. However, due to the covalent bond, the sustained effect as well as the potentially resulting health risks, including non-selective interactions with proteins that might trigger severe adverse effects such as organ toxicity or immune responses, might be omitted through a proteome wide screening for off-targets.[75,115,116]

Fueled by recent successes with covalent drugs and based on technological advances, it was possible to show that this medication class has progressed from serendipitous discoveries to a rational design approach. Constant improvements in screening methods, structure-based drug design and (chemo-)proteomic platforms enable the efficient optimization of drug candidates regarding their potency, reactivity and selectivity. Despite reservations about potential toxicity and off-target aspects, the covalent drug discovery strategy demonstrated to be an effective approach especially suited for targets believed to be hard-to-drug or undruggable. Additionally, to highlight how quickly this field is evolving, in 2024 Popow *et al*. presented heterobifunctional compounds that effectively degraded 13 out of the 17 most common KRAS mutation variants. These novel compounds added the Proteolysis Targeting Chimeras (PROTAC) technology to modern covalent drugs.[117]

1.6 (Chemo-)Proteomics

In the following chapter, the key concepts, devices and methodologies utilized in this dissertation will be elaborated. This will cover the fundamentals of (chemo-)proteomics, over to the description of instrumental setup of the LC-MS/MS, to the intricacies of sample preparation and data collection in order to obtain robust and meaningful results.

Proteomics is a bioanalytical discipline that specializes in the investigation of all proteins present in a sample and examines them on a quantitative and qualitative level. The human

proteome comprises of almost 20 000 proteins that carry out a variety of functions, including the assembly of structural or motor units, enzymatic processes, transport functions, signal transduction, and many more.[118–120]

1.6.1 Protein chemistry

Proteins are biopolymers composed of 20 proteinogenic amino acids (AA), or 21 if selenocysteine is included, whereby these building blocks are linked together by peptide bonds formed through a condensation reaction between an amino group and a carboxyl group, resulting in a specific AA sequence of the protein, also known as primary structure.[120,121] Other levels used to describe a protein are the secondary structure, which are motifs that can occur at certain points in the sequence, and the tertiary structure, describing how the entire sequence folds in the three-dimensional space under physiological conditions. If several peptide strands are organized in subunits, it is described in the quaternary structure. The functionality of a protein ultimately stems from the sequence of amino acids and its three-dimensional structures.[120] In some cases, proteins are functionalized with other biomolecules, including phosphates, ubiquitin, or sugars, which can trigger an activated state in the signaling cascade, prepare for transport, or their degradation. These so-called post-translational modifications give the proteins further biological context but make comprehensive investigations more complicated.[122,123] In recent years, advanced proteomic approaches have been extended towards investigating PTMs such as phospho-proteomics, which examines phosphorylation and dephosphorylation processes within signaling pathways, to elucidate how they are affected by diseases or pathomechanisms.[124]

By comparing proteins differentially, changes in the proteome can be identified, revealing which proteins are present and in what quantities, providing clues about their interactions and regulation processes in disease or biological states.[125] Using a suitable study design, these investigations can be expanded to include additional aspects such as the temporal resolution of a therapeutic or biological effect, where an experiment is started in parallel on a large scale with subsets of it being stopped and measured at defined time intervals, or dose dependencies, in titration-like approaches.[126,127]

1.6.2 Chemoproteomics

Chemoproteomics has evolved from proteomics and expands these experiments by including chemical probes into large-scale mass spectrometric investigations within physiologically relevant systems. Through the interactions of the compound of interest with the proteome,

protein targets can be identified, their binding sites examined, and the potential therapeutic effects of the drug candidate on the organism investigated. The aim is to identify specific targets across the proteome, assign them to pathways and thus elucidate a possible mode of action. In these experiments, selective reactions of the probes with the proteins play the main role, whereby a distinction can be made between activity-based, affinity-based and label-free approaches.[97,128,129] Description of these approaches with practical examples have been given in the previous section "*1.5.2 Chemoproteomic discovery platforms"* (*vide infra*).

1.6.3 Sample preparation for proteomic analysis

Depending on the objective of the scientific question, the analytical approaches for the experiments must be determined for the proteomic investigations, with the two most common methods being the top-down and bottom-up approaches. Both analytical methods involve similar steps, such as the separation of the samples *via* 2D gel electrophoresis or LC, measurement using a mass spectrometer, with subsequent bioinformatic evaluation and interpretation of the results.[125,130] Either method starts with whole cell lysates (WCL) of each sample, containing the entire content of the cells under investigation. These WCL can be generated by using an ultrasonic probe, followed by immediate heating to 95 °C to denature all released proteins, especially proteases from the proteasome, to minimize non-specific peptide cleavages.[63] Additionally, for proteomics experiments cells can also be separated into cytoplasmic and nuclear fractions giving localized information at subcellular resolution, providing a deeper insight into the underlying perturbations for the evaluation of the mode of action.[131]

If the research question revolves around the examination of all proteoforms within the proteome, the top-down approach would be the method of choice, since it focuses on the completely preserved proteins and their potential PTM patterns. However, this technique also has its disadvantages: Due to the heterogenous physicochemical properties of the various native proteins, separation cannot be performed as efficiently and the evaluation of the spectra is complicated by the multiple charges and increased isotope content, stemming from the size of the analytes (proteins > 50 kDa) which in turn requires a high-resolution mass spectrometer (HR-MS) to detect and distinguish those subtleties.[130,132]

The approach predominantly used in proteomics is the bottom-up analysis. The difference to the top-down approach is that the protein samples are enzymatically digested into peptides before MS measurement. For this purpose, the proteins are denatured by reagents like dithiothreitol (DTT) or tris(2-carboxyethyl) phosphine (TCEP), which first reduce present

disulfide bridges followed by their alkylation through iodoacetamide (IAA) or 2-chloroethylamine (2-CAM). The addition of highly purified proteases such as trypsin and Lys-C generate peptide chains with enzyme-specific cleaving sites. Finally, those peptides are then separated by LC, ionized by techniques such as Atmospheric Pressure Chemical Ionization (APCI) or Electrospray Ionization (ESI), followed by the detection of those ions according to their mass-to-charge (m/z) values in the mass spectrometer. The proteins are identified through two levels: first, the spectra of the ionized peptides are recorded (MS1) in the mass spectrometer, thereby determining the exact mass. The peptides are then fractionated, and the resulting spectra (MS2) provide information on the composition of the amino acid sequences. The combined results from MS1 and MS2 are then compared to *in silico* generated spectra from databases like UniProt, which allows for the identification of the detected peptides. The use of the bottom-up method enables high-throughput measurement, which facilitates the identification of large numbers of proteins. However, this also generates large volumes of data, which requires bioinformatic evaluation of the findings.[63,125,131]

1.6.4 Liquid chromatography tandem mass spectrometry

Through the implementation of the liquid chromatography coupled tandem mass spectrometry in proteomics investigations, it became possible to analyze samples in a continuous manner. This device generally consists of three units: a high-performance liquid chromatography (HPLC) system with a specialized separation column, an ionization source, and a mass analyzer. Due to this design, the LC-MS/MS can be utilized for a wide range of analytes by carefully selecting and adjusting the respective components. This flexibility in combination with powerful bioinformatic evaluation strategies, has established the LC-MS/MS as a pivotal tool in many areas of research such as drug discovery, molecular biology, cancer research and many more.[133,134] The following sections will describe the functionality and technical aspects of the device used in this thesis for (chemo-)proteomic investigations.

The first step in the measurement with an LC-MS/MS is to reduce the complexity in the contents of a sample mixture using a HPLC module. Liquid chromatography is an analytical method based on the interaction of analytes in the eluent (mobile phase) with the packing of a separation column (stationary phase). The stronger the interaction with the particles, the longer the analytes are retained in the column, resulting in separation along the time axis, thus creating a chromatogram. A LC unit consists of a solvent reservoir, a high-pressure pump, an injector coupled with an autosampler, a column, and a detector, which in this setup is a mass analyzer. Due to this design and respective elements, practically any type of analyte can be separated and

analyzed. Chromatographic parameters should be optimized for the analytes at hand, for example by adapting the solvent composition, an eluent gradient, the flow rate, core column parameters, as well as the selection of an appropriate column type that separates the analytes based on their physicochemical properties such as size, polarity, and chirality. Owing to this versatility, as well as their high sensitivity and robust measurements, LC devices have become a staple in many areas such as chemical quality assurance, bioanalytical examination of clinical samples and monitoring of environmental pollution.[135,136]

One of the most used modes for HPLC applications in biochemical analysis and drug development is reversed-phased liquid chromatography (RPLC), in which the mobile phase is polar, and the particles of the stationary phase are functionalized with aliphatic C18-chains. In proteomics, this type is used to separate the peptides in the samples after the enzymatic digestion based on their hydrophobic properties. Therefore, a gradient can be applied in the mobile phase, starting with an acidified aqueous solution and continuously increasing the organic content of the eluent. This causes hydrophilic peptides to elute first and more hydrophobic peptides to be then gradually released to the ionization unit over time, improving the sequence coverage of the proteome under investigation.[137,138]

The element that bridges the high- and low-pressure areas in the LC-MS is a capillary to which a high voltage between 1 and 5 kV is applied, thereby enabling Electrospray Ionization.[139] Depending on the polarity of the applied potential to the capillary, the device can be run in either positive or negative analysis mode. ESI is a robust and highly efficient ionization technique that can be used to examine femtomolar concentrations of analytes but is also gentle enough to minimize in-source fragmentation. This makes a wide range of small and large molecules amenable to MS measurement with the ionization process occurring in three steps: after the separation *via* LC, the analytes are pressed through the capillary into a heated chamber at atmospheric pressure where aerosol droplets are formed that have the same polarity as the applied voltage. Leaving the capillary tip through a Taylor conus, the solvents of the droplets start to evaporate until a critical point in surface charge density is reached, leading to a Coulomb explosion shrinking the droplet size. This process continues until only the analytes are left, receiving the electric charge and finally transitioning from the liquid phase to the gaseous. The resulting ions are then pulled into the focusing cone at the opposite end of the capillary, leading them to the entrance of the low-pressure area and accelerating the analytes towards the mass analyzer.[140–142]

In proteomics and other omics techniques the nano versions of liquid chromatography (nLC) and electrospray ionization (nESI) have proven to be very effective, due to several advantages over conventional LC-ESI setups. The use of separation columns with inner diameters of less than 100 µm, particle sizes between 1.7 and 5 µm, and flow rates of nanoliters per minute increase the separation efficiency, selectivity and sensitivity, which is beneficial for the detection of peptides deriving from low-abundant proteins.[143] The miniaturized dimensions of nESI enable the generation of finer aerosol droplets, improving the ionization of the analytes and therefore even further increasing the sensitivity.[144] In addition, the combination of nLC and nESI has the advantage of consuming less solvents, but at the expense of lower throughput due to longer measurement times as well as meticulous sample preparation to prevent clogging of capillary system.[145,146]

After the analytes have been transferred to the gaseous phase, they are led into the mass spectrometer, which operates under vacuum. The mass analyzer built into the system sorts the ions according to their m/z ratio through the influence of electric and/or magnetic fields before they reach a detector. Due to the growing demand for the analysis of clinical, pharmaceutical, and environmental samples using omics techniques in a high-throughput fashion, mass spectrometers have been continuously improved to enable in-depth analysis of even low-abundant analytes thus allowing for a more detailed description of (bio)chemical or environmental processes.[147] The following paragraphs will describe the most commonly used mass analyzers including quadrupole, ion trap, Orbitrap and time-of-flight devices.

Quadrupole mass analyzer consist of four parallel metal rods, where the opposing pairs have the same polarity with direct current (DC) and altering radio frequencies (RF) overlayed. This configuration creates a field between the four rods that stabilizes an oscillating trajectory for a small m/z range, thereby transporting ions or filtering them by varying the frequencies and voltages. One advantage of quadrupoles is their robust and simple design, which makes them affordable for mass spectrometry but with lower resolution and mass ranges than other mass analyzers.[148] A mass spectrometer that is frequently selected for its precision in routine monitoring tasks is the triple quadrupole (QqQ) mass spectrometer, which is the combination of three quadrupoles connected in series and is well suited for the targeted investigation of clinical studies as well as the control of environmental or factory processes.[147,149,150]

A further mass analyzer that has the capability to trap ions in the center of a small space through electric fields and store them temporarily is the ion trap. Harmonic excitation of frequencies can generate oscillations in those fields that eject ions within selected m/z windows from the

device in order to forward them to a detector or to fragment them sequentially to obtain structural information. Due to the repulsion through the Coulomb effect exerted from mutually charged particles, a limited number of ions can fit inside the trap, which is why devices with varying sizes and geometric shapes had been developed.[147] Ion traps offer the advantage of being sensitive and efficient, and it is also possible to perform fragmentation, but their scan rate is slower and overfilling of the trap can reduce the resolution of spectra.[151,152]

The Orbitrap is a high-resolution mass analyzer consisting of a spindle-shaped electrode surrounded by a cylindrical, statically charged electrode. An electrostatic potential is created between these two electrodes, which can stabilize ions in an orbital trajectory around the spindle. In addition to the rotation around the spindle, a movement in the form of a harmonic oscillator occurs along the longitudinal axis, with the frequency depending on the mass-to-charge ratio of the ions. Finally, Fourier transformation enables the corresponding mass spectra to be calculated from the frequency of all the recorded ions. Advantages of this instrument are its high mass accuracy and its capability to simultaneously analyze large numbers of analytes. However, drawbacks are the high acquisition costs of the device, and the evaluation as well as the interpretation of the measured data can be very time consuming.[147,153,154]

In time-of-flight (TOF) measurements, the analyte ions are accelerated in a static electric field and sent through a field-free space, where the differences in flight time resulting from the m/z ratios, with ions that have smaller m/z values arriving earlier at the detector than larger ones. One technical option to extend the flight time and thus increase the mass resolution and sensitivity is to install reflector plates in the analyzer. TOF mass analyzers offer very fast measurements with large dynamic ranges for high-throughput analysis of biomolecules. Yet, to fully utilize the potential of this instrument, it must be ensured that the initial acceleration voltage for the ions, as well as the temperature and vacuum in the drift chamber remain constant, as even small differences can lead to measurable deviations. Therefore, regular external calibration with standards is required to maintain consistent measurements. Furthermore, to obtain structural information a TOF unit must be combined with another mass analyzer or collision cell.[147,155]

1.6.5 Tandem mass spectrometry

To compensate for the shortcomings of individual devices, one or more mass analyzers are combined in so-called hybrid or tandem mass spectrometers (MS/MS). One such mass spectrometer is the timsTOF™ Pro from Bruker Daltonics, Inc., which incorporates a trapped ion mobility spectrometry (TIMS) analyzer, a quadrupole with a collision cell, and a TOF

analyzer to enable high sensitivity, measurement speed, and dynamic ranges for the analysis of complex biological samples (Figure 9).[147,156]

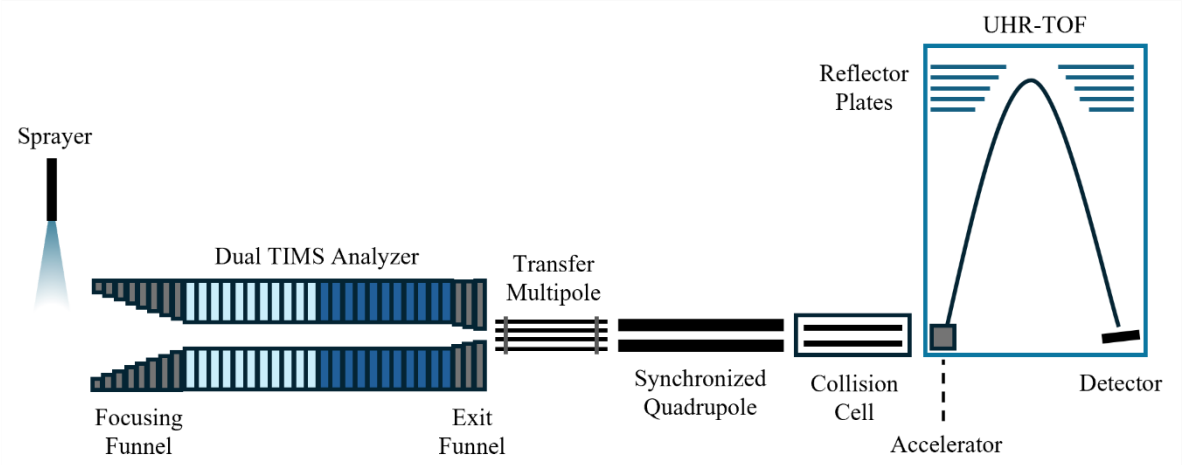

Figure 9: Schematic diagram of the components of the Bruker timsTOF Pro™. The capillary of the Sprayer unit is positioned orthogonally to the entrance of the trapped ion mobility spectrometry (TIMS) analyzer, with the first section, where the accumulation happens, shown in light blue and the second section, where the analytes are gradually released, depicted in dark blue. The ions are further transferred through a multipole to a quadrupole that is synchronized to the releases of the second TIMS section, followed by the collision cell. Finally, the analytes are measured in an ultra-high-resolution time-of-flight mass analyzer (UHR-TOF).

The TIMS analyzer utilizes a special form of ion mobility spectrometry (IMS) in which the generated ions are separated by the simultaneous application of electric fields and a constant gas flow, thereby reducing the complexity of the samples by exploiting another dimension. The heart of this analyzer are stacked ring electrodes, which are divided into four independent segments and through which a neutral carrier gas passes through. This electrode stack consists of two regions, with ions being accumulated in the first section through an RF potential, followed by their sequential release in the second section *via* an electric field gradient that counters the carrier gas. The collision cross section (CCS) of the respective ions allows for an additional dimension of separation due to the different ion mobilities making it possible to distinguish between isomers, conformers, and isobars with same m/z values. While the analyte ions are separated in the second section, the next ion packet is collected in section 1 in parallel, resulting in an almost complete measurement of all generated ions. Furthermore, a method called Parallel Acquisition Sequential Fragmentation (PASEF) is used throughout the entire procedure, in which the fragmentation process is coordinated with the ion mobility measurement.[157] After separation by the TIMS unit and subsequent transfer through a

quadruple, the ions are registered in ultra-high-resolution TOF analyzer using a multi-channel plate ion detector, that converts the signals into spectra.[147,156]

1.6.6 Data acquisition

For untargeted measurements, software-based technologies are additionally employed during the recording of features to enable a fast and automated process of fragmentation (MS2 spectra) and thus identification of selected analyte ions. The two most common programs for this are data-dependent acquisition (DDA) and data-independent acquisition (DIA), with the respective schematic processes presented in figure 10.[158]

In DDA, precursors from the MS1 survey scan are selected through the Top N principle, in which the most intense ions from each measurement cycle are separately isolated and fragmented. The resulting MS2 spectra are of very high quality, as they can be traced back to exactly one precursor ion, and the results can be interpreted using the corresponding DDA workflows. However, DDA also has disadvantages that lie in the stochastic nature as only the most intense peaks are selected for fragmentation, resulting in a less detailed analysis of the entire sample set. To circumvent this adverse effect, dynamic exclusion can be implemented, which ignores the precursors selected in the previous measurement cycle for a short period of time so that less intense analytes are also measured. Additionally, fluctuations between measurement runs might occur, which can be compensated by using bioinformatic tools.[158–160]

In contrast to DDA, in data-independent acquisition mode no individual precursors are selected but instead defined m/z ranges are systematically superimposed over the entire MS1 survey scan with all ions within those windows being fragmented. This strategy is intended to make the MS measurements independent from the abundance problem of DDA and enables investigations with very large proteome coverage and robust results. MS2 spectra in DIA contain information from all precursors of the respective m/z window and are therefore much more complex, which in turn requires advanced bioinformatic techniques and proprietary software solutions to deconvolute the corresponding content. Furthermore, the measured data sets can be reexamined at a later point in time for new scientific questions, for example by comparing them with specific spectral libraires.[158,159,161]

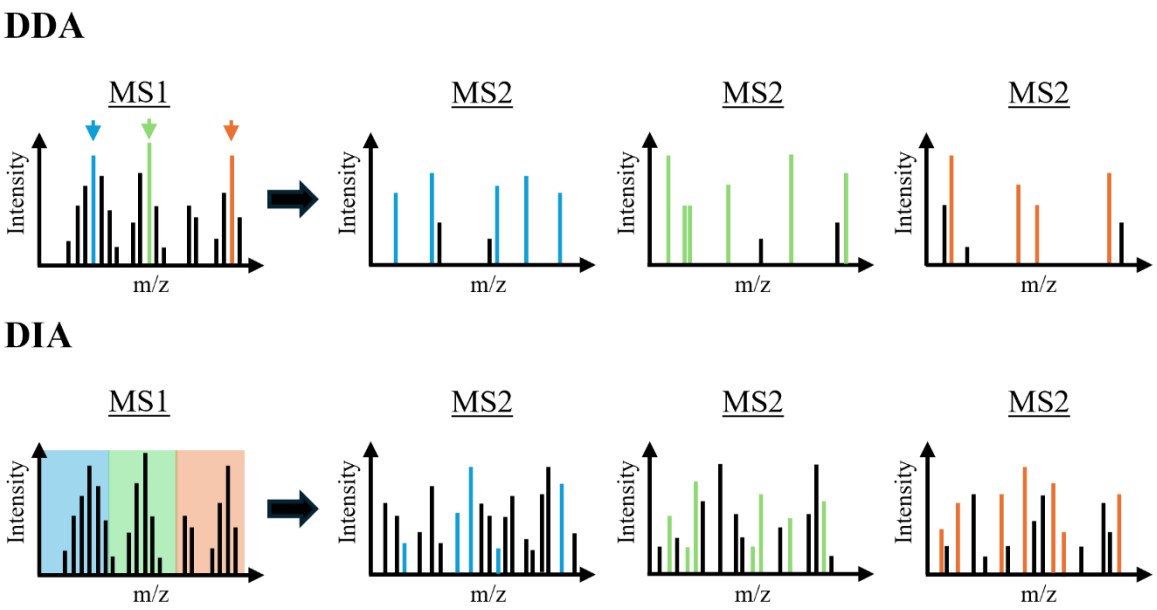

Figure 10: Comparison of data-dependent acquisition (DDA) and data-independent acquisition (DIA) processes: the top sequence depicts the DDA process in which the most intense ions from the MS1 are selected through the Top N principle (shown as arrows) for the fragmentation. The resulting MS2 spectra are of high quality as each spectrum derives from the respective precursor. The bottom sequence shows the DIA process, where a m/z window is superimposed over the entire MS1 with all ions within those windows being fragmented. Here, the MS2 spectra contain information from all precursors in each window which enables a larger coverage of the proteome but makes the interpretation more complex.

1.6.7 Protein identification

Proteins are identified in DDA from the measured peptide spectra through a spectrum-centric search utilizing specialized search engines which are integrated into programs like MaxQuant, Proteome Discoverer, or FragPipe.[162–164] For the search, experiment-relevant parameters are selected and protein sequence data, which are obtained for example from the UniProt database, are *in silico* digested and then compared against the measured spectra.[165] The result of this process is a scored list of amino acid sequences determined by peptide-spectrum matches (PSM), with exactly one sequence being assigned to each precursor. To evaluate the statistical confidence of the identifications, several calculations are performed taking abundance into account, such as the Benjamini-Hochberg correction for multiple testing, as well as comparisons with randomly generated decoy datasets to determine the false discovery rate (FDR), which ultimately yield p-values for the identified proteins.[125,166,167]

For the DIA approach, there are library-based and library-free strategies for identifying proteins. In library-based identifications, the experimental spectra are compared with those from spectral libraries, which in most cases originate form DDA experiments. These libraries contain information on the m/z-values of precursors and their fragmentation ions, retention times, and

signal intensities, which are used to assign a statistical score to the peptides, from which proteins can then be derived.[161] The advantage of the library-based method lies in the high reliability with which identification at the peptide level through the comparison with spectral libraries occurs and its capability to discover low-abundant proteins. However, the disadvantages of this approach are that generating high-quality libraries is costly and labor-intensive.[161,168] In analyses, using the library-free method, the raw data must be first deconvoluted using advanced algorithms, which generate datasets that can be directly compared to *in silico* predictions from sequence data to search for matches of calculated retention times and fragmentation patterns. Although this strategy eliminates the need for prior (DDA) measurements and facilitates comprehensive investigations, library-free identification requires significant computational power and depends on the efficiency of the detection algorithm as well as the subsequent bioinformatic parameters such as match score and FDR.[161,169,170]

1.6.8 Quantification

After measurement and data acquisition, the obtained results must be bioinformatically processed by translating signal intensities into concentrations or amounts. This can be achieved through two different approaches categorized into quantification methods that either utilize molecular labels or are label-free.[125,171]

Quantification strategies that use chemical labeling include techniques such as Tandem Mass Tags (TMT) and Isobaric Tags for Relative and Absolute Quantification (iTRAQ), in which the peptides in the samples are covalently labeled after enzymatic digestion. During the fractionation step of the MS measurement, reporter ions with specific masses are released, that can be assigned to a sample set. This labeling allows for the combination of multiple separate experiments into one pool, measuring them simultaneously and the subsequent calculation of the number of proteins is based on the different intensity ratios of the respective reporter ions, thus reducing the variance between individual measurement runs.[125,172,173] However, labeling can lead to an effect that isolates different precursors with similar m/z-values and retention times, thereby distorting the ratios during quantification.[174] For absolute quantification, this approach requires the addition of an internal standard to the samples, whose signal is compared to that of an endogenous protein to calculate the concentration or quantity from the resulting ratio.[171]

One method that introduces a label metabolically into peptides is Stable Isotope Labelling by Amino Acids in Cell Culture (SILAC). In this technique, cells are grown in cell culture media in which specific amino acids are labelled with deuterium (^{2}H), carbon-13 (^{13}C) and

nitrogen-15 (^{15}N), thereby generating a light, medium or heavy tag in newly synthesized proteins. The differently labelled samples are then combined in equal parts, digested, and measured. From the signal intensities and the resulting mass shifts, conclusions can be drawn about the quantities and ratios of the proteins present. Applying SILAC, many cell culture systems can be relatively quantified in a robust, simple and precise manner, but these experiments require a mass spectrometer with very high mass resolution and time of up to five doubling cycles for the tags to be fully incorporated.[175]

In label-free quantification (LFQ), there are two approaches for determining relative quantities: intensity-based calculations and spectral counting. For the intensity-based method, extracted ion chromatograms (XIC) of peptides are integrated, with the resulting peak areas set to be directly proportional to the amount of peptide present, thus enabling the comparison across the investigated samples. Spectral counting on the other hand infers the number of proteins in the entire sample set from the sum of MS2 spectra being assigned to a precursor.[176–178] Label-free quantification is a cheap method and can be applied to studies with large sample numbers, nonetheless this strategy is sensitive to run-to-run variations, which can be diminished through effective normalization.[179,180] In contrast, the label-based approaches permit more accurate quantification but are not suitable for high-throughput and large-scale studies due to higher costs and additional steps in sample preparation.[125,181]

1.6.9 Statistical evaluation

The initial statistical analysis of the data is performed in software such as Perseus from the MaxQuant Suite, Spectronaut, Skyline, or corresponding R or Python scripts, which normalize the values, calculate differential expressions, and visualize the data in the form of profile plots, principal component analysis (PCA), and Vulcano plots.[182–186] Afterwards, the processed data is further analyzed by using additional programs either exploratively or specifically to address a particular research question, or it can be put into biological context alongside other omics results. For this purpose, the values of significantly regulated proteins are used in spreadsheet programs to plot trends for functional groups in bubble plots or to calculate the degree of enrichment in pull-down experiments through differential comparison.[131,187,188] Additional analysis options are provided by online tools, like StringDB and DAVID Bioinformatics, to visualize interactions between proteins (or protein groups), functional enrichment in pathways, and the annotation of Gene Ontology terms as clusters in network analyses.[189–191] Finally, using compilers for the programming languages R or Python, fully automated and customized

pipelines can be created, that sort data, perform the desired calculations, and access online resources, ultimately generating finished reports, including figures.[192]

In summary, (chemo-)proteomics is a powerful analytical platform in the fields of drug discovery, biomedical research, and clinical studies for the discovery of target sites. With the continuous technological advancements and the development of new analytical methods and techniques, proteins are characterized with increasing precision, thereby enabling the detection of phenotypic or disease-related changes. Through differential comparison with references that represent for example a healthy phenotype, markers can be identified, and from these a hypothesis regarding the most likely mode of action can be derived, which has then to be verified through targeted follow-up studies.

1.7 Metallodrug candidates in drug discovery

Another medication class with distinctive therapeutic effects compared to conventional organic compounds are metal-based pharmaceuticals consisting of a metal center and organic ligand structures with Pt(II)-compounds like cisplatin amongst the oldest approved anticancer agents. Beyond cancer treatment, a wide variety of metal-containing active agents are applied on a plethora of medical conditions. This includes, for example, relief for gastrointestinal ailments (Bi), effective treatment of psychiatric conditions like depression and bipolar disorder (Li), as well as the application as contrast agents in medicinal imaging (Gd).[193,194] Additionally, radioisotopes of metals can also be utilized either as α- and β-emitters in targeted radiotherapy to irradiate cancer directly or as γ- or positron emitters in nuclear imaging.[195]

The most prominent candidate of metal-based anticancer agents is cisplatin which was discovered serendipitously in 1965. Ever since its approval in 1978, it has become an indispensable part of our cancer treatment repertoire, but it came with adverse effects. Based on the square planar structure of this platinum(II) lead molecule, several generations of anticancer drugs like carboplatin and oxaliplatin were further developed to mitigate cisplatin's drawbacks such as toxicity and developed resistance mechanisms.[8,196,197] Encouraged by the clinical success of the next generations of platinum-containing medications, the potential of other metal complexes were investigated, however, confined by the platinum paradigm that metal-containing drug candidates exert not only their therapeutic effects but also their non-selective toxicity through the crosslinking of DNA and thus induce apoptosis.[6,198] Nonetheless, interest in metal-based compounds never completely waned, with the discovery process

involving in most cases a screening of cell lines representing a biologically relevant disease phenotype to determine their cytotoxicity by comparing the resulting potencies. This methodology falls under the PDD approach with the definitive term of "Phenotypic Drug Discovery" we use today emerging only in the early 2010s.[199] With further investigations into that medication class and mechanism-focused experiments, evidence started to appear that metallodrugs can have a wide range of biological effects and modes of action, therefore leading to a shift in the initial paradigm. One such example - even from the platinum(II)-containing drugs - is oxaliplatin that targets the ribosomal biogenesis machinery rather than the DNA.[194,196,6]

1.7.1 Metallodrug candidates in clinical evaluation

Currently, ruthenium-containing compounds have produced the most promising metallodrug candidates which are being evaluated in clinical trials. BOLD-100 (formerly known as NKP-1339, IT-139), a Ru(III) complex, is investigated in combination with the chemotherapy regime FOLFOX for the treatment of solid tumors of colorectal and pancreatic cancers in a phase 1b/2a study (NCT04421820).[200] Even though its mode of action has not yet been fully elucidated, previous experimental data have shown that BOLD-100 interferes with multiple targets, including ER stress induction *via* modulating its key chaperone GRP78 paralleled by interacting with the ribosome and altering the lipid metabolism.[187,201] A different example from the ruthenium(II) compound family is TLD-1433 (Ruvidar®), which is being evaluated in a phase 2 clinical trial for the treatment of Bacillus Calmette-Guerin (BCG)-unresponsive bladder cancer through photodynamic therapy (NCT03945162).[202] This Ru(II)-complex is a photosensitizer that creates a conjugate with transferrin, which is recognized by the protein's respective receptor and is then transferred into the cell. Due to the upregulation of the transferrin receptor in many cancers, this compound showed good selectivity for diseased cells and low toxicity in the dark. However, upon irradiation with green light TLD-1433 generates cytotoxic reactive oxygen species (ROS), inducing apoptosis.[203]

Additional to these Ru-based active agents, also a gold(I)-complex is currently in clinical studies: Auranofin (Ridaura®). It is an orally administered drug, which was used as a medication for rheumatoid arthritis. In mechanistic investigations it was demonstrated to act as a prodrug that on one hand dysregulates the cellular redox homeostasis through the inhibition of the protein thioredoxin reductase and on the other hand that it also suppresses inflammatory signaling pathways.[204,205] With these properties, this gold-containing drug is being repurposed

and currently investigated as an anticancer, antiviral and antimicrobial compound (NCT01747798, NCT06805656, NCT02968927).[206–208]

Contrasting to these anticancer strategies, metals can also be utilized in targeted radiopharmaceutical therapy, with the example of the drug [^{177}Lu]Lu-PSMA-617 (Pluvicto®) for the treatment of castration-resistant prostate cancer metastases. In this field, radioactive isotopes are conjugated to targeting biomolecules which deliver the complexes selectively to the cancer cells that are then irradiated, reducing the damage to healthy tissue compared to conventional radiation therapy.[195,209] All mentioned metallodrug candidates in clinical trials are presented in figure 11.

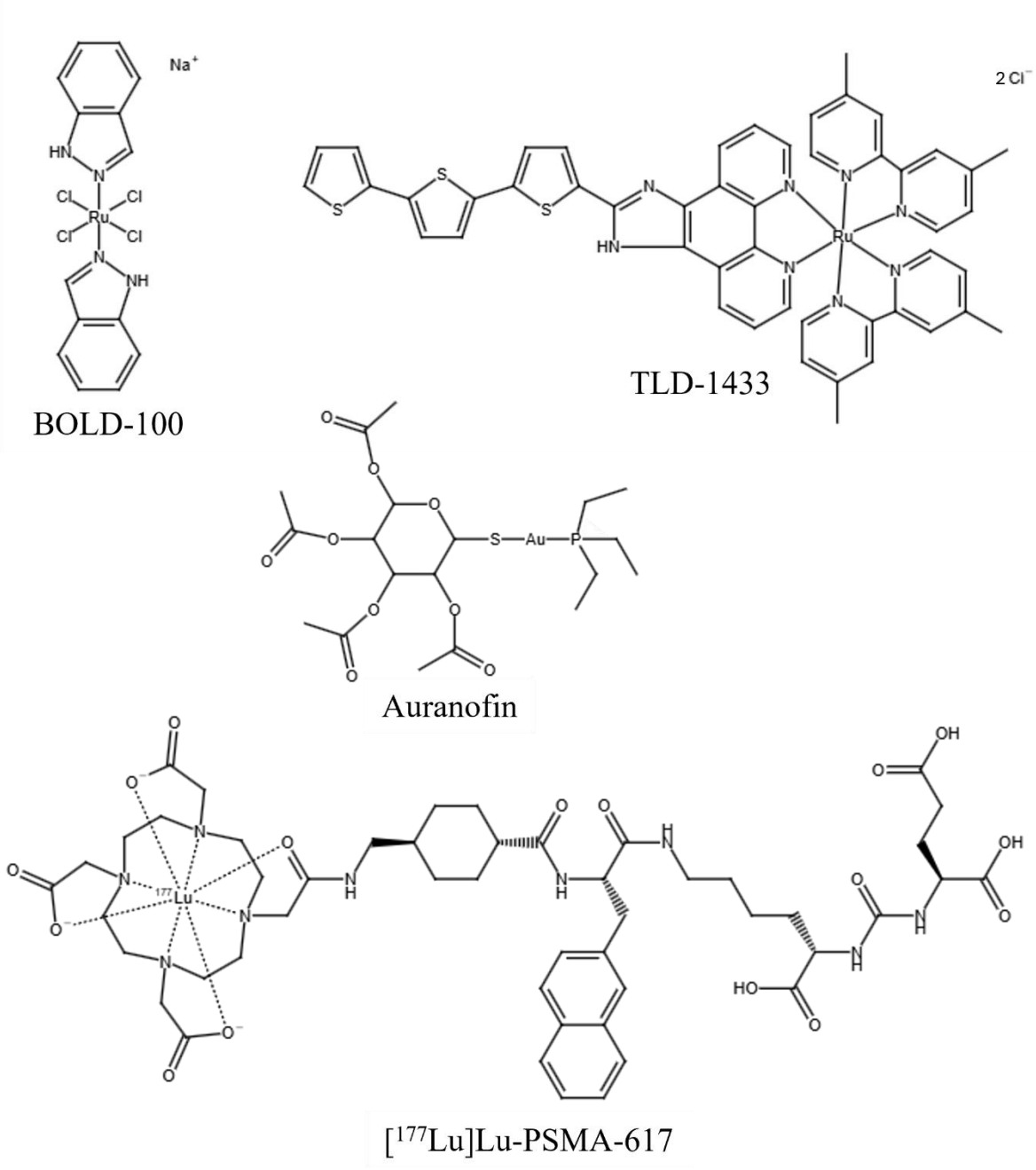

Figure 11: Molecular structures of metal-containing compounds in clinical trials. As an example in how many different ways metal-containing compounds can be applied, [^{177}Lu]Lu-PSMA-617(Pluvicto®) is a FDA-approved targeted radiopharmaceutical drug for the treatment of castration-resistant prostate cancer metastases.

1.7.2 Metallodrug candidates in preclinical investigation

Metal-containing small molecules provide many opportunities within a diverse chemical space. These include the variety of metals to select from, their oxidation states, and the corresponding coordination geometry which allow for the modification of pharmacological characteristics such as stability, bioavailability, and reactivity while reducing off-target effects.[210] The resulting complexes exhibit unique modes of action compared to organic drugs that can interact with a

variety of biochemical processes through redox reactions, and covalent or coordination bonds.[194,211] With those properties some metallodrug candidates can show remarkable selectivity for targets of certain types of cancer cells, enzymes or upregulated biomolecules, which will be highlighted with the experimental ruthenium-based compound plecstatin-1 (Figure 12). This Ru(arene) complex revealed in (chemo-)proteomic investigations in whole cell lysates the structural protein plectin as its main target which was confirmed in plectin knockout cells.[188] Further mechanistic examinations showed that this compound acts as a prodrug, where its initial activation through the hydrolysis of the metal-bound chloride ligand as well as its composition of hydrogen bond acceptors were essential for the selective engagement with plectin.[212] Treatment with plecstatin-1 destabilizes cytoskeletal structures, inhibits tumor growth and cell migration and additionally induces the integrated stress response, thus representing a viable strategy for novel antitumor treatment possibilities.[213,214]

Plecstatin-1 is an organometallic complex that belongs to the family of metal arenes, a compound class that garnered a lot of interest as nonplatinum-based drug candidates with MoAs different than DNA crosslinking. These small molecules can be designed with various transition metals, a hydrophobic arene, inert mono- or bidentate ligands, as well as a labile halido leaving group, to form so called half-sandwich or piano stool complexes.[215] Metal(arene) active agents are classified as prodrugs which require an activation, for example like a ligand exchange of the labile halido group for a water ligand, and subsequent formation of a coordination bond with the target, thereby exerting their therapeutic effect.[216] Due to this composition, this organometallic compound class is highly modifiable where its ligand system can be adjusted in regard to its pharmacokinetic properties influencing its anticancer activity and biological behavior, even achieving tailored selectivity and reactivity for either DNA or proteins, as it was shown for Ru(arene)-complexes by Adhireksan Z. *et al*.[217] Further, Ru-complexes and their Os-containing analogues have been extensively investigated, due to the similar chemical properties of both metals, with Os complexes exhibiting slower ligand exchange kinetics. As osmium is a softer metal than ruthenium in the hard-soft acid-base (HSAB) theory, and thus differs in its behavior towards biomolecules, varying arene and ligands affect the coordination mode. Therefore, this constellation is interesting for the global comparison and examination of structure-activity-relations starting with their potency differences in the *in vitro* antiproliferative activities.[218]

To broaden the scope of metal-based anticancer agents, medicinal chemists also examine the gold(III) compound class. These complexes incorporate bidentate C^N ligands, or tridentate

C^N^N or C^N^C cyclometalating ligand systems to stabilize an Au(III) metal center under physiological conditions and display a square planar coordination geometry.[219] Gold(III) drug candidates have demonstrated similar cytotoxic potencies in cancer cell lines compared to cisplatin, but with distinct mechanisms of action that generally prefer proteins over DNA as targets.[219,220] This can be partially explained on one hand with the HSAB theory that attributes gold an affinity for the nucleophiles thiol and selenol, and on the other hand with the selectivity that can be further carefully adjusted through the selection of the ancillary ligands.[220,221] In efforts to elucidate the MoA, experiments have shown that C^N cyclometalated Au(III) complexes can perform selective arylation where the compound first reversibly coordinates to a target protein and then - through a reduction and elimination step of either an Au(I) or Au(0) species - transfers the ligand system covalently to the nucleophilic moiety.[221–223] One of the validated targets of gold(III) drug candidates is the selenoprotein thioredoxin reductase 1 (TXNRD1), which maintains redox homeostasis in cells and by its inhibition, leading to ROS accumulation and subsequently to the induction of cell death. Since TXNRD1 was shown to be overexpressed in multiple aggressive cancer cell types, like head and neck squamous cell carcinoma or breast cancer, the selective targeting of this enzyme might be a viable therapeutic approach.[224,225]

1.7.3 Discovery process of metallodrug candidates

The modern discovery process of metallodrug candidates encompasses a multidisciplinary and iterative approach, utilizing techniques from phenotypic drug discovery. During the synthesis phase known active agents are modified or completely new ligand systems are created featuring metals such as gold, ruthenium, osmium, iron, copper, palladium, and many more, which are then tested for their anticancer potential.[193] Afterwards, mechanistic studies are conducted to reveal interactions between DNA, proteins or other biomolecules to obtain first indications on the mode of action.[5,220,226–228] To elucidate these novel MoAs the field of (chemo-)proteomics in particular has proven to be a very powerful tool.[229] However, this approach is only applicable to metallodrugs with a preference for targeting proteins over other biomolecules. In recent years, a wide range of techniques have been developed to interrogate the entire proteome from complex biological samples for targets of metallodrug candidates. Strategies that have successfully been implemented in metal-containing drug discovery efforts are the affinity-based and the label-free global target profiling which will be presented in the following paragraphs. For example, the AfBPP approach was used to identify protein targets of BOLD-100. After hydrolysis, the ruthenium-based drug candidate formed a stable adduct with

human serum albumin (HSA) which was immobilized through antibodies and unveiled two ribosomal subunits as interactors, which was supported by polyribosome formation in a profiling experiment in cancer cells.[187] As an alternative approach to investigate drug target interactions in intact cells, the compound of interest can be functionalized with two handles: one comprising of a photoreactive crosslinker like diazirine or benzophenone and the other bearing an alkyne residue for affinity enrichment or fluorescence marker conjugation. This concept revealed multiple target proteins of a C^N^C-cyclometalated Au(III) N-heterocyclic carbene (NHC) complex and its platinum(II) derivative, highlighting the cytoskeletal protein vimentin as an unconventional target.[230,231]

Label-free protein profiling in contrast, has the advantage that no chemical modification of the test compound is necessary before evaluating potential interactors by monitoring drug-induced stability changes of the protein targets.[5] Chemical, proteolytic and thermal stability changes are assessed, whereas thermal protein profiling demonstrated to be an effective strategy to map interaction partners of metallodrug candidates such as auranofin and an experimental Pt(II) complex.[232,233] The research group Sun for example, used a different label-free approach, where the antimicrobial effect of $AgNO_3$ was investigated in *Escherichia coli* (*E. coli*) through a sophisticated setup employing liquid chromatography gel electrophoresis inductively coupled plasma mass spectrometry (LC-GE-ICP-MS). This study revealed 34 silver binding proteins, with crucial targets for glycolysis in the TCA cycle and key enzymes for oxidative stress protection.[234] Additionally, a unique approach to identify targets of the metal-based compound class is the exploitation of metal-mediated ligand transfer reactions, in which a covalent bond between the ligand and a protein is formed. In this strategy, gold(III) complexes have proven to be especially favorable to conjugate ligands to cysteine thiols. Probes based on a C^N-cyclometalated gold(III) complex were utilized to profile modified cysteines in the bacterium *Staphylococcus Aureus* and uncovered 108 targets with 59 previously unknown ligand binding cysteines.[235]

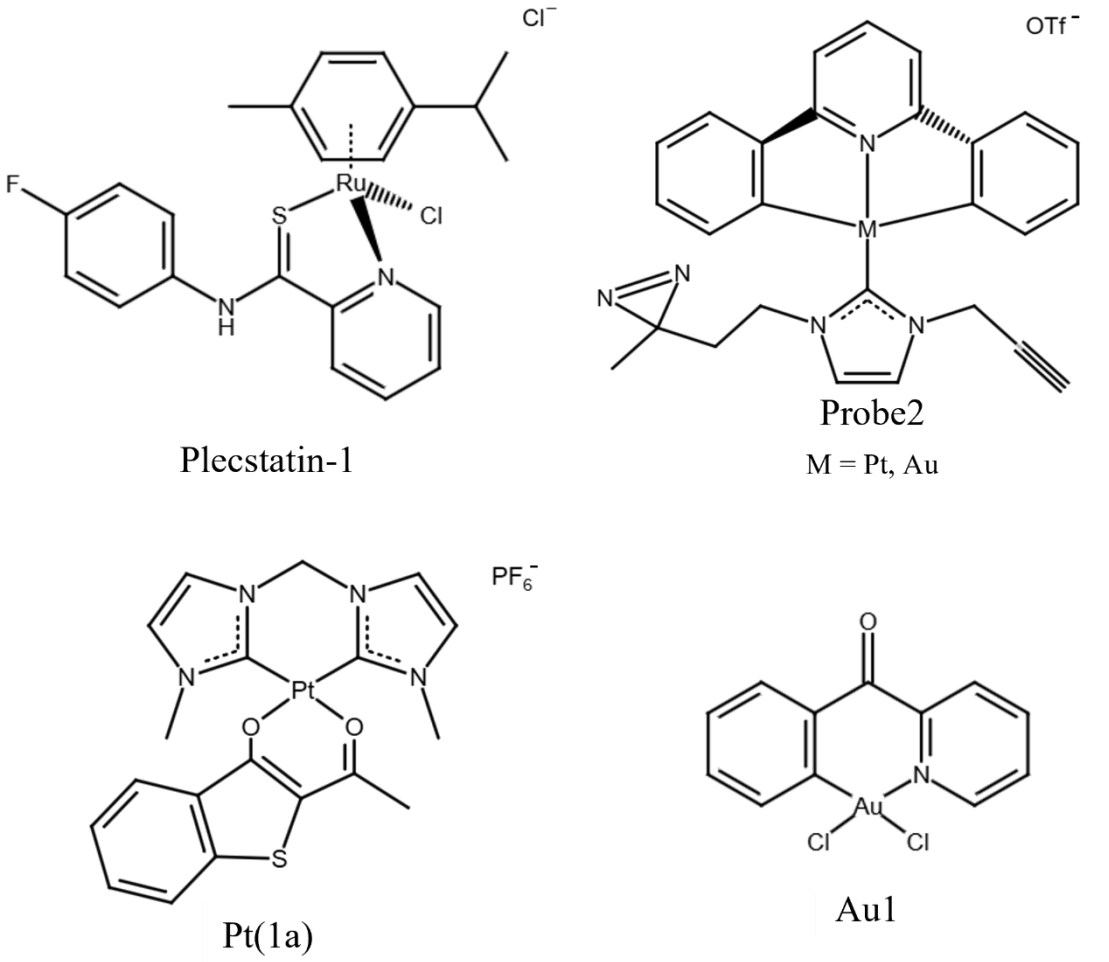

Figure 12: Molecular structures of experimental metal complexes with the names used in their original publication. The ruthenium(arene) Plecstatin-1 and the NHC complex Probe2 showed strong selectivity for unusual targets namely the structure proteins plectin and vimentin, respectively. Pt(1a) was used in a thermal protein profiling experiment to map its interaction partners, whereas Au1 was utilized to reveal cysteine binding sites in Staphylococcus Aureus through a metal-mediated ligand transfer reaction.

Combining the results from those assays with the findings from global proteomic profiling experiments performed with the same compounds yield a comprehensive target response profile, where the number of potential targets can be significantly reduced to the most likely direct interaction partners of the tested candidate. From mechanistic investigations like these, the most promising hit structure can also be identified. Independent of the discovery process, the therapeutic effects of the selected hit compound are ideally validated either by screening the compound against a focused library of molecular targets or confirmed in knockout/knockdown model systems.[4,188,236]

Metal containing complexes have been used effectively time and again, yet they remain an underutilized class of drugs due but not limited to toxicity concerns. Already their synthesis comes with challenges, where the desired properties like solubility, selectivity, adequate ligand

exchange kinetics and the potential development of resistance mechanisms against the treatment need to be balanced.[210,237] This might also involve metabolic byproducts resulting in either accumulation or quick clearance, potentially leading to toxicity and adverse effects.[238] In contrast, metal-based compounds represent a distinct and advancing class of drugs, that offer unique mechanisms of action and bear the potential for treating complex diseases or deliver approaches to overcome resistances.[6,193,211,239] Additionally, previously synthesized molecules can be reinvestigated in more detail since previous examinations were mainly based on cell viability or ROS assays, thereby limiting the mechanistic information to the induction of cell death. Metallodrug discovery is primarily governed by PDD approaches, which can capture the complexity of their chemical space and biological effects in an unbiased fashion. However, other research groups synthesize metal complexes using TDD methodologies, for example Meggers and colleagues, who created inert small molecules, where the metal center's coordination geometry facilitates 3D structures fitting into the known binding pockets of specific kinases, thus noncovalently inhibiting their activity.[240,241] By incorporating techniques from covalent drug discovery, the complexes' interaction partners can be determined, thus allowing for the deconvolution of its MoA, thereby reducing off-target effects and improving their efficacy.

2 Research Justification

Although medical research has made great progress over the past decades, there still remain unmet medical needs, especially in chronic multifactorial diseases such as cancer. Metal-based compounds are of particular interest in this context, as their structural versatility – due to the metal center and the ligand system – allows them to be designed as anticancer agents in a largely unexplored chemical space with respect to biological mechanisms. Selecting a metallodrug candidate is usually based on its potency to induce cell death in a phenotypic *in vitro* model, thus providing limited information about the mechanism of action or the molecular targets of the tested substance. A valuable tool for mode of action studies are mass spectrometric techniques, especially proteomic profiling and chemoproteomics, which were shown to be useful to characterize drug effects and enable target identification, respectively. Furthermore, proteomic techniques serve as largely unbiased hypothesis-generating procedures in phenotypic drug discovery to unveil drug effects on a molecular level as well as valuable instruments to explore covalently binding small molecules, which is a feature of a considerable fraction of metallodrug scaffolds. These approaches already proved useful to even identify *first-in-class* metal-based candidate drugs.

The aim of this dissertation is to establish and advance a proteomics-based discovery platform for the elucidation of the mode of action of metallodrug candidates. Therefore, chemoproteomic techniques shall be developed and extended to study target landscapes of selected metal-based candidates using novel immobilization strategies, or alternative mass spectrometry-based target identification approaches. Then, proteome profiling experiments will be extended to enable structure-activity relationships (SARs) based on perturbation signatures as an approach to select promising candidates from a series of compounds. The establishment of these proteomic methods will be accompanied by appropriately controlled cell culture models and additional compound-specific validation strategies. Finally, the *in vitro* proteome profiling will also be extended to an *in vivo* mouse model to characterize drug-induced antitumor effects in a systemic and local tumor environment. These tasks will be carried out in two main projects, focusing on two covalent metallodrug candidates: a) an organometallic gold(III)-compound that follows a novel metal-centered ligand transfer reactivity, and b) a highly cytotoxic organoruthenium derivative, with unexpected potency in resistant colon cancer cell lines.

The successful completion of these projects provides a comprehensive proteomic platform to enable the identification of target molecules and deliver a detailed understanding of their mechanisms of action. This new information will subsequently facilitate metal-based drug

candidate maturation. Furthermore, this dissertation could lay the foundation for distinguishing between systemic and local effects of an active metal-based anticancer agent at the protein level in animal models. Ultimately, this platform, which is specifically designed for phenotypically discovered metallodrugs, will increase their translatability by facilitating the identification of potential clinical candidates using a mechanism-based drug discovery process.

3 Results and Discussion

3.1 Gold-templated covalent targeting of the CysSec-dyad of thioredoxin reductase 1 in cancer cells

Lukas Skos [1,2,9], Claudia Schmidt [3,9], Sophie R. Thomas [3], Mihyun Park [3], Verena Geiger [3], Dominik Wenisch [4], Riccardo Bonsignore [5], Giorgia Del Favero [6,7], Thomas Mohr [1], Andrea Bileck [1,8], Christopher Gerner [1,7,8], Angela Casini [3], Samuel M. Meier-Menches [1,4,8,10]

[1] Department of Analytical Chemistry, University of Vienna, Waehringer Str. 38, 1090 Vienna, Austria

[2] Doctoral School of Chemistry, University of Vienna, Waehringer Str. 38, 1090 Vienna, Austria

[3] Medicinal and Bioinorganic Chemistry, Department of Chemistry, School of Natural Sciences, Technical University of Munich, Lichtenbergstr. 4, 85748 Garching, Germany

[4] Institute of Inorganic Chemistry, University of Vienna, Waehringer Str. 42, 1090 Vienna, Austria

[5] Dipartimento di Scienze e Tecnologie, Biologiche, Chimiche, e Farmaceutiche, Università degli Studi di Palermo, 90128 Palermo, Italy

[6] Department of Food Chemistry and Toxicology, University of Vienna, Waehringer Str. 38, 1090 Vienna, Austria

[7] Core Facility Multimodal Imaging, University of Vienna, Waehringer Str. 38, 1090 Vienna, Austria

[8] Joint Metabolome Facility, University of Vienna and Medical University of Vienna, Waehringer Str. 38, 1090 Vienna, Austria

[9] These authors contributed equally

[10] Lead contact

Cell Reports Physical Science, Volume 5, Issue 7, 102072

DOI: 10.1016/j.xcrp.2024.102072

This paper was selected for the collection “Chemical biology” from the journal *Cell Reports Physical Science* (https://www.cell.com/cell-reports-physical-science/collections/chemical-biology).

Contributions to this work:

- Conduction of cell culture maintenance, cell viability and synergy assays
- Conducting imaging experiments
- Performing proteomic experiments, incl. analytical verification of binding sites

- Sample preparation and data evaluation
- Involved in data interpretation and figure design
- Writing of the manuscript

Cell Reports
Physical Science

CellPress
OPEN ACCESS

Article

Gold-templated covalent targeting of the CysSec-dyad of thioredoxin reductase 1 in cancer cells

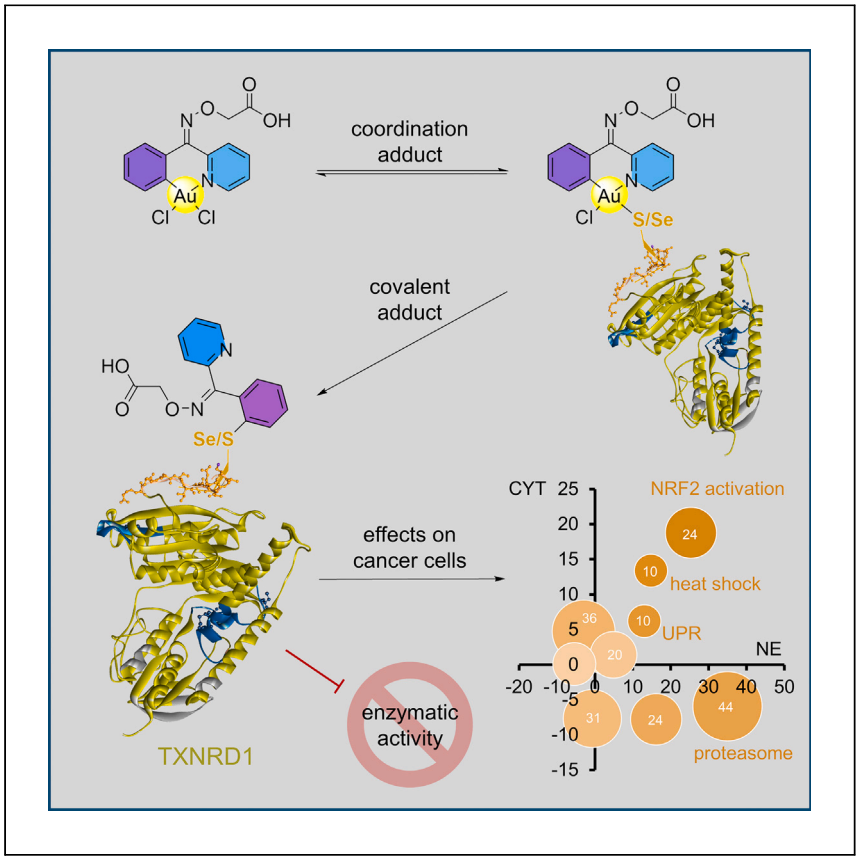

Skos et al. report a gold-templated, two-step covalent targeting mechanism that shows potential as an anticancer strategy. A C^N-cyclometalated gold(III) compound irreversibly targets TXNRD1 and inhibits its enzymatic activity in cell extracts by selective arylation, with dose-dependent, selective targeting of TXNRD1 demonstrated in cell lysates.

Lukas Skos, Claudia Schmidt, Sophie R. Thomas, ..., Christopher Gerner, Angela Casini, Samuel M. Meier-Menches

angela.casini@tum.de (A.C.)
samuel.meier-menches@univie.ac.at (S.M.M.-M.)

Highlights

A two-step, gold-templated covalent targeting mechanism is presented

A C^N-cyclometalated gold(III) compound irreversibly targets and inhibits TXNRD1

The CysSec-dyad of TXNRD1 is selectively targeted in a reducing environment

Skos et al., Cell Reports Physical Science 5, 102072
July 17, 2024
https://doi.org/10.1016/j.xcrp.2024.102072

Cell Reports
Physical Science

CellPress
OPEN ACCESS

Article

Gold-templated covalent targeting of the CysSec-dyad of thioredoxin reductase 1 in cancer cells

Lukas Skos,[1,2,9] Claudia Schmidt,[3,9] Sophie R. Thomas,[3] Mihyun Park,[3] Verena Geiger,[3] Dominik Wenisch,[4] Riccardo Bonsignore,[5] Giorgia Del Favero,[6,7] Thomas Mohr,[1] Andrea Bileck,[1,8] Christopher Gerner,[1,7,8] Angela Casini,[3,*] and Samuel M. Meier-Menches[1,4,8,10,*]

SUMMARY

Covalent drugs emerged as a promising addition to the arsenal of medicinal chemistry tools. Here, a gold-templated mechanism is exploited to enable the selective covalent targeting of the CysSec-dyad of thioredoxin reductase 1 (TXNRD1) in cancer cells. This two-step mechanism involves reversible coordination of a cyclometalated gold(III) compound, featuring a bidentate C^N ligand, to thiolates/selenolates, followed by reductive elimination and irreversible covalent cross-coupling reaction of the ligand to these nucleophiles. Following this reactivity, potent inhibition of TXNRD1 activity was shown *in vitro*, including cancer cell extracts. Selective arylation of the CysSec-dyad in the presence of reducing equivalents was seen in cell-free studies. Chemoproteomic studies showed that the proposed mechanism is selective toward specific protein targets, including TXNRD1. Proteome profiling revealed down-regulation of the detected selenoproteins, except TXNRD1, and induction of the NRF2-KEAP1 pathway. Metal-templated covalent targeting may prove useful to rationally expand the ligandable space of covalent drug discovery.

INTRODUCTION

Covalent drug discovery has made significant progress during the last decade.[1] Covalent inhibitors feature mildly reactive, electrophilic groups, including, among others, acrylamides, activated nitriles, or cyanamides.[2] Careful control of the reactivity of covalent warheads can achieve selectivity and prolong target engagement, thereby favorably altering pharmacodynamic profiles[3] of drug candidates to outperform classical non-covalent targeting strategies. The rational development of reactive covalent inhibitors had long been avoided in medicinal chemistry due to the perceived risks of off-target reactivity and their interference in biological assays.[1] Initial covalent drug discovery efforts were driven by incorporating reactive functional groups into known reversible inhibitors. For example, to overcome the T790M gatekeeper mutation in the EGF receptor of non-small cell lung cancer, afatinib was designed with an acrylamide moiety that reacts with Cys797 in the receptor and was approved in 2013.[4] More recent covalent drugs were discovered by electrophile-first approaches, such as sotorasib, a covalent inhibitor for KRAS(G12C) mutants.[5] Therefore, covalent target engagement is a promising strategy for hard-to-drug targets with shallow or cryptic binding pockets. Electrophile-first approaches are largely facilitated by chemoproteomic techniques.[6,7]

[1]Department of Analytical Chemistry, University of Vienna, Waehringer Str. 38, 1090 Vienna, Austria

[2]Doctoral School of Chemistry, University of Vienna, Waehringer Str. 38, 1090 Vienna, Austria

[3]Medicinal and Bioinorganic Chemistry, Department of Chemistry, School of Natural Sciences, Technical University of Munich, Lichtenbergstr. 4, 85748 Garching, Germany

[4]Institute of Inorganic Chemistry, University of Vienna, Waehringer Str. 42, 1090 Vienna, Austria

[5]Dipartimento di Scienze e Tecnologie, Biologiche, Chimiche, e Farmaceutiche, Università degli Studi di Palermo, 90128 Palermo, Italy

[6]Department of Food Chemistry and Toxicology, University of Vienna, Waehringer Str. 38, 1090 Vienna, Austria

[7]Core Facility Multimodal Imaging, University of Vienna, Waehringer Str. 38, 1090 Vienna, Austria

[8]Joint Metabolome Facility, University of Vienna and Medical University of Vienna, Waehringer Str. 38, 1090 Vienna, Austria

[9]These authors contributed equally

[10]Lead contact

*Correspondence: angela.casini@tum.de (A.C.), samuel.meier-menches@univie.ac.at (S.M.M.-M.)

https://doi.org/10.1016/j.xcrp.2024.102072

In this context, we decided to explore a medicinal inorganic chemistry approach, based on organogold compounds,[8] to develop anticancer metallodrugs acting via covalent bond formation reactions with pharmacological targets. Gold-based drugs are a class of metal-based anticancer agents[9] endowed with distinct modes of action (MoA) with respect to platinum-based anticancer agents,[10–14] and which can be categorized into gold(I) and gold(III) compound families that generally follow protein-targeting pathways, with a few remarkable exceptions.[15–17] Auranofin represents the benchmark gold(I) drug that was initially approved to treat rheumatoid arthritis and is currently being repurposed as an anticancer agent.[18] Among its validated modes of action, the inhibition of the selenoenzyme thioredoxin reductase 1 (TXNRD1) is particularly relevant,[19,20] since its selective inhibition can induce pro-apoptotic signals.[18,21] The metallodrug binding mode involves the formation of a reversible coordination bond to the selenocysteine in the protein's catalytically active site, following ligand exchange reactions at the gold(I) center.[19,22] Recently, it has been shown that gold(III) complexes may exert their anticancer activity by covalent targeting of proteins beyond the pure coordinative binding mode, and as such, emerge as new chemical tools for bioorthogonal transformations *in vitro* and *in vivo*, as well as novel drug leads.[23] For example, the anticancer gold(III) *meso*-porphyrin IX was shown to covalently modify protein cysteine thiols of TXN, peroxiredoxin (PRDX), and deubiquitinases.[24] In this example, the gold(III) center was crucial to activate the *meso*-carbons of the porphyrin ring toward nucleophilic substrates. In 2017, a study by Tanaka and co-workers reported on a cyclometalated gold(III) compound tethered to an *N*-glycoalbumin carrier, which by virtue of its Lewis acid character was capable of activating propargyl ester functions for binding to proteins by amide bond formation *in vivo*.[25] Some gold(III) organometallic compounds are also known to perform metal-templated covalent additions of ligands to biological nucleophiles, especially cysteine thiols.[26] In this context, we and others observed that cyclometalated gold(III) compounds featuring bidentate C^N ligands can template the formation of covalent aryl-peptide adducts via C–S cross-coupling at cysteine residues (Figure 1A).[21,27,28] According to density functional theory calculations combined with mass spectrometry (MS) studies, this involves a two-step reaction mechanism (Figure 1A).[29] First, the gold(III) coordinates to a thiolate/selenolate in *trans* position to the N-heterocycle of the C^N-cyclometalated ligand upon exchange with one of the ancillary ligands, forming a classical gold coordination bond. Second, a peptide bond nitrogen is required to exchange the N-heterocycle, which allows the C-S/Se cross-coupling reaction by reductive elimination. The reduced gold atom is released during this process. Interestingly, this gold-templated covalent reactivity was found to be selective toward thiols over other nucleophiles.[21] The mechanism combines the benefits of reversible coordination of gold(III) adducts for targeting thiol-based nucleophiles with the possibility of covalently modifying these sites. Such reactivity is unique to this family of organometallic gold(III) complexes and is not accessible by gold(I) compounds.[26,30,31]

Reactivity toward arylation can be tuned by structural changes of the chelating and ancillary ligands. [Au($C^{CO}N$)Cl_2] ($C^{CO}N$ = 2-benzoylpyridine; Figure 1B) was found to be more reactive than other C^N-cyclometalated derivatives.[29] Furthermore, cyclometalation is one of the main strategies to stabilize gold(III) centers, so that these compounds become sufficiently stable for potential medicinal applications or for functionalization for imaging and targeting purposes.[22,32]

Activity-based proteomic profiling of [Au($C^{CO}N$)Cl_2] in *Staphylococcus aureus* cell extracts showed that the compound can efficiently arylate cysteine thiol residues of >100 proteins, >50% of which were not engaged by the established

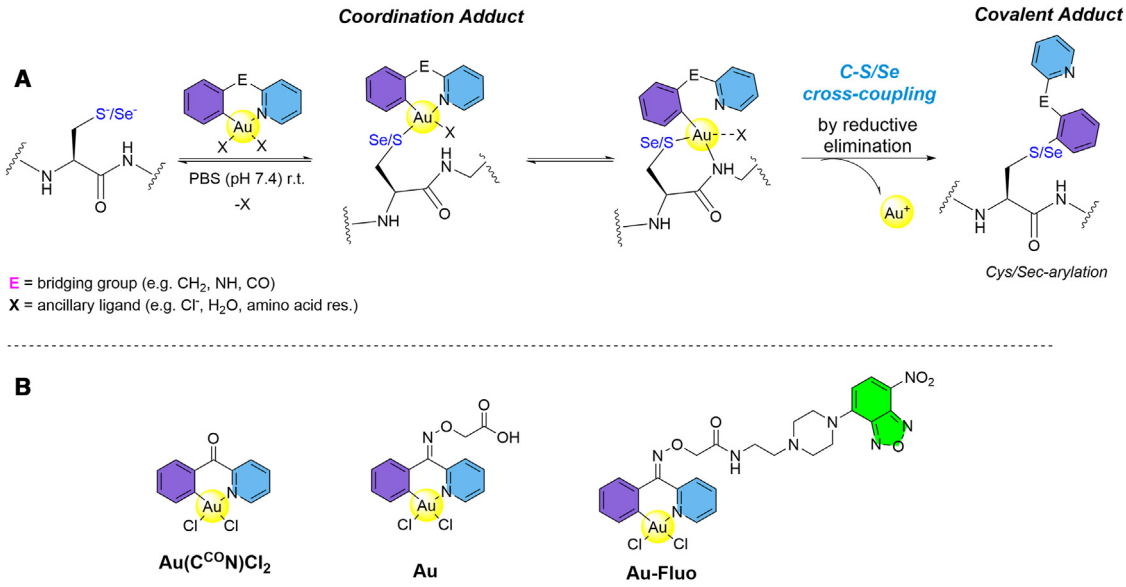

Figure 1. Mechanism of gold(III)-templated cross-coupling and chemical structures of the investigated compounds

(A) Proposed scheme of the reaction of C^N-cyclometalated gold(III) compounds with thiols and selenols of proteins. The binding proceeds via 2 steps: (1) the formation of a coordination adduct in which the gold(III) center binds directly to the S^-/Se^- nucleophiles and (2) C–S/Se cross-coupling reaction via reductive elimination and liberation of gold(0/I).

(B) Chemical structures of the parent compound [Au($C^{CO}N$)Cl_2] ($C^{CO}N$ = 2-benzoylpyridine) and of the investigated C^N-cyclometalated gold(III) analogs **Au** (with a functional carboxylic acid via an oxime) and **Au-Fluo**.

α-chloroacetamide.[33] Out of the ligandable sites, 10 potential arylation sites were assigned to be close to the respective functional protein sites; some of the identified proteins were already known targets for metal compounds with antibacterial effects.[33]

These initial results showed promise for gold(III)-templated covalent targeting as an anticancer strategy. Here, a cyclometalated gold(III) C^N complex featuring a carboxylic acid group on the ligand scaffold for further functionalization (**Au**, Figure 1B) was used to investigate metal-templated covalent targeting as an anticancer strategy in human SW480 colon cancer cells. In detail, we applied MS-based and complementary methods to validate the proposed reactivity. In general, besides other analytical techniques,[34–36] MS contributed toward elucidating the reactivity of metal-based candidates.[37–40] In the frame of increasingly mechanism-driven research,[41–43] metalloproteomic techniques were successfully established to characterize target landscapes,[41,44–51] metal interactomes,[52–54] or redox proteomes.[55] In this context, using chemoproteomic techniques, we saw target selectivity for TXNRD1 and found potent inhibition of TXNRD1 activity against the isolated enzyme and in cell extracts. In the presence of reducing equivalents, the CysSec-dyad of TXNRD1 was selectively arylated by **Au**, highlighting that selenocysteine may contribute to the coordinative targeting mechanism. Metal-templated covalent strategies may represent a promising strategy to expand the ligandable space in covalent drug discovery.

RESULTS AND DISCUSSION

The investigated C^N-cyclometalated gold(III) compounds template cross-coupling reactions to thiols

The parent substance [Au($C^{CO}N$)Cl_2] was modified to two oxime-containing C^N-cyclometalated compounds featuring either a functional carboxylic acid group (**Au**) or

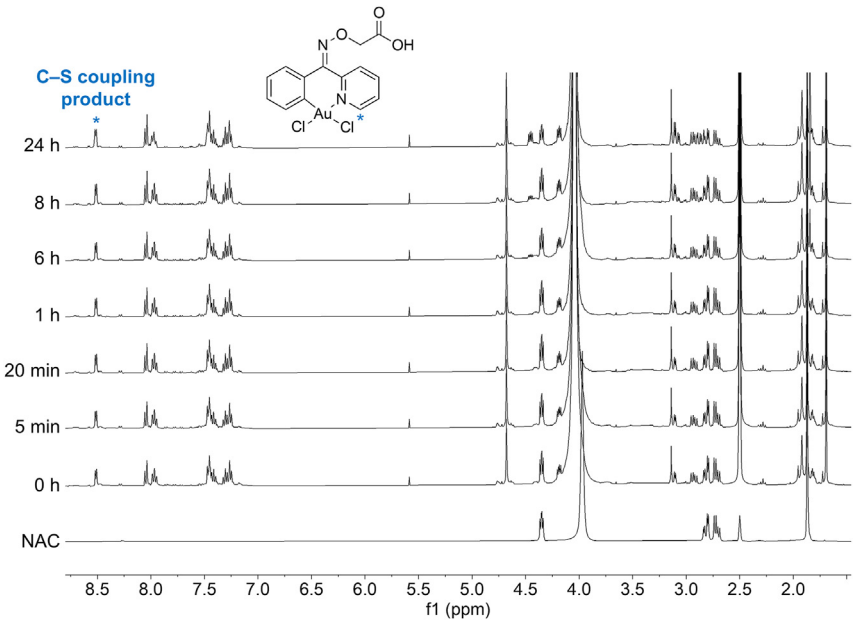

Figure 2. Reactivity of Au toward NAC

H-NMR spectra of **Au** reacting with 3 equiv of NAC in DMSO-d_6:D_2O (9:1). The spectrum of NAC alone is included as a reference. The characteristic shift of the α-H was observed (Δ = 0.78 ppm), indicating a rapid C–S coupling of **Au** with NAC.

a fluorescent tag (**Au-Fluo**). **Au** was synthesized according to a previously reported procedure.[52] The fluorescent derivative **Au-Fluo** was synthesized by amidation of **Au** with the 2-(-4-(7-nitrobenzo[*c*][1,2,5]oxadiazol-4-yl)piperazon-1-yl)ethane-1-amine fluorophore, and both compounds were characterized by standard analytical methods (Figures S1 and S2).

Since metal-based compounds are typically reactive molecules that can undergo ligand exchange reactions, the stability of the complexes **Au** and **Au-Fluo** was tested in DMSO-d_6:D_2O (9:1) by ^{1}H-NMR spectroscopy (Figures S3 and S4). The compounds were stable over 24 h under these conditions, as suggested by the observation of the characteristic doublet at 9.31 ppm for **Au** and **Au-Fluo**, corresponding to the proton adjacent to the Au-N bond in the pyridinyl ring (α-H).

Additionally, both compounds were investigated with respect to their ability to arylate thiols. The compounds were incubated under the same conditions in the presence of 3 equiv of *N*-acetylcysteine (NAC; Figures 2 and S5). The characteristic shift of the ^{1}H-NMR signal from 9.3 to 8.5 ppm of the α-H corresponding to thiol arylation[27] was observed for both **Au** and **Au-Fluo**. The kinetics of C–S bond formation varied only slightly, with **Au** inducing complete arylation within the timescale of the first measurement (time = 0 h), as also seen for [Au($C^{CO}N$)Cl_2] (Figure S6), whereas **Au-Fluo** required a few extra minutes.

Then, the interaction of **Au-Fluo** with BSA was studied using fluorescence spectroscopy. BSA represents a competitive binding model for **Au-Fluo** because it contains one free cysteine, several disulfide bridges, and several surface-exposed nucleophiles (e.g., imines) that can coordinate to the gold(III) center by ligand exchange. The luminescence properties of **Au-Fluo** were determined first (Figure 3A). The emission spectrum of **Au-Fluo** featured an excitation maximum at 493 nm and an

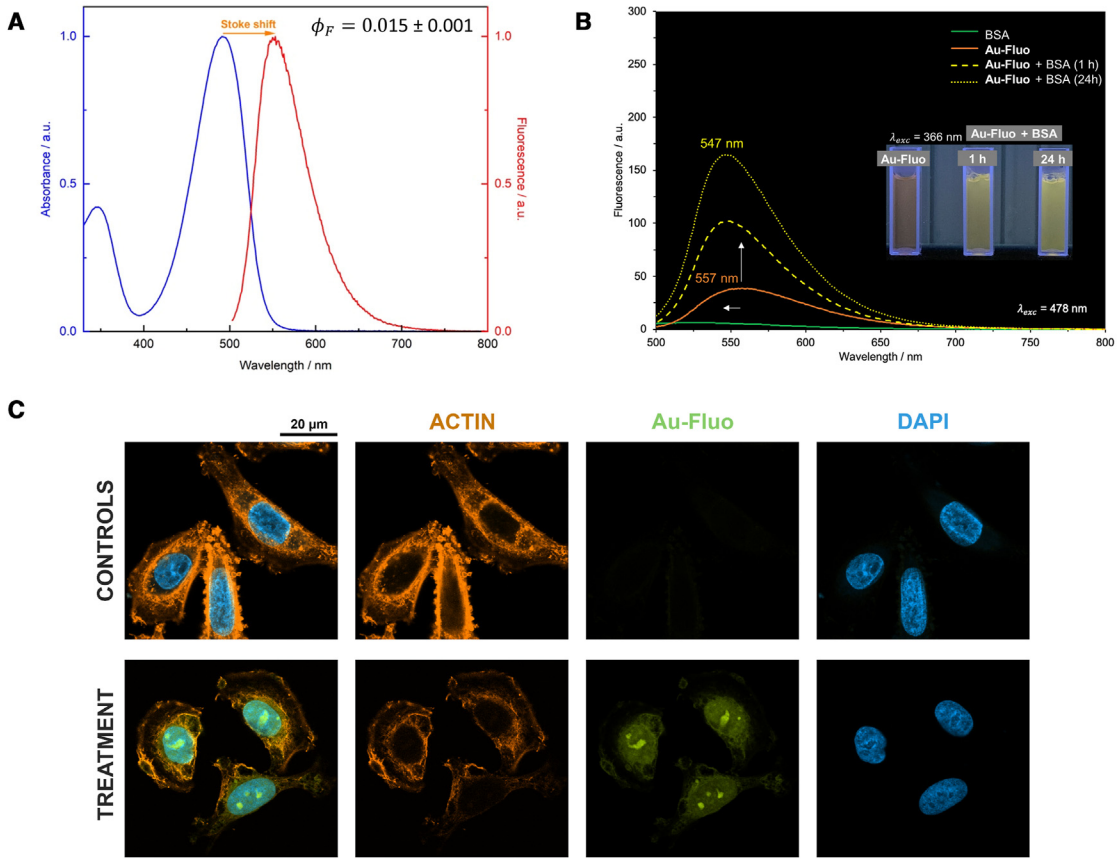

Figure 3. Fluorescence spectroscopy and microscopy studies of Au-Fluo

(A) Absorbance (blue, $\lambda_{abs,max}$ = 493 nm) and emission (red, $\lambda_{em,max}$ = 553 nm) spectrum of **Au-Fluo** in DMSO with the related Stokes shift (orange) of $\Delta\lambda$ = 62 nm, and the absolute fluorescence quantum yield (φ_F). For the emission spectrum, **Au-Fluo** was excited at the absorbance maximum of 493 nm.

(B) Fluorescence emission spectra recorded over time of the interaction between **Au-Fluo** (1 equiv) and BSA (10 equiv) at an excitation wavelength of 478 nm. Spectra were recorded in PBS (pH 7.4):DMSO (9:1), and samples were incubated at 37°C for 1 and 24 h. The spectra of BSA (green) and free **Au-Fuo** (orange) incubated for 24 h are also reported for comparison.

(C) Cellular distribution of **Au-Fluo** in SW480 cancer cells after a 4-h incubation studied by confocal fluorescence microscopy. DAPI (blue) indicates nuclei and phalloidin (red) indicates actin cytoskeleton. Green fluorescence of **Au-Fluo** was monitored after excitation at 469 nm and emission at 525 nm (GFP channel). Scale bar, 20 µm.

emission maximum at 553 nm in PBS:DMSO (9:1). For the study with BSA, 1 equiv of **Au-Fluo** and 10 equiv of BSA were dissolved in PBS (pH 7.4):DMSO (9:1) and incubated at 37°C for 1 and 24 h. Solutions of **Au-Fluo** and BSA at the same concentrations were analyzed as controls under the same conditions. Upon incubation for 1 h with BSA, the emission maximum underwent a blueshift toward 547 nm, indicating an arylation reaction potentially at the cysteine (Figure 3B). Most notably, the fluorescence intensity further increased by approximately 60% over 24 h.

The C^N-cyclometalated gold(III) compounds are moderately cytotoxic, and Au-Fluo distributes to the perinuclear and nuclear regions

The antiproliferative activity of the two compounds **Au** and **Au-Fluo** was determined in human SW480 colon cancer cells using the colorimetric MTT assay. Cells were incubated for 24 and 72 h. The compounds showed moderate cytotoxicity. The half-maximal effective concentration (EC_{50}) for growth inhibition was determined to be 62 ± 1 and 32 ± 6 µM for **Au** and **Au-Fluo**, respectively, after 24 h (Figure S7). After 72 h, the potency increased slightly to EC_{50} values of 31 ± 9 µM for **Au** and 20 ± 2 µM for **Au-Fluo**.

The fluorescence of **Au-Fluo** was further used to track its cellular distribution in SW480 cancer cells. Its excitation and emission spectra enabled excitation at 469 nm and data acquisition by green fluorescence in the microscope. For these studies, SW480 cells were treated with **Au-Fluo** at half-EC_{50} (16 μM) and EC_{50} (32 μM) concentrations for up to 24 h. The cellular distribution of **Au-Fluo** in SW480 cells was assessed by live-cell fluorescence microscopy (Figure S8). The medium had to be exchanged before analysis to reduce the background fluorescence. **Au-Fluo** was found to distribute into SW480 cancer cells, with a slight preference for the nuclear compartment after 4 h, and the distribution remained similar over 24 h. This experiment was repeated using confocal fluorescence microscopy benefiting from an increased resolution. After fixing and permeabilization, the cells were co-stained with phalloidin (red) as a marker for the actin cytoskeleton and with DAPI (blue) as a marker for the nucleus (Figure 3C). **Au-Fluo** was confirmed to distribute to the perinuclear region and into the nuclear compartment.

TXNRD1 is identified as a potential target of Au in SW480 cancer cell extracts

The gold-templated covalent targeting of **Au** was then investigated in the proteome of SW480 cancer cells using a chemoproteomics approach.[41,45] Coupling conditions of the carboxylate-containing **Au** to the amine-based Sepharose resin were optimized. The amidation reaction turned out to proceed selectively in an aqueous solution in the presence of 1.5 equiv of 1-ethyl-3-(3-dimethylaminopropyl) carbodiimide at pH 4 when using **Au** and 1 equiv of serotonin as a model amine. Amidation required at least 18 h to proceed, which led to the hydrolysis of one chlorido ligand at the gold(III) center and formation of a gold(III)-hydroxido complex, as detected by ion trap MS at *m/z* 661.11 (m_{theor} = 661.09) with a characteristic single chloride isotope pattern (Figure S9). These coupling conditions were employed for immobilizing **Au** on amine-containing Sepharose resins, but using a 3-fold excess of **Au** with respect to the available amines to increase the coupling efficiency. Since the buffer of the chemoproteomic experiment contained DTT as a reducing agent, the reactivity of **Au** toward DTT (1:2 equiv) was also investigated over the course of 70 min directly after mixing (Figure S10). In line with expectations, **Au** coordinated rapidly to DTT, but the cross-coupling reaction between the ligand and DTT progressed steadily over the entire incubation period. This indicated that DTT blocks immobilized **Au** only to a minor degree during the 2-h incubation of the chemoproteomic experiment since the coordination bond enables successive ligand exchanges until a final nucleophile traps the gold(III) complex.

The chemoproteomic experiment was performed using a differential approach (Figure 4A). The immobilized **Au** on Sepharose resin was exposed to a native protein whole-cell lysate of SW480 cancer cells for 2 h. During this time, the immobilized **Au** coordinates to nucleophiles under competitive conditions until a final nucleophilic moiety traps the complex and leads to an irreversible covalent bond. This approach is prone to non-selective binding of proteins to the resin due to hydrophobic interactions. To account for the latter, a separate competitive pull-down experiment was performed, where the native whole-cell lysate was pre-incubated for 2 h with free **Au** (12 μM) and then incubated for another 2 h with the **Au**-anchored resin. Pre-incubation with free **Au** leads to the irreversible arylation of potential interactors, which cannot be captured by the immobilized **Au** any longer, so that only non-selective interactors are detectable. Differences between the normal and the competitive pull-down reveals selective binding partners. Since we expected only covalently bound proteins to be attached to the resin after chemoselective arylation, we performed the proteolytic digestion directly on the beads, subsequent to harsh washing steps. After nano liquid chromatography-tandem MS (nLC-MS/MS)-based

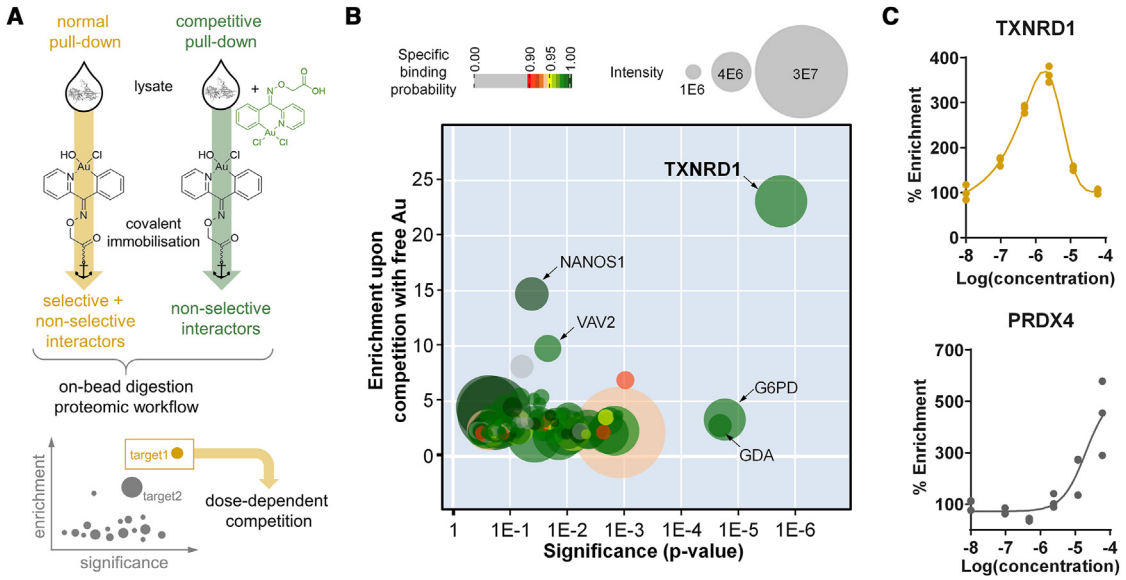

Figure 4. Target identification of immobilized Au using chemoproteomics

(A) **Au** was immobilized on amine Sepharose beads. Native protein cell lysates of SW480 cancer cells were prepared and either directly incubated with the immobilized probe (normal pull-down) or pre-treated with free **Au** (12 μM, competitive pull-down).

(B) Differential analysis of the normal and competitive pull-down experiments revealed selective binding to TXNRD1 from the native protein whole-cell lysate of SW480 cancer cells.

(C) Dose-dependent titration with free **Au** at 0 nM, 96 nM, 480 nM, 2.4 μM, 12 μM, and 60 μM revealed dose-dependent binding affinity for only TXNRD1 and PRDX4. The unusual titration curve indicates bis-arylation of TXNRD1 by **Au** possibly involving the CysSec-dyad. Each concentration was performed in 3 replicates.

proteomic analysis and evaluation, the potentially selective interactors were ranked by means of their enrichment efficiency and significance of interaction as calculated from the respective intensities in the normal and competitive pull-down (Figure 4B). A total of 2,833 proteins were identified in the pull-down from the whole-cell lysate of SW480 cancer cells. Strikingly, we identified the selenoprotein TXNRD1 as the most prominent selective interactor based on enrichment and significance (Figure 4B). TXNRD1 is a key player in the maintenance of the intracellular redox homeostasis within the TXN system, often overexpressed in cancers due to a constitutive activation of the transcription factor and stress sensor NRF2.[56] It is involved in apoptosis induction and has emerged as one of the main targets of cytotoxic gold complexes, including the clinically evaluated auranofin.[19,30,57] Human TXNRDs are homodimers coupled head to tail, each one containing a redox-active CysSec-dyad with sequential cysteine and selenocysteine residues at the C terminus responsible for the interaction of the enzyme with various substrates as well as TXN itself.[58]

The chemoproteomic approach was expanded to a dose-dependent competition experiment to verify the interaction with TXNRD1 and assess the potency of interaction.[47] This was achieved by titrating **Au** at increasing concentrations (0.096–60 μM) in the competitive pull-down. Once more, TXNRD1 was verified as an interactor of **Au** and showed a clear dose-dependent profile. However, in contrast to earlier observations,[47] we noted an unusual interaction profile suggesting that arylation of TXNRD1 by **Au** involves a second binding site. A 2:1 binding stoichiometry between **Au** and TXNRD1 was indicated by the apparent enrichment of TXNRD1 after the first arylation step, with a maximum at 2.4 μM and a nearly complete competition at 12 μM (Figure 4C). The catalytic CysSec-dyad of TXNRD1 potentially allows for two arylation events to occur. A further dose-dependent interaction was observed

with PRDX4, but only at the highest tested concentrations. PRDX4 is thus an unlikely target at pharmacologically relevant concentrations. It is worth noting that we did not observe other proteins with clear-cut dose-dependent profiles in the tested concentration range.

Au selectively arylates the catalytic CysSec-dyad on TXNRD1 in the presence of reducing equivalents

The selectivity of **Au** toward TXNRD1 in the chemoproteomic approach suggested the catalytic CysSec-dyad as a likely site of interaction and potentially enabling bis-adduct formation to occur. To characterize the terminal arylation sites, TXNRD1 was reacted with **Au** in a cell-free experiment using 0, 1, and 5 equiv of **Au**. Additionally, TXNRD1 was reacted with 1 equiv **Au** in the presence of 0, 1, and 5 equiv of NADPH as a reducing agent. Each sample was directly proteolytically digested and analyzed by nLC-MS/MS. To automatically detect modified peptides of TXNRD1 using MaxQuant (version 1.6.17.0), arylation and carbamidomethylation were customized as variable modifications on cysteine and selenocysteine. These experiments revealed a 96% sequence coverage of TXNRD1, including the C-terminal peptide that contains the catalytic CysSec-dyad (Figures 5A and S11A). The latter contained the sequence RSGASILQAGCUG (*m/z* 692.7775 [z = 2], m_{theor} = 692.7810) that showed a retention time (RT) of 28.2 min in this experimental setup (Figure 5B). Interestingly, already at a 1:1 molar ratio between TXNRD1 and **Au** in the absence of NADPH, two chromatographic signals for the arylated peptide (*m/z* 791.3072 [z = 2], m_{theor} = 791.3058) were observed, with RTs of 39.9 and 40.3 min, respectively. This indicated the presence of two distinct arylation sites on this peptide. Additionally, a bis-arylation product was observed (*m/z* 593.5517 [z = 3], m_{theor} = 593.5551) at RT = 49.1 min, supporting the possibility of two different binding sites on this peptide. The isotopic patterns of the different mass signals clearly showed the presence of selenium, revealing excellent simulation matches and mass accuracies of <5 ppm (Figures 5C and S11B). The four detected mass signals corresponding to the unmodified CysSec-dyad peptide (RT = 28.2 min), the two mono-arylated peptides (RT = 39.9 and 40.3 min), and the bis-arylated peptide (RT = 49.1 min) were individually selected for MS/MS analysis at their respective RTs (Figure 5D). MS/MS analysis revealed detailed information about the peptide sequence and the location of the arylation sites. The unmodified peptide was identified with characteristic b- and y-fragments.[40,59] The b_{11}^+ fragment represents an unmodified cysteine, while y_3^+ represents the unmodified C-terminal CUG fragment of this peptide. Interestingly, the b-fragments remained similar for the mono-arylated product at 40.3 min, including the b_{11}^+ fragment. In contrast, the detected y-fragments indicated an arylation product, and the arylated y_2^+ fragment [$y_2(Ar)^+$] provided direct proof of selenocysteine arylation on TXNRD1. The second mono-arylation product eluting at RT = 39.3 min did not feature the unmodified b_{11}^+ ion. Indeed, the lack of the b_{11}^+ ion and the detection of an arylated b_{11}^+ ion ($b_{11}(Ar)^+$) highlights that this species corresponds to a cysteine arylation product. Finally, the MS/MS spectrum of the bis-arylation product eluting at 49.1 min revealed a different set of fragments that supported simultaneous cysteine and selenocysteine arylation. For example, the fragments $y_2(Ar)^+$ and $y_3(2Ar)^+$ clearly evidenced bis-arylation of the CysSec-dyad of TXNRD1. This terminal peptide was neither observed unmodified or arylated in the proteome profiling experiments of SW480 cancer cells treated with **Au**. In addition to their characteristic *m/z* ratios, RTs, and fragmentation spectra, these C-terminal peptides also featured distinct ion mobilities supporting the structural impact of the arylation on the peptide (Figure S11C).

The reaction between TXNRD1 and **Au** in the absence of NADPH also revealed three other arylated peptides, among which was an N-terminal peptide containing the

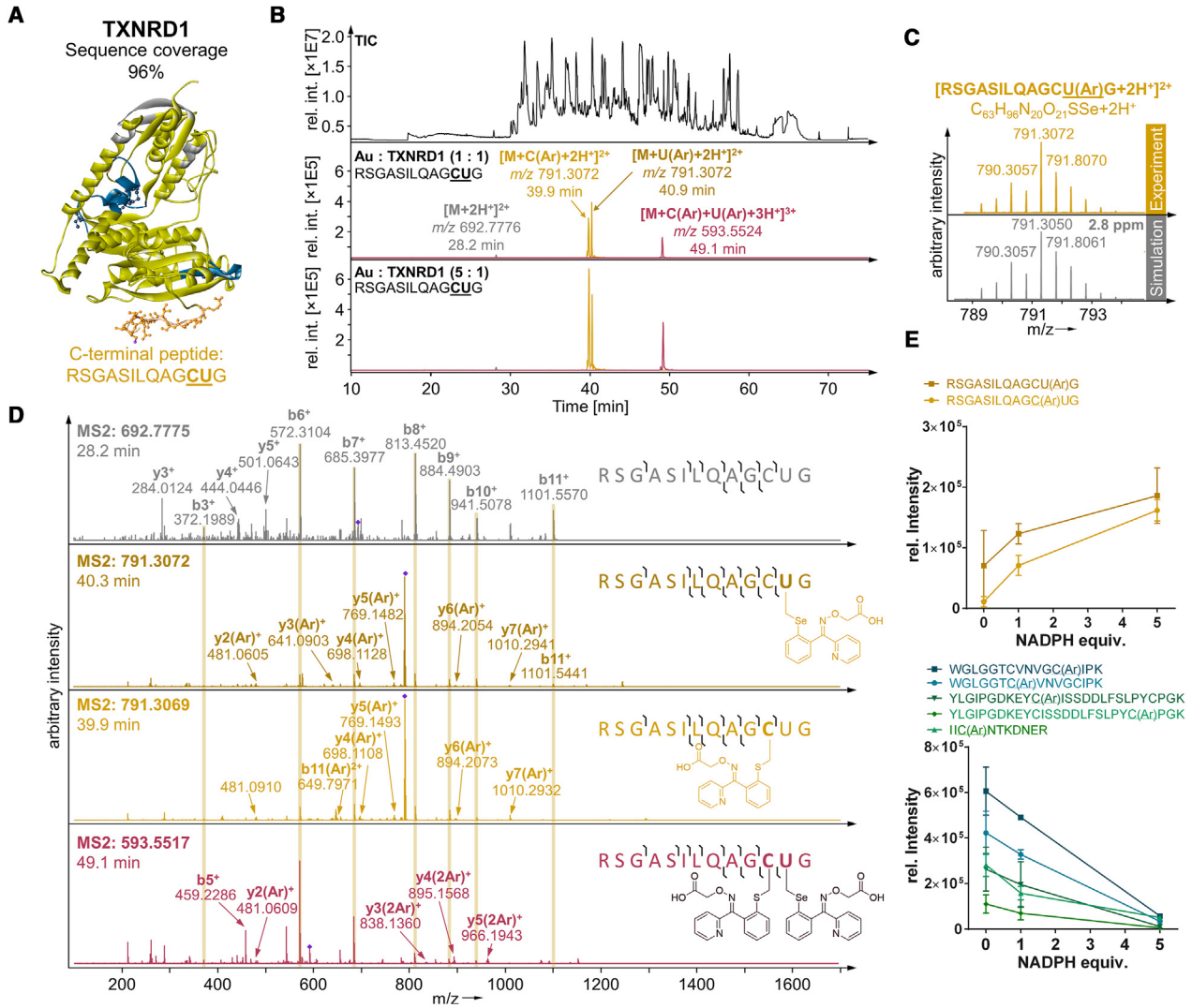

Figure 5. Identification of Au-templated arylation sites on TXNRD1

TXNRD1 (5 μg, 2.25 μM) was reacted with 0, 1, and 5 equiv of **Au** for 24 h. In a second setup, TXNRD1 was similarly reacted with 1 equiv of **Au** in the presence of 0, 1, and 5 equiv NADPH. Results are representative of 3 replicates. The protein was proteolytically digested and analyzed by nLC-MS/MS.

(A) A 96% sequence coverage of TXNRD1 was obtained.

(B) The chromatograms depict the total ion chromatogram, as well as the extracted ion chromatograms of the CU-containing C-terminal peptide. The reaction of TXNRD1 with **Au** in the absence of NADPH led to the arylation of the CysSec-dyad on TXNRD1. C- and U-arylations were observed at both molar ratios, as well as bis-arylations.

(C) The experimental mass signal and theoretical simulation of the isotope pattern of the mono-arylated C-terminal CU-containing peptide is shown.

(D) MS/MS experiments of the unmodified and covalently modified CysSec-dyad containing peptide unambiguously identified the location of the arylation sites on C and U.

(E) Increasing equivalents of NADPH (0, 1, 5 equiv) in the reaction between TXNRD1 and **Au** (1:1 equiv) led to an increase in the intensity of the arylation of the C-terminal CU-containing peptide, while all other arylated peptides considerably decreased in intensity. Data are shown as mean ± SD (n = 3).

CVNVGC motif that is known to coordinate gold (Figures 5E, S11D, and S11E).[60] These arylated species also increased in intensity with increasing **Au** equivalents. Interestingly, increasing equivalents of NADPH reduced the arylation efficiency on these sites, while at the same time the arylation of the C-terminal CysSec-containing peptide increased. This highlighted the selectivity of the gold-templated covalent targeting toward the C-terminal CysSec-dyad in the presence of reducing equivalents.

Au inhibits TXNRD1 activity

TXNRD1 activity was investigated to confirm the inhibitory effect of **Au** at the CysSec-dyad on enzymatic activity. **Au** was first tested against purified mammalian TXNRD1 and then against TXNRD1 in human A549 lung cancer cells. The cellular assays were performed in A549 cancer cells due to their abundant TXNRD1 expression, which is crucial for the sensitivity of the assay.[61] **Au** exhibits half-maximal inhibitory concentration (IC_{50}) values toward the isolated enzyme in the nanomolar range, corresponding to 0.069 $\pm$ 0.046 and 0.176 $\pm$ 0.045 μM at 15 and 75 min incubation time, respectively (Figure S12). **Au** is less potent than auranofin, showing an IC_{50} = 16 nM in the same experimental setup[62,63] but in line with previous studies on analogous cyclometalated gold(III) C^N complexes.[39,62] **Au** was then incubated with A549 cancer cells for 24 h, after which the cells were homogenized and the cell lysate extracted to determine the remaining TXNRD1 activity at different **Au** concentrations. **Au** inhibited the TXNRD1 activity *in cellulo* with an IC_{50} = 11.9 $\pm$ 3.8 μM. These results indicate that **Au** inhibits TXNRD1 activity in sufficiently low concentrations to account for its anticancer activities. Interestingly, the inhibitory concentration of **Au** *in cellulo* parallels the findings of the pull-down during dose-dependent competition (Figure 4C).

Overall, these data, together with the aforementioned chemoproteomic and MS studies, point toward the possible finding of **Au** as a metallodrug lead compound that exhibits an unprecedented mode of covalent TXNRD1 inhibition, compared to known covalent TXNRD1 inhibitors, including Ethaselen,[64] *TRi* compounds,[65] the half-mustard 2-chloroethyl ethyl sulfide,[66] cyclic selenylsulfides,[67] and other small molecules.[68,69]

Au treatment induces the NRF2-KEAP1 pathway, a key regulator of redox management capacity in cancer cells

The effects of sub-cytotoxic **Au** treatment (12 μM, 24 h) on SW480 cancer cells were evaluated by proteome profiling. The cytoplasmic (CYT) and nuclear (NE) protein fractions were separately processed and analyzed according to an established workflow using a data-dependent label-free quantification strategy.[70] A total of 4,347 protein groups were identified. As shown in Figure 6A, the correlation among biological replicates was typically around 0.85, as exemplified for two Au-treated NE fractions. This led to a clear separation of the proteome profiles of the different conditions, as revealed by principal-component analysis (Figure S13). Therein, the controls, **Au** treatments, and CYT and NE fractions were clearly separated, while the intra-condition replicates clustered together, indicating homogeneous treatment effects even in subcellular fractions. Of the total number of proteins, 117 and 465 protein groups were significantly regulated in the CYT and NE fractions, respectively (Figure S13B). Statistical significance was calculated using multiple testing-corrected *p* values based on 5% false discovery rate (FDR = 0.05 and S0 = 0.1). **Au** treatment induced heme oxygenase 1 (HMOX1), sulfiredoxin 1 (SRXN1), and heat shock 70-kDa protein 1A (HSPA1A) considerably in the CYT fraction. The induction of HSPA1A is also depicted in the profile plot highlighting the stability of the entire experiment (Figure 6B). Although **Au** targets TXNRD1, this protein was not found to be significantly regulated according to label-free quantification (LFQ) abundance (Figure 6B). The second putative binding partner PRXD4 was present in similar abundance and was also not significantly regulated (Figure 6C). Selenoprotein expression is known to depend on selenium availability.[71,72] **Au** treatment led to the significant down-regulation of the three detected selenoproteins glutathione peroxidase 1 (GPX1), GPX4, and the mitochondrial protein adenylyltransferase SelO (SELO), which may be explained by the reduction of the available intracellular selenium

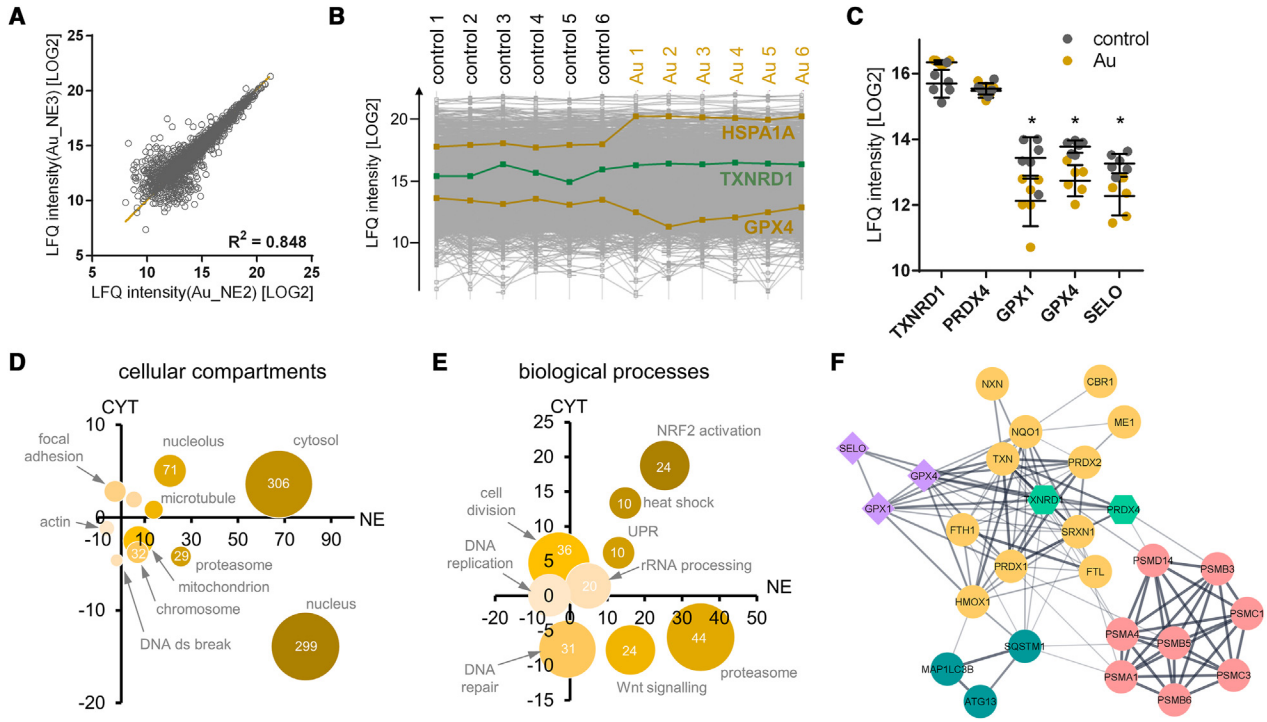

Figure 6. Effects of targeting TXNRD1 by Au in SW480 cancer cells

SW480 cancer cells were treated at sub-cytotoxic concentration of **Au** (12 μM, 24 h, $n = 6$). The protein content was fractionated into CYT and NE extracts and processed according to a data-dependent LC-MS/MS proteomics workflow.

(A) The scatterplot shows the distribution of the detected proteins according to the intensity of 2 representative biological replicates of nuclear extracts of **Au**-treated cells.

(B) The profile plot highlights the stability of protein abundance among biological replicates by visualizing the LFQ intensities of HSPA1A (significantly up-regulated), TXNRD1 (not regulated), and GPX4 (significantly down-regulated).

(C) While the selenoproteins GPX1, GPX4, and SELO are significantly down-regulated upon treatment, the potential targets TXNRD1 and PRDX4 are not. Significant protein regulations (*$p < 0.05$) were obtained after multiple testing correction using anFDR of 0.05 and S0 = 0.1. Data are represented as means and SDs ($n = 6$), including all individual data points.

(D) The significantly regulated proteins were grouped according to cellular compartment and visualized by plotting the summed $\log_2$(fold changes) according to CYT and NE. The size of the bubbles represents the number of regulated proteins in the group.

(E) The regulated proteins were also grouped according to biological processes and similarly visualized.

(F) The target-response network depicts the regulated proteins around the potential binding partners TXNRD1 and PRDX4, indicating effects on redox homeostasis (gold circles), protein degradation via the proteasome (rose circles), selenoproteins (purple diamonds), and autophagy (turquoise circles). Circle, up-regulated protein; diamond, down-regulated protein; hexagon, not regulated. Significantly regulated proteins were multiple testing corrected using a 5% FDR and S0 = 0.1.

pool after **Au** treatment. Selenium deficiency is known to lead to selenoprotein truncation, as a consequence of misinterpreting UGA as a normal stop codon instead of a codon for selenocysteine, and subsequent degradation by the proteasomal system.[73] It is probable that TXNRD1 remains unaffected because selenocysteine is located close to the C terminus.

The global effects of **Au** on the proteome of SW480 cancer cells were further illustrated by grouping the significantly regulated proteins according to Gene Ontology cellular compartments and biological processes, and plotting their summed fold changes according to CYT and NE fractions. We found cytosolic, nuclear, and nucleolar proteins to be the main disturbed cellular compartments (Figure 6D). Additionally, there seems to be a minor impact on mitochondria. The biological processes revealed the induction of NRF2 target genes as the strongest perturbation in both CYT and NE (Figures 6E; Table S1).[56,74] This is accompanied by the induction of HSPs and

an endoplasmic reticulum-based unfolded protein response, which is indicative of proteotoxic stress possibly due to non-specific gold-templated arylation reactions or the effects of the liberated gold(0/I) ions in these cells. Similarly to a previously reported gold(I) bis-N-heterocyclic carbene compound,[70] the proteasome was observed to be translocated into the nucleus. This may also be the consequence of proteotoxic stress. Indeed, we found the accumulation of green fluorescence from **Au-Fluo** in the nucleus by confocal microscopy (Figure 3C). These findings are supported by an analogous pathway representation with similar findings (Figure S13C).

The target-response network highlights the significantly regulated proteins in the neighborhood of the target protein TXNRD1 and PRDX4 (hexagons, Figure 6F). These proteins are located in the center of the network surrounded by a cluster of NRF2-induced redox proteins (yellow, e.g., HMOX1, SRXN1, TXN, PRDX1, and NADPH dehydrogenase [quinone] 1). The down-regulated selenoproteins GPX1, GPX4, and SELO (purple) are directly connected to these redox proteins and TXNRD1 as well. Autophagy-related proteins (turquoise, e.g., sequestosome 1 and autophagy-related protein 13) and proteasomal proteins (rose, e.g., proteasomal subunit alpha type-1 [PSMA1], PSMA4, and beta type-5), which digest irreversibly damaged proteins, were also found up-regulated. Therefore, **Au**-templated covalent targeting of TXNRD1 seems to impact proteins involved in maintaining the redox balance of SW480 cancer cells. As a consequence, cells try to cope with this challenge by inducing an NRF2 stress response and translocating the proteasome to the nuclear compartment. We further evaluated the induction of reactive oxygen species (ROS) in living SW480 cells by the **Au** treatment (2 h incubation). **Au** did not lead to ROS formation in this time interval in concentrations up to EC_{50} values (Figure S14).

To functionally evaluate the dependence of SW480 cancer cells on the induction of the NRF2 stress response upon treatment with **Au**, we tested for synergism[75] by co-treatment with the HMOX1 inhibitor OB-24.[76] HMOX1 was the most strongly up-regulated protein of the NRF2 target genes upon treatment with **Au** in both CYT and NE fractions (Figure S13C). HMOX1 protects cells from oxidative stress and has anti-apoptotic properties.[77] After determining the individual EC_{50} profiles of **Au** and OB-24 in SW480 cancer cells after 72 h of incubation, combination treatments were performed according to 0, EC_{10}, EC_{25}, EC_{50}, EC_{75}, and EC_{90} concentrations, for a total of 36 combinations. At EC_{75} concentrations of **Au**, a strong synergism (δ score >30) was observed with EC_{10} and EC_{25} concentrations of OB-24 (Figure S15). This verified the dependence of SW480 cancer cells on inducing the NRF2 stress response to cope with the TXNRD1-targeting ability of **Au**.

In summary, a cyclometalated gold(III) C^N complex is shown that covalently targets the CysSec-dyad of the selenoprotein TXNRD1 via a gold-templated reactivity. Using combined chemoproteomic and complementary methods, we have shown that this mechanism allows selective targeting of TXNRD1 in cancer cells by **Au**, leading to the potent inhibition of TXNRD1 activity. A fluorescent derivative of the title compound (**Au-Fluo**) enabled the investigation of the cellular distribution by fluorescence microscopy, showing that the compound can be efficiently taken up by cancer cells, and distributed to the perinuclear region and into the nuclear compartment. Although **Au** does not influence TXNRD1 abundance, significant proteome changes were found to be associated with maintaining the cellular redox balance. These changes were characterized by the down-regulation of the remaining selenoproteins and the induction of NRF2-derived redox proteins, but without accompanying ROS formation in SW480 cancer cells. Synergism studies revealed that the induction of

the NRF2 pathway is necessary for cancer cell survival upon treatment with **Au**. This metal-templated covalent targeting, fostering the formation of C–S/Se covalent bonds, can be used to design improved anticancer organogold candidates for covalent drug discovery. Furthermore, recent reports on the *in vitro*/*in vivo* anticancer effects of this family of cyclometalated gold(III) C^N complexes[78–82] could be revisited to consider this bioorthogonal reactivity as part of the compounds' MoA.

EXPERIMENTAL PROCEDURES

Resource availability

Lead contact

Further information and requests for resources should be directed to and will be fulfilled by the lead contact, Samuel M. Meier-Menches (samuel.meier-menches@univie.ac.at).

Materials availability

All materials generated in this study are available from the lead contact without restriction.

Data and code availability

The MS proteomics data have been deposited to the ProteomeXchange Consortium via the PRIDE partner repository with the dataset identifier PRIDE: PXD044971 (pull-down) and PRIDE: PXD044966 (profiling).

SUPPLEMENTAL INFORMATION

Supplemental information can be found online at https://doi.org/10.1016/j.xcrp.2024.102072.

ACKNOWLEDGMENTS

The authors are grateful to the Core Facility for Mass Spectrometry, the Core Facility Multimodal Imaging (Faculty of Chemistry, University of Vienna), and the Joint Metabolome Facility (University of Vienna and Medical University of Vienna), which are all members of the Vienna Life-Science Instruments. S.M.M.-M. acknowledges financial support from the Austrian Science Fund (P33238-N). S.R.T. acknowledges the TUM Global Postdoc Fellowship Scheme for funding. The authors thank Endre Kiss for helpful assistance during the confocal microscopy experiments.

AUTHOR CONTRIBUTIONS

Conceptualization, A.C. and S.M.M.-M. Methodology, L.S., C.S., C.G., A.C., and S.M.M.-M. Formal analysis, T.M., A.B., and C.G. Investigation, L.S., C.S., S.R.T., M.P., V.G., D.W., R.B., and G.D.F. Resources, G.D.F., C.G., A.C., and S.M.M.-M. Data curation, L.S., T.M., A.B., C.G., and S.M.M.-M. Writing – original draft, L.S., C.S., A.C., and S.M.M.-M. Writing – review and editing, all authors. Supervision, C.G., A.C., and S.M.M.-M.

DECLARATION OF INTERESTS

The authors declare no competing interests.

Received: October 18, 2023
Revised: May 3, 2024
Accepted: June 7, 2024
Published: June 28, 2024

REFERENCES

1. Boike, L., Henning, N.J., and Nomura, D.K. (2022). Advances in covalent drug discovery. Nat. Rev. Drug Discov. *21*, 881–898. https://doi.org/10.1038/s41573-022-00542-z.

2. Ertl, P., Altmann, E., and McKenna, J.M. (2020). The most common functional groups in bioactive molecules and how their popularity has evolved over time. J. Med. Chem. *63*, 8408–8418. https://doi.org/10.1021/acs.jmedchem.0c00754.

3. Lagoutte, R., Patouret, R., and Winssinger, N. (2017). Covalent inhibitors: An opportunity for rational target selectivity. Curr. Opin. Chem. Biol. *39*, 54–63. https://doi.org/10.1016/j.cbpa.2017.05.008.

4. Yu, H.A., and Pao, W. (2013). Targeted therapies: Afatinib-new therapy option for EGFR-mutant lung cancer. Nat. Rev. Clin. Oncol. *10*, 551–552. https://doi.org/10.1038/nrclinonc.2013.154.

5. Skoulidis, F., Li, B.T., Dy, G.K., Price, T.J., Falchook, G.S., Wolf, J., Italiano, A., Schuler, M., Borghaei, H., Barlesi, F., et al. (2021). Sotorasib for lung cancers with KRAS p.G12C mutation. N. Engl. J. Med. *384*, 2371–2381. https://doi.org/10.1056/NEJMoa2103695.

6. Mullard, A. (2023). Chemoproteomic trailblazer advances covalent candidate into the clinic, pushes allosteric agenda. Nat. Rev. Drug Discov. *22*, 689–690. https://doi.org/10.1038/d41573-023-00133-6.

7. Hacker, S.M., Backus, K.M., Lazear, M.R., Forli, S., Correia, B.E., and Cravatt, B.F. (2017). Global profiling of lysine reactivity and ligandability in the human proteome. Nat. Chem. *9*, 1181–1190. https://doi.org/10.1038/nchem.2826.

8. Casini, A., and Pöthig, A. (2024). Metals in cancer research: Beyond platinum metallodrugs. ACS Cent. Sci. *10*, 242–250. https://doi.org/10.1021/acscentsci.3c01340.

9. Boros, E., Dyson, P.J., and Gasser, G. (2020). Classification of metal-based drugs according to their mechanisms of action. Chem *6*, 41–60. https://doi.org/10.1016/j.chempr.2019.10.013.

10. Moreno-Alcántar, G., Picchetti, P., and Casini, A. (2023). Gold complexes in anticancer therapy: From new design principles to particle-based delivery systems. Angew. Chem. Int. Ed. *62*, e202218000. https://doi.org/10.1002/anie.202218000.

11. Mora, M., Gimeno, M.C., and Visbal, R. (2019). Recent advances in gold–NHC complexes with biological properties. Chem. Soc. Rev. *48*, 447–462. https://doi.org/10.1039/c8cs00570b.

12. Casini, A., Wai-Yin Sun, R., and Ott, I. (2018). Medicinal chemistry of gold anticancer metallodrugs. In Metallo-Drugs: Development and Action of Anticancer Agents, (De Gruyter), pp. 199–218. https://doi.org/10.1515/9783110470734-007.

13. Yue, S., Luo, M., Liu, H., and Wei, S. (2020). Recent advances of gold compounds in anticancer immunity. Front. Chem. *8*, 543. https://doi.org/10.3389/fchem.2020.00543.

14. Nardon, C., Boscutti, G., and Fregona, D. (2014). Beyond platinums: Gold complexes as anticancer agents. Anticancer Res. *34*, 487–492.

15. Schmidt, C., and Casini, A. (2022). Organometallic chemistry of gold-based drugs. In Comprehensive Organometallic Chemistry IV, (Elsevier), pp. 297–313. https://doi.org/10.1016/b978-0-12-820206-7.00032-9.

16. Bertrand, B., Stefan, L., Pirrotta, M., Monchaud, D., Bodio, E., Richard, P., Le Gendre, P., Warmerdam, E., de Jager, M.H., Groothuis, G.M.M., et al. (2014). Caffeine-based gold(I) N-heterocyclic carbenes as possible anticancer agents: Synthesis and biological properties. Inorg. Chem. *53*, 2296–2303. https://doi.org/10.1021/ic403011h.

17. Kaußler, C., Wragg, D., Schmidt, C., Moreno-Alcántar, G., Jandl, C., Stephan, J., Fischer, R.A., Leoni, S., Casini, A., and Bonsignore, R. (2022). "Dynamical docking" of cyclic dinuclear Au(I) bis-N-heterocyclic complexes facilitates their binding to G-quadruplexes. Inorg. Chem. *61*, 20405–20423. https://doi.org/10.1021/acs.inorgchem.2c03041.

18. Roder, C., and Thomson, M.J. (2015). Auranofin: Repurposing an old drug for a golden new age. Drugs R *15*, 13–20. https://doi.org/10.1007/s40268-015-0083-y.

19. Bindoli, A., Rigobello, M.P., Scutari, G., Gabbiani, C., Casini, A., and Messori, L. (2009). Thioredoxin reductase: A target for gold compounds acting as potential anticancer drugs. Coord. Chem. Rev. *253*, 1692–1707. https://doi.org/10.1016/j.ccr.2009.02.026.

20. Fan, C., Zheng, W., Fu, X., Li, X., Wong, Y.S., and Chen, T. (2014). Enhancement of auranofin-induced lung cancer cell apoptosis by selenocystine, a natural inhibitor of TrxR1 in vitro and in vivo. Cell Death Dis. *5*, e1191. https://doi.org/10.1038/cddis.2014.132.

21. Thomas, S.R., Bonsignore, R., Sánchez Escudero, J., Meier-Menches, S.M., Brown, C.M., Wolf, M.O., Barone, G., Luk, L.Y.P., and Casini, A. (2020). Exploring the chemoselectivity towards cysteine arylation by cyclometallated Au(III) compounds: New mechanistic insights. Chembiochem *21*, 3071–3076. https://doi.org/10.1002/cbic.202000262.

22. Bertrand, B., and Casini, A. (2014). A golden future in medicinal inorganic chemistry: The promise of anticancer gold organometallic compounds. Dalton Trans. *43*, 4209–4219. https://doi.org/10.1039/c3dt52524d.

23. Martínez-Calvo, M., and Mascareñas, J.L. (2018). Organometallic catalysis in biological media and living settings. Coord. Chem. Rev. *359*, 57–79. https://doi.org/10.1016/j.ccr.2018.01.011.

24. Tong, K.-C., Lok, C.-N., Wan, P.-K., Hu, D., Fung, Y.M.E., Chang, X.-Y., Huang, S., Jiang, H., and Che, C.-M. (2020). An anticancer gold(III)-activated porphyrin scaffold that covalently modifies protein cysteine thiols. Proc. Natl. Acad. Sci. *117*, 1321–1329. https://doi.org/10.1073/pnas.1915202117.

25. Tsubokura, K., Vong, K.K.H., Pradipta, A.R., Ogura, A., Urano, S., Tahara, T., Nozaki, S., Onoe, H., Nakao, Y., Sibgatullina, R., et al. (2017). In vivo gold complex catalysis within live mice. Angew. Chem. Int. Ed. *56*, 3579–3584. https://doi.org/10.1002/anie.201610273.

26. Thomas, S.R., and Casini, A. (2020). Gold compounds for catalysis and metal-mediated transformations in biological systems. Curr. Opin. Chem. Biol. *55*, 103–110. https://doi.org/10.1016/j.cbpa.2019.12.007.

27. Kung, K.K.Y., Ko, H.M., Cui, J.F., Chong, H.C., Leung, Y.C., and Wong, M.K. (2014). Cyclometalated gold(III) complexes for chemoselective cysteine modification via ligand controlled C-S bond-forming reductive elimination. Chem. Commun. *50*, 11899–11902. https://doi.org/10.1039/c4cc04467c.

28. de Paiva, R.E.F., Du, Z., Nakahata, D.H., Lima, F.A., Corbi, P.P., and Farrell, N.P. (2018). Gold-catalyzed C-S aryl-group transfer in zinc finger proteins. Angew. Chem. Int. Ed. *57*, 9305–9309. https://doi.org/10.1002/anie.201803082.

29. Wenzel, M.N., Bonsignore, R., Thomas, S.R., Bourissou, D., Barone, G., and Casini, A. (2019). Cyclometalated Au(III) complexes for cysteine arylation in zinc finger protein domains: Towards controlled reductive elimination. Chem. Eur J. *25*, 7628–7634. https://doi.org/10.1002/chem.201901535.

30. Casini, A., Guerri, A., Gabbiani, C., and Messori, L. (2008). Biophysical characterisation of adducts formed between anticancer metallodrugs and selected proteins: New insights from X-ray diffraction and mass spectrometry studies. J. Inorg. Biochem. *102*, 995–1006. https://doi.org/10.1016/j.jinorgbio.2007.12.022.

31. Geri, A., Massai, L., and Messori, L. (2023). Protein metalation by medicinal gold compounds: Identification of the main features of the metalation process through ESI MS experiments. Molecules *28*, 5196. https://doi.org/10.3390/molecules28135196.

32. Tong, K.-C., Hu, D., Wan, P.-K., Lok, C.-N., and Che, C.-M. (2020). Anticancer gold(III) compounds with porphyrin or N-heterocyclic carbene ligands. Front. Chem. *8*, 587207. https://doi.org/10.3389/fchem.2020.587207.

33. Schmidt, C., Zollo, M., Bonsignore, R., Casini, A., and Hacker, S.M. (2022). Competitive profiling of ligandable cysteines in Staphylococcus aureus with an organogold compound. Chem. Commun. *58*, 5526–5529. https://doi.org/10.1039/d2cc01259f.

34. Pushie, M.J., Pickering, I.J., Korbas, M., Hackett, M.J., and George, G.N. (2014). Elemental and chemically specific X-ray fluorescence imaging of biological systems. Chem. Rev. *114*, 8499–8541. https://doi.org/10.1021/cr4007297.

35. Davis, K.J., Carrall, J.A., Lai, B., Aldrich-Wright, J.R., Ralph, S.F., and Dillon, C.T. (2012). Does cytotoxicity of metallointercalators correlate with cellular uptake or DNA affinity? Dalton Trans. *41*, 9417–9426. https://doi.org/10.1039/c2dt30217a.

36. Lovett, J.H., and Harris, H.H. (2021). Application of X-ray absorption and X-ray fluorescence techniques to the study of metallodrug action. Curr. Opin. Chem. Biol. *61*,

135–142. https://doi.org/10.1016/j.cbpa.2020.12.004.

37. Casini, A., Vessières, A., and Meier-Menches, S.M. (2019). Metal-based Anticancer Agents ((Royal Society of Chemistry)). https://doi.org/10.1039/9781788016452.

38. Wenzel, M., and Casini, A. (2017). Mass spectrometry as a powerful tool to study therapeutic metallodrugs speciation mechanisms: Current frontiers and perspectives. Coord. Chem. Rev. *352*, 432–460. https://doi.org/10.1016/j.ccr.2017.02.012.

39. Meier, S.M., Gerner, C., Keppler, B.K., Cinellu, M.A., and Casini, A. (2016). Mass spectrometry uncovers molecular reactivities of coordination and organometallic gold(III) drug candidates in competitive experiments that correlate with their biological effects. Inorg. Chem. *55*, 4248–4259. https://doi.org/10.1021/acs.inorgchem.5b03000.

40. Hartinger, C.G., Groessl, M., Meier, S.M., Casini, A., and Dyson, P.J. (2013). Application of mass spectrometric techniques to delineate the modes-of-action of anticancer metallodrugs. Chem. Soc. Rev. *42*, 6186–6199. https://doi.org/10.1039/c3cs35532b.

41. Skos, L., Borutzki, Y., Gerner, C., and Meier-Menches, S.M. (2023). Methods to identify protein targets of metal-based drugs. Curr. Opin. Chem. Biol. *73*, 102257. https://doi.org/10.1016/j.cbpa.2022.102257.

42. Wang, H., Zhou, Y., Xu, X., Li, H., and Sun, H. (2020). Metalloproteomics in conjunction with other omics for uncovering the mechanism of action of metallodrugs: Mechanism-driven new therapy development. Curr. Opin. Chem. Biol. *55*, 171–179. https://doi.org/10.1016/j.cbpa.2020.02.006.

43. Zhou, Y., Li, H., and Sun, H. (2022). Metalloproteomics for biomedical research: methodology and applications. Annu. Rev. Biochem. *91*, 449–473. https://doi.org/10.1146/annurev-biochem-040320-104628.

44. Ha, J., Park, H., Park, J., and Park, S.B. (2021). Recent advances in identifying protein targets in drug discovery. Cell Chem. Biol. *28*, 394–423. https://doi.org/10.1016/j.chembiol.2020.12.001.

45. Meier, S.M., Kreutz, D., Winter, L., Klose, M.H.M., Cseh, K., Weiss, T., Bileck, A., Alte, B., Mader, J.C., Jana, S., et al. (2017). An organoruthenium anticancer agent shows unexpected target selectivity for plectin. Angew. Chem. Int. Ed. *56*, 8267–8271. https://doi.org/10.1002/anie.201702242.

46. Neuditschko, B., Legin, A.A., Baier, D., Schintlmeister, A., Reipert, S., Wagner, M., Keppler, B.K., Berger, W., Meier-Menches, S.M., and Gerner, C. (2021). Interaction with ribosomal proteins accompanies stress induction of the anticancer metallodrug BOLD-100/KP1339 in the endoplasmic reticulum. Angew. Chem. Int. Ed. *60*, 5063–5068. https://doi.org/10.1002/anie.202015962.

47. Neuditschko, B., King, A.P., Huang, Z., Janker, L., Bileck, A., Borutzki, Y., Marker, S.C., Gerner, C., Wilson, J.J., and Meier-Menches, S.M. (2022). An anticancer rhenium tricarbonyl targets Fe−S cluster biogenesis in ovarian cancer cells. Angew. Chem. Int. Ed. *61*, e202209136. https://doi.org/10.1002/anie.202209136.

48. Fung, S.K., Zou, T., Cao, B., Lee, P.-Y., Fung, Y.M.E., Hu, D., Lok, C.-N., and Che, C.-M. (2017). Cyclometalated gold(III) complexes containing N-heterocyclic carbene ligands engage multiple anti-cancer molecular targets. Angew. Chem. Int. Ed. *56*, 3892–3896. https://doi.org/10.1002/anie.201612583.

49. Wan, P.-K., Tong, K.-C., Lok, C.-N., Zhang, C., Chang, X.-Y., Sze, K.-H., Wong, A.S.T., and Che, C.-M. (2021). Platinum(II) N-heterocyclic carbene complexes arrest metastatic tumor growth. Proc. Natl. Acad. Sci. *118*, e2025806118. https://doi.org/10.1073/pnas.2025806118.

50. Sabatier, P., Beusch, C.M., Gencheva, R., Cheng, Q., Zubarev, R., and Arnér, E.S.J. (2021). Comprehensive chemical proteomics analyses reveal that the new TRi-1 and TRi-2 compounds are more specific thioredoxin reductase 1 inhibitors than auranofin. Redox Biol. *48*, 102184. https://doi.org/10.1016/j.redox.2021.102184.

51. Saei, A.A., Gullberg, H., Sabatier, P., Beusch, C.M., Johansson, K., Lundgren, B., Arvidsson, P.I., Arnér, E.S.J., and Zubarev, R.A. (2020). Comprehensive chemical proteomics for target deconvolution of the redox active drug auranofin. Redox Biol. *32*, 101491. https://doi.org/10.1016/j.redox.2020.101491.

52. Wang, H., Hu, L., Li, H., Lai, Y.-T., Wei, X., Xu, X., Cao, Z., Cao, H., Wan, Q., Chang, Y.-Y., et al. (2023). Mitochondrial ATP synthase as a direct molecular target of chromium(III) to ameliorate hyperglycaemia stress. Nat. Commun. *14*, 1738. https://doi.org/10.1038/s41467-023-37351-w.

53. Wang, H., Yan, A., Liu, Z., Yang, X., Xu, Z., Wang, Y., Wang, R., Koohi-Moghadam, M., Hu, L., Xia, W., et al. (2019). Deciphering molecular mechanism of silver by integrated omic approaches enables enhancing its antimicrobial efficacy in E. coli. PLoS Biol. *17*, e3000292. https://doi.org/10.1371/journal.pbio.3000292.

54. Wang, Y., Hu, L., Xu, F., Quan, Q., Lai, Y.-T., Xia, W., Yang, Y., Chang, Y.-Y., Yang, X., Chai, Z., et al. (2017). Integrative approach for the analysis of the proteome-wide response to bismuth drugs in Helicobacter pylori. Chem. Sci. *8*, 4626–4633. https://doi.org/10.1039/c7sc00766c.

55. Chiappetta, G., Gamberi, T., Faienza, F., Limaj, X., Rizza, S., Messori, L., Filomeni, G., Modesti, A., and Vinh, J. (2022). Redox proteome analysis of auranofin exposed ovarian cancer cells (A2780). Redox Biol. *52*, 102294. https://doi.org/10.1016/j.redox.2022.102294.

56. Dodson, M., de la Vega, M.R., Cholanians, A.B., Schmidlin, C.J., Chapman, E., and Zhang, D.D. (2019). Modulating NRF2 in disease: Timing Is everything. Annu. Rev. Pharm. Tox. *59*, 555–575. https://doi.org/10.1146/annurev-pharmtox-010818-021856.

57. Lu, Y., Ma, X., Chang, X., Liang, Z., Lv, L., Shan, M., Lu, Q., Wen, Z., Gust, R., and Liu, W. (2022). Recent development of gold(I) and gold(III) complexes as therapeutic agents for cancer diseases. Chem. Soc. Rev. *51*, 5518–5556. https://doi.org/10.1039/d1cs00933h.

58. Fritz-Wolf, K., Kehr, S., Stumpf, M., Rahlfs, S., and Becker, K. (2011). Crystal structure of the human thioredoxin reductase–thioredoxin complex. Nat. Commun. *2*, 383. https://doi.org/10.1038/ncomms1382.

59. Meier, S.M., Tsybin, Y.O., Dyson, P.J., Keppler, B.K., and Hartinger, C.G. (2012). Fragmentation methods on the balance: Unambiguous top–down mass spectrometric characterization of oxaliplatin–ubiquitin binding sites. Anal. Bioanal. Chem. *402*, 2655–2662. https://doi.org/10.1007/s00216-011-5523-0.

60. Angelucci, F., Sayed, A.A., Williams, D.L., Boumis, G., Brunori, M., Dimastrogiovanni, D., Miele, A.E., Pauly, F., and Bellelli, A. (2009). Inhibition of Schistosoma mansoni thioredoxin-glutathione reductase by auranofin: structural and kinetic aspects. J. Biol. Chem. *284*, 28977–28985. https://doi.org/10.1074/jbc.M109.020701.

61. Lechner, S., Müller-Ladner, U., Neumann, E., Spöttl, T., Schlottmann, K., Rüschoff, J., Schölmerich, J., and Kullmann, F. (2003). Thioredoxin reductase 1 expression in colon cancer: Discrepancy between in vitro and in vivo findings. Lab. Invest. *83*, 1321–1331. https://doi.org/10.1097/01.Lab.0000085189.47968.F8.

62. Jürgens, S., Scalcon, V., Estrada-Ortiz, N., Folda, A., Tonolo, F., Jandl, C., Browne, D.L., Rigobello, M.P., Kühn, F.E., and Casini, A. (2017). Exploring the C^N^C theme: Synthesis and biological properties of tridentate cyclometalated gold(III) complexes. Bioorg. Med. Chem. *25*, 5452–5460. https://doi.org/10.1016/j.bmc.2017.08.001.

63. Schmidt, C., Karge, B., Misgeld, R., Prokop, A., Franke, R., Brönstrup, M., and Ott, I. (2017). Gold(I) NHC Complexes: Antiproliferative Activity, Cellular Uptake, Inhibition of Mammalian and Bacterial Thioredoxin Reductases, and Gram-Positive Directed Antibacterial Effects. Chem. Eur J. *23*, 1869–1880. https://doi.org/10.1002/chem.201604512.

64. Wang, L., Yang, Z., Fu, J., Yin, H., Xiong, K., Tan, Q., Jin, H., Li, J., Wang, T., Tang, W., et al. (2012). Ethaselen: a potent mammalian thioredoxin reductase 1 inhibitor and novel organoselenium anticancer agent. Free Radic. Biol. Med. *52*, 898–908. https://doi.org/10.1016/j.freeradbiomed.2011.11.034.

65. Stafford, W.C., Peng, X., Olofsson, M.H., Zhang, X., Luci, D.K., Lu, L., Cheng, Q., Trésaugues, L., Dexheimer, T.S., Coussens, N.P., et al. (2018). Irreversible inhibition of cytosolic thioredoxin reductase 1 as a mechanistic basis for anticancer therapy. Sci. Transl. Med. *10*, eaaf7444. https://doi.org/10.1126/scitranslmed.aaf7444.

66. Jan, Y.-H., Heck, D.E., Gray, J.P., Zheng, H., Casillas, R.P., Laskin, D.L., and Laskin, J.D. (2010). Selective targeting of selenocysteine in thioredoxin reductase by the half mustard 2-chloroethyl ethyl sulfide in lung epithelial cells. Chem. Res. Toxicol. *23*, 1045–1053. https://doi.org/10.1021/tx100040k.

67. Zeisel, L., Felber, J.G., Scholzen, K.C., Poczka, L., Cheff, D., Maier, M.S., Cheng, Q., Shen, M., Hall, M.D., Arnér, E.S.J., et al. (2022). Selective cellular probes for mammalian thioredoxin reductase TrxR1: Rational design of RX1, a

modular 1,2-thiaselenane redox probe. Chem *8*, 1493–1517. https://doi.org/10.1016/j.chempr.2022.03.010.

68. Zhang, J., Zhang, B., Li, X., Han, X., Liu, R., and Fang, J. (2019). Small molecule inhibitors of mammalian thioredoxin reductase as potential anticancer agents: An update. Med. Res. Rev. *39*, 5–39. https://doi.org/10.1002/med.21507.

69. Zhang, B., Zhang, J., Peng, S., Liu, R., Li, X., Hou, Y., Han, X., and Fang, J. (2017). Thioredoxin reductase inhibitors: a patent review. Expert Opin. Ther. Pat. *27*, 547–556. https://doi.org/10.1080/13543776.2017.1272576.

70. Meier-Menches, S.M., Neuditschko, B., Zappe, K., Schaier, M., Gerner, M.C., Schmetterer, K.G., Del Favero, G., Bonsignore, R., Cichna-Markl, M., Koellensperger, G., et al. (2020). An organometallic gold(I) bis-N-heterocyclic carbene complex with multimodal activity in ovarian cancer cells. Chem. Eur J. *26*, 15528–15537. https://doi.org/10.1002/chem.202003495.

71. Schomburg, L., and Schweizer, U. (2009). Hierarchical regulation of selenoprotein expression and sex-specific effects of selenium. Biochim. Biophys. Acta *1790*, 1453–1462. https://doi.org/10.1016/j.bbagen.2009.03.015.

72. Touat-Hamici, Z., Bulteau, A.-L., Bianga, J., Jean-Jacques, H., Szpunar, J., Lobinski, R., and Chavatte, L. (2018). Selenium-regulated hierarchy of human selenoproteome in cancerous and immortalized cells lines. Biochim. Biophys. Acta *1862*, 2493–2505. https://doi.org/10.1016/j.bbagen.2018.04.012.

73. Lin, H.-C., Ho, S.-C., Chen, Y.-Y., Khoo, K.-H., Hsu, P.-H., and Yen, H.-C.S. (2015). SELENOPROTEINS. CRL2 aids elimination of truncated selenoproteins produced by failed UGA/Sec decoding. Science *349*, 91–95. https://doi.org/10.1126/science.aab0515.

74. Sporn, M.B., and Liby, K.T. (2012). NRF2 and cancer: The good, the bad and the importance of context. Nat. Rev. Cancer *12*, 564–571. https://doi.org/10.1038/nrc3278.

75. Ianevski, A., Giri, A.K., and Aittokallio, T. (2022). SynergyFinder 3.0: An interactive analysis and consensus interpretation of multi-drug synergies across multiple samples. Nucleic Acids Res. *50*, W739–W743. https://doi.org/10.1093/nar/gkac382.

76. Alaoui-Jamali, M.A., Bismar, T.A., Gupta, A., Szarek, W.A., Su, J., Song, W., Xu, Y., Xu, B., Liu, G., Vlahakis, J.Z., et al. (2009). A novel experimental heme oxygenase-1–targeted therapy for hormone-refractory prostate cancer. Cancer Res. *69*, 8017–8024. https://doi.org/10.1158/0008-5472.Can-09-0419.

77. Petrache, I., Otterbein, L.E., Alam, J., Wiegand, G.W., and Choi, A.M. (2000). Heme oxygenase-1 inhibits TNF-α-induced apoptosis in cultured fibroblasts. Am. J. Physiol. Lung Cell Mol. Physiol. *278*, L312–L319. https://doi.org/10.1152/ajplung.2000.278.2.L312.

78. Babak, M.V., Chong, K.R., Rapta, P., Zannikou, M., Tang, H.M., Reichert, L., Chang, M.R., Kushnarev, V., Heffeter, P., Meier-Menches, S.M., et al. (2021). Interfering with metabolic profile of triple-negative breast cancers using rationally designed metformin prodrugs. Angew. Chem. Int. Ed. *60*, 13405–13413. https://doi.org/10.1002/anie.202102266.

79. de Andrade Querino, A.L., de Sousa, A.M., Thomas, S.R., de Lima, G.M., Dittz, D., Casini, A., do Monte-Neto, R.L., and Silva, H. (2023). Organogold(III)-dithiocarbamate compounds and their coordination analogues as anti-tumor and anti-leishmanial metallodrugs. J. Inorg. Biochem. *247*, 112346. https://doi.org/10.1016/j.jinorgbio.2023.112346.

80. Kim, J.H., Ofori, S., Parkin, S., Vekaria, H., Sullivan, P.G., and Awuah, S.G. (2021). Anticancer gold(III)-bisphosphine complex alters the mitochondrial electron transport chain to induce in vivo tumor inhibition. Chem. Sci. *12*, 7467–7479. https://doi.org/10.1039/d1sc01418h.

81. Bertrand, B., Spreckelmeyer, S., Bodio, E., Cocco, F., Picquet, M., Richard, P., Le Gendre, P., Orvig, C., Cinellu, M.A., and Casini, A. (2015). Exploring the potential of gold(III) cyclometallated compounds as cytotoxic agents: variations on the C^N theme. Dalton Trans. *44*, 11911–11918. https://doi.org/10.1039/c5dt01023c.

82. Abás, E., Bellés, A., Rodríguez-Diéguez, A., Laguna, M., and Grasa, L. (2021). Selective cytotoxicity of cyclometalated gold(III) complexes on Caco-2 cells is mediated by G2/M cell cycle arrest. Metallomics *13*, mfab034. https://doi.org/10.1093/mtomcs/mfab034.

Cell Reports Physical Science, Volume *5*

Supplemental information

Gold-templated covalent targeting of the CysSec-dyad of thioredoxin reductase 1 in cancer cells

Lukas Skos, Claudia Schmidt, Sophie R. Thomas, Mihyun Park, Verena Geiger, Dominik Wenisch, Riccardo Bonsignore, Giorgia Del Favero, Thomas Mohr, Andrea Bileck, Christopher Gerner, Angela Casini, and Samuel M. Meier-Menches

SUPPLEMENTAL EXPERIMENTAL PROCEDURES

General

All reagents were commercially purchased from Sigma-Aldrich, Germany. All complexes were characterized by ^{1}H-, ^{13}C-NMR and ESI mass spectrometry and the purity (>95%) was assessed by elemental analysis. All NMR data were recorded on a Bruker AVANCE III 400 MHz spectrometer and the data was processed using Mnova. ^{1}H and ^{13}C NMR chemical shifts were referenced with the individual solvent residual peaks of the respective NMR solvents. Absorption and emission measurements were recorded on a Cary 60 UV-Vis spectrometer (Agilent Technologies) and Cary Eclipse Fluorescence Spectrophotometer (Agilent Technologies), respectively. High resolution mass spectrometry was performed on a MaXis qTOF (Bruker Daltonics). Elemental analyses were performed using a HEKA tech EURO EA element analyzer. [Au($C^{CO}N$)Cl_2], **Au**, and NPC (2-(-4-(7-nitrobenzo[c][1,2,5]oxadiazol-4-yl)piperazon-1-yl)ethane-1-amine) were synthesized according to previously established procedures [1-3].

Synthesis of Au-Fluo

The synthesis of **Au-Fluo** is shown in Scheme 2. A mixture of NPC (32 mg, 0.11 mmol, 1.0 equiv.), **Au** (52 mg, 0.10 mmol, 1.0 equiv.), HOBt · H_2O (43 mg, 0.28 mmol, 2.8 equiv.), EDC · HCl (58 mg, 0.30 mmol, 3.0 equiv.) was dissolved in dry DMF (1.0 mL) and stirred under N_2 atmosphere at room temperature for 24 h. After this time, the reaction mixture was diluted with DCM (50 ml), washed with H_2O (4 × 50 mL) and brine (1 × 50 mL) in respective order, and dried over anhydrous $MgSO_4$. The organic layer was then dried *in vacuo*. The crude product was dissolved in acetone, filtered, and precipitated by adding pentane to the filtrate. The precipitate was filtered off, and washed with hexane (46 mg, 0.57 mmol, 57% yield).

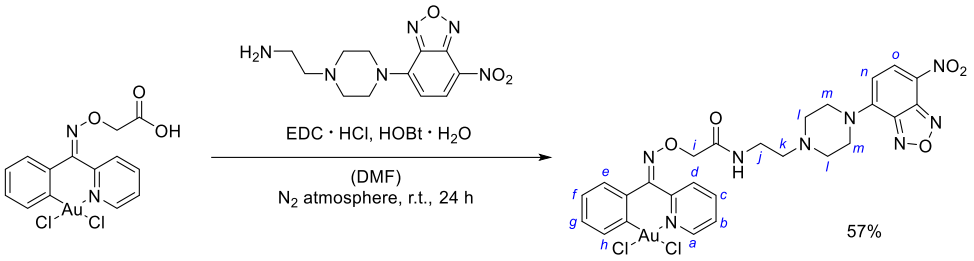

Synthesis of the gold(III) compound **Au-Fluo**.

^{1}H-NMR (400 MHz, 298.6 K, acetone-d_6) δ [ppm] = 9.50 (d, ^{3}J = 5.1 Hz, 1H, H_a), 8.75 (dd, ^{3}J = 8.0 Hz, 1.1 Hz, 1H, H_d), 8.53 (td, ^{3}J = 7.8 Hz, 1.5 Hz, 1H, H_c), 8.48 (d, ^{3}J = 9.0 Hz, 1H, H_o), 7.98 (ddd, ^{3}J = 7.6 Hz, 6.1 Hz, 1.6 Hz, 1H, H_b), 7.61 (dd, ^{3}J = 8.0 Hz, 1.0 Hz, 1H, H_h), 7.49 (dd, ^{3}J = 7.4 Hz, 1.8 Hz, 1H, H_e), 7.34 (td, ^{3}J = 7.4 Hz, 1.1 Hz, 1H, H_f), 7.33 (bs, 1H, N*H*), 7.27 (td, ^{3}J = 7.7 Hz, 1.8 Hz, 1H, H_g), 6.58 (d, ^{3}J = 9.1 Hz, 1H, H_n), 4.85 (d, ^{3}J = 2.6 Hz, 2H, H_i), 4.07 (d, ^{3}J = 3.6 Hz, 4H, H_m), 3.49 (dt, ^{3}J = 12.1 Hz, 6.2 Hz, 1H, H_j), 3.43 (dt, ^{3}J = 13.8 Hz, 6.8 Hz, 1H, H_j), 2.77–2.73 (m, 4H, H_l), 2.61 (t, ^{3}J = 6.2 Hz, 2H, H_k). **^{13}C-NMR** (101 MHz, 299.3 K, acetone-d_6) δ [ppm] = 168.72 (s, *C*=O), 153.55 (s, C_a), 143.75 (s, C_c), 139.31 (s, C=*C*-Au), 136.42 (s, C_o), 134.26 (s, C_h), 130.78 (s, C_g), 130.19 (s, C_d), 129.36 (s, C_e), 129.28 (s, C_f), 128.46 (s, C_b), 104.15 (s, C_n), 74.97 (s, C_i), 57.31 (s, C_k), 53.30 (s, C_l), 50.41 (s, C_m), 36.85 (s, C_j). **Elemental analysis** *calcd.* (%) for $C_{26}H_{25}AuCl_2N_8O_5$: C 39.16, H 3.16, N 14.05; *found* C 39.71, H 3.16, N 14.05.

Fluorescence quantum yield determination

The absolute fluorescence quantum yield (ϕ_F) of **Au-Fluo** (solvent: DMSO; c = 13.8 µM; V = 3 mL) was recorded in a quartz cuvette (10 mm × 10 mm) on a Hamamatsu Quantaurus-QY Absolute PL quantum yield spectrometer C11347-11 upon excitation of the sample at 485 nm (absorbance < 0.3). The final ϕ_F value was calculated as the mean ± standard deviation (n = 5) [4].

Stability studies and reactivity with model nucleophiles and serum albumin

The gold complexes (5 µmol, 1 equiv.) were tested for their stability by ^{1}H NMR in a mixture of DMSO-d_6 and D_2O (9 : 1, 500 µL) over time at 0 h, 1 h, 4 h, 8 h, 12 h and 24 h. Next, the ability of the gold complexes to arylate the cysteine of NAC was investigated in the same conditions as above, but with the addition of NAC (15 µmol, 3.0 equiv.) and at slightly different time intervals (0 min, 5 min, 20 min,

1 h, 6 h, 8 h and 24 h. Next, the ability of **Au-Fluo** to arylate the surface-exposed cysteine of BSA was tested by fluorescence spectroscopy (λ_{exc} = 478 nm). **Au-Fluo** (0.5 mM in 500 µL anhydrous DMSO, 1 equiv.) and BSA (0.5 mM in 4500 µL PBS solution, pH 7.4, 1.0 equiv.) were mixed and incubated in the dark at 37 °C for 1 h and 24 h. As references, the following solutions were prepared: 1) **Au-Fluo**: 0.5 mM **Au-Fluo** in 500 µL anhydrous DMSO was mixed with Biology Grade H_2O (2.428 mL) and PBS (2.072 mL); 2) BSA: 0.5 mM BSA in 4500 µL PBS was mixed with 500 µL anhydrous DMSO; 3) Blank: Anhydrous DMSO (500 µL), Biology Grade H_2O (2.428 mL) and PBS (2.072 mL) were mixed.

Cell culture of SW480 cancer cells

SW480 human colon carcinoma cells were kindly provided by Dr. Michael Jakupec, Institute of Inorganic Chemistry, University of Vienna. They were cultured in Eagle's Minimum Essential Medium (Sigma Aldrich), supplemented with heat-inactivated fetal bovine serum (10% v/v, Gibco), MEM non-essential amino acid solution 100× (1% v/v, Gibco), sodium pyruvate 100 mM (1% v/v, Gibco), and penicillin−streptomycin solution 100× (1% v/v, Gibco, containing penicillin G sodium salt at 10'000 units mL^{-1} and streptomycin sulphate at 10 mg mL^{-1}). The cells were cultured in adherent T75 flasks (Sarstedt) and were subcultured twice a week as the cells reached 75–80% growth area occupied of the flask. Trypsin/EDTA solution (0.25%, Sigma Aldrich) was used for cell detachment.

Viability assay of SW480 cancer cells

SW480 human colon carcinoma cells (10'000 cells/well) were seeded in flat-bottom 96-well plates (Corning) and incubated at 37 °C for 24 h in a humidified incubator at 5% CO_2 (HeraCell150i, Thermo Fisher Scientific). Stock solutions of the compounds in DMSO or were freshly prepared (40 mM **Au**; 40 mM **Au-Fluo**) and diluted with complete cell culture medium (final concentration of DMSO <0.1% v/v). The cells were incubated with the compounds for 24 h and 72 h. Then, the cell metabolism was colorimetrically determined using 3-(4,5-dimethylthiazol-2-yl)-2,5-diphenyl tetrazolium bromide (MTT). For this purpose, MTT reagent (20 µL, 5 mg mL^{-1} in PBS) was added to each well and further incubated for 4 h. The medium was gently removed and DMSO (100 µL) was added to dissolve the formazan crystals. Photometric quantification was performed at 570 nm with a Multiskan Go 1510 photometer (Thermo Fisher Scientific).

The absorbances were blank corrected and converted to relative proliferation. The EC_{50} values, representing the effective concentrations of 50% growth inhibition, were obtained using a sigmoidal fit of the experimental data. The final EC_{50}-values were calculated as the mean ± standard deviation of at least three independent experiments.

For synergy experiments, individual viability assays were performed for **Au** and OB-24 after 72 h incubation to determine EC_{10}, EC_{25}, EC_{50}, EC_{75} and EC_{90} concentrations in SW480 colon cancer cells after sigmoidal fitting of the viability curve. Together with an untreated control (0), **Au** and OB-24 were co-administered at all possible mixtures of those EC-dependent concentrations giving a total of 36 mixtures and incubated for 72 h. The cell metabolism was colorimetrically determined using MTT reagent in an analogous manner as above. The percentage of proliferation inhibition was determined and used as input in SynergyFinder 3.0 [5]. The synergy landscape was calculated using the Bliss-Loewe synergy score.

Cellular distribution of Au-Fluo by fluorescence microscopy

SW480 human colon carcinoma cells (200'000 cells per well) were seeded in flat-bottom 6-well plates (Sarstedt) in 2 mL complete medium and left to adhere at 37 °C and 5% CO_2 for 24 h in a humidified atmosphere (HeraCell150i, Thermo Fisher Scientific). The medium was removed. The cells were then treated with **Au-Fluo** at half EC_{50} and at EC_{50} concentration. The medium was again exchanged after further 4 h with phenol red free DMEM to reduce background fluorescence. Live-cell images were taken 4 h, and 24 h after treatment with a Lionheart FX (BioTek) in phase contrast mode and with a GFP filter cube (excitation at 469 nm, emission at 525 nm, BioTek) corresponding to green fluorescence.

Fluorescence experiments by confocal microscopy were carried in an identical manner compared to the live-cell imaging, but seeding 15'000 cells per well in chamber slides (µ-Slide 8 well, Ibidi GmbH, Germany). After 4 h treatment with **Au-Fluo**, the cells were washed with PBS and fixed with 3.7% formaldehyde at room temperature (10 min in the dark). A previously described [6,7] cells were then rinsed with PBS twice. Cells were permeabilized with 0.2% triton X-100 in PBS (15 min) and blocked with 1% BSA in PBS (1 h) at room temperature. Then, cells were stained with 200 µL phalloidin (Alexa Fluor, 1 : 500 dilution in PBS) at room temperature (1.5 h in the dark) and washed three times with washing buffer (0.05% triton X-100 in PBS) at room temperature (10 min in the dark) and twice with PBS. The slides were post-fixed with 3.7% formaldehyde for 10 min. Finally, the reactive sites were

masked with glycine (100mM in PBS, 5 min) and rinsed with PBS. PBS was removed and slides were mounted and sealed with 2-3 drops of ROTI-Mount FluoCare (Roth, Graz, Austria) with DAPI. Fluorescence images were acquired on a confocal laser scanning microscope Zeiss LSM800 (Zeiss, Jena, Germany) and processed with Zeiss ZEN (Blue edition) Software.

Immobilization conditions

Au (300 µM from a 23.3 mM stock solution in DMF) was activated for 30 min in the presence of 1-ethyl-3-(3-dimethylaminopropyl)carbodiimide (EDC, 360 µM) at pH 4 (HCl) and 37 °C. Activated **Au** (300 µM) was mixed with serotonin (600 µM from a 20 mM aqueous stock solution, pH 4, HCl) in a 1 : 2 molar ratio and incubated up to 24 h at 37 °C and under constant shaking (1100 rpm) in the dark. Aliquots of the reaction mixture were taken at different incubation times. Samples were diluted 1 : 20 to give a final concentration of 5 µM **Au**. ESI-MS data was acquired on an amazon speed ETD ion trap (Bruker Daltonics) in the positive and negative ion modes by direct injection using the following experimental parameters: HV capillary ±4.5 kV, end plate offset –500 V, dry temp 180 °C, nebulizer 3 bar, dry gas 5 L min^{-1}, scan range *m/z* 100–1400, target mass 600. Data was acquired using trapControl (Version 7.1.83.0) and processed using DataAnalysis (Version 4.1.359.0).

Interaction of Au with DTT

Au (10 µM from a fresh stock solution in DMSO) was mixed with DTT (20 µM) in ammonium carbonate buffer (20 mM) and immediately analyzed by flow-injection using an amazon speed ETD ion trap (Bruker Daltonics) in the positive ion modes over 70 min using the following experimental parameters: HV capillary ±4.5 kV, end plate offset –500 V, dry temp 180 °C, nebulizer 3 bar, dry gas 5 L min^{-1}, scan range *m/z* 100–1400, target mass 600, flow rate 5 µL min^{-1}. Data was acquired using trapControl (Version 7.1.83.0) and processed using DataAnalysis (Version 4.1.359.0).

Chemoproteomics

Immobilisation on beads: **Au** (3200 nmol in 1300 µL ddH_2O; 0.01% v/v DMSO) was activated with 1.5 eq. EDC (4800 nmol in 650 µL ddH_2O) at pH 4 (HCl) and incubated for 45 min at 37 °C. CarboxyLink™ Coupling Gel slurry (800 nmol in 50 µL, Thermo Scientific, Ref 20266) was washed three times with aqueous solution (100 µL, pH 4.0, HCl) in 2 mL Eppendorf tubes. After centrifugation (6000 g,

2 min, RT) the supernatant was removed and the activated **Au** (4 equiv., 3200 nmol in 1950 µL) was added to the beads and incubated for 20 h at 37 °C under constant shaking (1400 rpm) in the dark. Drug-immobilized beads were washed twice with 1×PBS (1 mL) and centrifuged (960 g, 2 min, 4 °C). The slurry was resuspended in 1×PBS (800 µL) and aliquoted six times to obtain 100 µL of drug-immobilized beads (100 nmol).

Preparation of whole cell lysates: SW480 cells (2×10^6) were seeded in adherent T75 cell culture flasks (Sarstedt) and expanded at 37 °C and 5% CO_2 for 48 h in an incubator. The cells in each flask were washed twice with 1×PBS (5 mL) and PBS was removed completely. Native lysis buffer (2 mL) was added and the cells were scraped from the bottom of the flask and collected in 15 mL Falcon tubes. The native lysis buffer consisted of NaCl (100 mM), Tris HCl (50 mM), $MgCl_2$ (1.5 mM), NaF (25 mM), Triton X-100 (0.2%), glycerol (5%), TLCK (10 µg mL^{-1}), DTT (1 mM), Na_3VO_4 (1 mM), PMSF (1 mM) and 1% protease and phosphatase inhibitor cocktail (Roche), at pH 7.4. The samples were kept on ice or at 4 °C in a thermo shaker throughout the following procedure. The samples were homogenized by shear stress by pushing the cell suspension 23-times through 2 mL syringe with a 15 cm needle (23G). Complete cell lysis was monitored by microscopy. The suspension was centrifuged (960 g, 5 min, 4°C). Supernatants were collected and combined in a 50 mL falcon tube and subsequently aliquoted into 2 mL Eppendorf tubes (1.584 mL lysate per tube). The whole cell lysate (1.584 mL) from one T75 is sufficient for triplicates of one pull-down condition.

Normal and competitive pull-downs with **Au**: A stock solution of **Au** (40 mM in DMSO) was freshly prepared and diluted with 1×PBS to the desired concentrations. Each **Au** aliquot (16 µL) or control (DMSO mock, 16 µL) was added to SW480 whole cell lysate (1.584 mL, 1 : 100 dilution) and incubated at 4 °C, for 2 h under constant shaking (1400 rpm) in the dark. First, the normal pull-down was performed with mock-treated controls and the competitive pull-down using 12 µM **Au** for preincubation. The second pull-down was performed in a dose-dependent manner using mock-treated controls for normal pull-down and five stepped concentrations of **Au** preincubations (9.6 nM, 48 nM, 2.4 µM, 12 µM and 60 µM) for competitive pull-down. Each condition was performed in triplicates.

The individual pre-treated SW480 whole cell lysates (500 µL, s. above) were added onto the drug-immobilized beads (100 nmol, s. above) in 2 mL Eppendorf tubes and incubated for 4 h at 4 °C under constant shaking (1400 rpm). Then, the samples were transferred onto spin columns (MobiSpin column F with fixed outlet plug, inserted small 10 µm filter and screw cap, MobiTech, No° M105010S).

Samples containing the beads and whole cell lysates were centrifuged (2000 g, 1 min, RT) and the lysate flow-through containing unbound proteins was discarded. Covalent arylation of target proteins leads to their irreversible coupling to the resin that allows for thorough washing steps. The beads were further washed four times with native lysis buffer, and three times with ABC buffer (500 µL, 50 mM). Finally, the beads were centrifuged in the same settings to dryness. The dried beads on the spin columns were suspended in 50 µL sodium deoxycholate buffer (SDC, 50 µL, 0.4 g SDC in 9500 µL ddH_2O and 500 µL 2M Tris-HCl, pH 8.8) and transferred into 1.5 mL Eppendorf tubes. The spin columns were washed again with SDC buffer (50 µL) and also transferred into the 1.5 Eppendorf tube. The combined fractions were heated to 95 °C for 5 min, centrifuged (1200 g, 1 min, RT), and the supernatant was removed. The beads were again washed with SDC buffer (100 µL) and again processed as before. Finally, SDC buffer (100 µL) was added and heated to 95°C for 5 min. Samples were stored in SDC buffer at –20 °C.

Sample processing: To each sample containing the beads in SDC buffer (100 µL), 11 µL of a freshly prepared reduction and alkylation buffer was added (100 mM tris(2-carboxyethyl)phosphine (TCEP), 400 mM 2-chloracetamide (2-CAM) in 940 µL ddH_2O and 60 µL 5 M NaOH, pH 7–8), and incubated for 5 min at 45 °C under constant shaking (1400 rpm) in the dark. The samples were cooled to RT and trypsin/Lys-C buffer (1.1 µL) was added. The trypsin/Lys-C buffer was prepared from Trypsin/Lys-C Mix Mass Spec Grade (20 µg, PROMEGA, USA) dissolved in 100 µL of a mixture of $CaCl_2$ (2 mM) in ddH_2O (9995 µL) and 5 µL concentrated acetic acid. Samples were digested for 18 h at 37 °C under constant shaking (1400 rpm). Thereafter, the sample solution was reduced in a SpeedVac at 45 °C and dissolved in styrenedivinylbenzene – reversed phase sulfonate (SDB-RPS) loading buffer (100 µL, trifluoracetic acid (TFA) 1% v/v; isopropanol 99% v/v). The samples were transferred onto prepared SDB-RPS stage tips equipped with two plugs (Empore™ styrenedivinylbenzene – reversed phase sulfonate solid phase extraction disks, 47 mm, CDS Analytical, USA). Loaded stage tips were put into an adapter on 2 mL Eppendorf tubes and centrifuged (1500 g, 8 min, RT). The samples were washed with loading buffer (100 µL, TFA 1% v/v; isopropanol 99% v/v), wash buffer (100 µL, TFA 0.2% v/v; acetonitrile 5% v/v; ddH_2O 94.8% v/v) and centrifuged after each washing step (1500 g, 8 min, RT). Peptides were eluted by the addition of freshly prepared elution buffer (60 µL, NH_4OH 5% v/v; ddH_2O 35% v/v; acetonitrile 60% v/v) and centrifugation (1500 g, 5 min, RT) into glass inserts, which were dried in a SpeedVac at 45 °C. Digested and dried samples were stored at –20 °C.

Cell-free interaction studies of selenoproteins with Au and Au-Fluo

Interaction: Stock solutions of **Au** (40 µM in DMSO) were freshly prepared. Five micrograms of recombinant human thioredoxin reductase 1 (TXNRD1, 9 µM, 1.0 µg μL^{-1}, non-tagged, 90% Sec content, >95% purity, SelENZYME AB) were transferred into 1.5 mL Eppendorf tubes and diluted to 20 µL with ammonium bicarbonate buffer (20 µM) resulting in 2.25 µM TXNRD1. TXNRD1 was mixed with 0, 1 and 5 equiv. of **Au**, corresponding to 0 µL, 20 µL of 2.25 µM **Au** and 20 µL of 12.25 µM **Au** in ABC buffer, respectively. Untreated proteins were mixed with 20 µL ABC buffer containing 0.3% DMSO as mock control. Similarly, TXNRD1 (5 µg, 2.25 µM) was reacted with 1 equiv. of **Au** in the presence of 0, 1 and 5 equiv. NADPH. Each combination was performed in triplicates and reactions were incubated for 24 h at 37 °C and under constant shaking (600 rpm) in the dark.

Sample processing: The samples containing 5 µg of protein in 40 µL ABC buffer were topped up with 60 µL SDC buffer and directly reduced and alkylated with 11 µL of a mixture of TCEP and 2-CAM (100 mM TCEP, 400 mM 2-CAM in 940 µL ddH_2O and 60 µL 5 M NaOH, pH 7–8) for 5 min at 45 °C. This was followed by 18 h digestion with 2.2 µL trypsin/Lys-C (1 : 50 enzyme-to-substrate ratio) at 37 °C. The trypsin/Lys-C buffer was prepared from Trypsin/Lys-C Mix Mass Spec Grade (20 µg, PROMEGA, USA) dissolved in 100 µL of a mixture of $CaCl_2$ (2 mM) in ddH_2O (9995 µL) and 5 µL concentrated acetic acid. Then, the sample solutions were reduced in a SpeedVac, reconstituted in SDB-RPS loading buffer (TFA 1% v/v, isopropanol 99% v/v) and loaded onto SDB-RPS StageTips. The samples were washed with loading buffer (100µL), wash buffer (100 µL, TFA 0.2% v/v; acetonitrile 5% v/v; ddH_2O 94.8% v/v) and centrifuged after each washing step (1’500 g, 8 min, RT). Peptides were eluted by the addition of freshly prepared elution buffer (60 µL, NH_4OH 5% v/v; ddH_2O 35% v/v; acetonitrile 60% v/v) and centrifugation (1500g, 5min, RT) into glass inserts, which were dried in a SpeedVac at 45 °C. Digested and dried samples were stored at –20 °C.

Proteomic profiling of Au-treated SW480 cancer cells

Treatment: SW480 human colon carcinoma cells were seeded in adherent T25 flasks (Sarstedt) at 2×10^6 cells per well and left to adhere in complete cell culture medium. After 24 h, the medium was exchanged with fresh complete medium (DMSO mock control) or fresh medium containing freshly

dissolved **Au** (12 µM from 40 mM stock solution in DMSO) and incubated for another 24 h. Each condition was carried out in hexuplicates. The cells were processed according to a nucleocytoplasmic fractionation protocol as previously described.[8] All steps were performed on ice. The medium was removed and the cells were washed twice with 1×PBS (3 mL). Then, PBS was thoroughly removed. Isotonic lysis buffer (10 mM HEPES, 10 mM NaCl, 3.5 mM $MgCl_2$, 1 mM EGTA, 0.25 M Sucrose, 0.5% Triton X-100) containing protease inhibitors (1% PMSF, Sigma, and 1% protease and phosphatase inhibitor cocktail, Roche) was added to the wells, the cells were scraped off and transferred into labelled 15 mL Falcon tubes. The cellular membrane was ruptured using shear stress by pressing the cell suspension through a syringe 9–12 times. Membrane rupture with intact nuclei was monitored under a microscope. After centrifugation (960 g, 5 min), the supernatant containing the cytoplasmic (CYT) proteins was transferred into ice-cold ethanol (1 : 5, HPLC grade) and precipitated overnight at –20 °C. The pellet containing the nuclei was incubated with a hypertonic solution (10 mM Tris-HCl, 1 mM EDTA and 0.5 M NaCl) and subsequently with NP-40 buffer (10 mm Tris-HCl, 1 mm EDTA and 0.5% Triton X-100) containing protease inhibitors (1% PMSF, Sigma, and 1% protease and phosphatase inhibitor cocktail, Roche). After centrifugation (960 g, 5 min), the soluble nuclear (NE) proteins were also transferred into ice-cold ethanol (1 : 5, HPLC grade) and precipitated overnight at –20 °C. The precipitated proteins were finally pelleted by centrifugation (5000 g, 30 min, 4 °C), the solution was decanted and the pellet dried under vacuum.

Samples were dissolved in lysis buffer (64 mM DTT, 8 M urea, 20% SDS, 1 M TEAB at pH 7.55) and denatured at 95 °C for 5 min. The protein amount was then quantified using a BCA assay. A total of 20 µg protein per sample was used for processing. Proteins were reduced with DTT (64 mM) and carbamidomethylated with iodoacetamide (48 mM). Proteolytic digestion was performed using the ProtiFi S-trap technology[9] and samples were loaded onto S-trap mini cartridges. Trapping buffer (methanol 90% v/v, 0.1 M TEAB) was added. Samples were thoroughly washed and digested with 0.5 µg trypsin/Lys-C mix (Promega) at 37 °C for 2 h (1 : 40 enzyme-to-protein ratio). Peptides were eluted, dried and stored at –20 °C.

LC-MS/MS Analysis

Dried samples in glass inserts were dissolved with 5 µL of a peptide standard mix consisting of the four synthetic peptides at 10 fmol in 30% formic acid (Glu1-fribrinopeptideB, EGVNDNEEGFFSAR; M28, TTPAVLDSDGSYFLYSK; HK0, VLETKSLYVR and HK1, VLETK(ε-Ac)SLYVR) and diluted with loading buffer (40 µL, acetonitrile 2% v/v, TFA 0.05% v/v; ddH_2O 97.95% v/v). The glass inserts were transferred into 2 mL Eppendorf tubes filled with 400 µL ddH_2O. The samples were sonicated for 5 min (20% power), centrifuged (5000 g, 7 min, RT) and transferred into labelled HPLC vials.

LC-MS/MS analyses were performed employing a timsTOF Pro mass spectrometer (Bruker Daltonics, Bremen, Germany) hyphenated to a Dionex UltiMate™ 3000 RSLCnano system (Thermo Scientific, Bremen, Germany). Samples were analyzed in data-dependent acquisition mode by label free quantification (LFQ) shotgun proteomics in PASEF mode [10]. Samples were loaded on an Acclaim™PepMap™ C18 HPLC pre-column (2 cm × 100 µm, 100 Å, Thermo Fisher Scientific™, Vienna, Austria) at a flow rate of 10 µL min^{-1}. After trapping, peptides were eluted at a flow rate of 300 nL min^{-1} and separated on an Aurora series CSI UHPLC emitter column (25 cm × 75 µm, 1.6 µm C18, Ionopticks, Fitzroy, Australia) applying an 8–40% gradient of mobile phase B (79.9% ACN, 20% H2O, 0.1% FA) in mobile phase A (99.9% H2O, 0.1% FA).

Pull-down and protein interaction: The injection volume was 2 µL. The gradient was selected to run over 40 min giving a total run time of 85 min. The samples from the pull-down and the protein interaction were acquired in technical duplicates.

Proteome profiling: The injection volume was 5 µL. The gradient for the proteome profiling was selected to run over 90 min giving a total run time of 135 min per sample.

Data processing and analysis

Pull-down: Raw data from the timsTOF Pro MS was processed based on LFQ proteomics by MaxQuant (Version 1.6.17.0), including the built-in Andromeda search engine, and searched against the UniProt Database (version 11/2021, 20’375 entries). Non-redundant Swissprot entries with at least one unique peptide were used for identifying protein groups. The first and main search peptide tolerance was 50 and 25 ppm, respectively. The false discovery rate (FDR) was fixed to 0.01 on the peptide and protein level. Match between runs was disabled. For pull-downs, oxidation of methionine and N-terminal acetylation were set as variable modifications and carbamidomethylations of cysteine (C, Cys) and

selenocysteine (U, Sec) were set as fixed modification. Further evaluation was performed with Perseus (Version 1.6.14) using LFQ intensities of the MaxQuant result file. After filtering potential contaminants the LFQ values were Log(2)-transformed. Only those protein groups were considered for data evaluation, which were detected three times in at least one condition. Permutation-based FDR was set to 0.05 and S0 = 0.1 for multi-parameter corrected significance testing of protein enrichment. Pull-down data was visualized using an in-house tool and GraphPad Prism (Version 6.07).

The enrichment [%] was calculated in analogy to a cytotoxicity dose-response curve. First, the de-Log LFQ intensities of a given potential interactor of **Au** from individual pull-down experiments were calculated for all concentration steps (5 concentrations, each n = 3). Then, all LFQ intensities were normalized to the mean LFQ intensity of the pull-down without competition (*i.e.* **Au** = 0 µM) and then plotted as a function of enrichment [%] according to competitor concentration.

Protein interaction: Raw data from the timsTOF Pro MS was processed based on LFQ proteomics by MaxQuant (Version 1.6.17.0), including the built-in Andromeda search engine, and searched against a Fasta file containing only TXNRD1, including isoforms. Non-redundant Swissprot entries with at least one unique peptide were used for identifying protein groups. The first and main search peptide tolerance was 50 and 25 ppm, respectively. The false discovery rate (FDR) was fixed to 0.01 on the peptide and protein level. Match between runs was disabled. For protein interaction studies, carbamidomethylations of cysteine and selenocysteine, arylations of cysteine and selenocysteine and oxidation of methionine were set as variable modifications. Further evaluation was performed with Perseus (Version 1.6.14) using peptide lists of the MaxQuant result file. Potential contaminants were filtered to evaluated the detected peptides related to TXNRD1. Then, mass spectrometric analysis and extracted ion chromatograms were directly performed in DataAnalysis (Version 6.313.6.0, Bruker Daltonics).

Proteome profiling: Raw data from the timsTOF Pro MS was processed based on LFQ proteomics by MaxQuant (Version 1.6.17.0), including the built-in Andromeda search engine, and searched against the UniProt Database (version 11/2021, 20’375 entries). Only non-redundant Swissprot entries with at least two peptides were used for identifying protein groups. The first and main search peptide tolerance was 50 and 25 ppm, respectively. The false discovery rate (FDR) was fixed to 0.01 on the peptide and protein level. Match between runs was enabled with an alignment time window of 0.7 min. Oxidation of methionine and N-terminal acetylation were set as variable modifications. Carbamidomethylations of cysteine (C, Cys) and selenocysteine (U, Sec) were set as fixed modifications. The statistical evaluation

was performed with Perseus (Version 1.6.14) using LFQ intensities of the MaxQuant result file. After filtering potential contaminants the LFQ values were Log(2)-transformed. Only those protein groups were considered for data evaluation, which were detected five times in at least one condition. Permutation-based FDR was set to 0.05 and S0 = 0.1 for multi-parameter corrected significance testing of protein regulation. The final dataset was further analyzed using the web-based applications DAVID bioinformatics Resources (Version 6.8) and STRING (Version 10.0).

Inhibition of mammalian TXNRD1 *in situ*

For the enzyme inhibition assay, an established DTNB-coupled activity microplate reader-based assay was performed [11]. For this purpose, commercially available rat liver TXNRD1 (CAS: 9074-14-0, Sigma-Aldrich) was purchased and diluted with Ultrapure water (18.2 MΩ/0.56 µS at 25 °C, provided by a BerryPure®mini from Berrytec) to achieve a concentration of 3.58 U/mL. Stock solutions were freshly prepared with either DMSO further diluted with phosphate buffer (pH 7.0). 25 µL of the enzyme solution was added to 25 µL of the test compounds in graded concentrations. For each compound, a control was prepared (25 µL of the enzyme solution mixed with 25 µL 1% DMF in phosphate buffer (no compound). In an additional control experiment, it was evaluated that the test compounds do not exhibit any absorption at the respective wavelength or reduce the DTNB in the absence of the enzyme. For this purpose, 25 µL of the highest test concentration of each compound and 25 µL phosphate buffer (no enzyme) were mixed and proceeded as follows. The final DMSO concentration was ≤0.5% v/v in each well. All resulting solutions were incubated under moderate shaking for 75 min at 37 °C in a 96-well plate. To each well, 225 µL of preheated (37°C) reaction mixture (1 mL reaction mixture consists of 500 µL PBS buffer pH 7.0, 80 µL EDTA solution (100 mM, pH 7.5), 20 µL BSA solution (0.2%), 100 µL of NADPH solution (20 mM) and 300 µL Millipore water) was added and the reduction started immediately by addition of 25 µL of a 20 mM ethanolic DTNB solution. After proper mixing, the formation of 5-TNB was monitored by a Tecan Infinite 200pro® plate reader at 412 nm 10 times in 30 s intervals for about 5 min. The increase in 5-TNB concentration over time followed a linear trend (r^2>0.990), and the enzymatic activities were calculated as the slopes (increase in absorbance per second) thereof. The

IC_{50} values were calculated as the concentration of compound decreasing the enzymatic activity of the untreated control by 50% and are given as the means and standard deviation of three experiments.

Cell culture of A549 non-small cell lung cancer cells

A549 lung cancer cells maintained in Dulbecco's modified Eagle's medium (high glucose, pyruvate, no glutamine), which was supplemented with heat inactivated fetal bovine serum (qualified, South American origin, 10% v/v), gentamicin sulphate solution 50 mg/mL (1% v/v, 50 mg/L end concentration), and L-glutamine solution 200 nM (1% v/v, 2 nM end concentration) and were passaged twice a week. All reagents were purchased from GibcoTM at Thermo Scientific, and solvents from Sigma Aldrich if not stated differently. Ultrapure water (18.2 MΩ/0.56 µS at 25 °C) was provided by a BerryPure®mini from Berrytec. A549 were obtained from Cell Line Service (CLS, Eppelheim, Germany).

Viability assays in A549 non-small cell lung cancer cells

A549 cells (6000 cells/well) in cell culture media were transferred to a flat bottom 96-well microtiter plate and incubated at 37 °C/5% CO_2 for 24 h. Stock solutions of **Au** in DMSO were freshly prepared and diluted with the respective cell culture medium to graded concentrations (a final concentration of DMSO: 0.1% v/v). After 24 h of exposure, the metabolically active cells were quantified by 3-(4,5-dimethylthiazol-2-yl)-2,5-diphenyl tetrazolium bromide (MTT, Sigma-Aldrich) staining and the absorptions were calculated as the delta of two measurements of the same well at wavelengths 570 and 690 nm by an Infinite 200pro® plate reader (Tecan). The EC_{50} value (half-maximal effective concentrations) were determined as the concentration that caused 50% inhibition of cell proliferation compared to untreated control (0.1% DMSO in DMEM). The results were calculated as the mean and standard deviation of at least three independent experiments.

Inhibition of human TXNRD1 in A549 cancer cells

To evaluate the inhibition of human TXNRD1 in A549 lung epithelial cancer cells, we utilized an assay kit (ab83463, Abcam). A549 cells were seeded in 6-well plates at a density of 0.9 x 10E6 cells/well in the respective cell culture medium. Following a 24 h incubation period, cells were treated with various

concentrations of **Au** (ranging from 3.1 to 100 µM), dissolved in DMSO at a final concentration of 0.1%, or with 0.1% DMSO as a control, and then incubated at 37°C with 5% CO_2 for an additional 24 h.

After treatment, the media was aspirated, and cells were washed with PBS (pH 7.4). Subsequently, 200 µL of TXNRD1 buffer (included in the kit) was added to each well, and cells were scraped gently, suspended in the buffer, and collected. All samples were homogenized using a Dounce tissue grinder (80 strokes per sample with the tight pestle) and kept on ice throughout the experiment. The cell lysates were then centrifuged at 10'000 g for 15 minutes at 4°C, and the supernatant was collected for further analysis. The protein concentration in the supernatant was determined using the Bradford method with bovine serum albumin as a standard [12].

Next, the protein content was normalized to 10 µg protein per sample. Samples were diluted with TXNRD1 buffer and further proceeded according to the assay protocol. The absorbance was measured at 412 nm using a Tecan Infinite 200 pro® plate reader at 30-second intervals for 20 min.

The difference in absorbance between lysates containing no TXNRD1 inhibitor (representing total DTNB conversion of all reducing proteins in the lysate) and lysates containing TXNRD1 inhibitor (representing DTNB conversion of all reducing proteins except TXNRD1 in the lysate) provided the activity attributable to TXNRD1 [11]. The data were analyzed, and IC_{50} values were determined using non-linear curve fitting with Origin 2019. The data is shown as mean and standard deviation of three replicates.

ROS-Assay (DCFH-DA Assay)

The (sub)confluent colon carcinoma cell line SW480 was trypsinized for 5 minutes in a humidified incubator at 37°C and under a 5% CO_2-atmosphere. Supplemented MEM (*Sigma Aldrich*; supplements: 10% heat inactivated FCS (fetal calf serum; *Serana*), 1mM sodium pyruvate, 4mM L-glutamine, and 1% v/v non-essential amino acid solution) was added to stop trypsinization, and cells were centrifuged for 3 min at 1200 rpm (*Thermo Scientific*, Megafuge 1.0R).

After aspiration of the supernatant, the cell pellet was resuspended in supplemented MEM. Afterwards, SW480-cells were seeded in 100 µL aliquots in densities of 2.5 x 10^4 cells/well in a 96-well clear flat-bottom microplate (*CytoOne*, TC-treated). Incubated at 37°C for 24 hours, cells were washed with 200 µL Hanks' balanced salt solution (HBSS; *Sigma Aldrich*; supplemented with 1% heat inactivated FCS). Then, cells were treated with 100 µL/well of 25 µM 2',7'-dichlorofluorescin diacetate (DCFH-DA; *Sigma Aldrich*), dissolved in supplemented HBSS, for 45 min at 37°C. After washing the cells with 200

µL of supplemented HBSS, test compounds diluted in supplemented phenol-red-free Opti-MEM (Gibco; supplemented with 1% heat inactivated FCS) were added in 200 µL triplicates, and TBHP (tert-butylhydroperoxide) was used as positive control. Subsequently, fluorescence (ex/em = 485/516 nm) was measured every 10 min for a total period of 2 h with a microplate reader (BioTek, Synergy HT). Blank-corrected values were represented in relation to negative controls (treated with drug-free supplemented Opti-MEM) from three independent experiments.

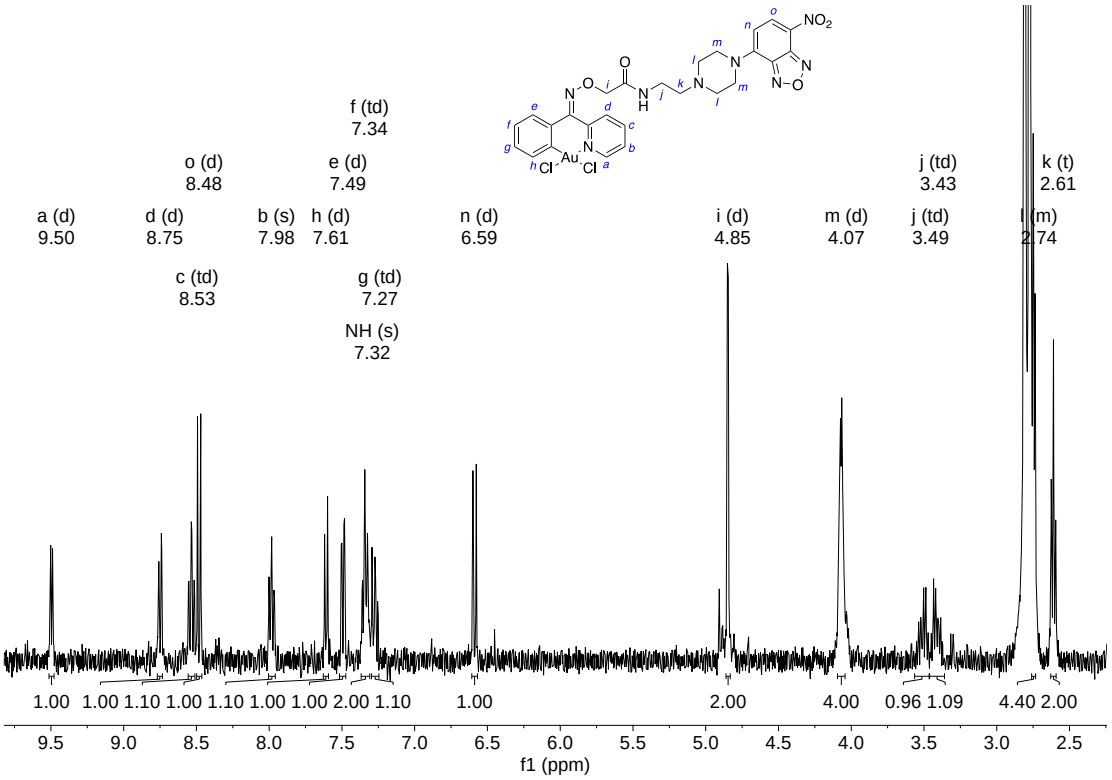

Figure S1. ^{1}H NMR spectrum of **Au-Fluo** in acetone-d_6.

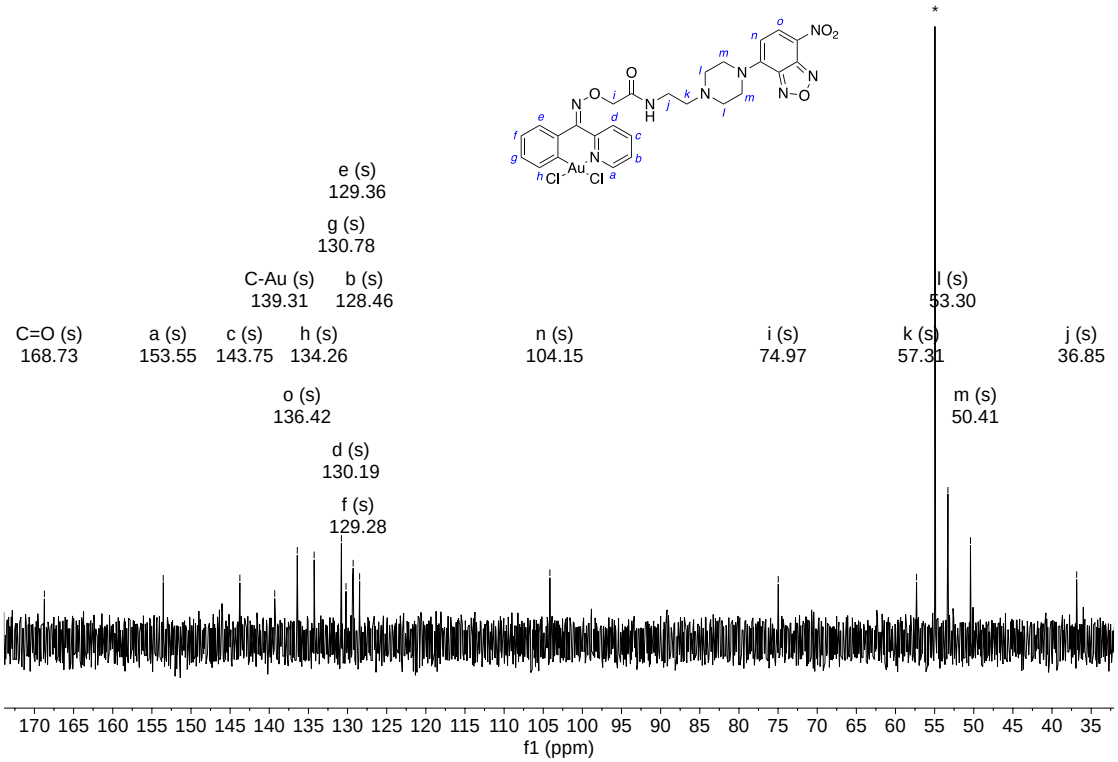

Figure S2. ^{13}C NMR spectrum of **Au-Fluo** in acetone-d_6.

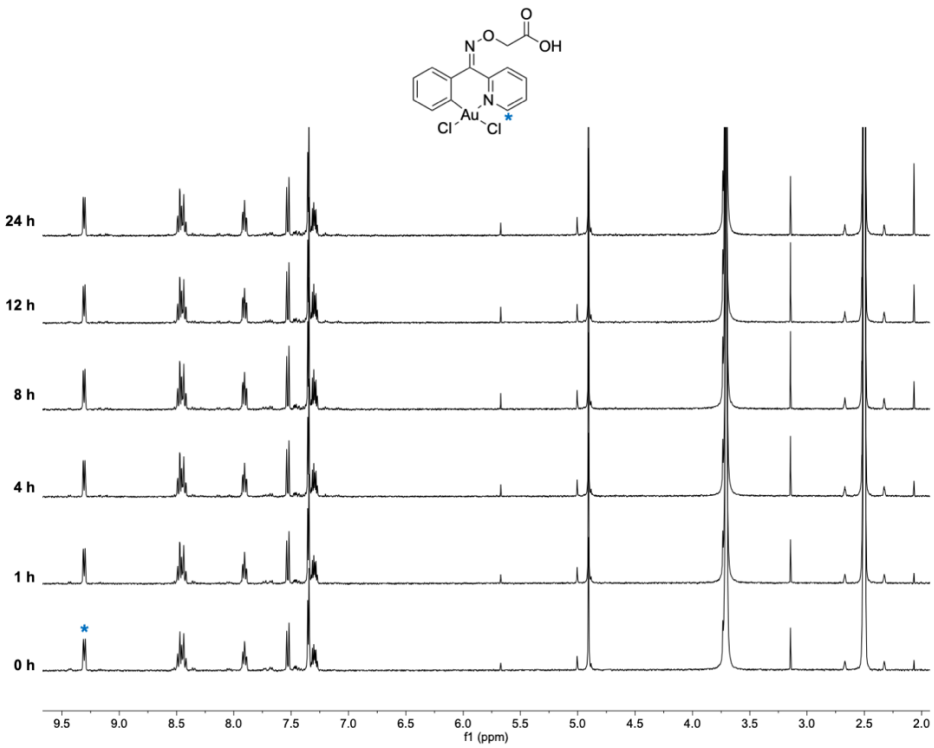

Figure S3. Stability of Au in aqueous solution. Stability kinetics were followed over 24 h for **Au** in a DMSO-d_6 : D_2O (9 : 1) mixture by ^{1}H-NMR. No shift of the α-H (blue asterisk) was observed, indicating high stability of **Au** in aqueous conditions.

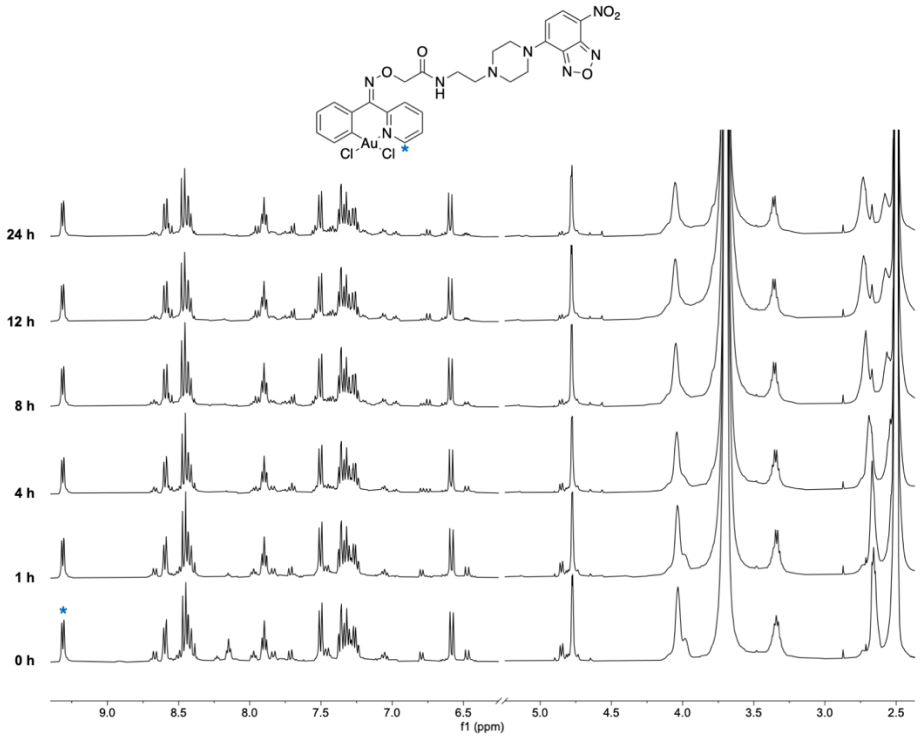

Figure S4. Stability of Au-Fluo in aqueous solution. Stability kinetics were followed over 24 h for **Au-Fluo** in a DMSO-d_6 : D_2O (9 : 1) mixture by ^{1}H-NMR. No shift of the α-H (blue asterisk) was observed, indicating high stability of **Au-Fluo** in aqueous conditions.

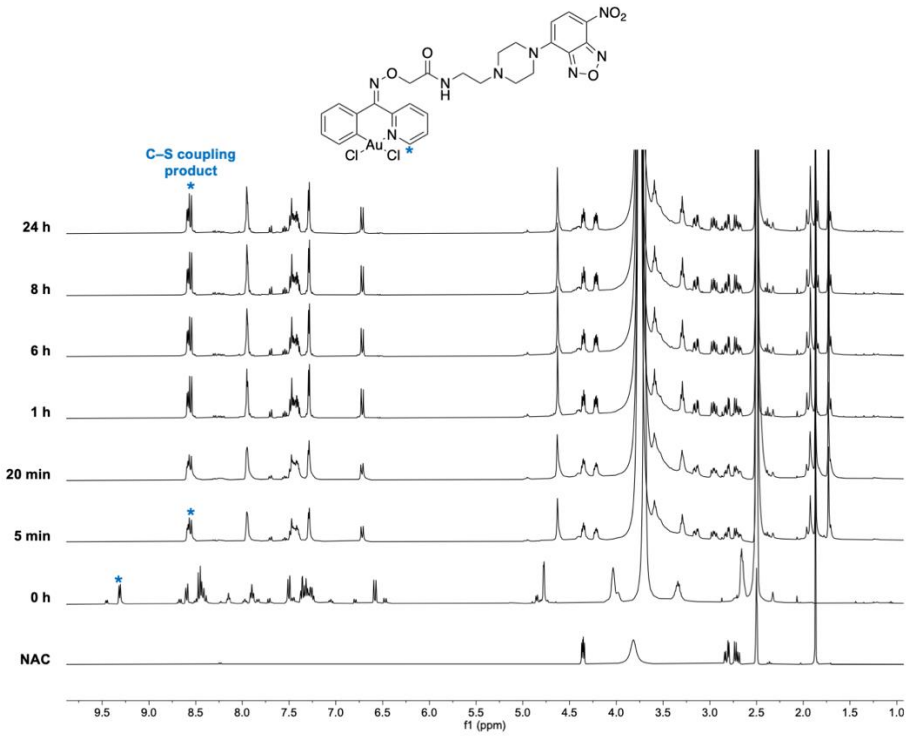

Figure S5. Reactivity of Au-Fluo towards *N*-acetylcysteine (NAC). The reactivity of **Au-Fluo** towards 3 equiv. of NAC in a DMSO-d_6 : D_2O (9 : 1) mixture was monitored by ^{1}H-NMR. The characteristic shift of the α-H (blue asterisk) was observed (Δ = 0.75 ppm), indicating a rapid C–S coupling of **Au-Fluo** with NAC.

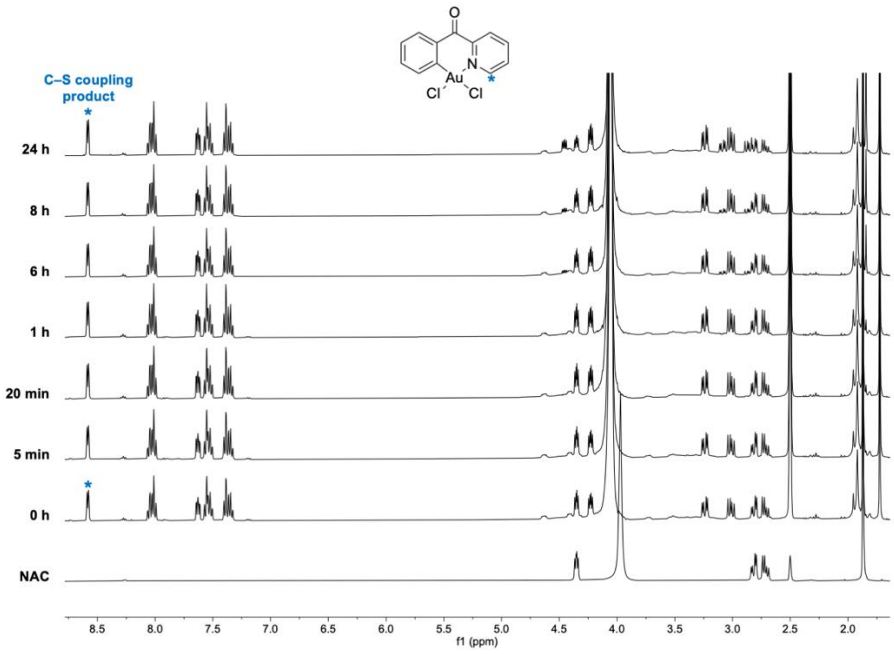

Figure S6. Reactivity of [Au($C^{CO}N$)Cl_2] towards *N*-acetylcysteine (NAC). The reactivity of [Au($C^{CO}N$)Cl_2] towards 3 equiv. of NAC in a DMSO-d_6 : D_2O (9 : 1) mixture was monitored by ^{1}H-NMR. The characteristic shift of the α-H (blue asterisk) was observed (Δ = 0.78 ppm), indicating a rapid C–S coupling of [Au($C^{CO}N$)Cl_2] with NAC.

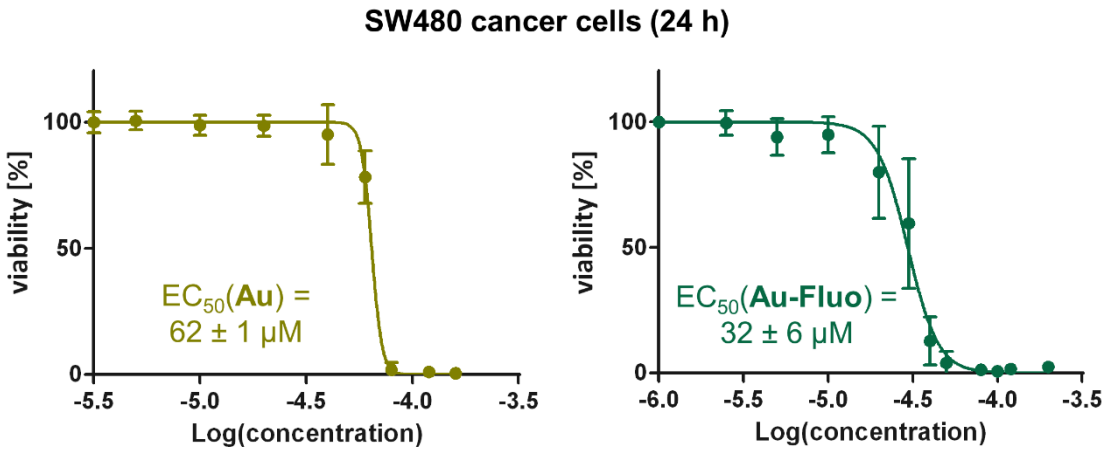

Figure S7. The cytotoxicity profiles of SW480 cancer cells treated with Au and Au-Fluo for 24 h. The final EC_{50}-values were calculated as the mean ± standard deviation of at least three independent experiments, each in at least 3 technical replicates.

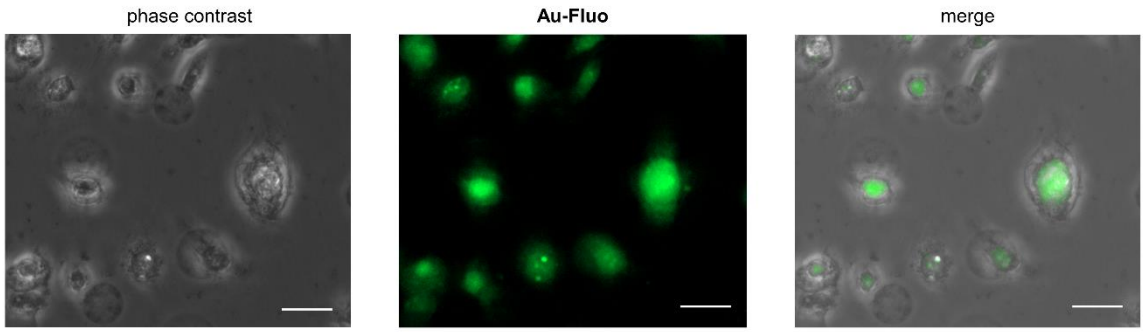

Figure S8. Cellular distribution of Au-Fluo (half-EC_{50}, 24 h) in SW480 cancer cells after 4 h incubation studied by live-cell fluorescence microscopy. Green fluorescence was monitored after excitation at 469 nm and emission at 525 nm (GFP channel). The scalebar indicates 25 µm.

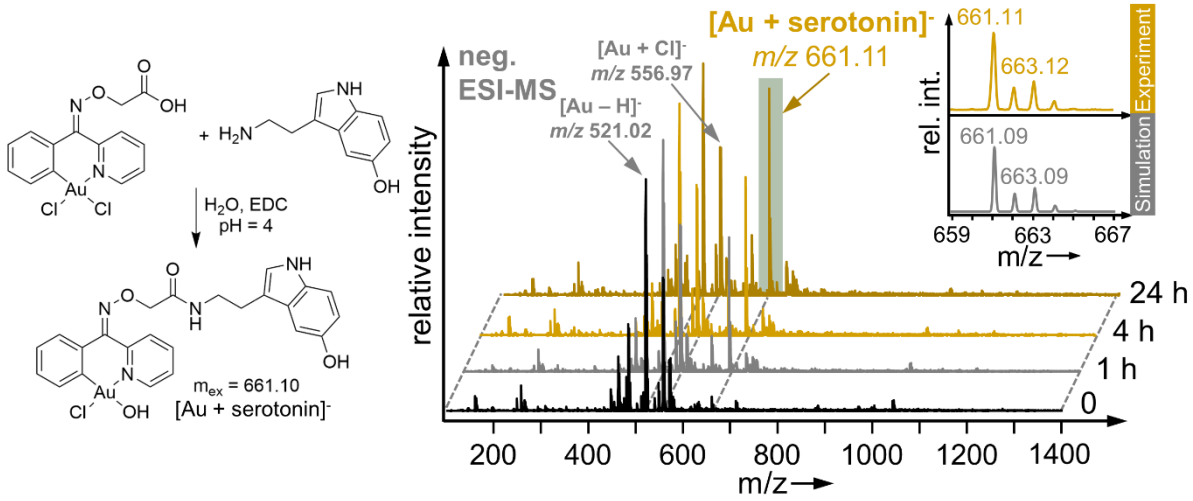

Figure S9. Optimization of coupling reaction. The compound **Au** was immobilized on amine-sepharose beads. The amidation reaction was tested in solution with serotonin. After 30 min pre-incubation of serotonin with 1-ethyl-3-(3-dimethylaminopropyl)carbodiimide (EDC), the coupling to **Au** was achieved over 24 h at pH = 4 (HCl) as revealed by mass spectrometry in the negative ionization mode.

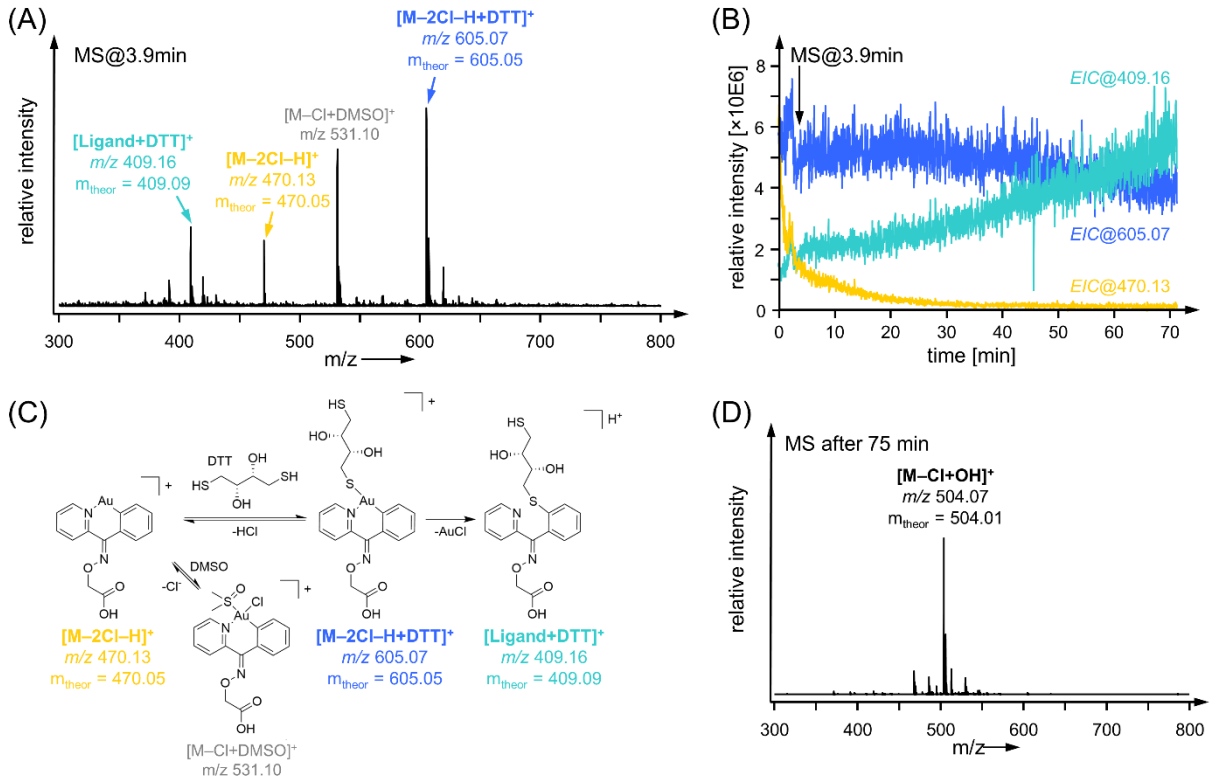

Figure S10. Reactivity of Au towards dithiothreitol (DTT). **Au** was exposed to 2 equivalents of DTT and the reaction was recorded over 70 min directly after mixing using an ion trap mass spectrometer. (**A**) The full mass spectrum after 3.9 min in the positive ion mode shows the observed species. The DMSO-adduct appears because **Au** is initially dissolved in DMSO. There is no reactivity towards DMSO. (**B**) Kinetic aspects of the reaction are revealed by plotting the relative intensities of species corresponding to **Au** (yellow), the **Au**-DTT adduct (blue) and the arylation product (turquois). (**C**) The reaction scheme highlights the two-step reactivity of **Au** towards DTT, which is characterized by rapid coordination and subsequent slower cross-coupling reacting by reductive elimination. (**D**) The full mass spectrum of a solution containing only **Au** after 75 min incubation shows that the compound remains intact in aqueous solution.

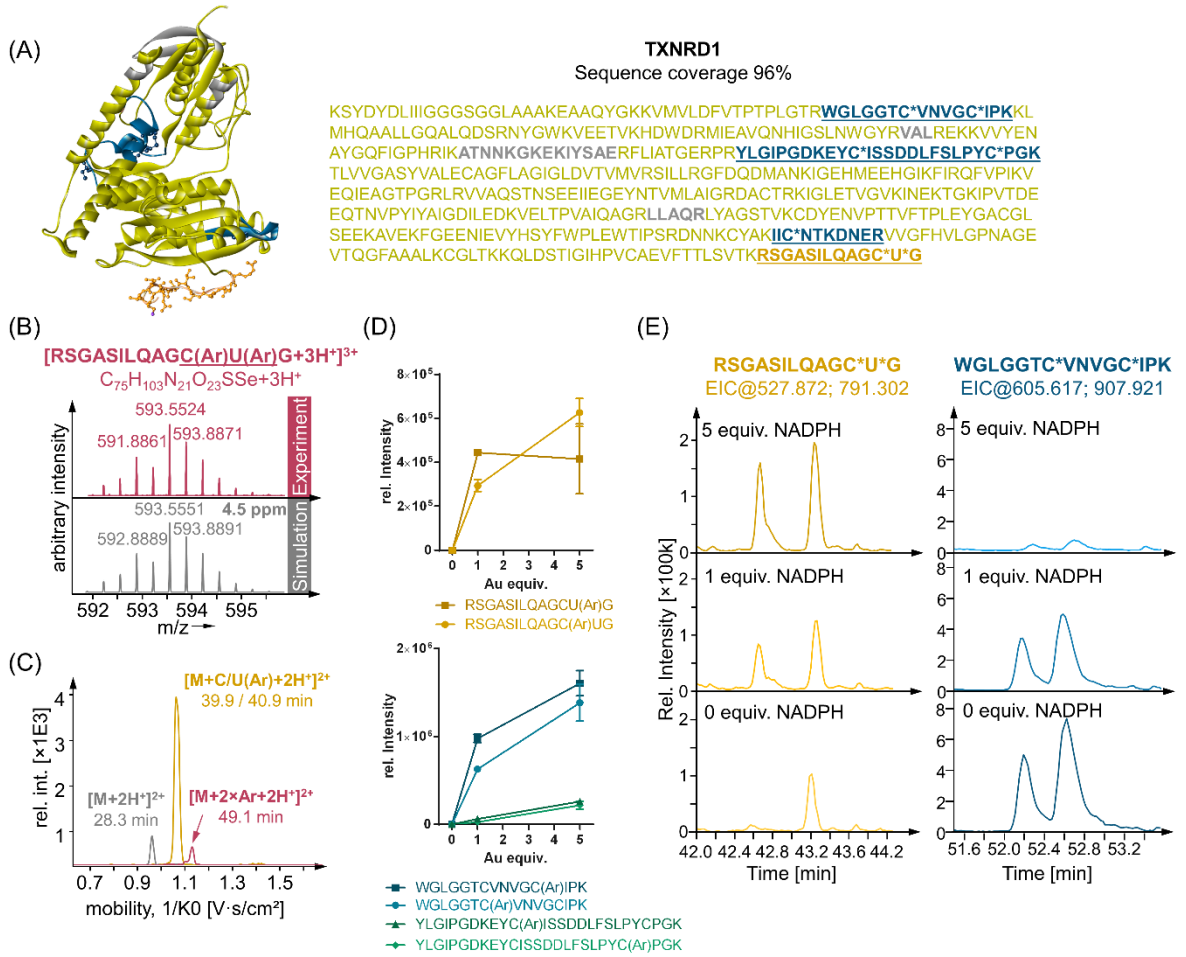

Figure S11. Identification of Au-templated arylation sites on TXNRD1. (**A**) The exact sequence coverage of the thioredoxin reductase 1 monomer is shown. Grey sequences were not detected. The underlined sequences depict those that featured an arylation product, designated with an asterisk (*). (**B**) The experimental mass signal and theoretical simulation of the isotope pattern of the bis-arylated C-terminal CU-containing peptide are shown. (**C**) The different arylation products of the C-terminal peptide of TXNRD1 feature distinct ion mobilities that are proportional to their mass. (**D**) Increasing equivalents of **Au** in the reaction with TXNRD1 in the absence of NADPH led to an increase in the intensity of the arylation of the C-terminal CU-containing peptide, but also on three other peptides. Data shown as mean ± standard deviation (n = 3) (**E**) Excerpts of the extracted ion chromatograms of the mono-arylated C-terminal CU-containing peptide (left) and the mono-arylated N-terminal CVNVGC-containing peptide as a function of increasing NADPH equivalents illustrate the trend in selectivity towards the CU-containing peptide.

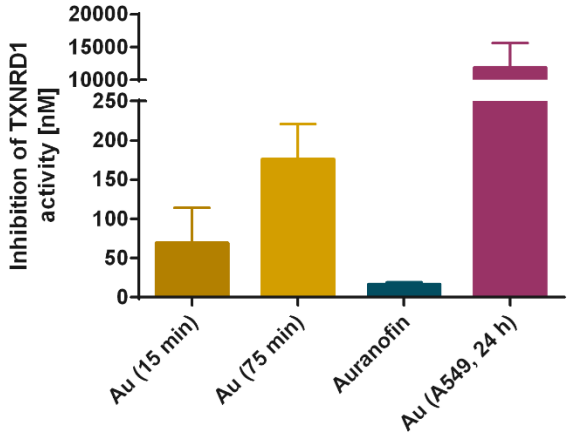

Figure S12. Inhibition of TXNRD1 activity by Au. Au was incubated with isolated TXNRD1 for either 15 min (A) or 75 min (B) in a dose-dependent manner or exposed to A549 cancer cells for 24 h. The potency of enzyme inhibition (nM) was assessed following the procedures of DTNB-coupled plate reader assays. Data points are represented as means ± standard deviation (n = 3). Data for Auranofin taken from [11]. Both the parent substance [Au($C^{CO}N$)Cl_2] and **Au** showed EC_{50} >100 µM in A549 cancer cells.

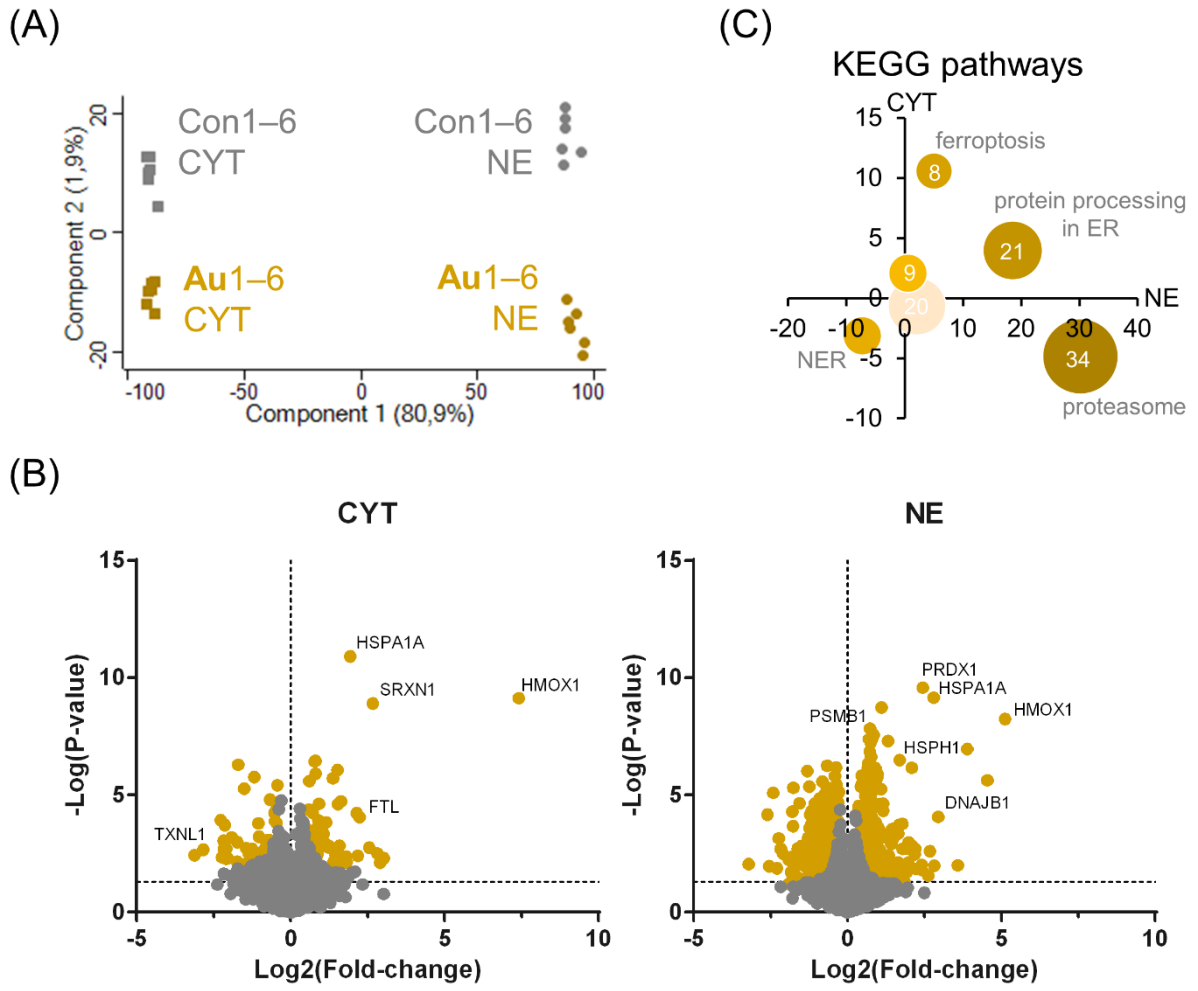

Figure S13. Proteomic profiling of SW480 cancer cells treated with Au. SW480 colon cancer cells were incubated for 24 h at 12 µM with **Au** (n = 6). Six biological replicates were performed for control (DMSO treated) and **Au**-treated cells. After the incubation, the cells were fractionated into cytoplasmic (CYT) and insoluble (NE) fractions. Each sample was proteolytically digested and analyzed by a mass spectrometry-based proteomic workflow. (**A**) The principal component analysis shows a clear separation of cytoplasmic and nuclear fractions and additionally, a clear treatment effect on the entire proteome based on the 4347 identified protein groups. (**B**) The volcano plots of the cytoplasmic (CYT) and nuclear/insoluble (NE) fractions display the effects of the **Au**-treatment on the proteome of SW480 cancer cells. The significantly regulated proteins are highlighted in gold. The most regulated proteins were additionally marked. (**C**) The affected KEGG pathways by the treatment with **Au** are shown based on the significantly regulated proteins. The position reflects summed regulations in the CYT (y-axis) and NE (x-axis) of each pathway. The numbers in the bubbles represent the number of proteins detected for each pathway.

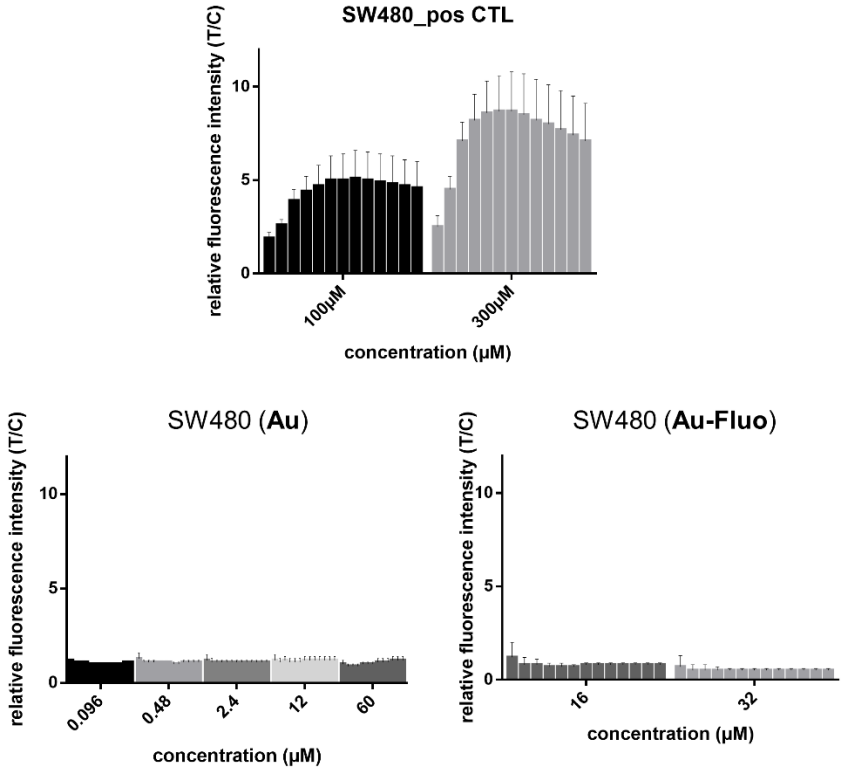

Figure S14. DCFH-DA assay to analyze the induction of reactive oxygen species (ROS) in SW480 cancer cells. Treatment with H_2O_2 was used as the positive control. Cells were treated with **Au** and **Au-Fluo** at the indicated concentrations. ROS were analyzed over the course of 2 h in 10 min intervals. Data points are shown as mean ± standard deviation (n = 3).

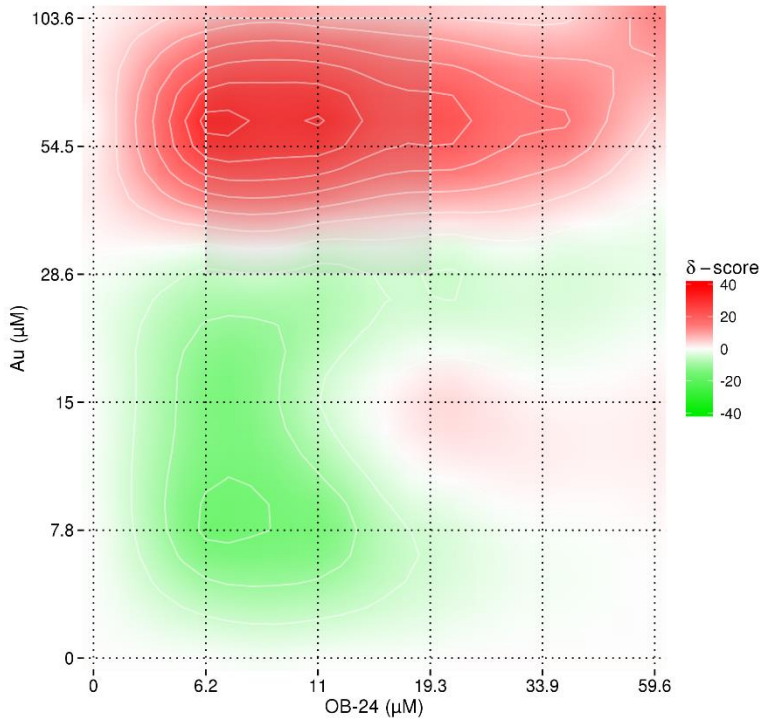

Figure S15. Synergism of Au and OB-24 co-treatment on viability of SW480 cancer cells. SW480 colon cancer cells were treated with a combination of **Au** and OB-24 at different concentrations that correspond to 0, EC_{10}, EC_{25}, EC_{50}, EC_{75} and EC_{90}. A total of 36 co-treatments were carried out and viability was assessed after 72 h incubation using the colorimetric MTT assay. The synergy landscape was obtained by SynergyFinder 3.0 using the Bliss-Loewe synergy score (δ-score) [5]. A δ-score of >10 indicates synergism (red) and a δ-score of <(-10) indicates antagonism (green).

Table S1. List of the 24 significantly regulated NRF2 target genes in SW480 cancer cells upon treatment with Au. They make up the protein group “NRF2 activation” of Figure 4E.

Protein Name	Accession N°	Log2(FC_CYT)	Log2(FC_NE)
Heme oxygenase 1	P09601	7,41	5,12
Sequestosome-1	Q13501	2,90	1,98
Sulfiredoxin-1	Q9BYN0	2,67	0,00
Ferritin light chain	P02792	2,14	0,00
Ferritin heavy chain	P02794	1,59	0,00
NAD(P)H dehydrogenase [quinone] 1	P15559	0,60	0,54
NADP-dependent malic enzyme	P48163	0,52	0,00
Autophagy-related protein 13	O75143	1,81	0,00
Carbonyl reductase [NADPH] 1	P16152	0,84	0,00
Peroxiredoxin-1	Q06830	-0,08	2,45
Thioredoxin	P10599	0,23	1,87
Peroxiredoxin-2	P32119	-0,30	1,78
Receptor-type tyrosine-protein phosphatase gamma	P23470	-0,03	0,64
Proteasome subunit alpha type-1	P25786	-0,29	1,92
Proteasome subunit alpha type-4	P25789	-0,36	0,67
Proteasome subunit beta type-3	P49720	-0,07	0,75
Proteasome subunit beta type-5	P28074	-0,05	0,69
Proteasome subunit beta type-6	P28072	-0,25	1,65
26S protease regulatory subunit 4	P62191	0,10	0,85
26S protease regulatory subunit 6A	P17980	-0,07	0,65
26S proteasome non-ATPase regulatory subunit 14	O00487	0,08	0,81
Microtubule-associated proteins 1A/1B light chain 3B	Q9GZQ8	1,07	1,55
Nucleoredoxin	Q6DKJ4	-0,38	1,39
Glutathione peroxidase 1	P07203	-1,31	0,00

REFERENCES

[1] Lee, J.J., Kim, Y.S., Nam, E., Lee, S.Y., Lim, M.H., and Kim, C. (2016). A PET-based fluorometric chemosensor for the determination of mercury(ii) and pH, and hydrolysis reaction-based colorimetric detection of hydrogen sulfide. Dalton Trans. *45*, 5700-5712. https://10.1039/c6dt00147e.

[2] Kung, K.K., Ko, H.M., Cui, J.F., Chong, H.C., Leung, Y.C., and Wong, M.K. (2014). Cyclometalated gold(III) complexes for chemoselective cysteine modification via ligand controlled C-S bond-forming reductive elimination. Chem. Commun. *50*, 11899-11902. https://10.1039/c4cc04467c.

[3] Zhu, Y., Cameron, B.R., Mosi, R., Anastassov, V., Cox, J., Qin, L., Santucci, Z., Metz, M., Skerlj, R.T., and Fricker, S.P. (2011). Inhibition of the cathepsin cysteine proteases B and K by square-planar cycloaurated gold(III) compounds and investigation of their anti-cancer activity. J. Inorg. Biochem. *105*, 754-762. https://10.1016/j.jinorgbio.2011.01.012.

[4] Schininà, B., Martorana, A., Colabufo, N.A., Contino, M., Niso, M., Perrone, M.G., De Guidi, G., Catalfo, A., Rappazzo, G., Zuccarello, E., et al. (2015). 4-Nitro-2,1,3-benzoxadiazole derivatives as potential fluorescent sigma receptor probes. RSC Adv. *5*, 47108-47116. https://10.1039/c5ra08639f.

[5] Ianevski, A., Giri, A.K., and Aittokallio, T. (2022). SynergyFinder 3.0: An interactive analysis and consensus interpretation of multi-drug synergies across multiple samples. Nucleic Acids Res. *50*, W739-W743. https://10.1093/nar/gkac382.

[6] Meier-Menches, S.M., Neuditschko, B., Zappe, K., Schaier, M., Gerner, M.C., Schmetterer, K.G., Del Favero, G., Bonsignore, R., Cichna-Markl, M., Koellensperger, G., et al. (2020). An organometallic gold(I) bis-N-heterocyclic carbene complex with multimodal activity in ovarian cancer cells. Chem. Eur. J. *26*, 15528-15537. https://10.1002/chem.202003495.

[7] Jarolim, K., Del Favero, G., Pahlke, G., Dostal, V., Zimmermann, K., Heiss, E., Ellmer, D., Stark, T.D., Hofmann, T., and Marko, D. (2016). Activation of the Nrf2-ARE pathway by the alternaria alternata mycotoxins altertoxin I and II. Arch. Toxicol. *91*, 203-216. https://10.1007/s00204-016-1726-7.

[8] Neuditschko, B., King, A.P., Huang, Z., Janker, L., Bileck, A., Borutzki, Y., Marker, S.C., Gerner, C., Wilson, J.J., and Meier-Menches, S.M. (2022). An anticancer rhenium tricarbonyl targets Fe−S cluster biogenesis in ovarian cancer cells. Angew. Chem. Int. Ed. *61*, e202209136. https://10.1002/anie.202209136.

[9] Zougman, A., Selby, P.J., and Banks, R.E. (2014). Suspension trapping (STrap) sample preparation method for bottom-up proteomics analysis. Proteomics *14*, 1006. https://10.1002/pmic.201300553.

[10] Weiss, T., Taschner-Mandl, S., Janker, L., Bileck, A., Rifatbegovic, F., Kromp, F., Sorger, H., Kauer, M.O., Frech, C., Windhager, R., et al. (2021). Schwann cell plasticity regulates neuroblastic tumor cell differentiation via epidermal growth factor-like protein 8. Nat. Commun. *12*, 1624. https://10.1038/s41467-021-21859-0.

[11] Schmidt, C., Karge, B., Misgeld, R., Prokop, A., Franke, R., Brönstrup, M., and Ott, I. (2017). Gold(I) NHC Complexes: Antiproliferative Activity, Cellular Uptake, Inhibition of Mammalian and Bacterial Thioredoxin Reductases, and Gram-Positive Directed Antibacterial Effects. Chem. Eur. J. *23*, 1869-1880. https://10.1002/chem.201604512.

[12] Bradford, M. (1976). A Rapid and sensitive method for the quantitation of microgram quantities of protein utilizing the principle of protein-dye binding. Anal. Biochem. *72*, 248-254. https://10.1016/0003-2697(76)90527-3.

3.2 Selectivity for TP53 signalling drives the mode of action of a highly potent *N*,*O*,*O*-tridentate naphthoquinone-based organo-ruthenium anticancer drug candidate

Alexander Rosner,[‡,a,b] Lukas Skos,[‡,b,c] Theresa Mendrina,[a,d], Dina Baier, [a,d,e] Michaela Hejl,[a,c] Yasmin Borutzki,[a,b,c] Mathias Gradl,[d] Heiko Geisler,[a] Thomas Mohr,[d,e] Anton Legin,[a] Michael Jakupec,[a,f] Andrea Bileck,[c,e] Christopher Gerner,[c,e] Gunda Koellensperger,[c] Petra Heffeter,[d,e] Walter Berger,[d,e] Bernhard K. Keppler,[a,e] Wolfgang Kandioller, *[,a,e] Samuel M. Meier-Menches, *[,a,c,f]

[a] Institute of Inorganic Chemistry, University of Vienna, Waehringer Str. 42, 1090 Vienna, Austria.

[b] Doctoral School in Chemistry, University of Vienna, Waehringer Str. 38, 1090 Vienna, Austria.

[c] Department of Analytical Chemistry, University of Vienna, Waehringer Str. 38, 1090 Vienna, Austria.

[d] Center for Cancer Research and Comprehensive Cancer Center, Medical University Vienna, Borschkegasse 8a, Vienna, 1090, Austria.

[e] Joint Metabolome Facility, University of Vienna and Medical University of Vienna, Waehringer Str. 38, 1090 Vienna, Austria.

[f] Research Cluster "Translational Cancer Therapy Research", Vienna, 1090, Austria.

[‡] These authors contributed equally.

* Corresponding authors

Chemical Science, 2025, Volume 16, 15652-15665

DOI: 10.1039/d5sc00735f

Contributions to this work:

- Conduction of cell culture experiments
- Performing proteomics experiments: SAR for proteomic profiling, *in vivo* proteomic profiling
- Sample preparation and data evaluation
- Involved in data interpretation and figure design
- Writing of the manuscript

Chemical Science

ROYAL SOCIETY OF CHEMISTRY

EDGE ARTICLE

View Article Online
View Journal

Cite this: DOI: 10.1039/d5sc00735f

All publication charges for this article have been paid for by the Royal Society of Chemistry

Selectivity for TP53 signalling drives the mode of action of a highly potent *N,O,O*-tridentate naphthoquinone-based organo-ruthenium anticancer drug candidate†

Alexander Rosner, ‡[ab] Lukas Skos, ‡[bc] Theresa Mendrina,[ad] Dina Baier, [ade] Michaela Hejl,[ae] Yasmin Borutzki, [abc] Mathias Gradl, [d] Heiko Geisler, [a] Thomas Mohr, [df] Anton Legin, [a] Michael A. Jakupec, [ae] Andrea Bileck, [cf] Christopher Gerner, [cf] Gunda Koellensperger, [c] Petra Heffeter, [de] Walter Berger, [de] Bernhard K. Keppler, [ae] Wolfgang Kandioller *[ae] and Samuel M. Meier-Menches *[acf]

The metallodrug candidate [(3-ethyl-4-oxo-(pyrazolyl)-dihydronaphthalene)(cymene)ruthenium(II)] (**1a**) was recently shown to exhibit exceptional antiproliferative activity towards the chemo-resistant SW480 cancer cell line with nanomolar potency. This study was conducted to elucidate the determining parameters of the mode of action of this *N,O,O*-tridentate organoruthenium compound *in vitro* and *in vivo*. Four metal(arenes) based on 3-ethyl naphthoquinone (3-Et-NQ, **a**) and 3-morpholine naphthoquinone (3-Morph-NQ, **b**) with ruthenium (**1**) and osmium (**2**) were synthesized and characterized. The 3-Morph-NQ ligand increased the solubility of the complexes, but showed a 30-fold reduction in antiproliferative activity compared to the 3-Et-NQ ligand and its complexes served as biologically inactive analogues. The solution reactivity of the four compounds was ligand- and metal-dependent, but they all showed selectivity for amino acids over nucleotides at biologically relevant concentrations. Drug effects were elucidated by proteome profiling at subcellular resolution and showed a pronounced ligand-dependent impact. The 3-Et-NQ containing ruthenium- and osmium(arenes) down-regulated TP53 as a central hub in the perturbation network, connected to down-regulated proliferative MAPK3 signalling. Complex **1a** strongly down-regulated TP53 and potently inhibited cell cycle progression at the G2/M phase. Furthermore, **1a** was found to disrupt the TP53-DDX3X-p21 signalling axis by direct interaction with DDX3X and loss of p21 expression. The 3-Et-NQ complexes, particularly **1a**, showed tumour inhibitory effects *in vivo* in a CT26 colon carcinoma mouse model, while the 3-Morph-NQ complexes were inactive. Tissue proteome analyses of livers of **1a**-treated mice displayed similar stress responses as observed *in vitro*. Finally, tumour tissue of **1a**-treated mice revealed down-regulated EGFR, consistent with the impact on the TP53 signalling axis *in vitro*.

Received 27th January 2025
Accepted 4th July 2025

DOI: 10.1039/d5sc00735f

rsc.li/chemical-science

1. Introduction

The clinical success of the platinum anticancer agents cisplatin, carboplatin and oxaliplatin in conjunction with the DNA-targeting paradigm fuelled research efforts in the field of metals in medicine over decades.[1,2] Gradual accumulation of experimental evidence, however, confirmed that the spectrum of biological effects of non-platinum metal-based anticancer drugs and drug candidates is more diverse and includes protein or metabolic targets.[3–6] Molecular profiling technologies, *e.g.*,

[a]*Institute of Inorganic Chemistry, University of Vienna, Waehringer Str. 42, Vienna, 1090, Austria. E-mail: samuel.meier-menches@univie.ac.at; wolfgang.kandioller@univie.ac.at*

[b]*Doctoral School in Chemistry, University of Vienna, Waehringer Str. 38, Vienna, 1090, Austria*

[c]*Department of Analytical Chemistry, University of Vienna, Waehringer Str. 38, Vienna, 1090, Austria*

[d]*Center for Cancer Research and Comprehensive Cancer Center, Medical University Vienna, Borschkegasse 8a, Vienna, 1090, Austria*

[e]*Research Cluster "Translational Cancer Therapy Research", Vienna, 1090, Austria*

[f]*Joint Metabolome Facility, University of Vienna and Medical University of Vienna, Waehringer Str. 38, Vienna, 1090, Austria*

† Electronic supplementary information (ESI) available: Materials and methods, compound characterization, Fig. S1–S21, Tables S1 and S2. Data S1 containing the regulome input. See DOI: https://doi.org/10.1039/d5sc00735f

‡ These authors contributed equally.

transcriptomics[7] and (metallo-)proteomics,[8,9] contributed towards a recent trend in mechanism-driven (metallo-)drug discovery.[6,10,11] For example, based on transcriptomic studies, it was shown that the mode of action of oxaliplatin involves interference with ribosome biogenesis rather than direct DNA platination,[12] which rationalizes its use in adjuvant chemotherapy of stage III colon cancer.[13]

Ruthenium-based anticancer candidate drugs are among the most advanced classes of non-platinum therapeutics.[2,14] This is highlighted by two representatives that are in clinical stages of investigation: first, BOLD-100 (formerly KP1339, IT-139, Fig. 1),[15] a ruthenium(III) complex, is currently evaluated in a phase Ib/IIa study against gastrointestinal tumours and features promising interim clinical outcomes (NCT04421820).[16,17] Preclinical investigations on the mode of action (MoA) revealed a multimodal profile,[18] including modulation of GRP78 with endoplasmic reticulum (ER) stress induction, accompanied by ribosomal interactions.[19] Alterations in lipid metabolism were recently discovered[20] and revealed that glucose-deprived cancer cells showed an enhanced vulnerability towards BOLD-100 treatment.[21] Second, the ruthenium(II)-based complex TLD-1433 was employed in the treatment of bladder cancer using photodynamic therapy[22,23] and is currently undergoing a promising phase II study (NCT03945162).[24–26]

Pioneered by the groups of Sadler[27] and Dyson,[28] the family of organometallic ruthenium(II) and osmium(II) arene complexes is widely investigated.[14] Typically, this metal(arene) motif is a reactive moiety that can be fine-tuned by versatile ligand systems, which in turn affect the antiproliferative properties of the complexes.[14,29–32] Mono- and bidentate ligands are employed that are inert with respect to ligand exchange, while the remaining ligand sites are occupied by labile halido leaving groups. Such metal(arene) compounds are prodrugs, where the halido site undergoes ligand exchange reactions, *e.g.*, by aquation. This activates the prodrug, which can subsequently react with molecular targets by forming a coordination bond.[6,14,32,33] Numerous studies reported on the metalation of biological nucleophiles by metallodrugs in cell-free studies,[34–36] while the selectivity of these agents for certain nucleophiles is more challenging to investigate in a biological context.[37] The nucleosome core particle was among the first relevant model systems to evaluate the binding selectivity of metal(arenes) towards nucleotides or amino acids.[3] Interestingly, it was shown that ligand variation in ruthenium(arenes) would dictate the DNA *versus* protein reactivity and selectivity. Later, using a chemoproteomic approach, the ruthenium(arene) compound plecstatin-1 (Fig. 1) was found to exhibit unprecedented selectivity towards plectin in the cellular context.[38] Modulation of plectin by plecstatin-1 induced distinct phenotypes that mirrored genetic plectin knockout,[39] and shows promising antitumour activity against hepatocellular carcinoma.[40] Furthermore, activation and reactivity by coordination was also found to be crucial for mediating the interaction of plecstatin-1 to plectin.[41] Amongst others, an organo-osmium compound was found to exploit a metabolic vulnerability of mutated complex I in cellular respiration of a cancer cell line by a metabolic shift from glycolysis to oxidative phosphorylation.[42]

Consequently, it seems that the choice of the ligand scaffold strongly determines the biological effects of metal(arenes).[14] The substitution of halido leaving groups of metal(arenes) with inert oxalato ligands retained cytotoxic potency in some cases,[43] whereas inert tridentate ligand systems were found to reduce the cytotoxic potency,[44,45] although some exceptions to this rule exist.[46] This indicates that the formation of a coordination bond between the metal(arene) and a molecular target is generally necessary to obtain cytotoxic metal(arenes) and underlines the importance of ligand exchange kinetics for this family of metal-based anticancer candidate drugs.

Some of us recently reported on ruthenium(arene) derivatives based on a novel tridentate *N*,*O*,*O*-ligand system, which were formed *in situ* from bioactive hydroxy-1,4-naphthoquinones and 1,2-diazoles.[47] Interestingly, these compounds, of which [(3-ethyl-4-oxo-(pyrazolyl)-dihydronaphthalene)(cymene)ruthenium(II)] (**1a**, Fig. 1) is a promising representative, exhibited exceptional antiproliferative potency in the nanomolar range in a rather chemo-resistant colon carcinoma cell line,[47,48] where the hydroxy-1,4-naphthoquinone ligands were largely inactive (showing half-maximal growth inhibition (IC_{50}) at >100 μM). Although naphthoquinones are known inhibitors of NAD(P)H:quinone oxidoreductase 1 (NQO1),[49] their organometallic complexes only moderately inhibited NQO1 relative to their cytotoxic potency suggesting that the potency of **1a** is governed by the intact complex.[50] It was then also shown that these compounds neither interacted with DNA nor produced reactive oxygen species (ROS).[48] These findings led us to hypothesize that the compounds must follow a specific MoA independent of NQO1 inhibition that may explain their excellent potency *in vitro*. Here, we investigated the antiproliferative and tumour-inhibiting effects of highly potent metal(arenes) based on *N*,*O*,*O*-tridentate ligand systems to elucidate their MoA *in vitro* and *in vivo*. For this purpose, we synthesized a small panel of structurally related naphthoquinone-containing metal(arenes) and investigated their stability, as well as solution reactivity. We further evaluated structure–activity relationships (SARs) on the level of the proteome *in vitro* at a subcellular resolution and mechanistically confirmed specific effects on the TP53 signalling axis, which also seemed to manifest *in vivo*.

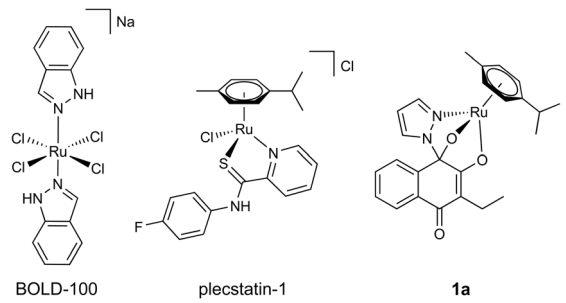

Fig. 1 Chemical structures of the clinically investigated ruthenium(III) complex BOLD-100 (left), and the investigational organoruthenium(II) derivatives plecstatin-1 (middle) and **1a** (right).

2. Results and discussion

2.1 Synthesis and characterization

A small panel of structurally related *N*,*O*,*O*-tridentate metal(-arenes) was synthesized to derive structure–activity relationships with respect to reactivity and biological activity. Starting from 3-ethyl naphthoquinone (3-Et-NQ, a) ruthenium(arene) lead compound **1a** and its osmium analogue **2a** were synthesized according to recently reported literature (Fig. 2A).[48] To increase the solubility of the complexes, 3-morpholine naphthoquinone (3-Morph-NQ, b) was prepared and coordinated to the respective organometallic fragments yielding complexes **1b** and **2b**. The complexation reactions were performed in a one-pot microwave-assisted reaction in the presence of pyrazole, the NQ ligand, the dimeric metal(arene) precursor and triethylamine, to obtain the neutral *N*,*O*,*O*-tridentate-based organometallics. The complexes were obtained in good yields and were characterized by nuclear magnetic resonance (NMR), mass spectrometry (MS) and elemental analysis (ESI, Fig. S1–S9†). Formation of the desired complexes was confirmed by ^{1}H- and ^{13}C-NMR spectroscopy. The OH proton of the free ligand vanished upon coordination and furthermore, the arene signals were found as four distinguishable doublets, which indicated successful coordination of the NQ ligand. Formation of the expected tridentate complexes could be unambiguously confirmed by the presence of the hemiaminal carbon at around 100 ppm in the corresponding ^{13}C-NMR spectra (ESI, Fig. S2–S5†). Proton and sodium adducts of the respective organometallics were found in HR-MS studies and the observed isotopic patterns are in good agreement for mononuclear Ru species (ESI, Fig. S6–S9†). Elemental analyses revealed the hygroscopic nature of the compounds due to the increased O-content in all complex samples. The obtained data confirmed sufficient purity for further biological examinations. As expected, the introduction of the 3-Morph-NQ fragment remarkably increased the solubility of the complexes by a factor of 2–7 compared to their 3-Et-analogues in phosphate buffered saline (PBS, Fig. 2B).

(A)

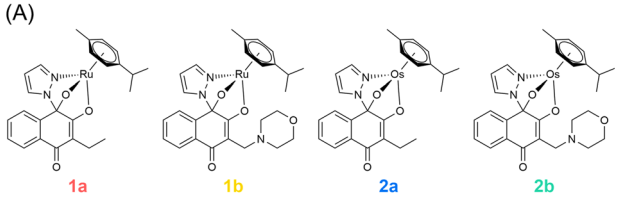

(B)

Compound	Solubility in PBS [mM]	Intact compound after 24 h: Aqueous medium	Intact compound after 24 h: Nucleophile mixture	IC_{50}(SW480, 24h) [μM]
1a	0.17	42%	4%	0.62 ± 0.04
1b	1.22	47%	7%	38 ± 5
2a	0.21	45%	19%	1.2 ± 0.1
2b	0.4	37%	43%	36 ± 7

(C)

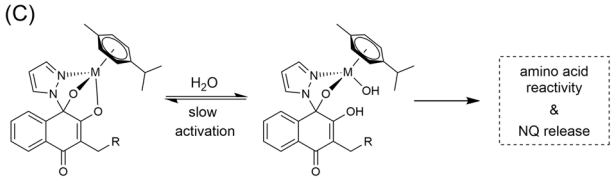

Fig. 2 (A) Chemical structures of the investigated naphthoquinone-based metal(arenes) in this study. (B) Table highlighting solubility in phosphate buffered saline (PBS, with 1% DMSO), percentage of intact compound remaining after 24 h in aqueous medium and in the presence of the biological nucleophiles cysteine, methionine, histidine, adenosine triphosphate and guanosine triphosphate, each at 50 μM as revealed by mass spectrometry. Concentration of 50% growth inhibition (IC_{50}) is displayed in the SW480 colon carcinoma cell line after 24 h incubation. (C) The scheme shows the proposed reactivity of the *N*,*O*,*O*-tridentate metal(arenes).

2.2 Stability and reactivity

These *N*,*O*,*O*-tridentate complexes were previously found to be highly stable and featuring slow activation kinetics. Nevertheless, they are activated by hydrolysis of the most labile M–O bond (Fig. 2C).[48] Further hydrolysis releases the NQ ligand, because the free hemiaminal-containing NQ is unstable and the presence of biological nucleophiles accelerated NQ release.[48] Here, the reactivity of **1a** towards biological nucleophiles was investigated by NMR, UV-vis spectroscopy and ESI-MS to assess concentration-dependent reactivity differences. Compound **1a** was incubated in an equimolar ratio with 9-ethylguanine and methionine or cysteine in D_2O/20% DMSO. The samples were analysed on a 500 MHz NMR spectrometer after 0 h, 1.5 h and 24 h. At 1 mM, **1a** remained remarkably stable in both the methionine- and cysteine-containing samples over the incubation period and no effects on chemical shifts were observed (ESI, Fig. S10†). The aromatic proton of 9-ethylguanine was consistently found at 7.6 ppm.

In contrast to the NMR analysis, the compounds were diluted to 40 μM and 80 μM for **1a**/**2a** and **1b**/**2b**, respectively and their stability was assessed by UV-vis spectroscopy continuously over 96 h (ESI, Fig. S11†). Under these biologically more relevant concentrations, the compounds showed ligand exchange reactions with distinct isosbestic points. While the ruthenium derivatives **1a**/**1b** hydrolysed more rapidly over 24 h (**1a** 75%, **1b** 76%, **2a** 85%, **2b** 94% of intact complex), the ethyl-NQ-containing organometallics **1a**/**2a** seem to hydrolyse more extensively over 96 h (**1a** 53%, **2a** 61%, **1b** 64%, **2b** 84% of intact complex).

In order to elucidate the transformation products of hydrolysis at micromolar concentrations, the four compounds were analogously incubated at 50 μM and analysed by ESI-MS[34] in a time-dependent manner after 1.5 h, 24 h and 72 h. The four complexes of this series were quite stable over 24 h (ESI, Fig. S12†), but gradually released the NQ-ligands over the course of 72 h, which was observed by the formation of characteristic metal(cymene)-dimers containing pyrazole as bridging ligands. In addition, the observation of the free 3-Morph-NQ ligand after 24 h further supported the previously established activation mechanism (ESI, Fig. S12†). A mass signal, which was probably generated by in-source fragmentation corresponded to pyrazole-release. Ruthenium- and osmium organometallics behaved

similarly, although osmium derivatives showed slower hydrolysis kinetics (ESI, Fig. S12†). In general, the intensity of the intact compounds after 24 h at 50 μM corresponded to approximately 40% of the total intensity of the mass spectrum in all four cases, not accounting for ionization efficiency (Fig. 2B).

Then, the compounds were analogously incubated with an equimolar mixture of cysteine, methionine, histidine, adenosine triphosphate and guanosine triphosphate to verify coordination preferences for amino acids over nucleotides. The reactivity of the four compounds was qualitatively similar, characterized by release of the NQ ligands and formation of mainly methionine and histidine-adducts with the metal(arene) (ESI, Fig. S13†). No metalation of the nucleotides was observed. In contrast to other *O*,*O*-ligand systems, which are typically deactivated within minutes by ligand release under such conditions,[51,52] the *N*,*O*,*O*-tridentate organometallics studied here were characterized by increased stability. Nonetheless, **1a** and **1b** reacted nearly quantitatively within 24 h, while the Os analogues reacted at a slower rate so that intact **2a** and **2b** were still observable at 19% and 43% after 24 h, respectively (Fig. 2B and ESI, Fig. S12†). Again, the 3-Morph-NQ ligand was detected upon release from the metal centre, but hydrolysis dimers were not observed in the presence of bionucleophiles (ESI, Fig. S13†). The reactivity of the compounds towards an equimolar concentration of the model protein ubiquitin was characterized by similar kinetic behaviours and reactivity (ESI, Fig. S14†).

As the NMR, UV-vis and MS investigations showed, the activation and reaction kinetics of the studied complexes were clearly concentration dependent. Interestingly, we observed a stronger impact of the metal than the ligand on kinetics of activation over 24 h and adduct formation in the presence of biological nucleophiles in the following order: **1a** ≥ **1b** > **2a** > **2b**. The slower ligand exchange kinetics of osmium(II) – compared to ruthenium(II)arenes – is a known phenomenon.[52,53] It originates from osmium being a third-row transition metal and therefore, being more inert compared to the second-row transition metal ruthenium. Indeed, isosteric osmium organometallics often exhibit longer half-lives of hydrolysis.[29]

2.3 Antiproliferative activity *in vitro*

Compound **1a** showed potent antiproliferative activity with an IC_{50}-value of 0.046 ± 0.007 μM in the rather chemo-resistant SW480 colon cancer cell line over a 96 h incubation time (Table S1†).[48] Interestingly, *N*,*O*,*O*-tridentate ruthenium(arenes) of this type were selectively active towards the SW480 cancer cell line,[48] while the naphthoquinone ligands were previously found to be largely inactive *in vitro* (ESI, Table S1†).[48] The antiproliferative activity of the four compounds **1a**, **1b**, **2a** and **2b** was then examined towards SW480 cells over a 24 h incubation time corresponding to the MoA studies below. The 3-Et-NQ complexes **1a** and **2a** showed IC_{50}-values of 0.62 ± 0.04 μM and 1.2 ± 0.1 μM, respectively and the 3-Morph-NQ complexes **1b** and **2b** showed IC_{50}-values of 38 ± 5 and 36 ± 7 μM, respectively (Fig. 2B, ESI, Fig. S15 and Table S1†). Thus, the ethyl derivatives **1a** and **2a** were >30 times more potent compared to their morpholine-analogues **1b** and **2b**, which showed only moderate cytotoxicity and serve as biologically inactive analogues. Moreover, the ruthenium-derivative **1a** was slightly more potent than the osmium analogue **2a**. Such an effect was not observed for the morpholine-derived compounds. It was previously shown that IC_{50}-values of representatives of this compound family based on a 24 h incubation featured lower potency compared to a 96 h incubation.[50] Nonetheless, the 3-Et-NQ complexes investigated here retained significant antiproliferative activity even after an incubation time of 24 h. This supported the fact that they do not exert their biological effect *via* direct DNA damage, but might involve other mechanisms. Furthermore, the pronounced antiproliferative activity of the 3-Et-NQ complexes must be due to specific mechanistic aspects, which were not perturbed by the 3-Morph-NQ complexes. This motivated the proteomics experiments detailed below.

2.4 Proteome-wide effects in SW480 cancer cells

To gain insight into potential modes of action and derive structure–activity relationships on a molecular level, proteomic profiling experiments were carried out based on label-free quantification (LFQ) by nano-liquid chromatography tandem mass spectrometry (nLC-MS/MS). SW480 cancer cells were treated for 24 h with each compound at concentrations corresponding approximately to their individual IC_{50} values. Six replicates were used per condition. The perturbations were evaluated at subcellular resolution by fractionating cells into cytoplasmic (CYT) and nuclear (NE) protein fractions. Those have been separately proteolytically digested and analysed (Fig. 3A). The perturbations with the 3-Et-NQ and 3-Morph-NQ complexes were performed against their respective solvent-treated controls (CON), yielding a total of 72 samples. Scatter plots and principal component analyses of the samples revealed good precision of the method, as well as a strong and largely homogeneous impact of the treatments according to the respective conditions (ESI, Fig. S16†). The principle component analysis further revealed that **1b** and **2b** predominantly affected the nuclear fraction of the proteome (ESI, Fig. S16B†). A total of 5657 proteins were identified under all conditions combined. Statistical significance of individual protein regulations was calculated by multiple testing-corrected *P*-values based on 5% false discovery rate (FDR = 0.05 and S_0 = 0.1). With respect to the number of significantly regulated proteins, **1a** and **2a** affected more strongly the cytoplasmic fraction, while **1b** and **2b** showed a predominant impact on nuclear fractions, indicating that the ligand directs the global impact of the perturbation. The dynamic range of significantly regulated proteins was large, from 16 regulated proteins by **1b** in CYT to 1773 regulated proteins by **2b** in NE (ESI, Table S2†).

The significantly regulated proteins of each treatment were then categorized into functional groups based on significantly enriched terms according to gene ontology cellular compartments (GO CC), biological processes (GO BP), and KEGG pathways (Fig. 3B and C, ESI, Fig. S17 and Data S1†). The position of each group represents the summed fold-changes of the individual proteins in the group according to the subcellular space,

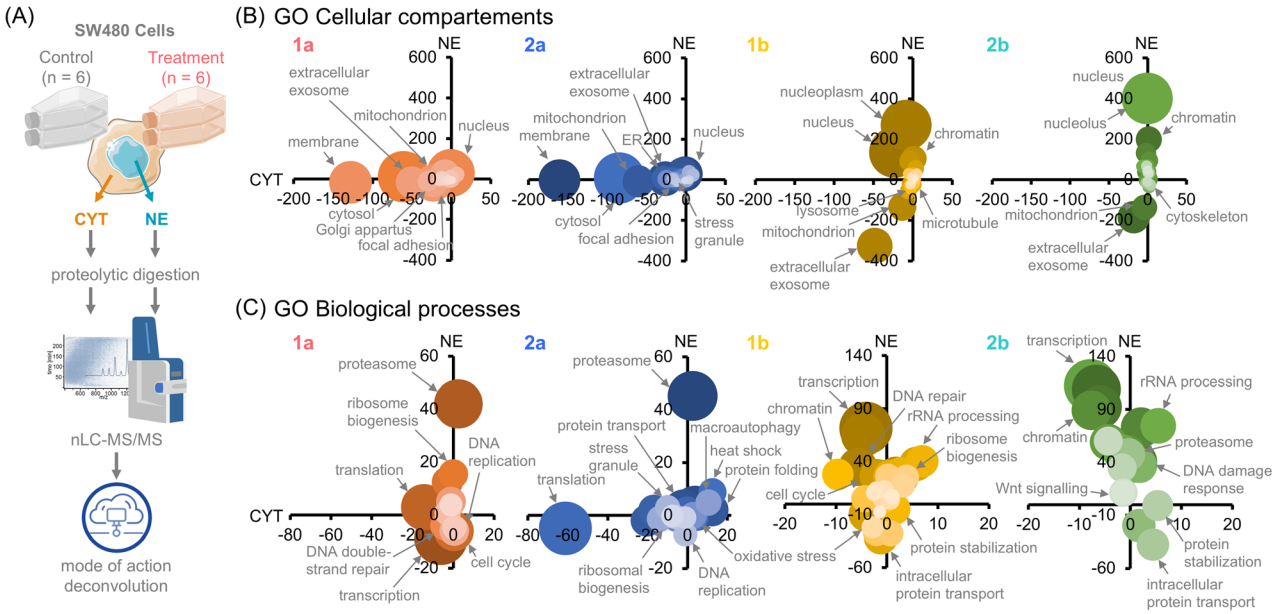

Fig. 3 (A) SW480 cell populations were treated in hexuplicates. Cytoplasmic (CYT) and nuclear (NE) protein fractions were obtained. Samples were proteolytically digested and analysed by nano-liquid chromatography tandem mass spectrometry (nLC-MS/MS) in a data-dependent analysis mode. Proteomic perturbation data were then used for mode of action deconvolution. Regulomes of individual treatments are shown where each protein group was obtained from a term enrichment analysis according to gene ontology (GO) cellular compartments (B) or biological processes (C). The size of the bubbles correlates with the number of proteins in the group.

i.e., CYT and NE fractions, while the size represents the number of proteins in each group.

Categorizing regulated proteins according to GO CC terms provides a global overview of the effects of each perturbation on cellular compartments.[54] Again, the ligand type had a major influence on the perturbation profiles, since compounds based on 3-Et-NQ and 3-Morph-NQ led to changes predominantly in the cytoplasmic and nuclear fraction, respectively. Moreover, the identities of the groups overlapped significantly in compounds containing the same ligand. Compounds **1a** and **2a**, bearing the 3-Et-NQ ligand, induced a significant down-regulation of groups corresponding to the membrane, cytosol, mitochondria, extracellular exosomes and focal adhesion (Fig. 3B). Treatment with the ruthenium complex **1a** additionally resulted in the down-regulation of proteins related to the Golgi apparatus, while **2a** was associated with a stress granule group. The 3-Morph-NQ complexes **1b** and **2b** induced an upregulation of nuclear and nucleolar proteins, chromatin-related proteins, but down-regulated mitochondrial and extracellular exosome proteins. In more detail, compound **1b** specifically regulated microtubular and lysosomal proteins, while **2b** modulated cytoskeletal proteins.

In the next step, the perturbations were categorized according to GO BP to reveal the impact of a compound on biological processes in treated SW480 cancer cells (Fig. 3C). GO BP terms represent molecular programs that an organism tries to achieve and span various levels of biological organization.[54] In fact, the groups of the proteasome, rRNA processing and ribosomal biogenesis were observed in all four treatments. On the one hand, complexes **1a** and **2a** were characterized by an upregulation of proteasomal proteins in the nuclear fraction and down-regulation of translational proteins in the cytoplasm. Additionally, cell cycle proteins were also down-regulated in the nuclear fraction and stress granule assembly was specific for **1a** and **2a**. On the other hand, compounds **1b** and **2b** featured the upregulation of transcriptional, chromatin-associated and rRNA processing proteins, while proteins for intracellular transport were down-regulated in the nuclear fraction. Proteins associated with protein stabilization were slightly upregulated in the cytoplasmic fraction. Compounds **1b** and **2b** had 13 common BP groups, among which were additionally DNA damage response, mRNA splicing and regulation of the apoptotic process. Interestingly, the cell cycle and mRNA transport groups were specific for the ruthenium(arene), while there were no specific groups for the osmium(arene) moiety.

The KEGG pathway analysis revealed quite compound-specific perturbations, but also showed the proteasome as a commonly upregulated pathway in the nuclear fraction (ESI, Fig. S17†). Overall, these data revealed detailed information about the impact of four organometallics on SW480 cancer cells and enabled the derivation of ligand-specific, metal-specific and compound-specific drug effects with relevance to their MoA.

Next, we investigated shared proteins across the treatments. Notably, despite the similarities of the functional groups in the regulomes, there were only a few overlapping proteins regulated in all four treatments (ESI, Fig. S18A†). The shared upregulated proteins in CYT and NE were searched using STRING,[55] which revealed a pronounced proteasomal cluster, stemming from the nuclear fraction (ESI, Fig. S18B†). This was connected to the sole shared upregulated protein, sequestosome-1 (SQSTM1), which is known to have cytoprotective effects by acting as a bridge between ubiquitinylated proteins and autophagosomes.[56] The

proteasome was also among the few shared protein groups in the regulome (Fig. 3C). Additionally, we also observed the chaperone heat shock 70 kDa protein 1A (HSPA1A) upregulated in all treatments. Interestingly, there were no clusters among the shared down-regulated proteins, supporting the surprising fact that there is only a low overlap of regulated proteins in this panel of structurally similar organometallics (ESI, Fig. S18B†). Notable commonly down-regulated proteins include Prolow-density lipoprotein receptor-related protein 1 (LRP1) and basal cell adhesion molecule (BCAM). The former plays a role in endocytosis[57] and the latter in cell adhesion and motility.[58] There was also only a small number of shared regulated proteins when considering the same metal(arene) scaffold with the different ligands, but there was some overlap of the ruthenium- and osmium(arenes) bearing the same ligand. This highlighted again the stronger impact of the ligand on cellular responses on the proteome level compared to the metal(arene). This correlated with the IC_{50} values of the respective ligand systems, where the ethyl- and morpholine-derivatives dictated the antiproliferative potency irrespective of the metal(arene). NQO1, the target of the naphthoquinone ligands, was not regulated by any of the compounds investigated here (ESI, Fig. S19†).

2.5 Specific effects of the 3-Et-NQ complexes

To investigate molecular effects that might be responsible for the increased potency of the 3-Et-NQ complexes compared to the 3-Morph-NQ complexes, a STRING network analysis was performed with the shared regulated proteins only between **1a** and **2a** (ESI, Fig. S18†). Among the upregulated proteins, representatives of cellular stress responses were found, *e.g.*, NRF2 targets, heat shock response and cytoplasmic stress granules (ESI, Fig. S20A†). The NRF2-associated proteins were heme oxygenase 1 (HMOX1), glutamate-cysteine ligase regulatory subunit (GCLM) and oxidative stress-induced growth inhibitor 1 (OSGIN1). The heat shock response included HSPA1A and the ER chaperone BiP (GRP78, HSPA5), while the induction of the former was a feature of all four complexes.

The downregulated proteins featured an extensive network covering cell cycle, translation, mitochondrial respiration and extracellular matrix interactions (ESI, Fig. S20B†). Interestingly, the cellular tumour antigen p53 (TP53) was found as a central hub in the cell cycle network (Fig. 4A), together with mitogen-activated protein kinase (MAPK3) and signal transducer and activator of transcription 6 (STAT6), suggesting that a TP53-mediated antiproliferative effect would be crucial for the activity of the 3-Et-NQ complexes. TP53 is a known tumour suppressor and regulates cell cycle, DNA repair and apoptosis.[59] TP53 is mutated in many tumours.[60] SW480 cancer cells contain high levels of a doubly mutated TP53, with gain-of-function properties. Strikingly, TP53 was the strongest down-regulated protein upon treatment of SW480 cancer cells with **1a** in the cytoplasmic fraction (Fig. 4B), but not for **2a** (Fig. 4C). This suggests

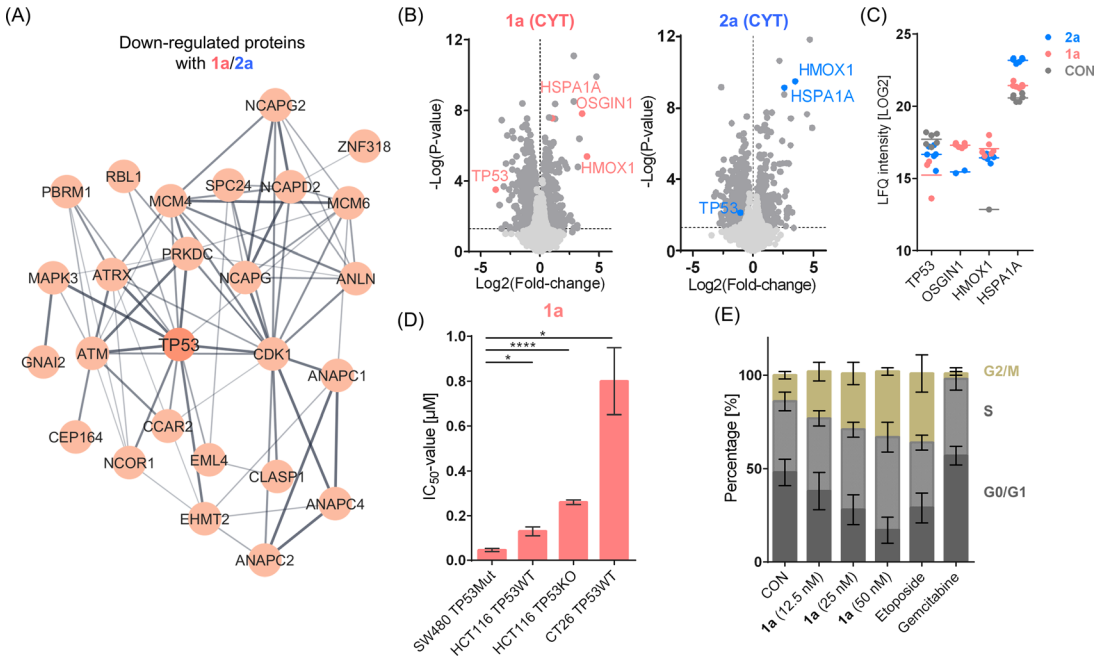

Fig. 4 (A) STRING subnetwork of the shared 26 down-regulated proteins after treating SW480 cancer cells with **1a** or **2a** displaying the core cluster around TP53 related to cell cycle. (B) Volcano plots showing the proteome changes in the cytoplasmic (CYT) fractions of SW480 cells upon treatment with **1a** and **2a**. Proteins with statistically significant regulations are shown in dark grey (FDR = 0.05, S_0 = 0.1). (C) Protein abundances in LOG2 space for selected proteins in control SW480 cells (CON) and upon treatment with either **1a** or **2a**. Six replicates were performed per condition. If not shown, proteins were not detected. (D) Bar chart of the IC_{50} values of **1a** in cell lines with different TP53 status, *i.e.*, mutated (Mut), wild-type (WT) or knockout (KO). Cells were exposed for 96 h. Values are presented as means ± standard deviation. Significance was calculated by an unpaired two-tailed *t* test with Welch's correction: **p*-value <0.05, *****p*-value<0.0001. (E) Cell cycle analysis of SW480 cancer cells treated with **1a** for 24 h at the indicated concentrations. Etoposide (100 nM) and gemcitabine (10 nM) served as controls for G2/M and G0/G1 arrest, respectively. Values are presented as means ± standard deviation.

that **1a** induces a more potent response compared to **2a** and can efficiently destabilize TP53 levels in SW480 cells.

2.6 Compound 1a is specifically active in SW480 cancer cells with mutated gain-of-function TP53

To verify the involvement of TP53 in the MoA of **1a**, its cytotoxicity was examined using the HCT116 cell line, which contains wildtype TP53 (ref. 61) and for which a TP53-knock-out variant was available. Interestingly, the IC_{50} value of **1a** in the HCT116 TP53 wild-type (TP53WT) was 0.13 ± 0.02 μM and thus, approximately four-fold less potent compared to the SW480 cells (Fig. 4D). Moreover, the HCT116 TP53-knockout (TP53KO) cell line exhibited an IC_{50} value of 0.26 ± 0.01 μM, further reducing the potency by a factor of two, underscoring the dependence of cytotoxic potency on TP53 status of **1a**. The IC_{50} value of **1a** in the murine CT26 colon carcinoma cells, containing wildtype TP53,[62] was determined to be 0.80 ± 0.15 μM. Consequently, **1a** was most active towards the TP53-mutated SW480 cell line. This cell line depends on TP53-mediated signalling for proliferation.[63] TP53 controls the S and G2/M checkpoints of the cell cycle. Therefore, destabilizing TP53 would lead to an accumulation of cells in these phases of the cell cycle. SW480 cancer cells were treated with **1a** at increasing concentrations from 12.5 to 50 nM for 24 h and the cell cycle distribution was assessed (Fig. 4E). A dose-dependent increase in the S and G2/M phases of the cell cycle was clearly observed in the range of the IC_{50}. The potency of **1a** treatment on cell cycle distribution was similar to the positive control etoposide for which a 100 nM treatment was applied, but contrasted to gemcitabine, which induced a G0/G1 arrest. Importantly, the topoisomerase II poison[64] etoposide induces to DNA double strand breaks and a TP53-mediated DNA damage response.[65]

2.7 Compound 1a deregulates the TP53-DDX3X-p21 signalling axis

For further in-depth investigation, we assessed TP53 and downstream effector p21 expression. In whole cell lysates, no down-regulation of TP53 was observed upon **1a** treatment (Fig. 5A). However, immunofluorescence staining revealed decisive loss of TP53 signal intensity (Fig. 5B and C), corroborating the findings from proteome profiling (*cf.* Fig. 4A and B). Again, etoposide was used as positive control for the induction of TP53 expression and indeed showed enhanced nuclear accumulation of TP53 (Fig. 5B). Additionally, changes of TP53

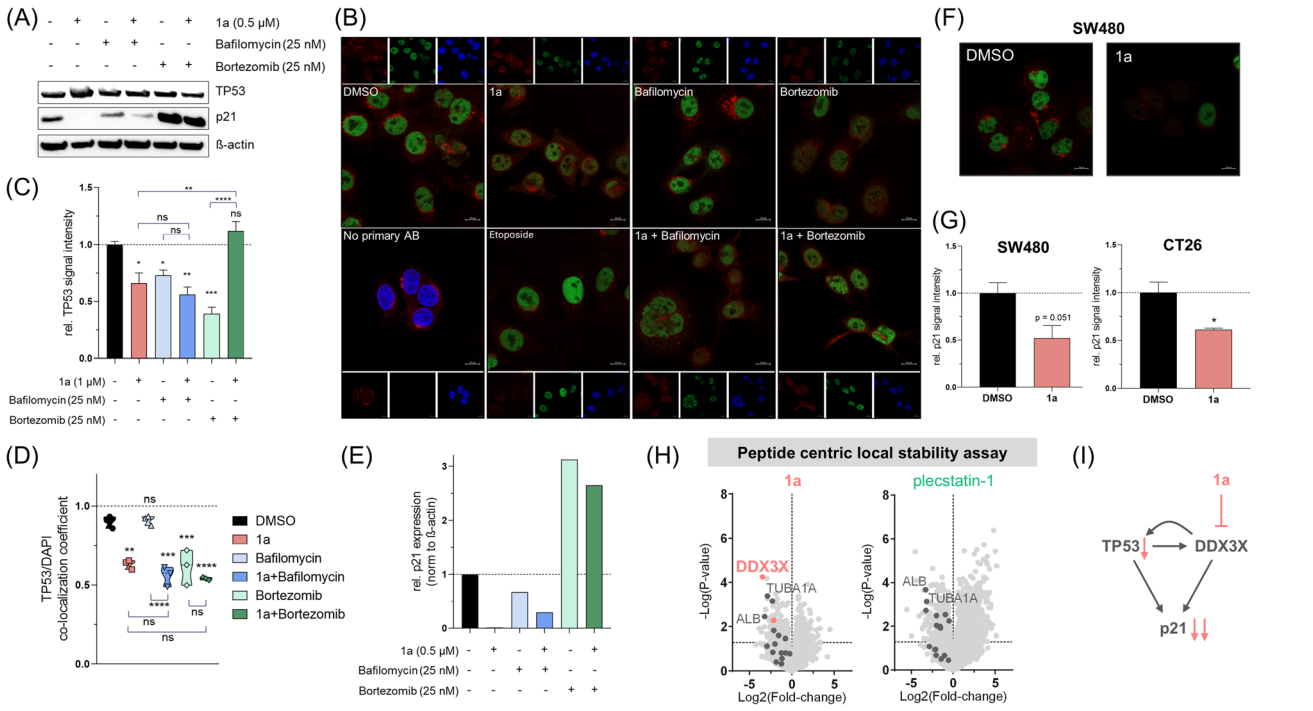

Fig. 5 (A) Protein expression levels of TP53 and p21 in whole cell lysates of SW480 cells treated with indicated compounds for 24 h and analyzed by western blotting. β-Actin served as loading control. (B) Immunofluorescence staining of TP53 (green) in SW480 cells following treatment with 1 μM of **1a** without or with 25 nM of bafilomycin or bortezomib compared to DMSO control or 100 nM of etoposide for 24 h. Cytoplasm and nuclei were stained using rhodamine-labelled wheat germ agglutinin (WGA, red) and DAPI (blue), respectively. (C) Mean TP53 signal intensity relative to DMSO control quantified from (B). One-way ANOVA with Tukey's multiple comparisons test: *$p < 0.05$, **$p < 0.005$, ***$p < 0.0005$, ****$p < 0.0001$. (D) TP53/DAPI co-localization coefficient calculated from (B). (E) p21 protein expression relative to DMSO control, normalized to β-actin quantified from (A) using Image J. (F) Immunofluorescence staining of p21 (green) in SW480 cells following treatment with **1a** (1 μM) as compared to control for 24 h. Cytoplasm was stained using rhodamine-labelled WGA (red). (G) Quantification of p21 immunofluorescence signal following treatment with **1a** (1 μM) as compared to control for 24 h in SW480 (F) and CT26 cells. Unpaired two-tailed Student's *t*-test: *$p < 0.05$. (H) Peptide centric local stability assay was performed to identify potential direct interaction partners of **1a** and plecstatin-1, revealing DDX3X as a specific interactor of **1a**. Each dot depicts a tryptic peptide. (I) Scheme of the proposed impact of **1a** on the TP53-DDX3X-p21 signalling axis.

expression were assessed after incubation with subtoxic concentrations (ESI, Fig. S21†) of bafilomycin or bortezomib, which are inhibitors of lysosomal acidification and the proteasome, respectively, with the aim to reveal potential degradation routes of TP53. While both inhibitors on their own reduced TP53 signals, only combination with bortezomib induced accumulation of TP53 indicating the proteasome to be mainly responsible for TP53 degradation and turnover in SW480 cancer cells. Moreover, assessment of the TP53/DAPI co-localization coefficient revealed that **1a** and bortezomib retained TP53 in the cytoplasm in a comparable manner (Fig. 5D). Drug combination did not further enhance this effect. Assessment of TP53 expression in CT26 cells revealed downregulation associated with proteasomal degradation pathway (ESI, Fig. S22†), in line with observations in SW480 cells. Growth arrest is induced by p21 upon p21 promoter transactivation by TP53.[66] Consequently, p21 expression levels were also analysed upon treatment. Unexpectedly, **1a** treatment significantly reduced p21 expression in SW480 and CT26 cells (Fig. 5A, E–G), which also seemed to be degraded *via* the proteasomal pathway (Fig. 5E).

A recently reported[67] peptide centric local stability assay was then performed to determine whether **1a** would directly interact with TP53 or p21. The method relies on a limited-proteolysis strategy, where ligand-binding on target proteins is expected to increase the stability of the proteins against proteolytic digestion. This specifically enables the identification of target proteins of small molecules. For this purpose, a SW480 whole cell lysate was treated with DMSO, **1a** (1 μM) or plecstatin-1 (20 μM), each in four replicates (Fig. 5H). Being a ruthenium(arene) derivative, plecstatin-1 was used to assess potential non-specific interactors of the ruthenium(cymene) fragment. Among the identified 930 proteins from 2666 peptides for **1a**, we did not detect TP53, or p21, probably due to the limited digestion efficiency. However, among the selective interaction partners, we found specific peptides of ATP-dependent RNA helicase DDX3X, tubulin alpha-1A (TUBA1A) and albumin (ALB). Several peptides of TUBA1A and ALB were also found to be stabilized by plecstatin-1 indicating low specificity. This results in DDX3X being the most probable direct binding partner of **1a** among the subpopulation of identified proteins. Interestingly, DDX3X interacts with TP53 and can change the accumulation of TP53 in the cytoplasm and nucleus.[68] It was demonstrated previously that the interaction of DDX3X with TP53 is dependent on the mutational status of the latter and moreover, p21 transcription is promoted by DDX3X *via* direct interaction with SP1 in a TP53-dependent[69] and -independent manner.[70] This, together with our data, suggests that **1a** impairs TP53 functionality leading to p21 loss, which seems to be mediated by direct interaction of **1a** with DDX3X (Fig. 5I) and might explain the exceptional potency of this compound towards the rather chemoresistant SW480 cancer cell line.

2.8 Anti-tumour activity in the CT26 mouse model

Tumour inhibition of the four compounds was evaluated in subcutaneous CT26 allografts using BALB/c mice, since it represents an appropriate immune competent mouse model to study colon carcinoma. The compounds were administered intraperitoneally (i.p.) over two weeks at doses of 10 mg kg^{-1} for the 3-Et-NQ complexes and 30 mg kg^{-1} for the 3-Morph-NQ complexes. The different dosages were selected as maximal tolerable doses (MTDs) after an initial toxicity screen (data not shown).

Compounds **1a** and **2a** were found to significantly inhibit tumour growth compared to vehicle-treated controls, while **1b** and **2b** were inactive (Fig. 6A). Consequently, the nature of the ligand not only determines *in vitro* activity, but also drives *in vivo* tumour inhibition. Compound **1a** achieved significant tumour inhibition featuring a significant 44% reduction in tumour volume on day 13 (Fig. 6B).

Furthermore, tumour, organs and blood of the **1a**-treated mice were collected 4 h after the last injection. The average metal content was quantified by inductively coupled plasma mass spectrometry of tissue homogenates using the ^{101}Ru isotope. Intraperitoneally administered compounds are primarily absorbed through the portal circulation, which can

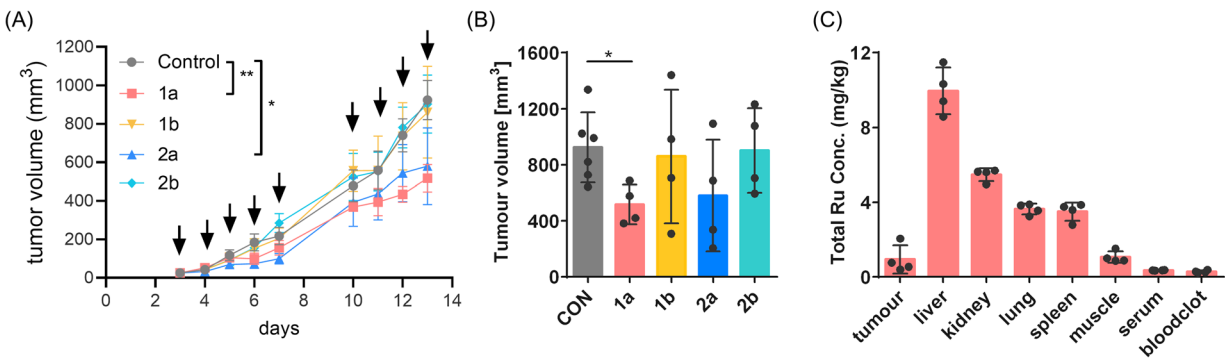

Fig. 6 (A) Anticancer activity of the indicated compounds *in vivo*. CT26-bearing BALB/c mice were treated i.p. over two weeks (indicated by arrows) with 10 mg kg^{-1} of 3-Et-NQ complexes (**1a** and **2a**) and with 30 mg kg^{-1} of 3-Morph-NQ complexes (**1b** and **2b**). Data are presented as mean ± SEM. Statistical significance was tested by two-way ANOVA using Dunnett's multiple comparison test. *$p < 0.05$, **$p < 0.01$. (B) Bar chart showing the tumour volume at the last day in vehicle-treated controls and compound-treated mice. Bars represent mean values. Significance was calculated by an unpaired two-tailed *t* test with Welch's correction: *p-value <0.05. (C) Tumour, organs and blood were collected of **1a**-treated mice and the total ^{101}Ru content was quantified by inductively coupled plasma mass spectrometry. Bars represent mean values.

lead to a substantial liver exposure.[71] Indeed, **1a** distributed to the liver, where a ^{101}Ru content of 10 ± 1 mg kg^{-1} was detected (Fig. 6C). A smaller amount accumulated in the tumour, corresponding to 0.9 ± 0.7 mg kg^{-1} ^{101}Ru. This paralleled earlier findings of other metal(arenes) in this tumour model.[72] Interestingly, **1a** neither accumulated in blood serum nor in the blood clot with ^{101}Ru contents consistently <0.4 mg kg^{-1}.

2.9 Evaluation of drug effects *in vivo*

The significant tumour-inhibition of **1a** together with the selective impact on TP53-mediated signalling motivated investigations into *in vivo* drug effects. For this purpose, an additional 1-week experiment was performed by treating BALB/c mice bearing CT26 tumours with **1a** administered at 10 mg kg^{-1} for five consecutive days. The experiment confirmed the statistically significant tumour inhibition of **1a** (Fig. 7A). On day five, tumour, liver and blood were harvested two hours after the last injection of **1a**. Blood plasma and livers were harvested to obtain insight into systemic drug effects and tumours were collected to obtain information about local effects of the candidate drug.

Liver tissue for histological assessment was fixed with formaldehyde and then paraffin-embedded. Haematoxylin and eosin (H&E) was used to stain tissue slices. Despite being the most exposed organ, liver sections of **1a**-treated mice showed largely healthy physiology (Fig. 7B).

For proteomic workup, the fresh tissue samples were quickly rinsed with PBS and shock-frozen in liquid nitrogen. Blood plasma was immediately prepared by centrifugation of the collected blood in ethylenediaminetetraacetic acid (EDTA) tubes. The samples were analysed in technical duplicates due to the expected larger heterogeneity and statistical evaluation was

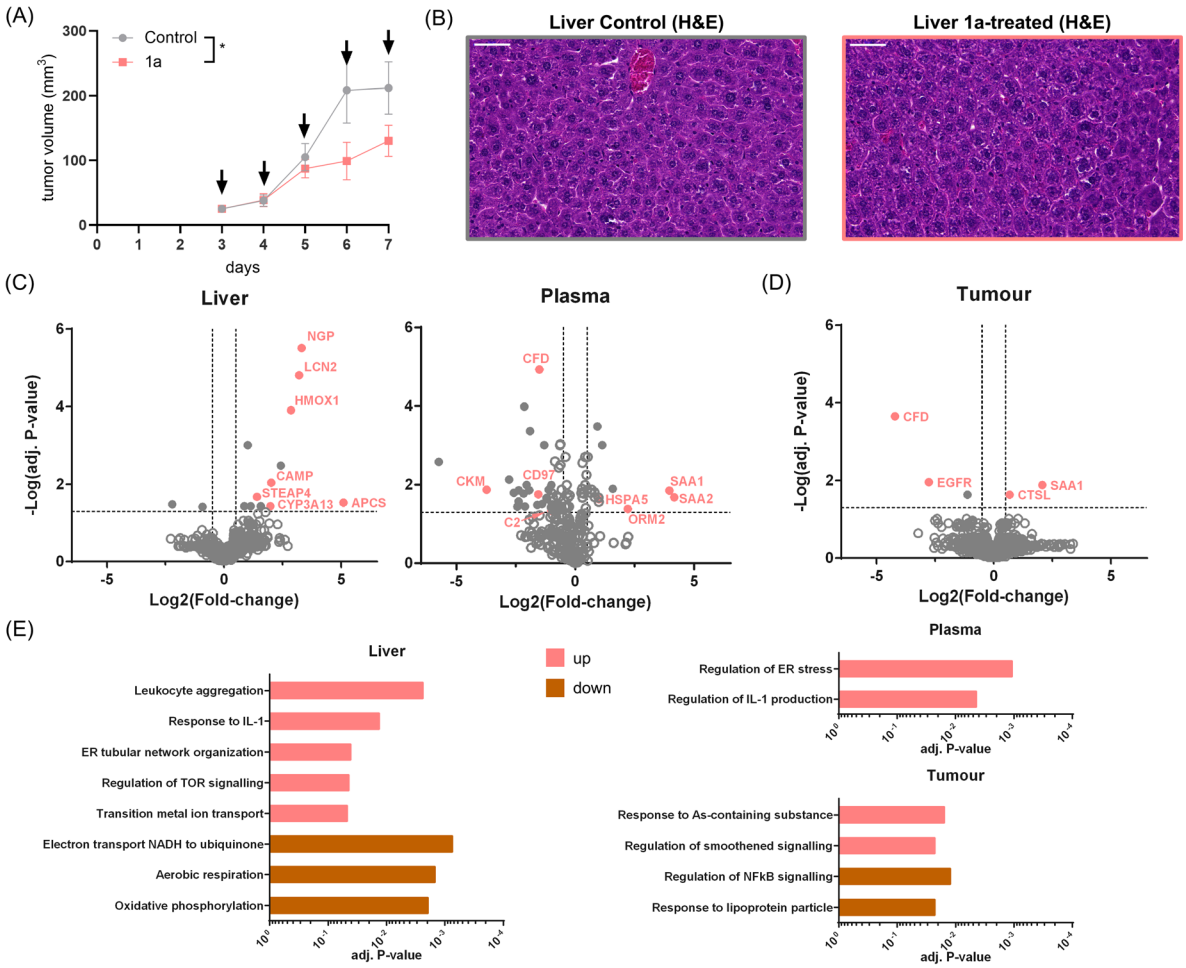

Fig. 7 (A) Anticancer activity of **1a** *in vivo*. CT26-bearing BALB/c mice were treated i.p. on five consecutive days (indicated by arrows) at a dose of 10 mg kg^{-1}. Impact on tumour growth; data are presented as mean ± SEM. Statistical significance was tested using the mixed-effects model (REML): **p*-value <0.05. Tumour, liver and blood plasma of these mice were collected and analysed by proteome profiling. (B) Representative microscopy images of liver tissue harvested from untreated and treated mice. Tissues were paraffin-embedded, followed by cutting and histological staining by hematoxylin and eosin (H&E). Pictures were taken using a Slidescanner (magnification: 40×; scale bar: 50 μm). (C) Volcano plots of the proteomic effects of **1a**-treated *versus* vehicle-treated mice highlighting systemic effects in the liver and blood plasma. Statistical significance was calculated using LIMMA and a multiple-testing correction based on Benjamini–Hochberg. (D) Volcano plot of the proteomic effects of **1a**-treated *versus* vehicle-treated mice highlighting local effects in the tumour. Statistical significance was calculated using LIMMA and a multiple-testing correction based on Benjamini–Hochberg. (E) Gene set variation analysis (GSVA) of the tissue proteomic data according to upregulated and down-regulated GO BPs. Bars represent adjusted *P*-values of statistically significant term enrichments.

performed using the LIMMA algorithm[73] and gene set variation analysis (GSVA).[74] A total of 2770 proteins were identified in liver with 14 statistically significantly regulated proteins and 285 proteins in plasma samples with 79 statistically significant regulations (Fig. 7C). Then, proteomic analysis revealed 3867 proteins in tumour samples of which 5 showed statistically significant regulations (Fig. 7D). Statistical significance was calculated based on multi-parameter testing-adjusted *P*-values $\geq$0.05. The distribution of **1a** in CT26 tumour-bearing mice had revealed a significant accumulation in the liver and minor amounts in tumour tissue, suggesting a potential involvement of systemic contributions to its tumour-inhibiting effect.

Although the liver showed a normal physiology, the proteomic data evidenced the upregulation of detoxification enzymes in **1a**-treated mice, *e.g.*, cytochrome P450 3A13 (CYP3A13), heme oxygenase 1 (HMOX1) and metalloreductase STEAP4 (STEAP4, Fig. 7C). As one of the most exposed organs to **1a**, the upregulation of HMOX1 also correlated with the *in vitro* drug effects.

Moreover, the induction of lipocalin-2 (LCN2), neutrophil granule protein (NGP), serum amyloid *P*-component (APCS) and cathelicidin antimicrobial peptide (CAMP) indicated a drug-induced acute phase response in the liver. These effects were further supported by the statistically significant enrichment of GO BP terms in the GSVA (Fig. 6E and ESI, Table S3†), *e.g.*, "response to IL-1" and "leukocyte activation". The upregulated term "transition metal ion transport" was indicative of metal transport, including iron homeostasis and "TOR signalling" related to a restriction of nutrients under this treatment challenge. This was complemented by a down-regulation of several terms related to mitochondrial respiration, which can accompany an acute phase response (Fig. 7E).[75,76]

Acute phase proteins were also found upregulated in blood plasma of **1a**-treated mice (Fig. 7C). The liver-derived c-reactive protein (CRP), serum amyloid A (SAA1/SAA2), APCS and α_1-acid glycoprotein 2 (ORM2) are classical acute phase markers in plasma. While CRP and SAA1/SAA2 are usually mediating pro-inflammatory processes,[77] ORM2 has immunomodulatory properties and might dampen excessive inflammation reactions.[78] Several complementary components were found to be down-regulated, including C2, C5, C8alpha-gamma and complement factor D (CFD). Similarly, GSVA in plasma revealed a term related to "regulation of IL-1 production", involved in inflammatory and immune regulatory processes.

The most pronounced changes in the tumour mirrored those in plasma, including regulated SAA1 and CFD, which may represent a consequence of tumour vasculature, and do not directly represent **1a**-treatment in the tumour (Fig. 7D). GSVA revealed a decreased "regulation of NFkB signalling" and an induction of "response to As-containing substance". The latter included HMOX1, similarly to the observed effects in the liver and *in vitro* in SW480 cells. This is representative of the stress response induced by **1a** at the tumour site. Moreover, EGFR was found to be down-regulated in **1a**-treated mice. This receptor of the MAPK3 pathway is linked to TP53 and directly involved in proliferation signalling.[79,80] Indeed, down-regulated EGFR was connected to down-regulated RHOA and ACTN4 signalling, as well as RELA (p65, NFkB) (ESI, Fig. S23†). Furthermore, DDX3X was shown to regulate EGFR in breast cancer.[81] Down-regulation of EGFR *in vivo* might therefore reflect a further crucial direct effect of **1a** targeting the TP53-DDX3X-p21 signalling axis as revealed from the *in vitro* experiments.

3. Conclusions

Metal(arenes) containing *N*,*O*,*O*-tridentate ligands, which were obtained *in situ* from dimeric metal precursors, diazoles and naphthoquinone ligands, showed exceptional antiproliferative activity in the nanomolar range, while the ligands alone were largely inactive. In contrast to other metal(arenes) containing bidentate ligands, this family is kinetically inert over a prolonged time period, but retains reactivity by hydrolysis of a metal–oxygen bond of the naphthoquinone ligand. Preferential binding of the complexes to amino acids over nucleotides was confirmed, accompanied by release of the naphthoquinone ligand from the complex. Among the four complexes, the ligand strongly determines the antiproliferative activity with the 3-ethyl naphthoquinone organometallics showing >30-fold higher potency compared to the 3-morpholino derivatives. Similarly, the ligand influenced protein perturbation profiles more strongly than the metal. The shared effects of the 3-ethyl naphthoquinone organometallics revealed TP53 as a central hub in the perturbation network, directly impacting on proliferative signalling. Furthermore, the mutant TP53 cell line SW480 seemed to be particularly sensitive to these compounds. The ruthenium lead compound considerably affected cell cycle progression at the G2/M phase, which was associated with disturbance of the TP53-DDX3X-p21 signalling axis and loss of p21 expression, probably mediated by direct modulation of DDX3X. The 3-ethyl naphthoquinone organometallics also showed anticancer activity in the CT26 mouse model, where especially the ruthenium(arene) derivative significantly reduced tumour size. Drug effects of the 3-ethyl naphthoquinone containing an organoruthenium complex were then assessed in the same mouse model by proteome profiling. To distinguish direct from indirect drug effects at the tumour site, systemic responses were considered. As a result, the down-regulated EGFR in the tumour was identified as the direct effect of treatment. EGFR levels were previously found to be controlled by TP53-DDX3X-p21 signalling. The strategy presented here can be used to elucidate the modes of action of phenotypically discovered metal-based anticancer drugs *in vitro* and *in vivo*. The antitumour activity of **1a** *via* the TP53-DDX3X-p21 signalling axis and its dependence on the mutational status of TP53 warrants further mechanistic investigations.

Data availability

Proteomic data were submitted to the ProteomeXchange Consortium (**https://proteomecentral.proteomexchange.org/**) and are available in the PRIDE partner repository with identifiers PXD059756 (*in vitro*), PXD059761 (*in vivo* plasma) and PXD059773 (*in vivo* tissue).

Author contributions

Conceptualization, P. H., S. M. M.-M. and W. K.; data curation, A. R., L. S., T. Me., T. Mo., A. B., P. H., M. A. J., S. M. and M.-M.; formal analysis, A. R., L. S., T. Me., H. G., T. Mo., and A. L.; funding acquisition, P. H., W. B., C. G., G. K., B. K., W. K., and S. M. M.-M.; investigation, A. R., L. S., T. Me., D. B., M. H., Y. B., M. G., H. G., A. B., and A. L.; methodology, P. H., S. M. M.-M. and W. K.; project administration, P. H., S. M. M.-M. and W. K.; resources, P. H., W. B., G. K., C. G., M. A. J., B. K., S. M. M.-M. and W. K.; supervision, P. H., W. B., G. K., C. G., M. A. J., S. M. M.-M. and W. K.; validation, D. B., P. H., W. B., G. K., C. G., M. A. J., S. M. M.-M. and W. K.; visualization, A. R., L. S., T. Me., D. B., A. L., and S. M. M.-M.; writing – original draft preparation, A. R., L. S., T. Me., M. A. J., P. H., W. K. and S. M. M.-M.; writing – review and editing, A. R., L. S., D. B., P. H., W. K. and S. M. M.-M.; all authors have read and agreed to the published version of the manuscript.

Ethical statement

All experiments were carried out with male BALB/c mice according to the regulations of the Ethics Committee for the Care and Use of Laboratory Animals at the Medical University Vienna (BMWF-2022-0.770.291), following the guidelines from the Austrian Animal Science Association and the Federation of European Laboratory Animal Science Associations (FELASA).

Conflicts of interest

There are no conflicts to declare.

Acknowledgements

The authors are grateful to the Research Cluster "Translational Cancer Therapy Research", the Core Facility for Mass Spectrometry, the Core Facility Multimodal Imaging (Faculty of Chemistry, University of Vienna) and the Joint Metabolome Facility (University of Vienna and Medical University of Vienna), which are all members of the Vienna Life-Science Instruments (VSLI). S. M. M.-M. acknowledges partial financial support by the Austrian Science Fund (FWF, Grant DOI: 10.55776/PAT2536323). The authors express great appreciation to Gerhard Zeitler (financed by the Mahlke-Obermann Stiftung) for animal care and Christoph Baumgartinger for ICP-MS measurements. We also thank Lukas Kenner for the pathological assessment of the H&E-stained tissue slides and Thomas Iellici for assistance with the PELSA experiment.

References

1 D. Wang and S. J. Lippard, Cellular processing of platinum anticancer drugs, *Nat. Rev. Drug Discov.*, 2005, **4**, 307–320.
2 *Metal-based anticancer agents*, ed. A. Casini, A. Vessières and S. M. Meier-Menches, Royal Society of Chemistry, London, 2019, DOI: 10.1039/9781788016452.
3 Z. Adhireksan, G. E. Davey, P. Campomanes, M. Groessl, C. M. Clavel, H. Yu, A. A. Nazarov, C. H. F. Yeo, W. H. Ang, P. Dröge, U. Rothlisberger, P. J. Dyson and C. A. Davey, Ligand substitutions between ruthenium–cymene compounds can control protein *versus* DNA targeting and anticancer activity, *Nat. Commun.*, 2014, **5**, 3462.
4 K. J. Franz and N. Metzler-Nolte, Introduction: metals in medicine, *Chem. Rev.*, 2019, **119**, 727–729.
5 E. Boros, P. J. Dyson and G. Gasser, Classification of metal-based drugs according to their mechanisms of action, *Chem*, 2020, **6**, 41–60.
6 L. Skos, Y. Borutzki, C. Gerner and S. M. Meier-Menches, Methods to identify protein targets of metal-based drugs, *Curr. Opin. Chem. Biol.*, 2023, **73**, 102257.
7 I. Romero-Canelón and P. J. Sadler, Systems approach to metal-based pharmacology, *Proc. Natl. Acad. Sci. U. S. A.*, 2015, **112**, 4187–4188.
8 Y. Wang, H. Li and H. Sun, Metalloproteomics for unveiling the mechanism of action of metallodrugs, *Inorg. Chem.*, 2019, **58**, 13673–13685.
9 Y. Zhou, H. Li and H. Sun, Metalloproteomics for biomedical research: methodology and applications, *Annu. Rev. Biochem.*, 2022, **91**, 449–473.
10 Mechanism matters, *Nat. Med.*, 2010, **16**, 347.
11 H. Wang, Y. Zhou, X. Xu, H. Li and H. Sun, Metalloproteomics in conjunction with other omics for uncovering the mechanism of action of metallodrugs: mechanism-driven new therapy development, *Curr. Opin. Chem. Biol.*, 2020, **55**, 171–179.
12 P. M. Bruno, Y. Liu, G. Y. Park, J. Murai, C. E. Koch, T. J. Eisen, J. R. Pritchard, Y. Pommier, S. J. Lippard and M. T. Hemann, A subset of platinum-containing chemotherapeutic agents kills cells by inducing ribosome biogenesis stress, *Nat. Med.*, 2017, **23**, 461–471.
13 C. Gallois, Q. Shi, L. D. Pederson, T. André, T. J. Iveson, A. F. Sobrero, S. Alberts, A. de Gramont, J. A. Meyerhardt, T. George, et al., Oxaliplatin-based adjuvant chemotherapy in older patients with stage III colon cancer: an ACCENT/IDEA pooled analysis of 12 trials, *J. Clin. Oncol.*, 2024, **42**, 2295–2305.
14 S. M. Meier-Menches, C. Gerner, W. Berger, C. G. Hartinger and B. K. Keppler, Structure–activity relationships for ruthenium and osmium anticancer agents – towards clinical development, *Chem. Soc. Rev.*, 2018, **47**, 909–928.
15 R. Trondl, P. Heffeter, C. R. Kowol, M. A. Jakupec, W. Berger and B. K. Keppler, NKP-1339, the first ruthenium-based anticancer drug on the edge to clinical application, *Chem. Sci.*, 2014, **5**, 2925–2932.
16 G. M. O'Kane, J. L. Spratlin, P. Kavan, R. A. Goodwin, E. McWhirter, D. Thompson, M. Jones, E. R. McAllister, A. Machado, Y. Lemmerick, L. Wilson and J. Pankovich, BOLD-100-001 (TRIO039): a phase Ib dose-escalation study of BOLD-100 in combination with FOLFOX chemotherapy in patients with advanced gastrointestinal solid tumors, *J. Clin. Oncol.*, 2021, **39**, TPS145.
17 H. A. Burris, S. Bakewell, J. C. Bendell, J. Infante, S. F. Jones, D. R. Spigel, G. J. Weiss, R. K. Ramanathan, A. Ogden and

D. Von Hoff, Safety and activity of IT-139, a ruthenium-based compound, in patients with advanced solid tumours: a first-in-human, open-label, dose-escalation phase I study with expansion cohort, *ESMO Open*, 2016, **1**, e000154.

18 B. J. Park, P. Raha, J. Pankovich and M. Bazett, Utilization of cancer cell line screening to elucidate the anticancer activity and biological pathways related to the ruthenium-based therapeutic BOLD-100, *Cancers*, 2022, **15**, 28.

19 B. Neuditschko, A. A. Legin, D. Baier, A. Schintlmeister, S. Reipert, M. Wagner, B. K. Keppler, W. Berger, S. M. Meier-Menches and C. Gerner, Interaction with ribosomal proteins accompanies stress induction of the anticancer metallodrug BOLD-100/KP1339 in the endoplasmic reticulum, *Angew. Chem., Int. Ed.*, 2021, **60**, 5063–5068.

20 D. Baier, T. Mendrina, B. Schoenhacker-Alte, C. Pirker, T. Mohr, M. Rusz, B. Regner, M. Schaier, N. Sgarioto, N. J. M. Raynal, K. Nowikovsky, W. M. Schmidt, P. Heffeter, S. M. Meier-Menches, G. Koellensperger, B. K. Keppler and W. Berger, The lipid metabolism as target and modulator of BOLD-100 anticancer activity: crosstalk with histone acetylation, *Adv. Sci.*, 2023, **10**, 2301939.

21 D. Baier, B. Schoenhacker-Alte, M. Rusz, C. Pirker, T. Mohr, T. Mendrina, D. Kirchhofer, S. M. Meier-Menches, K. Hohenwallner, M. Schaier, E. Rampler, G. Koellensperger, P. Heffeter, B. Keppler and W. Berger, The anticancer ruthenium compound BOLD-100 targets glycolysis and generates a metabolic vulnerability towards glucose deprivation, *Pharmaceutics*, 2022, **14**, 238.

22 S. Bonnet, Ruthenium-based photoactivated chemotherapy, *J. Am. Chem. Soc.*, 2023, **145**, 23397–23415.

23 S. Monro, K. L. Colón, H. Yin, J. Roque, P. Konda, S. Gujar, R. P. Thummel, L. Lilge, C. G. Cameron and S. A. McFarland, Transition metal complexes and photodynamic therapy from a tumor-centered approach: challenges, opportunities, and highlights from the development of TLD1433, *Chem. Rev.*, 2018, **119**, 797–828.

24 L. D. Lilge, G. Kulkani, A. Mandel, N. Perlis, M. Nesbitt, R. White, W. Embree, M. Jewett and T. Hasan, *Presented in Part at the 17th International Photodynamic Association World Congress*, 2019.

25 Y. Wang, J. N. Staudinger, T. L. Mindt and G. Gasser, Theranostics with photodynamic therapy for personalized medicine: to see and to treat, *Theranostics*, 2023, **13**, 5501–5544.

26 NCT03945162, *A Phase II Clinical Study of Intravesical Ruvidar® in Patients With BCG-Unresponsive Non-Muscle Invasive Bladder Cancer ("NMIBC") Carcinoma In-Situ ("CIS") or Patients Who Are Intolerant to BCG Therapy ("Study II")*, **https://clinicaltrials.gov/study/NCT03945162**, accessed 01 January 2024.

27 R. E. Morris, R. E. Aird, P. del Socorro Murdoch, H. Chen, J. Cummings, N. D. Hughes, S. Parsons, A. Parkin, G. Boyd, D. I. Jodrell and P. J. Sadler, Inhibition of cancer cell growth by ruthenium(II) arene complexes, *J. Med. Chem.*, 2001, **44**, 3616–3621.

28 C. S. Allardyce, P. J. Dyson, D. J. Ellis and S. L. Heath, [Ru(η6-p-cymene)Cl2(pta)] (pta = 1,3,5-triaza-7-phosphatricyclo [3.3.1.1]decane): a water soluble compound that exhibits pH dependent DNA binding providing selectivity for diseased cells, *Chem. Commun.*, 2001, 1396–1397.

29 P. C. A. Bruijnincx and P. J. Sadler, in *Advances in Inorganic Chemistry*, ed. R. van Eldik and C. D. Hubbard, Academic Press, 2009, vol. 61, pp. 1–62.

30 A. Levina, A. Mitra and P. A. Lay, Recent developments in ruthenium anticancer drugs, *Metallomics*, 2009, **1**, 458–470.

31 C. G. Hartinger and P. J. Dyson, Bioorganometallic chemistry—from teaching paradigms to medicinal applications, *Chem. Soc. Rev.*, 2009, **38**, 391–401.

32 E. J. Anthony, E. M. Bolitho, H. E. Bridgewater, O. W. L. Carter, J. M. Donnelly, C. Imberti, E. C. Lant, F. Lermyte, R. J. Needham, M. Palau, P. J. Sadler, H. Shi, F.-X. Wang, W.-Y. Zhang and Z. Zhang, Metallodrugs are unique: opportunities and challenges of discovery and development, *Chem. Sci.*, 2020, **11**, 12888–12917.

33 G. Süss-Fink, Areneruthenium complexes as anticancer agents, *Dalton Trans.*, 2010, **39**, 1673–1688.

34 M. Wenzel and A. Casini, Mass spectrometry as a powerful tool to study therapeutic metallodrugs speciation mechanisms: current frontiers and perspectives, *Coord. Chem. Rev.*, 2017, **352**, 432–460.

35 A. Merlino, T. Marzo and L. Messori, Protein metalation by anticancer metallodrugs: a joint ESI MS and XRD investigative strategy, *Chem.–Eur. J.*, 2017, **23**, 6942–6947.

36 M. Cziferszky, D. Truong, C. G. Hartinger and R. Gust, Determination of relative stabilities of metal-peptide bonds in the gas phase, *Chem.–Eur. J.*, 2021, **27**, 16401–16406.

37 C. Schmidt, M. Zollo, R. Bonsignore, A. Casini and S. M. Hacker, Competitive profiling of ligandable cysteines in Staphylococcus aureus with an organogold compound, *Chem. Commun.*, 2022, **58**, 5526–5529.

38 S. M. Meier, D. Kreutz, L. Winter, M. H. M. Klose, K. Cseh, T. Weiss, A. Bileck, B. Alte, J. C. Mader, S. Jana, et al., An organoruthenium anticancer agent shows unexpected target selectivity for plectin, *Angew. Chem., Int. Ed.*, 2017, **56**, 8267–8271.

39 M. Prechova, Z. Adamova, A.-L. Schweizer, M. Maninova, A. Bauer, D. Kah, S. M. Meier-Menches, G. Wiche, B. Fabry and M. Gregor, Plectin-mediated cytoskeletal crosstalk controls cell tension and cohesion in epithelial sheets, *J. Cell Biol.*, 2022, **221**, e202105146.

40 Z. Outla, G. Oyman-Eyrilmez, K. Korelova, M. Prechova, L. Frick, L. Sarnova, P. Bisht, P. Novotna, J. Kosla, P. Bortel, et al., Plectin-mediated cytoskeletal crosstalk as a target for inhibition of hepatocellular carcinoma growth and metastasis, *eLife*, 2025, **13**, 102205.

41 S. M. Meier-Menches, K. Zappe, A. Bileck, D. Kreutz, A. Tahir, M. Cichna-Markl and C. Gerner, Time-dependent shotgun proteomics revealed distinct effects of an organoruthenium prodrug and its activation product on colon carcinoma cells, *Metallomics*, 2019, **11**, 118–127.

42 J. M. Hearn, I. Romero-Canelón, A. F. Munro, Y. Fu, A. M. Pizarro, M. J. Garnett, U. McDermott,

N. O. Carragher and P. J. Sadler, Potent organo-osmium compound shifts metabolism in epithelial ovarian cancer cells, *Proc. Natl. Acad. Sci. U. S. A.*, 2015, **112**, E3800–E3805.

43 W. H. Ang, E. Daldini, C. Scolaro, R. Scopelliti, L. Juillerat-Jeannerat and P. J. Dyson, Development of organometallic ruthenium-arene anticancer drugs that resist hydrolysis, *Inorg. Chem.*, 2006, **45**, 9006–9013.

44 M. V. Babak, S. M. Meier, A. A. Legin, M. S. Adib Razavi, A. Roller, M. A. Jakupec, B. K. Keppler and C. G. Hartinger, Am(m)ines make the difference: organoruthenium am(m)ine complexes and their chemistry in anticancer drug development, *Chem.–Eur. J.*, 2013, **19**, 4308–4318.

45 F. Wang, A. Habtemariam, E. P. L. van der Geer, R. Fernández, M. Melchart, R. J. Deeth, R. Aird, S. Guichard, F. P. A. Fabbiani, P. Lozano-Casal, I. D. H. Oswald, D. I. Jodrell, S. Parsons and P. J. Sadler, Controlling ligand substitution reactions of organometallic complexes: tuning cancer cell cytotoxicity, *Proc. Natl. Acad. Sci. U. S. A.*, 2005, **102**, 18269–18274.

46 C. G. Martínez-De-León, R. d. C. Flores Vallejo, A. Rodríguez-Álvarez, M. L. Villareal and J.-M. Grévy, Synthesis, characterization and cytotoxic activity of cationic half-sandwich Ru(II) complexes stabilized by iminophosphorane N,N,S and N,N,Se tridentate ligands, *New J. Chem.*, 2020, **44**, 20676–20687.

47 H. Geisler, D. Wernitznig, M. Hejl, N. Gajic, M. A. Jakupec, W. Kandioller and B. K. Keppler, Novel phthiocol-based organometallics with tridentate coordination motif and their unexpected cytotoxic behaviour, *Dalton Trans.*, 2020, **49**, 1393–1397.

48 H. Geisler, J. Westermayr, K. Cseh, D. Wenisch, V. Fuchs, S. Harringer, S. Plutzar, N. Gajic, M. Hejl, M. A. Jakupec, P. Marquetand and W. Kandioller, Tridentate 3-substituted naphthoquinone ruthenium arene complexes: synthesis, characterization, aqueous behavior, and theoretical and biological studies, *Inorg. Chem.*, 2021, **60**, 9805–9819.

49 C. E. Pereyra, R. F. Dantas, S. B. Ferreira, L. P. Gomes and F. P. Silva-Jr, The diverse mechanisms and anticancer potential of naphthoquinones, *Cancer Cell Int.*, 2019, **19**, 207.

50 K. Cseh, H. Geisler, K. Stanojkovska, J. Westermayr, P. Brunmayr, D. Wenisch, N. Gajic, M. Hejl, M. Schaier, G. Koellensperger, M. A. Jakupec, P. Marquetand and W. Kandioller, Arene variation of highly cytotoxic tridentate naphthoquinone-based ruthenium(II) complexes and in-depth *in vitro* studies, *Pharmaceutics*, 2022, **14**, 2466.

51 É. A. Enyedy, É. Sija, T. Jakusch, C. G. Hartinger, W. Kandioller, B. K. Keppler and T. Kiss, Solution equilibria of anticancer ruthenium(II)-(η6-p-cymene)-hydroxy(thio)pyr(id)one complexes: Impact of sulfur *vs.* oxygen donor systems on the speciation and bioactivity, *J. Inorg. Biochem.*, 2013, **127**, 161–168.

52 W. Kandioller, E. Balsano, S. M. Meier, U. Jungwirth, S. Göschl, A. Roller, M. A. Jakupec, W. Berger, B. K. Keppler and C. G. Hartinger, Organometallic anticancer complexes of lapachol: metal centre-dependent formation of reactive oxygen species and correlation with cytotoxicity, *Chem. Commun.*, 2013, **49**, 3348–3350.

53 J. Hildebrandt, N. Häfner, D. Kritsch, H. Görls, M. Dürst, I. B. Runnebaum and W. Weigand, Highly cytotoxic osmium(II) compounds and their ruthenium(II) analogues targeting ovarian carcinoma cell lines and evading cisplatin resistance mechanisms, *Int. J. Mol. Sci.*, 2022, **23**, 4976.

54 S. Carbon, E. Douglass, B. M. Good, D. R. Unni, N. L. Harris, C. J. Mungall, S. Basu, R. L. Chisholm, R. J. Dodson, E. Hartline, et al., The gene ontology resource: enriching a GOld mine, *Nucleic Acids Res.*, 2021, **49**, D325–D334.

55 D. Szklarczyk, R. Kirsch, M. Koutrouli, K. Nastou, F. Mehryary, R. Hachilif, A. L. Gable, T. Fang, N. T. Doncheva, S. Pyysalo, P. Bork, L. J. Jensen and C. von Mering, The STRING database in 2023: protein–protein association networks and functional enrichment analyses for any sequenced genome of interest, *Nucleic Acids Res.*, 2023, **51**, D638–D646.

56 G. Bjørkøy, T. Lamark, A. Brech, H. Outzen, M. Perander, A. Øvervatn, H. Stenmark and T. Johansen, p62/SQSTM1 forms protein aggregates degraded by autophagy and has a protective effect on huntingtin-induced cell death, *J. Cell Biol.*, 2005, **171**, 603–614.

57 K. Yamamoto, S. D. Scilabra, S. Bonelli, A. Jensen, C. Scavenius, J. J. Enghild and D. K. Strickland, Novel insights into the multifaceted and tissue-specific roles of the endocytic receptor LRP1, *J. Biol. Chem.*, 2024, **300**, 107521.

58 M. Schön, V. Hogenkamp, B. Gregor Wienrich, M. P. Schön, C. Eberhard Klein and R. Kaufmann, Basal-cell adhesion molecule (B-CAM) is induced in epithelial skin tumors and inflammatory epidermis, and is expressed at cell–cell and cell–substrate contact sites, *J. Invest. Dermatol.*, 2000, **115**, 1047–1053.

59 H. Wang, M. Guo, H. Wei and Y. Chen, Targeting p53 pathways: mechanisms, structures and advances in therapy, *Signal Transduct. Target. Ther.*, 2023, **8**, 92.

60 X. Chen, T. Zhang, W. Su, Z. Dou, D. Zhao, X. Jin, H. Lei, J. Wang, X. Xie, B. Cheng, Q. Li, H. Zhang and C. Di, Mutant p53 in cancer: from molecular mechanism to therapeutic modulation, *Cell Death Dis.*, 2022, **13**, 974.

61 X. Chen, H. Guan, X. D. Liu, D. F. Xie, Y. Wang, T. Ma, B. Huang and P. K. Zhou, p53 positively regulates the expression of cancer stem cell marker CD133 in HCT116 colon cancer cells, *Oncol. Lett.*, 2018, **16**, 431–438.

62 J. C. Castle, M. Loewer, S. Boegel, J. de Graaf, C. Bender, A. D. Tadmor, V. Boisguerin, T. Bukur, P. Sorn, C. Paret, M. Diken, S. Kreiter, Ö. Türeci and U. Sahin, Immunomic, genomic and transcriptomic characterization of CT26 colorectal carcinoma, *BMC Genomics*, 2014, **15**, 190.

63 H. Solomon, N. Dinowitz, I. S. Pateras, T. Cooks, Y. Shetzer, A. Molchadsky, M. Charni, S. Rabani, G. Koifman, O. Tarcic, Z. Porat, I. Kogan-Sakin, N. Goldfinger, M. Oren, C. C. Harris, V. G. Gorgoulis and V. Rotter, Mutant p53 gain of function underlies high expression levels of colorectal cancer stem cells markers, *Oncogene*, 2018, **37**, 1669–1684.

64 T. T. Le and M. D. Wang, Topoisomerase II and etoposide — a tangled tale, *Nat. Chem. Biol.*, 2023, **19**, 546–547.
65 D. Menendez, J. R. Anand, C. C. Murphy, W. J. Bell, J. Fu, N. Slepushkina, E. Buehler, S. E. Martin, M. Lal-Nag, J. L. Nitiss and M. A. Resnick, Etoposide-induced DNA damage is increased in p53 mutants: identification of ATR and other genes that influence effects of p53 mutations on Top2-induced cytotoxicity, *Oncotarget*, 2022, **13**, 332–346.
66 D. W. Wu, W. S. Liu, J. Wang, C. Y. Chen, Y. W. Cheng and H. Lee, Reduced p21(WAF1/CIP1) *via* alteration of p53-DDX3 pathway is associated with poor relapse-free survival in early-stage human papillomavirus-associated lung cancer, *Clin. Cancer Res.*, 2011, **17**, 1895–1905.
67 K. Li, S. Chen, K. Wang, Y. Wang, L. Xue, Y. Ye, Z. Fang, J. Lyu, H. Zhu, Y. Li, et al., A peptide-centric local stability assay enables proteome-scale identification of the protein targets and binding regions of diverse ligands, *Nat. Methods*, 2024, **22**, 278–282.
68 M. Sun, T. Zhou, E. Jonasch and R. S. Jope, DDX3 regulates DNA damage-induced apoptosis and p53 stabilization, *Biochim. Biophys. Acta, Mol. Cell Res.*, 2013, **1833**, 1489–1497.
69 D. W. Wu, M. C. Lee, J. Wang, C. Y. Chen, Y. W. Cheng and H. Lee, DDX3 loss by p53 inactivation promotes tumor malignancy *via* the MDM2/Slug/E-cadherin pathway and poor patient outcome in non-small-cell lung cancer, *Oncogene*, 2014, **33**, 1515–1526.
70 J. Mo, H. Liang, C. Su, P. Li, J. Chen and B. Zhang, DDX3X: structure, physiologic functions and cancer, *Mol. Cancer*, 2021, **20**, 38.
71 A. Al Shoyaib, S. R. Archie and V. T. Karamyan, Intraperitoneal route of drug administration: should it be used in experimental animal studies?, *Pharm. Res.*, 2019, **37**, 12.
72 M. H. M. Klose, S. Theiner, C. Kornauth, S. M. Meier-Menches, P. Heffeter, W. Berger, G. Koellensperger and B. K. Keppler, Bioimaging of isosteric osmium and ruthenium anticancer agents by LA-ICP-MS, *Metallomics*, 2018, **10**, 388–396.
73 M. E. Ritchie, B. Phipson, D. Wu, Y. Hu, C. W. Law, W. Shi and G. K. Smyth, LIMMA powers differential expression analyses for RNA-sequencing and microarray studies, *Nucleic Acids Res.*, 2015, **43**, e47.
74 S. Hänzelmann, R. Castelo and J. Guinney, GSVA: gene set variation analysis for microarray and RNA-Seq data, *BMC Bioinform.*, 2013, **14**, 7.
75 A. D. Cherry and C. A. Piantadosi, Regulation of mitochondrial biogenesis and its intersection with inflammatory responses, *Antioxid. Redox Signal.*, 2015, **22**, 965–976.
76 K. R. LeFort, W. Rungratanawanich and B.-J. Song, Contributing roles of mitochondrial dysfunction and hepatocyte apoptosis in liver diseases through oxidative stress, post-translational modifications, inflammation, and intestinal barrier dysfunction, *Cell. Mol. Life Sci.*, 2024, **81**, 34.
77 E. Malle and F. C. De Beer, Human serum amyloid A (SAA) protein: a prominent acute-phase reactant for clinical practice, *Eur. J. Clin. Investig.*, 2003, **26**, 427–435.
78 F. Ceciliani and C. Lecchi, The immune functions of α1acid glycoprotein, *Curr. Protein Pept. Sci.*, 2019, **20**, 505–524.
79 K. Oda, Y. Matsuoka, A. Funahashi and H. Kitano, A comprehensive pathway map of epidermal growth factor receptor signaling, *Mol. Syst. Biol.*, 2005, **1**, 2005.0010.
80 T. L. F. Ho, M. Y. Lee, H. C. Goh, G. Y. N. Ng, J. J. H. Lee, S. Kannan, Y. T. Lim, T. Zhao, E. K. H. Lim, C. Z. J. Phua, et al., Domain-specific p53 mutants activate EGFR by distinct mechanisms exposing tissue-independent therapeutic vulnerabilities, *Nat. Commun.*, 2023, **14**, 1726.
81 S. A. Glynn, G. M. Bol, V. Raman, P. van der Groep, J. F. Vermeulen, A. H. Patel, E. van der Wall and P. J. van Diest, Expression of the RNA helicase DDX3 and the hypoxia response in breast cancer, *PLoS ONE*, 2013, **8**, e63548.

Supporting Information to

Selectivity for TP53 signalling drives the mode of action of a highly potent *N,O,O*-tridentate naphthoquinone-based organoruthenium anticancer drug candidate

Alexander Rosner,[1,2,‡] Lukas Skos,[2,3,‡] Theresa Mendrina,[1,4] Dina Baier,[1,4,5] Michaela Hejl,[1,3] Yasmin Borutzki,[1,2,3] Mathias Gradl,[4] Heiko Geisler,[1] Thomas Mohr,[4,6] Anton Legin,[1] Michael Jakupec,[1,5] Andrea Bileck,[3,6] Christopher Gerner,[3,6] Gunda Koellensperger,[3] Petra Heffeter,[4,5] Walter Berger,[4,5] Bernhard K. Keppler,[1,5] Wolfgang Kandioller,[1,5,] Samuel M. Meier-Menches,[1,3,6,*]*

[1] Institute of Inorganic Chemistry, University of Vienna, Waehringer Str. 42, 1090 Vienna, Austria.

[2] Doctoral School of Chemistry, University of Vienna, Waehringer Str. 38, 1090 Vienna, Austria.

[3] Department of Analytical Chemistry, University of Vienna, Waehringer Str. 38, 1090 Vienna, Austria.

[4] Centre for Cancer Research and Comprehensive Cancer Centre, Medical University Vienna, Borschkegasse 8a, Vienna, 1090, Austria.

[5] Research Cluster "Translational Cancer Therapy Research", Vienna, 1090, Austria.

[6] Joint Metabolome Facility, University of Vienna and Medical University of Vienna, Waehringer Str. 38, 1090 Vienna, Austria.

Table of contents

Materials and methods

Chemicals

2-Hydroxy-3-(morpholinomethyl)naphthalene-1,4-dione[1] (**b**), ruthenium dimer $[RuCl_2(p\text{-cym})]_2$ and osmium dimer $[OsCl_2(p\text{-cym})]_2$ (both dimers ref.[2]) were synthesized in accordance to published procedures. Following chemicals, materials and solvents were used without further purification: ruthenium(III)chloride hydrate (Johnson Matthey), osmium tetroxide (Johnson Matthey), 1*H*-pyrazole (Acros), triethylamine (Fisher/Acros), 25% aqueous ammonium hydroxide solution (Loba), morpholine (Alfa Aesar), 37-41% aqueous formaldehyde solution (Fluka), 2-hydroxy-1,4-naphthoquinone (Acros-Fisher), acetaldehyde (Sigma-Aldrich), L-proline (Merck) and Hantzsch ester (TCI). Methanol (Sigma-Aldrich), ethyl acetate (Riedel-de Haën), ethanol (96%, Brenntag), dichloromethane (DCM) (Sigma-Aldrich) and *n*-hexane (Sigma-Aldrich) were used without further purification. DCM was dried over anhydrous calcium chloride, filtrated and stored over molecular sieve (4 Å) under inert conditions.

Instrumentation

Microwave syntheses were conducted using a Biotage® Initiator+ instrument. Compounds were purified using a Biotage® Isolera™ System with silica packed columns (silica 60, 40–63 µM, Macherey-Nagel). NMR spectra were measured on an AV III HD 700 Bruker BioSpin 700 MHz instrument or an AV III 600 Bruker BioSpin 600 MHz spectrometer. High resolution ESI mass spectra of the metalacycles were recorded at the Mass Spectrometry Center of the University of Vienna (Faculty of Chemistry) on a Bruker maXis ESI-Qq-TOF mass spectrometer. Elemental analyses were performed by the Microanalytical Laboratory of the University of Vienna with a Eurovector EA 3000(2009) equipped with a high temperature pyrolysis furnace (HT, Hekatech, Germany, 2009). Elemental analyses samples were weighed on a Sartorius SEC 2 ultra-micro balance with ±0.1 µg resolution. Sample weights of 1–3 mg were used. For calibration two NIST-certified reference materials were used: sulfanilamide ($C_6H_8N_2O_2S$) and BBOT (2, 5-bis-(5-tert-butyl-2-benzoxazol-2-yl)-thiophenone, $C_{26}H_{26}N_2O_2S$).

The limit of quantification (LOQ) was 0.05 w-% for C, H, N and 0.02 w-% for S. The presented values are the average of determinations in triplicate. UV-Vis spectra were recorded on a Perkin Elmer lambda 35 photometer, PTP (Peltier Temperature Programmer), equipped with a Julabo AWC 100 recirculating cooler.

Ligand synthesis

2-Ethyl-3-hydroxynapthalene-1,4-dione (**a**)

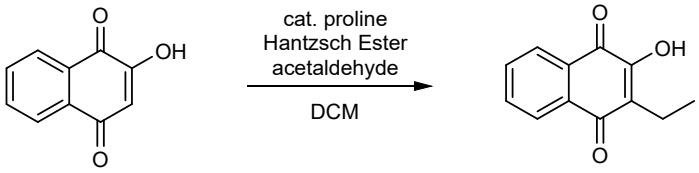

Synthesis of ligand (**a**).

Lawsone (501 mg, 2.88 mmol, 1 equiv.), Hantzsch ester (824 mg, 3.25 mmol, 1.1 equiv.) and acetaldehyde (321 µL, 253 mg, 5.74 mmol, 2 equiv.) were dissolved in dry DCM (20 mL) and stirred for five minutes at r.t.. L-Proline (66 mg, 0.57 mmol, 0.2 equiv.) was added and the yellow suspension was stirred under microwave irradiation (85 °C, 25 min). The resulting dark red organic solution was washed with 1:10 diluted hydrochloric acid and brine. The organic layer was dried over anhydrous sodium sulfate and solvent was removed under reduced pressure. Pure product was obtained *via* column chromatography (silica, gradient 40–80% DCM in *n*-hexane) as a yellow solid (463 mg, 2.29 mmol, 80%).

^{1}H NMR (600 MHz, $CDCl_3$) δ 8.13 (dd, *J* = 7.7, 1.0 Hz, 1H, CH arom. 6/9), 8.08 (dd, *J* = 7.6, 1.1 Hz, 1H, CH arom. 6/9), 7.75 (ddd, *J* = 7.6, 1.3 Hz, 1H, CH arom. 7/8), 7.68 (ddd, 1H, CH arom. 7/8), 7.27 (s, 1H, OH), 2.63 (q, *J* = 7.5 Hz, 2H, CH_2), 1.15 (t, *J* = 7.5 Hz, 3H, CH_3) ppm.

^{13}C NMR (151 MHz, $CDCl_3$) δ 184.7 (4), 181.7 (11), 152.9 (12), 135.0 (7/8), 133.1 (5/10), 133.0 (7/8), 129.6 (5/10), 126.9 (6/9), 126.2 (6/9), 126.1 (3), 16.9 (2), 12.8 (1) ppm.

Complex synthesis

General procedure

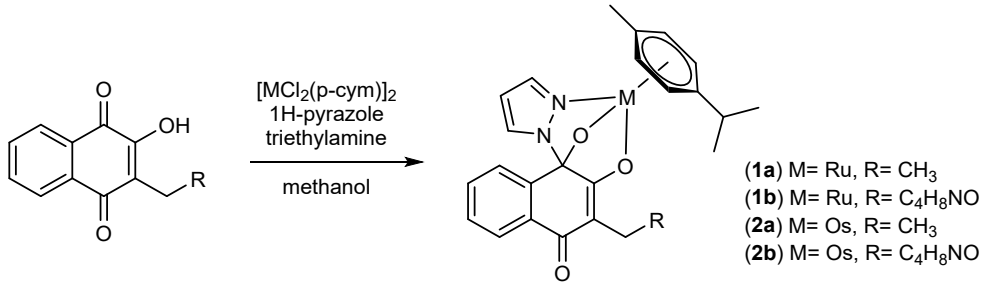

General procedure for synthesis of complexes (**1a**, **2a**, **1b**, **2b**).

The metal dimer (1 equiv.), pyrazole (1.9 equiv.) and the respective naphthoquinone derivative (1.9 equiv.) were dissolved in methanol (12 mL) and triethylamine (6 equiv.) was added. Stirring under microwave irradiation (60 °C, 20 min) was followed by solvent removal under reduced pressure. The crude product was purified *via* column chromatography (silica, isocratic, 70% ethyl acetate, 5% triethylamine in *n*-hexane or 10% methanol, 2% ammonium hydroxide in ethyl acetate). The product fractions were combined and the solvent was removed under reduced pressure. The formed greenish or brown hygroscopic solids were dried at 60 °C *in vacuo*.

[3-Ethyl-4-oxo-(1H-κN^2-pyrazol-1-yl)-1,4-dihydronaphtalene1,2-bis(olato)-κO^1-κO^2)(η^6-p-cymene)ruthenium(II)] (**1a**)

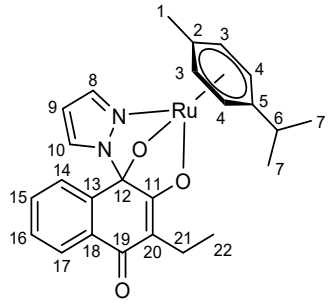

Complex **1a**.

The product was synthesized according to the general procedure, using ruthenium(II) dimer (302 mg, 0.493 mmol, 1 equiv.), 2-ethyl-3-hydroxynaphthalene-1,4-dione **a** (191 mg, 0.944 mmol, 1.9 equiv.), pyrazole (62 mg, 0.906 mmol, 1.8 equiv.) and triethylamine (410 µL, 297 mg, 2.939 mmol, 6 equiv.) in methanol (12 mL). Crude product was purified *via* column chromatography (silica, isocratic 85% ethyl acetate and 5% triethylamine in *n*-hexane). The desired compound was obtained as greenish solid (297 mg, 0.59 mmol, 74%).

^{1}H NMR (700 MHz, MeOD) δ 8.33 (d, 1H, 8), 8.14 – 8.05 (m, 1H, 14), 7.63 – 7.55 (m, 3H, 15–17), 6.68 (dd, J = 2.5, 0.4 Hz, 1H, 10), 6.34 (d, J = 2.4, 2.4 Hz, 1H, 9), 5.97 (d, J = 6.3 Hz, 1H, 4), 5.86 (d, J = 5.5 Hz, 1H, 4), 5.61 (d, J = 3.6 Hz, 2H, 3), 2.87 (hept, J = 6.9 Hz, 1H, 6), 2.41 – 2.34 (m, 1H, 21), 2.33 (s, 3H, 1), 2.32 – 2.26 (m, 1H, 21), 1.34 & 1.33 (s, 3H, 7), 0.88 (t, J = 7.4 Hz, 3H, 22) ppm.

^{13}C NMR (176 MHz, MeOD) δ 183.5 (11 or 19), 183.1 (11 or 19), 141.4 (8), 137.7 (13 or 18), 134.4 (13 or 18), 132.2 (15–17), 131.2 (15–17), 127.9 (10), 127.7 (15–17), 127.1 (14), 112.3 (20), 108.7 (9), 101.3 (5), 98.6 (2), 94.9 (12), 83.3 (4), 82.86 (4), 80.2 (3), 80.1 (3), 32.7 (6), 23.1 (7), 22.8 (7), 18.3 (1), 16.9 (21), 13.7 (22) ppm.

ESI-HR-MS [M+H^{+}] m/z found: 505.1059 (505.1065), [M+Na^{+}] m/z found: 527.0884 (527.0879).

Elemental analysis calculated for $C_{25}H_{26}N_2O_3Ru \cdot 0.35\ H_2O$: C 58.89%, H 5.28%, N 5.49%, O 10.51%;

Found elemental composition: C 58.55%, H 5.26%, N 5.57%, O 10.25%.

[3-(Morpholinomethyl)-4-oxo-(1H-κN^2-pyrazol-1-yl)-1,4-dihydronaphtalene-1,2-bis(olato)-κO^1-κO^2)(η^6-p-cymene)ruthenium(II)] (**1b**)

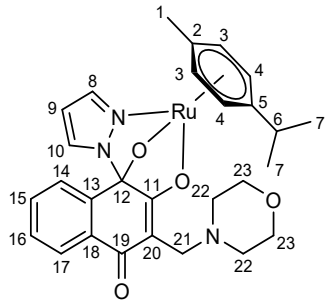

Complex **1b**.

The product was synthesized according to the general procedure, using ruthenium(II) dimer (308 mg, 0.503 mmol, 1 equiv.), 2-hydroxy-3-(morpholinomethyl)naphthalene-1,4-dione **b** (308 mg, 0.967 mmol, 1.9 equiv.), pyrazole (68 mg, 1 mmol, 2 equiv.) and triethylamine (10 µL, 297 mg, 2.939 mmol, 6 equiv.) in methanol (12 mL). Crude product was purified *via* column chromatography (silica, isocratic 10% methanol and 2% ammonium hydroxide in ethyl acetate). The desired compound was obtained as a brownish oil, which solidified during drying *in vacuo* at 60 °C (295 mg, 0.51 mmol, 51%).

^{1}H NMR (600 MHz, MeOD) δ 8.35 (d, J = 2.1 Hz, 1H, 8), 8.14 – 8.09 (m, 1H, 14), 7.67 – 7.61 (m, 3H, 15–17), 6.73 – 6.71 (m, 1H, 10), 6.36 – 6.34 (m, 1H), 9), 5.99 (d, J = 5.9 Hz, 1H, 4), 5.91 (d, J = 6.7 Hz, 1H, 4), 5.64 (d, J = 5.9 Hz, 1H, 3), 5.58 (d, J = 5.9 Hz, 1H, 3), 3.58 – 3.52 (m, 4H, 23), 3.50 (d, *J* = 12.4 Hz, 1H, 21), 3.41 (d, *J* = 12.4 Hz, 1H, 21), 2.86 (hept, J = 6.9 Hz, 1H, 6), 2.45 – 2.35 (m, 2H, 22), 2.33 (s, 3H, 1), 2.27 – 2.20 (m, 2H, 22), 1.34 & 1.33 (d, J = 2.1 Hz, 3H, 7) ppm.

^{13}C NMR (150.95 MHz, MeOD) δ 186.3 (11 or 19), 183.7 (11 or 19), 141.6 (8), 137.7 (13 or 18), 134.0 (13 or 18), 132.6 (15-17), 131.4 (15-17), 128.1 (10), 127.8 (15-17), 127.4 (14), 109.0 (9), 104.3 (20), 100.8 (5), 98.8 (2), 95.0 (12), 83.8 (4), 83.1 (4), 80.1 (3), 78.0 (3), 67.4 (23), 54.0 (22), 50.6 (21), 32.6 (6), 23.2 (7), 22.8 (7), 18.5 (1) ppm.

ESI-HR-MS [M+H$^+$] m/z found: 576.1427 (576.1436).

Elemental analysis calculated for $C_{28}H_{31}N_3O_4Ru \cdot 0.85\ H_2O$: C 57.01%, H 5.59%, N 7.12%, O 13.15%;

Found elemental composition: C 56.73%, H 5.33%, N 7.28%, O 12,94%.

[3-Ethyl-4-oxo-(1H-κN^2-pyrazol-1-yl)-1,4-dihydronaphtalene1,2-bis(olato)-κO^1-κO^2)(η^6-p-cymene)osmium(II)] (**2a**)

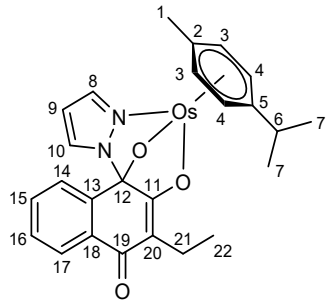

Complex **2a**.

The product was synthesized according to the general procedure, using osmium(II) dimer (200 mg, 0.253 mmol, 1 equiv.), 2-ethyl-3-hydroxynaphthalene-1,4-dione **a** (99 mg, 0.488 mmol, 1.9 equiv.), pyrazole (33 mg, 0.477 mmol, 1.9 equiv.) and triethylamine (212 µL, 154 mg, 1.518 mmol, 6 equiv.) in methanol (12 mL). Crude product was purified *via* column chromatography (silica, isocratic 85% ethyl acetate and 5% triethylamine in *n*-hexane). Desired compound was obtained as a greenish solid (219 mg, 0.37 mmol, 73%).

^{1}H NMR (600 MHz, MeOD) δ 8.29 (d, 1H, 8), 8.16 – 8.11 (m, 1H, 14), 7.66 – 7.59 (m, 3H, 15–17), 6.87 (dd, J = 2.5, 0.4 Hz, 1H, 10), 6.41 – 6.37 (m, 1H, 9), 6.18 (d, J = 5.4 Hz, 1H, 4), 6.09 (d, J = 5.5 Hz, 1H, 4), 5.84 (d, J = 5.5 Hz, 1H, 3), 5.81 (d, J = 5.5 Hz, 1H, 3), 2.74 (hept, 1H, 6), 2.40 (s, 3H, 1), 2.39 – 2.28 (m, 2H, 21), 1.32 & 1.30 (d, J = 1.6 Hz, 3H, 7), 0.88 (t, J = 7.4 Hz, 3H, 22) ppm.

^{13}C NMR (151 MHz, MeOD) δ 183.8 (11 or 19), 183.0 (11 or 19), 141.4 (8), 136.7 (13 or 18), 134.5 (13 or 18), 132.4 (15–17), 131.6 (15–17), 127.8 (15–17), 127.6 (10), 127.3 (14), 112.0

(20), 109.4 (9), 98.2 (12), 91.1 (5), 89.0 (2), 73.8 (4), 73.2 (4), 70.4 (3), 70.3 (3), 33.1 (6), 23.5 (7), 23.1 (7), 18.6 (1), 17.0 (21), 13.6 (22) ppm.

ESI-HR-MS [M+H$^+$] m/z found: 595.1620 (595,1628), [M+Na$^+$] m/z found: 617.1440 (617.1447).

Elemental analysis calculated for $C_{25}H_{26}N_2O_3Os \cdot 0.3\ H_2O$: C 50.20%, H 4.48%, N 4.68%, O 8.83%;

Found elemental composition: C 49.93%, H 4,38%, N 4.68%, O 8.61%.

[3-(Morpholinomethyl)-4-oxo-(1H-κN^2-pyrazol-1-yl)-1,4-dihydronaphtalene-1,2-bis(olato)-κO^1-κO^2)(η^6-p-cymene)osmium(II)] (**2b**)

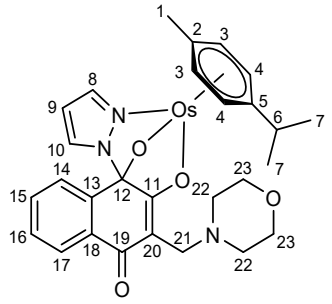

Complex **2b**.

The product was synthesized according to the general procedure, using osmium(II) dimer (202 mg, 0,255 mmol, 1 equiv.), 2-hydroxy-3-(morpholinomethyl)naphthalene-1,4-dione **b** (136 mg, 0.498 mg, 1.9 equiv.), pyrazole (33 mg, 0,485 mmol, 1.9 equiv.) and triethylamine (212 µL, 154 mg, 1.518 mmol, 6 equiv.) in methanol (12 mL). Crude product was purified *via* column chromatography (silica, isocratic 10% methanol and 2% ammonium hydroxide in ethyl acetate). Desired compound was obtained as a brownish oil, which solidified during drying *in vacuo* at 60 °C (178 mg, 0.51 mmol, 51%).

^{1}H NMR (600 MHz, MeOD) δ 8.31 (d, J = 2.2 Hz, 1H, 8), 8.18 – 8.14 (m, 1H, 14), 7.70 – 7.64 (m, 3H, 15–17), 6.92 (d, J = 2.6 Hz, 1H, 10), 6.42 – 6.40 (m, 1H, 9), 6.21 (d, J = 5.5 Hz, 1H,

4), 6.14 (d, J = 5.5 Hz, 1H, 4), 5.86 (d, J = 6.3 Hz, 1H, 3), 5.79 (d, J = 5.5 Hz, 1H, 3), 3.57 – 3.53 (m, 3H, 23), 3.52 – 3.40 (m, 2H, 21), 2.74 (hept, J = 6.9 Hz, 1H, 6), 2.42 – 2.22 (m, 4H, 22), 2.40 (s, 3H, 1) 1.32 & 1.31 (d, J = 1.6 Hz, 3H, 7) ppm.

^{13}C NMR (150.95 MHz, MeOD) δ 186.0 (11 or 19), 184.3 (11 or 19), 141.7 (8), 136.6 (13 or 18), 134.1 (13 or 18), 132.8 (15–17), 131.6 (15–17), 127.8 (15–17), 127.8 (10), 127.6 (14), 109.7 (9), 104.1 (20), 98.4 (12), 90.6 (5), 89.2 (2), 74.5 (4), 73.6 (4), 70.3 (3), 70.2 (3), 67.4 (23), 54.1 (22), 50.7 (21), 33.1 (6), 23.5 (7), 23.2 (7), 18.8 (1) ppm.

ESI-HR-MS [M+H$^+$] m/z found: 666.1994 (665.1920).

Elemental analysis calculated for $C_{28}H_{31}N_3O_4Os \cdot 1.1\ H_2O$: C 49.19%, H 4.90%, N 6.15%, O 11.94%;

Found elemental composition: C 48.87%, H 4.73%, N 6.39%, O 11.71%.

Stability Study by UV-Vis Spectroscopy

All four compounds were freshly diluted in PBS (1% DMSO) from a DMSO stock solution at 20 °C. Compounds **1a**/**2a** were diluted to 40 µM, while compounds **1b**/**2b** were diluted to 80 µM. The stability of the compounds was monitored in a UV-Vis spectrophotometer (Perkin Elmer lambda 35 photometer) over 96 h by acquiring an UV-Vis spectrum every 30 mins. The percentage of the remaining intact compound was calculated by the ratio of the maximum absorbance of the tridentate complexes' characteristic absorption band around 350–370 nm after a given timepoint (A) compared to the one directly after dilution (A_0).

Stability and Reactivity Studies by Mass Spectrometry

All four compounds were freshly prepared at 40 mM in DMSO. They were diluted in H_2O (VWR, LC-MS grade) to obtain 50 µM solutions in triplicates per compound. Thereof, one

aliquot was used for stability testing of the respective test substance in aqueous solution. Another aliquot was spiked with an equimolar ubiquitin solution (50 µM in H_2O) to test the interaction with this protein. Further, an aliquot of each of the four compounds **1a**, **1b**, **2a** and **2b** were equimolarly added (50 µM) to a mixture of three amino acids and two nucleotides (Cys/Met/His/ATP/GTP; each 50 µM in aqueous solution) to test the interaction with small biological nucleophiles. All samples were mixed and incubated in a shaking incubator at 37 °C with speed set to 1000 rpm in the dark (Eppendorf ThermoMixer® C). After 1.5 h, 24 h and 72 h, 300 µL per sample were transferred to fresh reaction vessels, immediately frozen in liquid N_2 and stored at –20 °C until measurement.

Samples were diluted to a concentration of 2.5 µM with an organic eluent (49.5% v/v acetonitrile, 49.5% v/v methanol,1% v/v H_2O), except ubiquitin containing samples which were diluted to the same concentration with acidified H_2O (0.1% v/v formic acid). The samples were then analysed by flow-injection using an amazon speed ETD ion trap (Bruker Daltonics) in the positive ion mode over 0.4 min using the following experimental parameters: HV capillary ±4.5 kV, end plate offset –500 V, dry temp 180 °C, nebulizer 3 bar, dry gas 5 L min^{-1}, scan range *m/z* 200–1400, target mass *m/z* 900, flow rate 5 µL min^{-1}. For ubiquitin containing samples, the scan range was adapted to *m/z* 300–2200 with a target mass of *m/z* 1100. Data was acquired using trapControl (Version 7.1.83.0) and processed using DataAnalysis (Version 4.1.359.0).

Cell cultures

SW480 human colon carcinoma cells were obtained from the American Type Culture Collection (ATCC, Manassas, VA, USA) and cultured in Eagle's minimum essential medium (Sigma Aldrich), supplemented with heat-inactivated fetal bovine serum (10% v/v, Gibco), MEM non-essential amino acid solution 100× (1% v/v, Gibco), sodium pyruvate 100 mM (1% v/v, Gibco), and penicillin−streptomycin solution 100× (1% v/v, Gibco, containing penicillin G sodium salt at 10'000 units mL^{-1} and streptomycin sulphate at 10 mg mL^{-1}). The cells were

cultured in adherent T75 flasks (Sarstedt) in a humidified incubator at 37 °C and 5% CO_2 (HeraCell150i, Thermo Fisher Scientific) and subcultured three times a week as the cells reached 75–80% growth area occupied.

HCT116 human colon carcinoma cells (from ATCC) as well as a p53KO variant thereof (kindly provided by B. Vogelstein, Ludwig Center at Johns Hopkins University, Baltimore, MD, USA) were grown in McCoy's 5A medium (Sigma-Aldrich) supplemented with 4 mM L-glutamine (Sigma-Aldrich) and 10% heat-inactivated foetal bovine serum (Serana, Pessin, Germany). CT-26 murine colon carcinoma cells (from ATCC) were grown in Dulbecco's modified minimum essential medium/Ham's F12 nutrient mix (DMEM/F12, Sigma-Aldrich) supplemented with 4 mM L -glutamine (Sigma-Aldrich) and 10% heat-inactivated foetal bovine serum (Serana). These cell lines were cultured in adherent T75 flasks (Starlab, Hamburg, Germany) in a humidified incubator (Binder CB210) at 37 °C and 5% CO_2 and subcultured twice a week. Trypsin/EDTA solution (0.25%, Sigma-Aldrich) was used for detachment of all cell lines.

Viability assays

SW480 human colon carcinoma cells (4.000 cells/well for the ethyl complexes; 4.000 and 10.000 cells/well for the morpholino complexes) were seeded in flat-bottom 96-well plates (Corning) and incubated at 37 °C for 24 h in a humidified incubator at 5% CO_2 (HeraCell150i, Thermo Fisher Scientific). Stock solutions of the compounds were freshly prepared in DMSO (10 mM **1a**; 10 mM **1b**; 40 mM **2a**; 40 mM **2b**) and diluted to 0.01, 0.05, 0.1, 0.2, 0.5, 1, 5 and 10 µM in complete cell culture medium for the ethyl compounds and 5, 10, 20, 40, 60, 80, 120, 160 µM for the morpholino compounds (final concentration of DMSO ≤0.4% v/v). The cells were incubated with the compounds for 24 h and 72 h. Then, the cell metabolism was colorimetrically determined using 3-(4,5-dimethylthiazol-2-yl)-2,5-diphenyl tetrazolium bromide (MTT). For this purpose, MTT reagent (20 µL, 5 mg mL^{-1} in phosphate-buffered saline, PBS) was added to each well and further incubated for 4 h. The medium was gently

removed and 100 µL DMSO was added to dissolve the formazan crystals. Photometric quantification was performed at 570 nm with a Multiskan Go 1510 photometer (Thermo Fisher Scientific).

The absorbances were blank corrected and converted to relative proliferation. The IC_{50} values (concentration of 50% growth inhibition) were obtained using a sigmoidal fit of the experimental data and calculated as the mean ± standard deviation of at least three independent experiments, each in at least triplicates.

HCT116, HCT116 p53KO (each 2.000 cells/well) and CT-26 cells (500 cells/well) were seeded in 100 µL/well into flat-bottom 96-well plates (Starlab) and incubated at 37 °C for 96 h in a humidified incubator (Binder CB210) at 5% CO_2. The test compound was dissolved in DMSO, serially diluted in the appropriate cell culture medium (see section above) to final DMSO concentrations of ≤0.5% v/v and 100 µL aliquots added to wells in triplicates. After incubation for 96 h, the drug-containing media were replaced with 100 µL/well of a 1 : 6 MTT (in PBS) / RPMI 1640 mixture and plates incubated for 4 h. Then, the supernatants were removed and formazan crystals dissolved in 150 µL of DMSO per well. Optical densities were measured with a microplate reader (ELx808, Biotek) at a wavelength of 550 nm (and a reference wavelength of 690 nm) and blank corrected. The IC_{50} values were interpolated from concentration-effect curves and averaged from at least three independent experiments.

For combination drug testing using **1a** and bafilomycin or bortezomib, SW480 or CT26 cells (each 3.000 cells/well) were seeded in 100 µL/well into flat-bottom 96-well plates (Starlab) and incubated at 37 °C for 24 h in a humidified incubator (Binder CB210) at 5% CO_2. Complex **1a**, bafilomycin or bortezomib were dissolved in DMSO and diluted in appropriate cell culture medium to respective concentrations. After 24 h of treatment, plates were measured by MTT assay as described above.

Cell cycle

Colon carcinoma cells (SW480) were seeded into 12-well plates (CytoOne, Starlab) in densities of 1×10^5 cells per well (in 1 mL complete medium). After 24 h, cells were treated with

different concentrations of **1a**, which was freshly dissolved in DMSO and instantly diluted in medium. Etoposide (causing G2/M phase arrest) and gemcitabine (causing G1/S arrest) were applied as positive controls. Plates were incubated at 37 °C, 5% CO_2 in a moist atmosphere for 24 h. Following the exposure, cells were collected via *trypsinization*, washed with supplemented medium and PBS, and subsequently stained with the DNA-intercalating dye propidium iodide (PI) diluted in hypotonic fluorochrome solution (HFS: 0.1% v/v Triton X-100, 0.1% w/v sodium citrate in H_2O; PI/HFS mixture: 40 µg mL^{-1}, 500 µL per probe). The PI solution was added to the HFS shortly before use and the cells were stained in the dark at 4 °C overnight. The fluorescence of all samples was measured no longer than 20 h after staining by means of flow cytometry (Guava easyCyte 8HT, Millipore).

Proteome profiling of compound-treated SW480 cancer cells

SW480 human colon carcinoma cells were seeded in adherent T25 flasks (Sarstedt) at 2×10^6 cells per well and left to adhere in complete cell culture medium. After 24 h, the medium was exchanged with fresh complete medium (DMSO mock control) or fresh medium containing freshly dissolved compound (0.17 µM **1a**, 0.26 µM **2a**, 34 µM **1b**, 43 µM **2b** from 40 mM stock solution in DMSO, respectively) and incubated for another 24 h. Each condition was carried out in hexuplicates. The cells were processed according to a nucleocytoplasmic fractionation protocol as previously described.[3] All steps were performed on ice. The medium was removed, and the cells were washed twice with 1×PBS (phosphate buffered saline, 3 mL). Then, PBS was thoroughly removed. Isotonic lysis buffer (10 mM HEPES, 10 mM NaCl, 3.5 mM $MgCl_2$, 1 mM EGTA, 0.25 M Sucrose, 0.5% Triton X-100) containing protease inhibitors (1% PMSF, Sigma, and 1% protease and phosphatase inhibitor cocktail, Roche) was added to the flasks, the cells were scraped off and transferred into labelled 15 mL Falcon tubes. The cellular membrane was ruptured using shear stress by pressing the cell suspension through a syringe 9–12 times. Membrane rupture with intact nuclei was monitored under a microscope. After centrifugation (960 g, 5 min), the supernatant containing the cytoplasmic (CYT) proteins was transferred into new tubes containing ice-cold ethanol (1 : 5, HPLC grade) and precipitated

overnight at –20 °C. The pellet containing the nuclei was incubated with a hypertonic solution (10 mM Tris-HCl, 1 mM EDTA and 0.5 M NaCl) and subsequently diluted 1:10 with NP-40 buffer (10 mm Tris-HCl, 1 mm EDTA and 0.5% Triton X-100) containing protease inhibitors (1% PMSF, Sigma, and 1% protease and phosphatase inhibitor cocktail, Roche). After centrifugation (960 g, 5 min), the soluble nuclear (NE) proteins were also transferred into new tubes containing ice-cold ethanol (1 : 5, HPLC grade) and precipitated overnight at –20 °C. The precipitated proteins were finally pelleted by centrifugation (5000 g, 30 min, 4 °C), the solution was decanted and the pellet dried under vacuum.

Samples were then dissolved in lysis buffer (8 M urea, 20% SDS, 1 M TEAB at pH 7.55) and denatured at 95 °C for 5 min. The protein amount was then quantified using a BCA assay. A total of 20 µg protein per sample was used for processing. Proteins were reduced with 50 µL of DTT (64 mM) and carbamidomethylated with 50 µL of iodoacetamide (486 mM). Proteolytic digestion was performed using the ProtiFi S-trap technology.[4] Briefly, samples were loaded onto S-trap mini cartridges followed by the addition of trapping buffer (methanol 90% v/v, 0.1 M TEAB). Afterwards. samples were thoroughly washed and digested with 0.5 µg trypsin/Lys-C mix (Promega) at 37 °C for 2 h (1 : 40 enzyme-to-protein ratio). Peptides were eluted, dried in a SpeedVac and stored at –20 °C.

Immunoblotting

SW480 cells (2×10^6) were seeded in 1 mL medium in 6-well plates in a total volume of 2 mL and allowed to adhere overnight. Cells were treated for 24 h with respective compounds at indicated concentrations. For whole cell lysates, samples were collected, proteins isolated, and Western blotting performed as described in detail previously.[5] In brief, protein concentration was determined using the Micro BCA™ Protein Assay Kit (Thermo Fisher Scientific, Waltham, MA, USA). Proteins were separated using sodium dodecyl sulfate polyacrylamide gel electrophoresis and subsequently transferred onto polyvinylidene difluoride membranes (Thermo Fisher Scientific). Primary antibodies p53 (DO-1) (1 : 200, MS-187-P0) and p21 (12D1) (1 : 800, #2947) were purchased from Thermo Fisher Scientific or

Cell Signaling Technology (Danvers, MA, USA), respectively. Horseradish-peroxidase-linked secondary antibodies, anti-mouse IgG (Fc specific) antibody (#7076S) and anti-rabbit IgG antibody (#7074S) were purchased from Cell Signaling Technology (Danvers, MA, USA). Anti-ß-actin (AC-15) (A5441, 1:2000) was obtained from Sigma-Aldrich (St. Louis, MO, USA). Protein expression was quantified using Image J (version 1.54p).

Immunofluorescence

SW480 and CT26 cells were grown at a density of $6.7x10^4$ cells/mL on 8-well glass coverslips (80841, ibidi GmbH, Gräfelfing, Germany) in 300 µL complete media. The next day, cells were treated with respective compounds for 24 h. Cells were fixed with 4%(v/v) paraformaldehyde for 15 min at RT, followed by washing, blocking and permeabilization with 5%(w/v) BSA and 0.3% (w/v) Triton-X-100 for 60 min. Primary antibodies p53 (DO-1) (1 : 100) or p21 (12D1) (1 : 500) were diluted in 1% BSA-0.3% Triton-X-100 in PBS and incubated overnight at 4 °C. One well was incubated without primary antibody as background control. Cells were washed and stained with secondary goat anti-mouse AlexaFlour-488 (1 : 500 dilution, A-11029, Thermo Fisher Scientific) or goat anti-rabbit AlexaFlour-488 (1 : 500 dilution, A-11034, Thermo Fisher Scientific) antibodies for 1 h at RT. Following, cells were stained with 0.2% Wheat Germ Agglutinin (WGA)-Rhodamine (RL-1022, Vector Laboratories, Inc.) and 0.1% DAPI (62248, Thermo Fisher Scientific) for staining of plasma membrane and nuclei, respectively, according to manufacturer's recommendations. Slides were washed and covered using VECTASHIELD® HardSet™ Antifade Mounting Medium (VECH-1400, Szabo Scandic, Vienna, Austria). Images were acquired on a Zeiss LSM 800 Confocal Laser Scanning Microscope equipped with an Pln Apo 63×/1.4 Oil DICII objective using Zeiss ZEN blue software (version 3.4.91.00000, Carl Zeiss Microscopy GmbH). Laser intensities and detector gains were maintained at the same level during all imaging sessions. Signal intensity calculations and TP53/DAPI weighed co-localization coefficient analysis were done using ImageJ or ZEN blue software, respectively.

Peptide Local Stability Assay

SW480 cancer cells were cultivated in complete medium as above in two T75 adherent flasks. The protein extraction was performed on ice. The flasks were washed twice with PBS (1×, 5 mL) and the wash solution was completely removed. Then, PBS (1×, 2mL, containing 1% PPC) was added in each T75 flak. The cells were scraped off and the cell suspension was transferred to 15 mL falcon tubes. After four freeze-thaw cycles using liquid nitrogen and a water bath (37 °C), the falcons were centrifuged (3500 rpm, 5 min, 4 °C) to pellet cell debris. The clear supernatant was pooled in a 5 mL Eppendorf tube and kept on ice. The protein concentration was determined using a BCA assay as described above and adjusted to 1 µg/µL using PBS (1×, containing 1% PPC). Then, 50 µL (= 50 µg protein) were aliquoted into individual Eppendorf tubes (4x untreated, 4x **1a**-treated, 4x plecstatin-1 treated). Stock solutions of **1a** (50 µM in DMSO) and plecstatin-1 (1 mM in DMSO) were prepared. One microliter of DMSO or compound solution was added to each condition giving final concentrations of **1a** at 1 µM and plecstatin-1 at 20 µM. The 12 samples were incubated for 2 h at 4 °C under constant shaking (800 rpm). Thereafter, partial native trypsinization was performed at an enzyme-to-substrate ratio of 1 : 2.2 with trypsin/LysC (Promega) for 60 s at 37 °C and under constant shaking (1000 rpm). Then, 8M guanidine HCl (165 µL, in 60 mM HEPES, pH 8.2) was added to quench the digestion. The peptidic samples were reduced with tris-(2-carboxyethyl)-phosphine (12 µL, 200 mM) and alkylated with 2-chloroacetamide (12 µL, 800 mM). The samples were heated to 95 °C for 5 mins under constant shaking (1400 rpm). The sample solutions were then concentrated in a SpeedVac until reaching around 50 µL, diluted with 100 µL styrenedivinylbenzene-reverse phase sulfonate (SDB-RPS) loading buffer (99% iPrOH, 1% TFA) and finally desalted *via* SDB-RPS StageTips. This step also removes undigested proteins. Peptides were eluted with freshly prepared SDB-RPS elution buffer (2.4 mL ACN, 1.6 mL H_2O, 20 µL NH_4OH), completely dried in a SpeedVac and stored at –20 °C.

In vivo Experiments

Animals. All experiments were carried out with male Balb/c mice according to the regulation of the Ethics Committee for the Care and Use of Laboratory Animals at the Medical University Vienna (BMWF-2022-0.770.291), the guidelines from the Austrian Animal Science Association and the Federation of European Laboratory Animal Science Associations (FELASA). The animals were kept in a pathogen-free conditions, controlled environment with 12 h light–dark cycle with *ad libitum* access to food and water. Every procedure was done in a laminar airflow cabinet.

Treatment. CT-26 cells (5×10^5 in 50 µL serum-free medium) were injected subcutaneously (s.c.) into the right flank of ten– to eleven-week-old male Balb/c mice. Three days after cell injection, all compounds (dissolved in 10% DMSO in water) were administered intraperitoneally (i.p.) in a concentration of 10 mg/kg in case of **1a**/**2a** and 30 mg/kg in case of **1b**/**2b**. Regarding anticancer activity experiments, mice were treated on 5 consecutive days over 2 weeks. Four hours after the last treatment **1a**-treated mice were sacrificed and analysed for ruthenium levels in tissue *via* ICP-MS measurements. In case of the proteomic profiling experiment, mice were treated with **1a** in a concentration of 10 mg/kg dissolved in 10% DMSO in water for 5 consecutive days. On the last day, 2 h after the last treatment, mice were euthanized, and blood was collected in an EDTA tube via heart punctation. Tumours and livers were harvested, quickly rinsed with PBS and snap-frozen in liquid nitrogen. Blood plasma was obtained by centrifugation (2×10 min at 900 g). Samples were stored at –80 °C until processing.

Histological evaluation. Liver tissues from mice treated for 5 days (control and **1a**) were fixed in 4% formaldehyde (Carl Roth, #P087.3) after dissection, paraffin-embedded and sliced in 3.5 µm thick sections. Hematoxylin and eosin (H&E) staining was performed as previously described in Feldman and Wolfe *et al.*,[6] followed by scanning with a 3D Histech Microscopic High Throughput slide scanner for Brightfield. The Papanicolaou's solution 1a Harris'

hematoxylin solution as well as the Eosin Y disodium salt were purchased from MERCK. The Scott's solution was bought from Morphisto.

Sample Processing. All steps were performed on ice. The frozen tissue samples (weights ranging from 8.6–51.5 mg) were transferred to 15 mL Falcon tubes containing 150 µL sodium deoxycholate lysis buffer (SDC; 0.4 g SDC, 500 µL Tris·HCl (pH 8.8) in 9.5 mL H_2O) and homogenized with a sonication probe (Bandelin Sonoplus HD 2070; Bandelin Electronic GmbH & Co. KG, Berlin, Germany). After sonication the homogenates were centrifuged at 10.000 g for 5 minutes and the resulting supernatant was transferred to new reaction tubes. Tissue samples were diluted at a ratio of 1 : 10, heated at 95 °C for 5 min and stored at –20 °C. EDTA-anticoagulated plasma samples were diluted in SDC buffer at a ratio of 1 : 20, heated at 95 °C for 5 min and stored at –20 °C. The protein concentration of each sample was determined using a BCA assay. The proteolytic digestion was performed according to an in-solution protocol.[7] Twenty µg of protein was reduced and alkylated with 10 µL of a mixture containing 100 mM tris(2-carboxyethyl)phosphine (TCEP) and 400 mM 2-chloroacetamide (2-CAM) for 5 min at 45 °C, followed by 18 h digestion with Trypsin/Lys-C (1:100 enzyme-to-substrate ratio) at 37 °C. Next, samples were concentrated in a vacuum concentrator, diluted with 100 µL styrenedivinylbenzene-reverse phase sulfonate (SDB-RPS) loading buffer (99% iPrOH, 1% TFA) and then desalted *via* SDB-RPS StageTips. Peptides were eluted with freshly prepared SDB-RPS elution buffer (2.4 mL ACN, 1.6 mL H_2O, 20 µL NH_4OH), completely dried in a SpeedVac and then stored at –20 °C.

nLC-MS/MS Analysis

Nano-LC-MS/MS analysis was performed as described previously.[8] Briefly, dried samples in glass inserts were dissolved with 5 µL of a peptide standard mix consisting of four synthetic peptides at 10 fmol in 30% formic acid (Glu1-fribrinopeptideB, EGVNDNEEGFFSAR; M28, TTPAVLDSDGSYFLYSK; HK0, VLETKSLYVR and HK1, VLETK(ε-Ac)SLYVR) and diluted

with loading buffer (40 µL, acetonitrile 2% v/v, TFA 0.05% v/v; ddH_2O 97.95% v/v). The glass inserts were transferred into 2 mL Eppendorf tubes filled with 400 µL ddH_2O, sonicated for 5 min (20% power), centrifuged (5000 g, 7 min, RT) and transferred into labelled HPLC vials. MS data was acquired employing a timsTOF Pro mass spectrometer (Bruker Daltonics, Bremen, Germany) hyphenated to a Dionex UltiMate™ 3000 RSLCnano system (Thermo Scientific, Bremen, Germany). Samples were analysed using data-dependent acquisition and label free quantification (LFQ) shotgun proteomics in PASEF mode.[9] From each sample 5 µL were loaded on an Acclaim™PepMap™ C18 HPLC pre-column (2 cm × 100 µm, 100 Å, Thermo Fisher Scientific™, Vienna, Austria) at a flow rate of 10 µL min^{-1}. After trapping, peptides were eluted at a flow rate of 300 nL min^{-1} and chromatographic separation was achieved on an Aurora series CSI UHPLC emitter column (25 cm × 75 µm, 1.6 µm C18, Ionopticks, Fitzroy, Australia) applying a gradient from 7–40% of mobile phase B (79.9% ACN, 20% H2O, 0.1% FA) in mobile phase A (99.9% H2O, 0.1% FA). For *in vitro* samples and *in vivo* tissue proteomics, a gradient over 90 min was used giving a total run time of 135 min per sample. In vivo plasma samples were analysed using a 43 min gradient giving a total run time of 85 min. Additionally, *in vivo* samples were measured in technical duplicates.

Data processing and analysis

Raw data obtained from the timsTOF Pro MS was processed based on LFQ proteomics by MaxQuant (Version 1.6.17.0),[10] including the built-in Andromeda search engine, and searched against the UniProt Database.[11] Separate searches for the *in vitro* and *in vivo* data sets were conducted by using a fasta-file for the human proteome (version 11/2021, 20'375 entries) and a fasta-file for the mouse proteome (version 06/2021, 17'519 entries), respectively. Only non-redundant Swissprot entries with at least two identified peptides per protein were used for identifying protein groups. The first and main search peptide tolerance was 50 and 25 ppm, respectively. The false discovery rate (FDR) was fixed to 0.01 on the peptide and protein level. Match between runs was enabled with an alignment time window of 0.7 min. Oxidation of methionine and N-terminal acetylation were set as variable modifications whereas

carbamidomethylation of cysteines was set as fixed modification. The statistical evaluation was performed with Perseus (Version 1.6.14)[12] using LFQ intensities of the MaxQuant result file. After filtering potential contaminants the LFQ values were Log(2)-transformed. Prior to Log(2)-transformation, the mean of the *in vivo* technical duplicates was calculated. Only those protein groups were considered for data evaluation, which were detected at least five times in at least one condition. Missing data points were imputed. Permutation-based FDR was set to 0.05 and S0 = 0.1 for multi-parameter corrected significance testing of protein regulation. The final dataset was further analysed using the web-based applications DAVID bioinformatics Resources (Version 6.8)[13] and STRING (Version 10.0).[14]

Additionally, statistical analysis of protein regulations from the *in vivo* samples was performed using the LIMMA R-package.[15] P-values where adjusted according to Benjamini-Hochberg[16] and a gene set variation analysis was performed (GSVA).[17] Protein Sets where constructed using the molecular signature database.[18]

ICP-MS Analysis

Total metal content in organs harvested from **1a**-treated mice was determined by inductively coupled plasma mass spectrometry (ICP-MS) on an Agilent 7800 instrument and Agilent SPS 4 autosampler using the following parameters: RF power 1550, carrier gas (Ar) 1.08 $L \cdot min^{-1}$, plasma gas (Ar) 15 $L \cdot min^{-1}$, dwell time 0.1 s, 12 replicates with 100 sweeps. A nickel cone was used and ^{101}Ru, ^{115}In and ^{185}Re isotopes were monitored. Data was processed by Agilent MassHunter (Version C.01.04) software.

All ^{101}Ru-values were blank corrected. The lower limit of quantification of the method was 0.071 µg L^{-1}. Organs, tumour and blood were digested with nitric acid (20% w/w) and diluted with ultrapure water to reach a final nitric acid concentration <4%.

Supplemental ^{1}H- and ^{13}C-NMR spectra for compound characterization

2-Ethyl-3-hydroxynapthalene-1,4-dione (**a**)

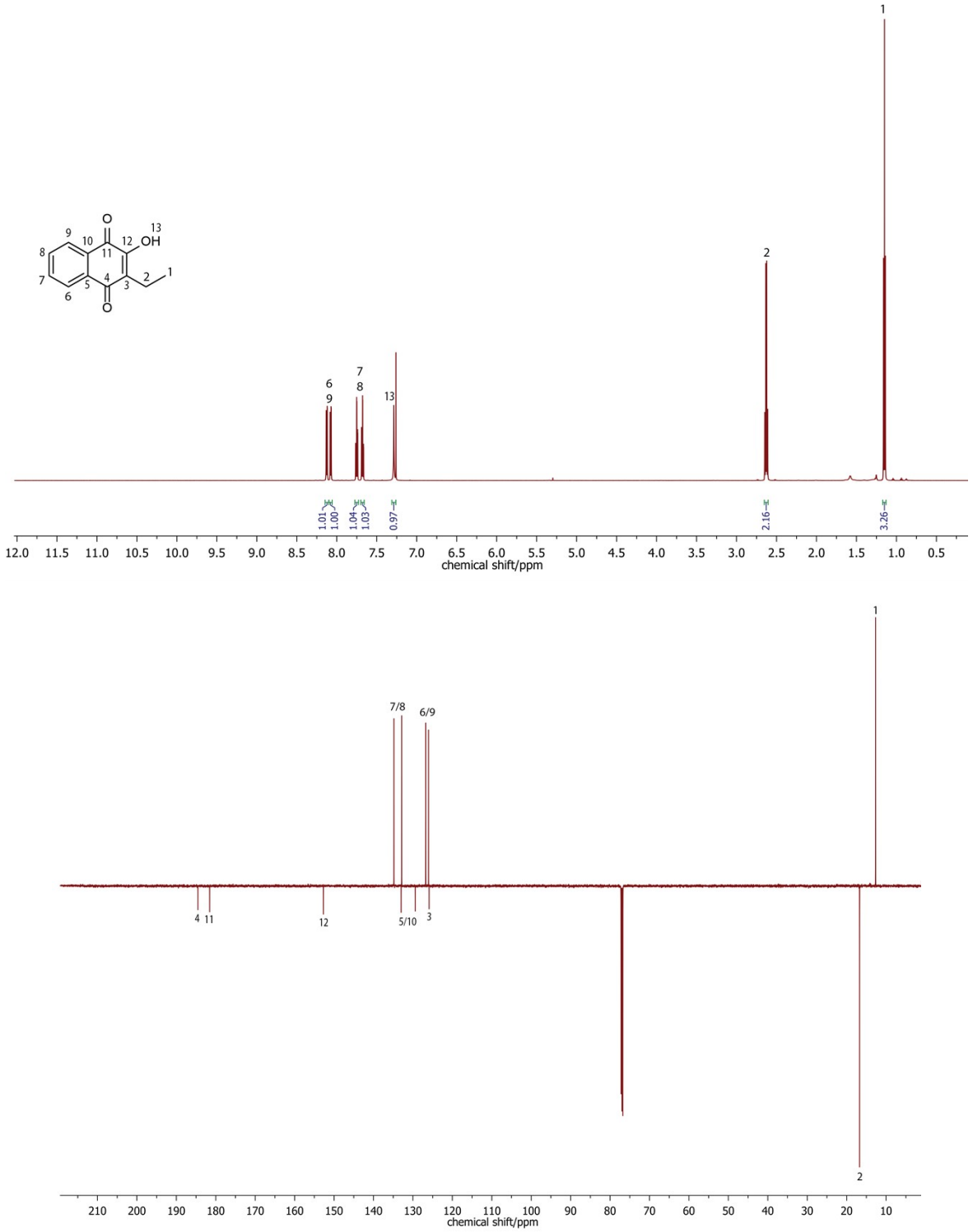

Suppl. Figure S1. Structure and atom numbering (above), ^{1}H-NMR (centre) and ^{13}C-NMR (below) in $CDCl_3$.

[3-Ethyl-4-oxo-(1H-κN^2 -pyrazol-1-yl)-1,4-dihydronaphtalene1,2-bis(olato)-κO^1-κO^2)(η^6-p-cymene)ruthenium(II)] (**1a**)

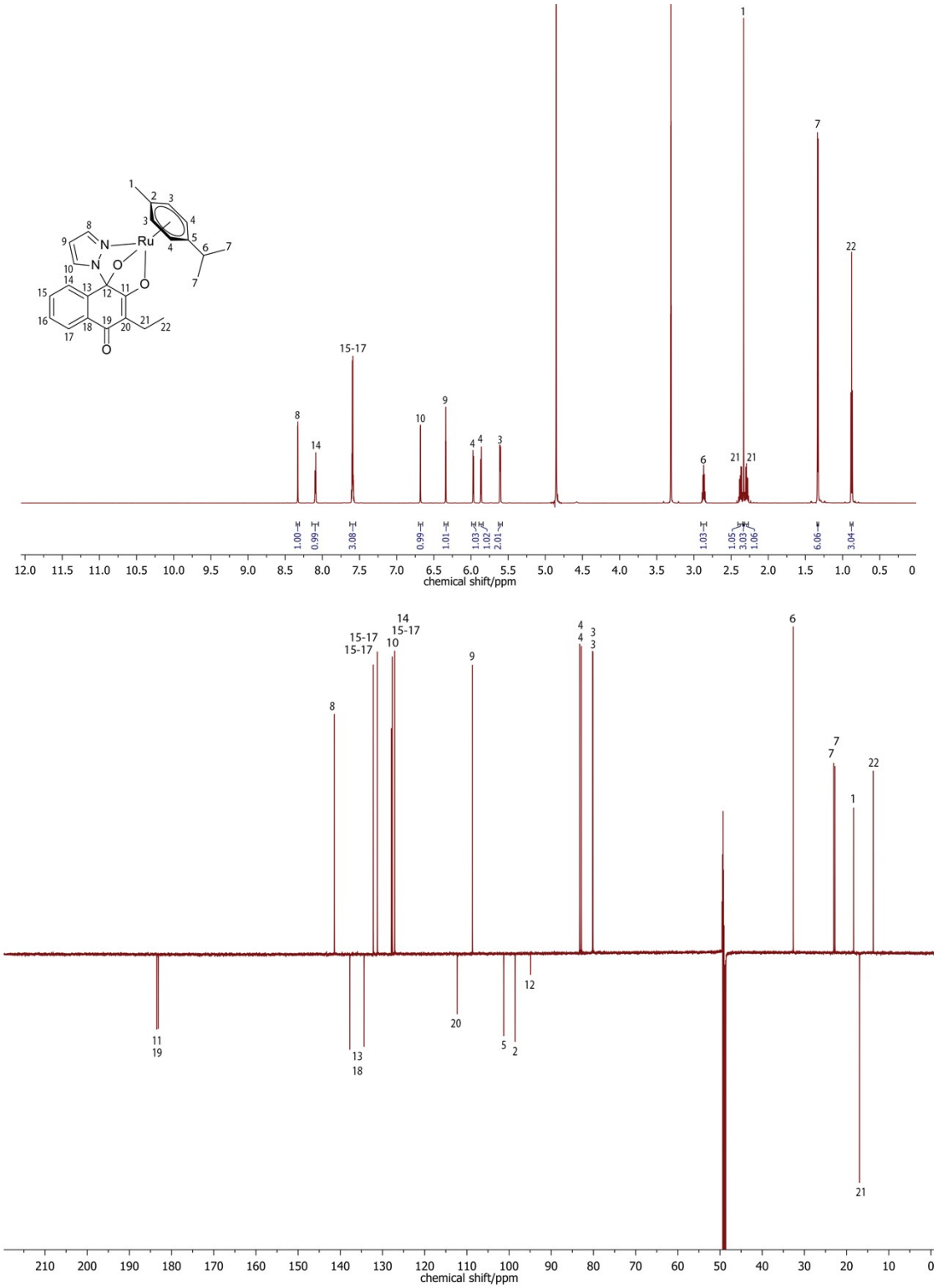

Suppl. Figure S2. Structure and atom numbering (above), ^{1}H-NMR (centre) and ^{13}C-NMR (below) of complex (**1a**) in MeOD.

[3-(Morpholinomethyl)-4-oxo-(1H-κN^2-pyrazol-1-yl)-1,4-dihydronaphtalene-1,2-bis(olato)-κO^1-κO^2)(η^6-p-cymene)ruthenium(II)] (**1b**)

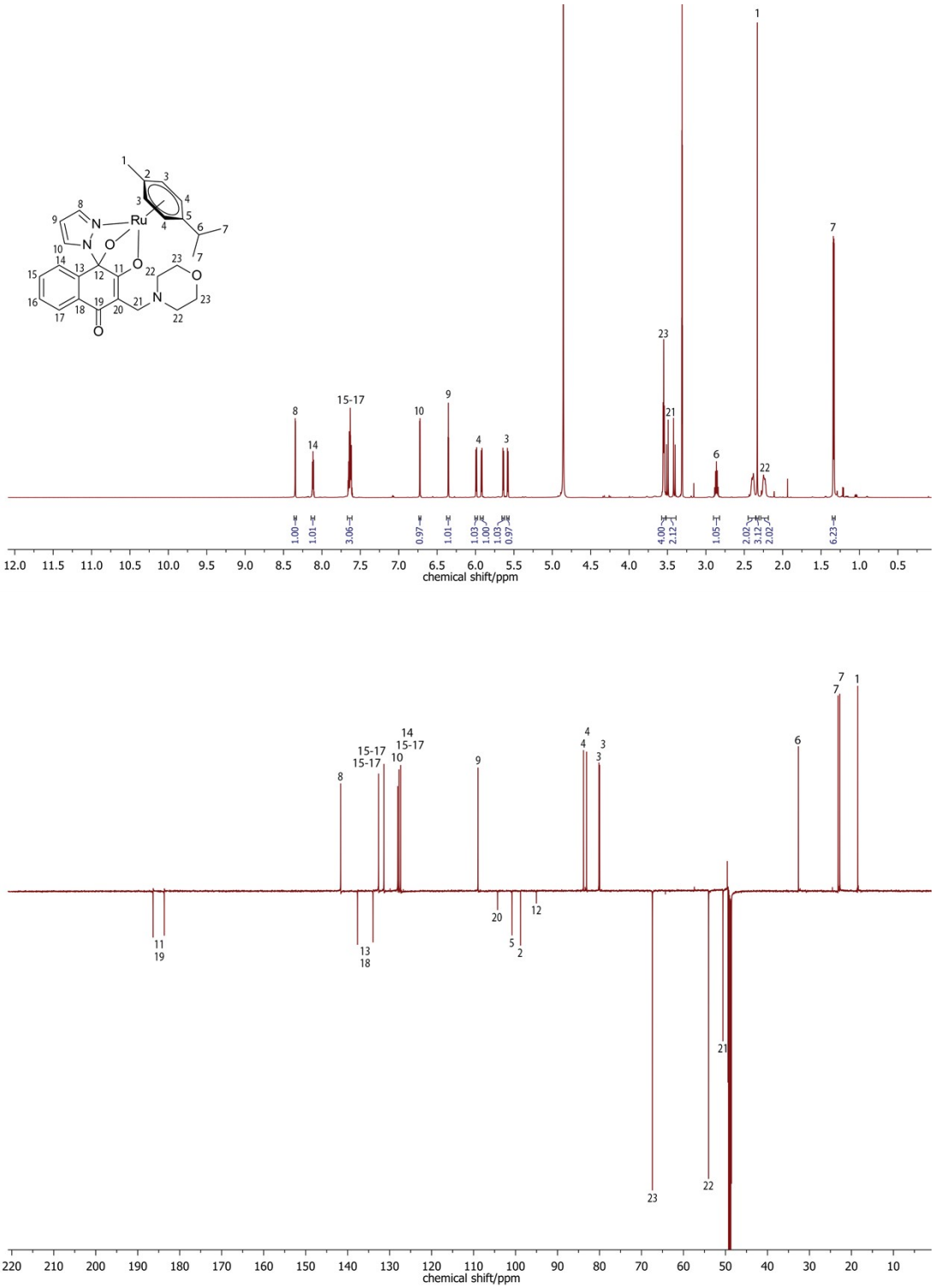

Suppl. Figure S3. Structure and atom numbering (above), ^{1}H-NMR (centre) and ^{13}C-NMR (below) of complex (**1b**) in MeOD.

[3-Ethyl-4-oxo-(1H-κN^2-pyrazol-1-yl)-1,4-dihydronaphtalene1,2-bis(olato)-κO^1-κO^2)(η^6-p-cymene)osmium(II)] (**2a**)

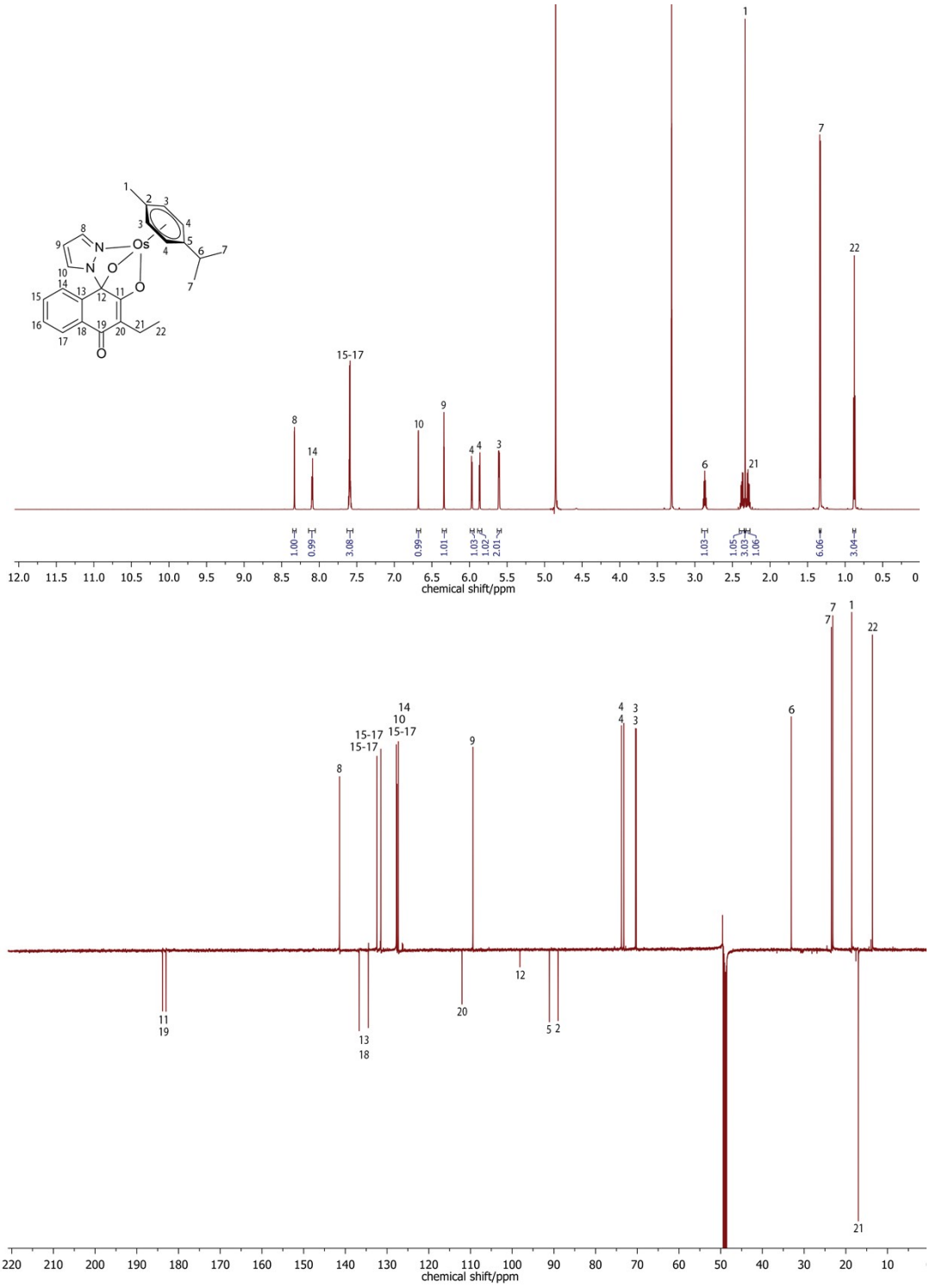

Suppl. Figure S4. Structure and atom numbering (above), ^{1}H-NMR (centre) and ^{13}C-NMR (below) of complex (**2a**) in MeOD.

[3-(Morpholinomethyl)-4-oxo-(1H-κN^2-pyrazol-1-yl)-1,4-dihydronaphtalene-1,2-bis(olato)-κO^1-κO^2)(η^6-p-cymene)osmium(II)] (**2b**)

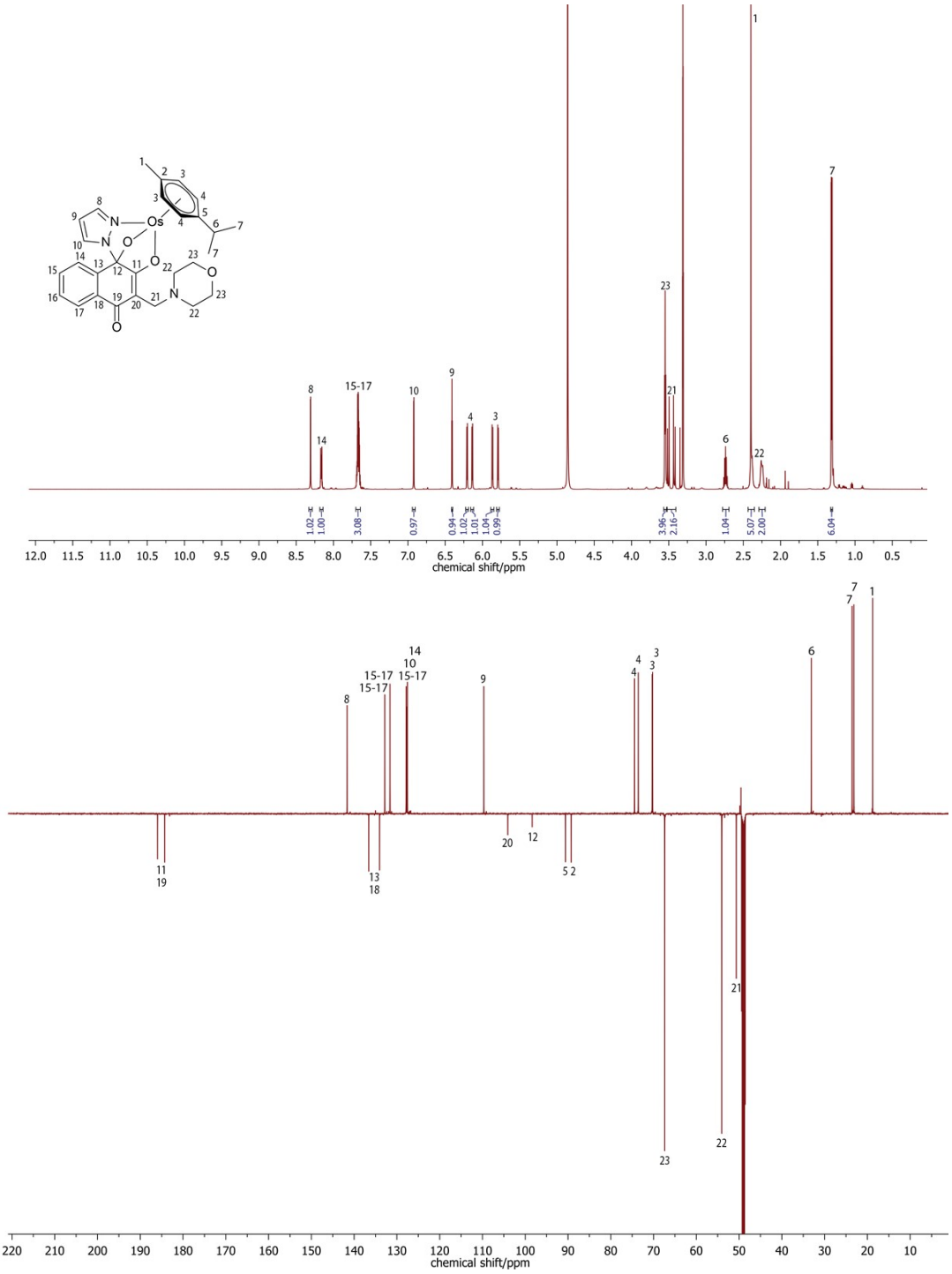

Suppl. Figure S5. Structure and atom numbering (above), ^{1}H-NMR (centre) and ^{13}C-NMR (below) of complex (**2b**) in MeOD.

Supplemental ESI-MS spectra for compound characterization

[Ethyl-4-oxo-(1H-κN^2-pyrazol-1-yl)-1,4-dihydronaphtalene1,2-bis(olato)-κO^1-κO^2)(η^6-p-cymene)ruthenium(II)] (**1a**)

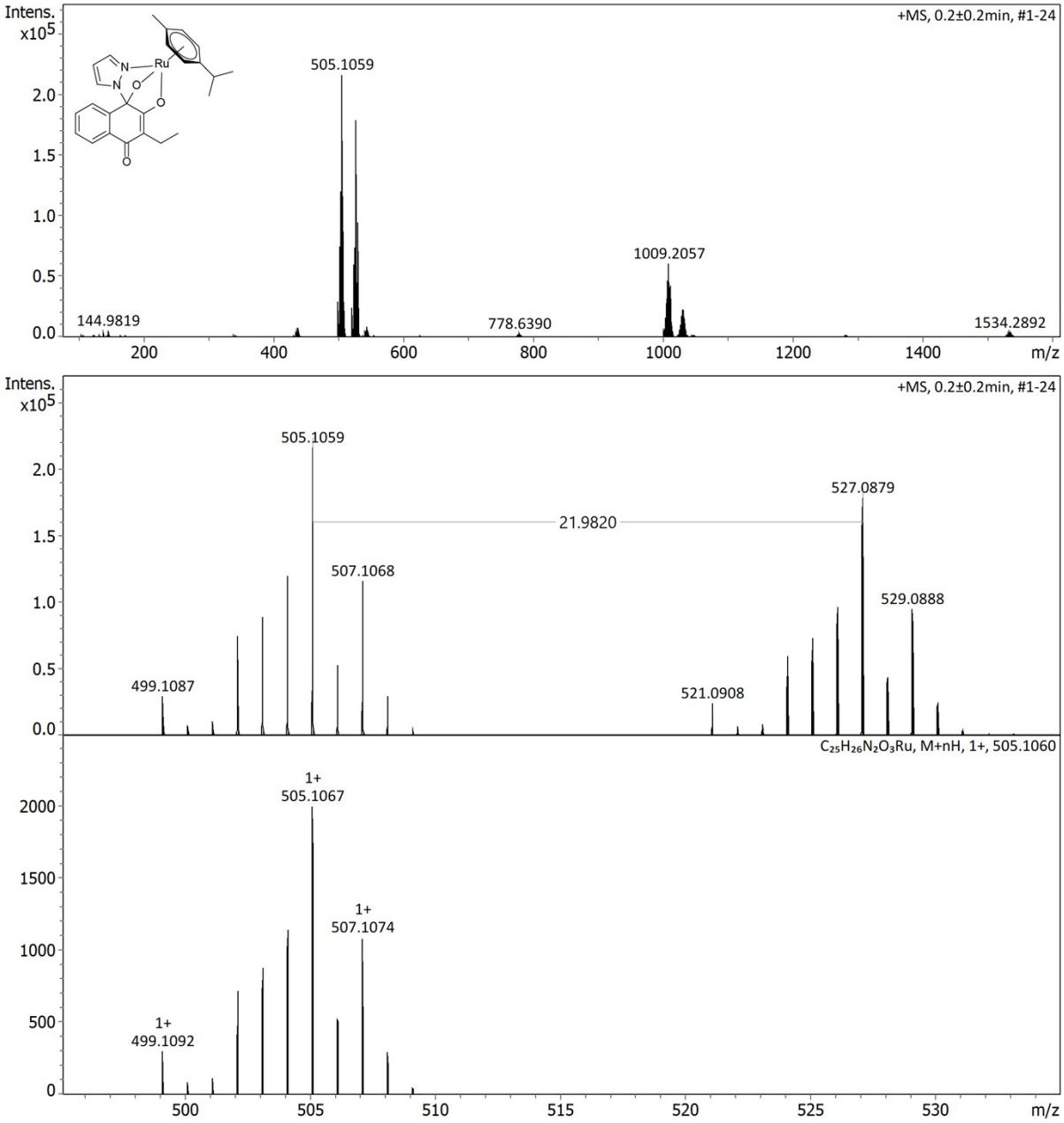

Suppl. Figure S6. HRMS spectrum of complex (**1a**)**.**

[3-(Morpholinomethyl)-4-oxo-(1H-κN^2-pyrazol-1-yl)-1,4-dihydronaphtalene-1,2-bis(olato)-κO^1-κO^2)(η^6-p-cymene)ruthenium(II)] (**1b**)

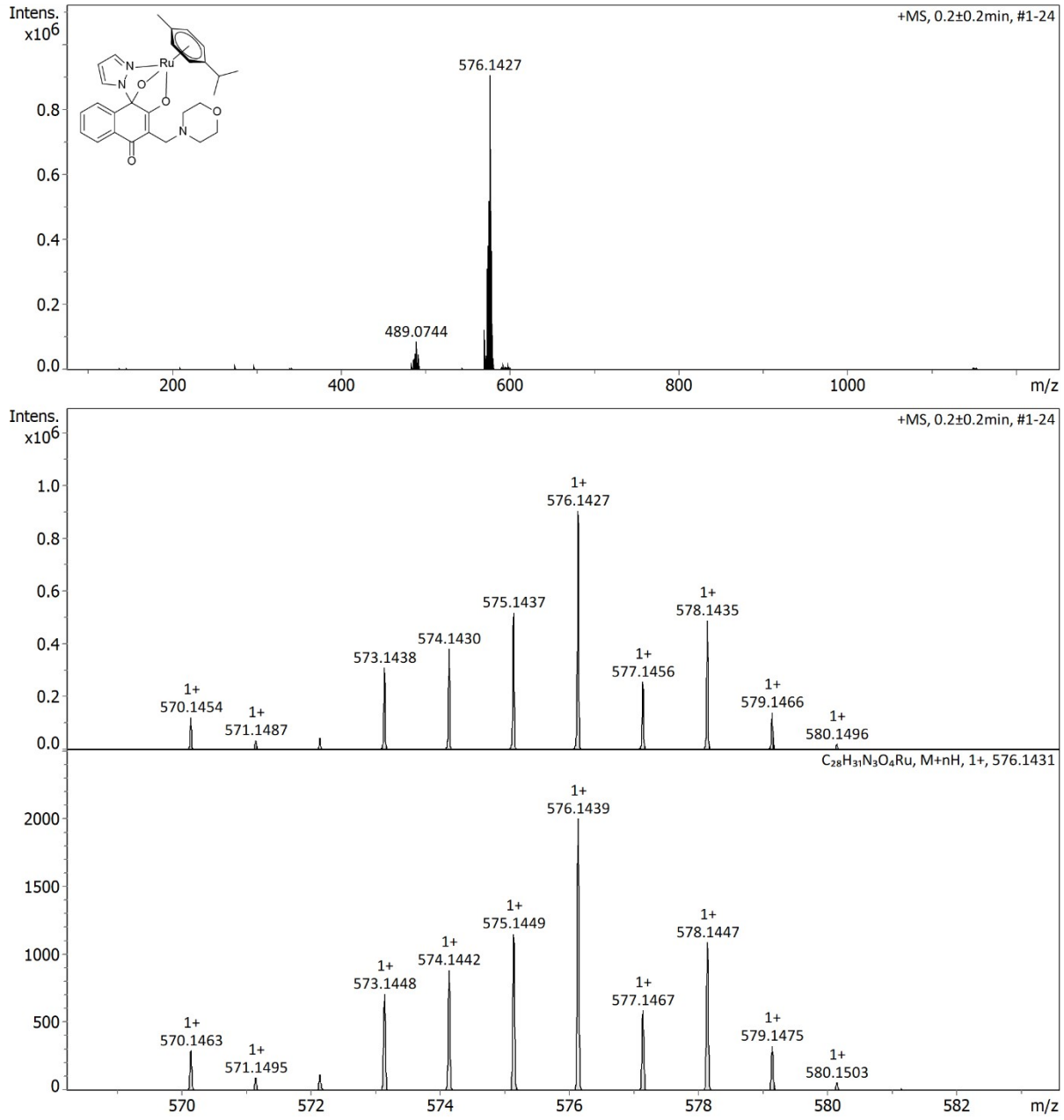

Suppl. Figure S7. HRMS spectrum of complex (**1b**).

[Ethyl-4-oxo-(1H-κN^2-pyrazol-1-yl)-1,4-dihydronaphtalene1,2-bis(olato)-κO^1-κO^2)(η^6-p-cymene)osmium(II)] (**2a**)

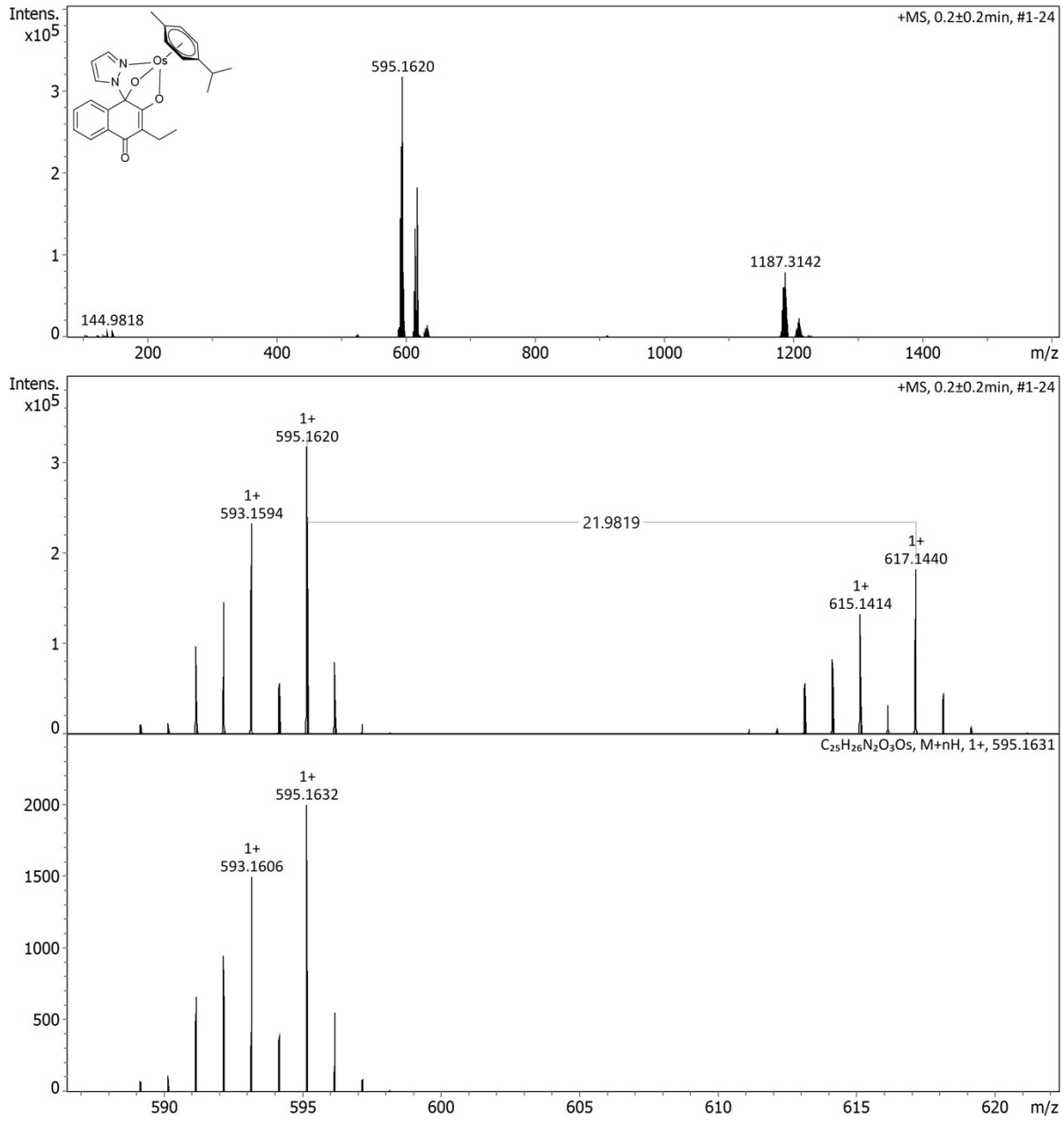

Suppl. Figure S8. HRMS spectrum of complex (**2a**).

[3-(Morpholinomethyl)-4-oxo-(1H-κN^2-pyrazol-1-yl)-1,4-dihydronaphtalene-1,2-bis(olato)-κO^1-κO^2)(η^6-p-cymene)osmium(II)] (**2b**)

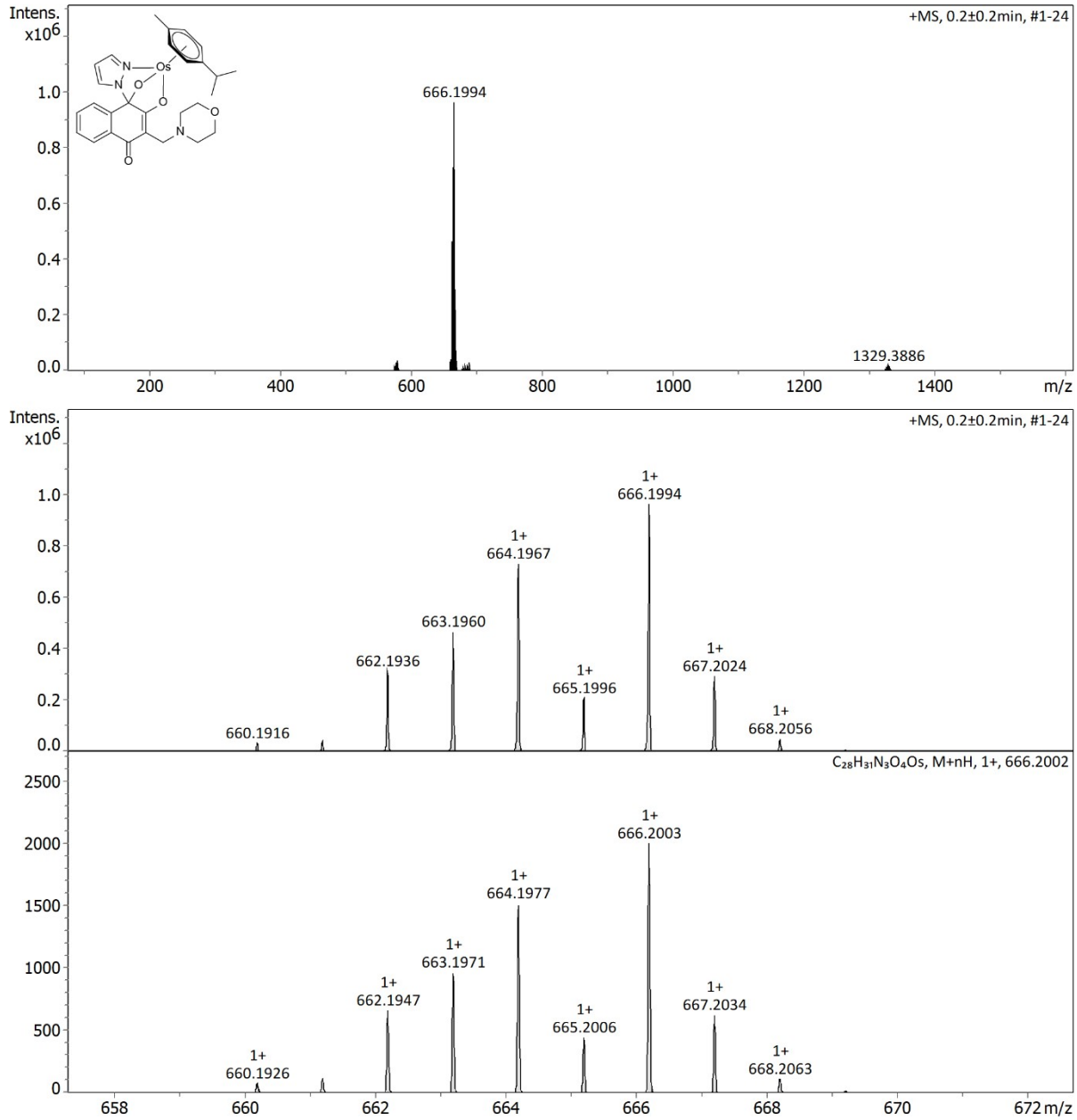

Suppl. Figure S9. HRMS spectrum of complex (**2b**).

Supplemental Figures

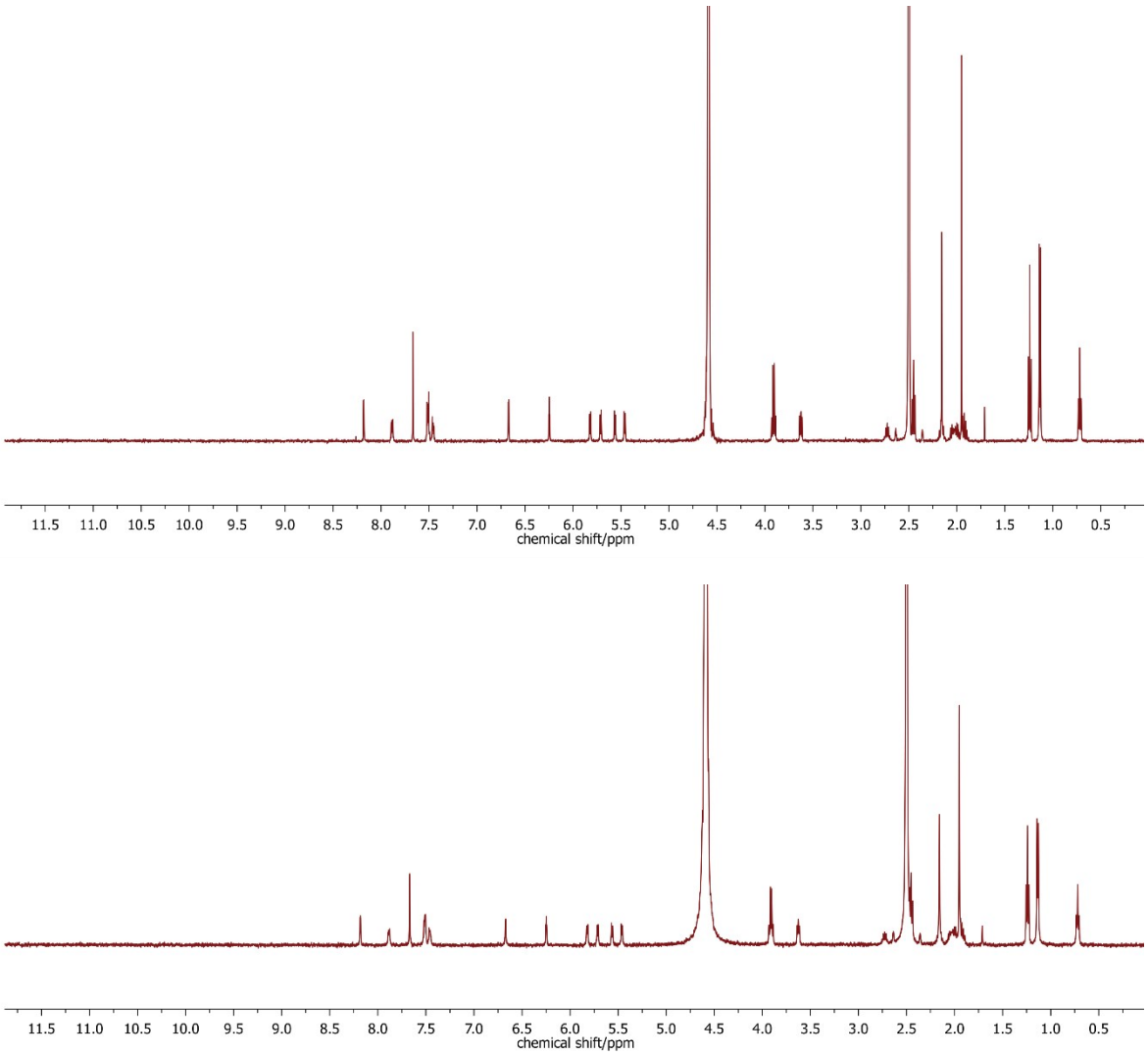

Suppl. Figure S10. Representative spectra of complex **1a**, 9-ethylguanine and methionine in D_2O/20% DMSO at 0 h (above) and after 1.5 h (below).

(A)

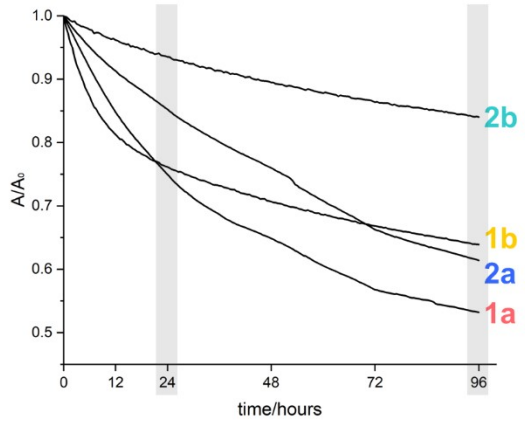

Intact complex [%(A/A0)]	24 h	96 h
2b	94	84
1b	76	64
2a	85	61
1a	75	53

(B)

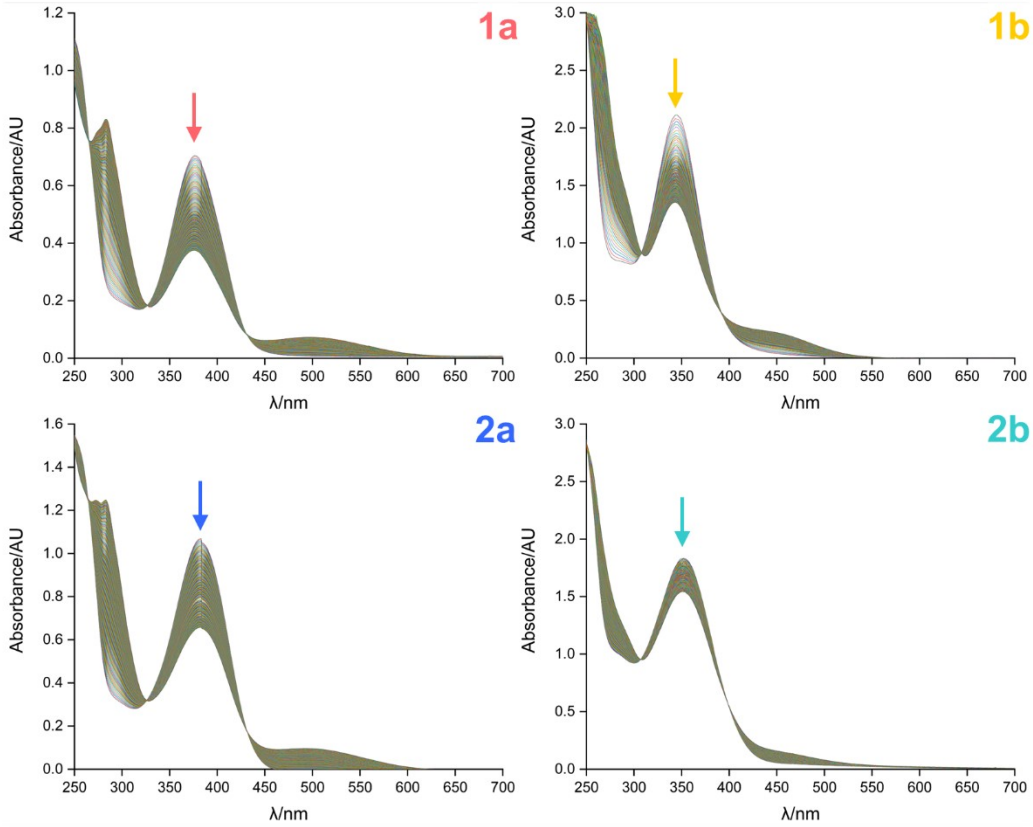

Suppl. Figure S11. UV-Vis stability studies of **1a**/**2a** at 40 µM and **1b**/**2b** at 80 µM in PBS (1% DMSO) over the course of 96 h. UV-Vis spectra were acquired every 30 min over the entire incubation period. (**A**) Time-dependent percentage of the remaining intact compound at the absorption maximum of around 350–370 nm with 24 h and 96 h highlighted. (**B**) Individual kinetic UV-Vis spectra over 96 h.

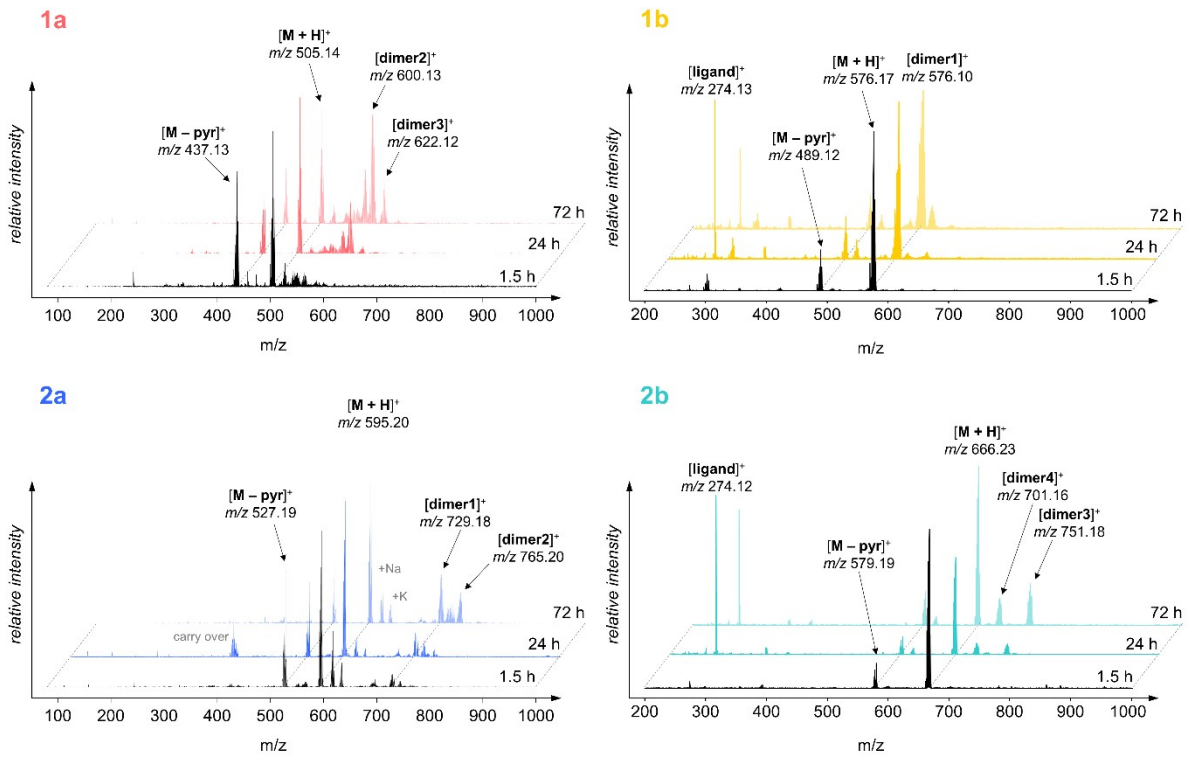

Suppl. Figure S12. ESI-MS spectra of the incubation of the four metal(arene) compounds in aqueous solution. Mass spectra were acquired after 1.5 h, 24 h and 72 h. Identified mass signals are annotated. Dimers refer to different dinuclear metal(arenes) with diverse bridging ligands, including pyrazole.

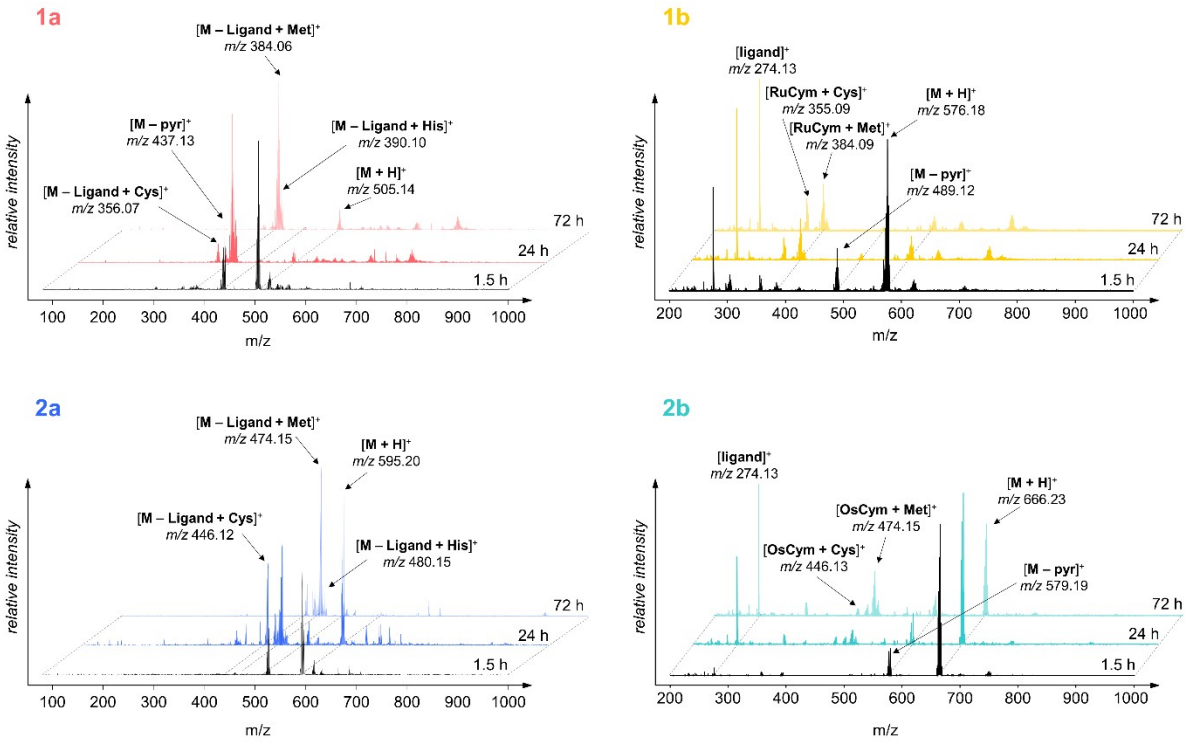

Suppl. Figure S13. ESI-MS spectra of the incubation of the four metal(arene) compounds of this study at equimolar concentration with a mixture of cysteine (Cys), methionine (Met), histidine (His), adenosine triphosphate (ATP) and guanosine triphosphate (GTP). Mass spectra were acquired after 1.5 h, 24 h and 72 h. Identified mass signals are annotated.

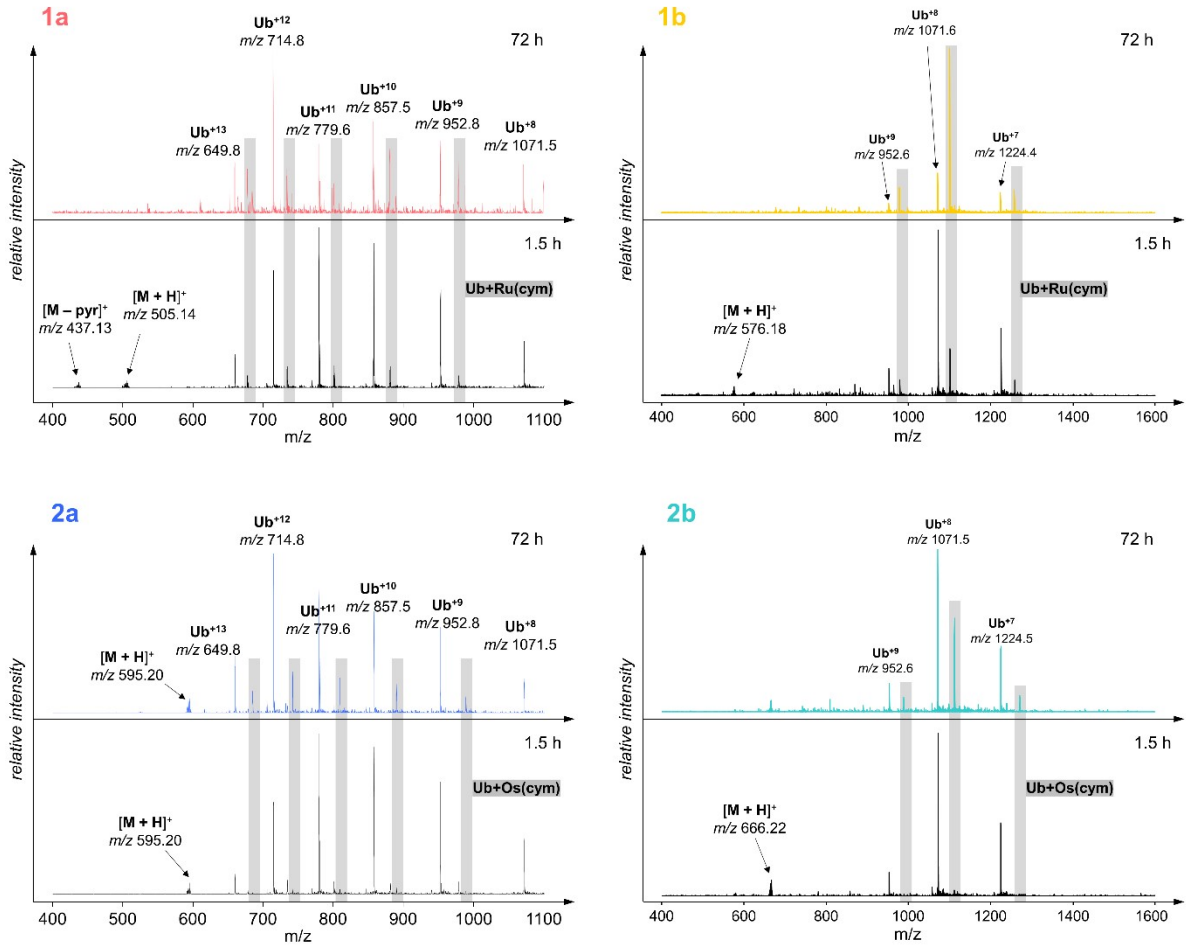

Suppl. Figure S14. ESI-MS spectra of the incubation of the four metal(arene) compounds of this study with an equimolar concentration of ubiquitin. Mass spectra are shown after 1.5 h and 72 h of incubation and metal(arene) adducts are highlighted in grey background. Intact compounds were observed after 1.5 h.

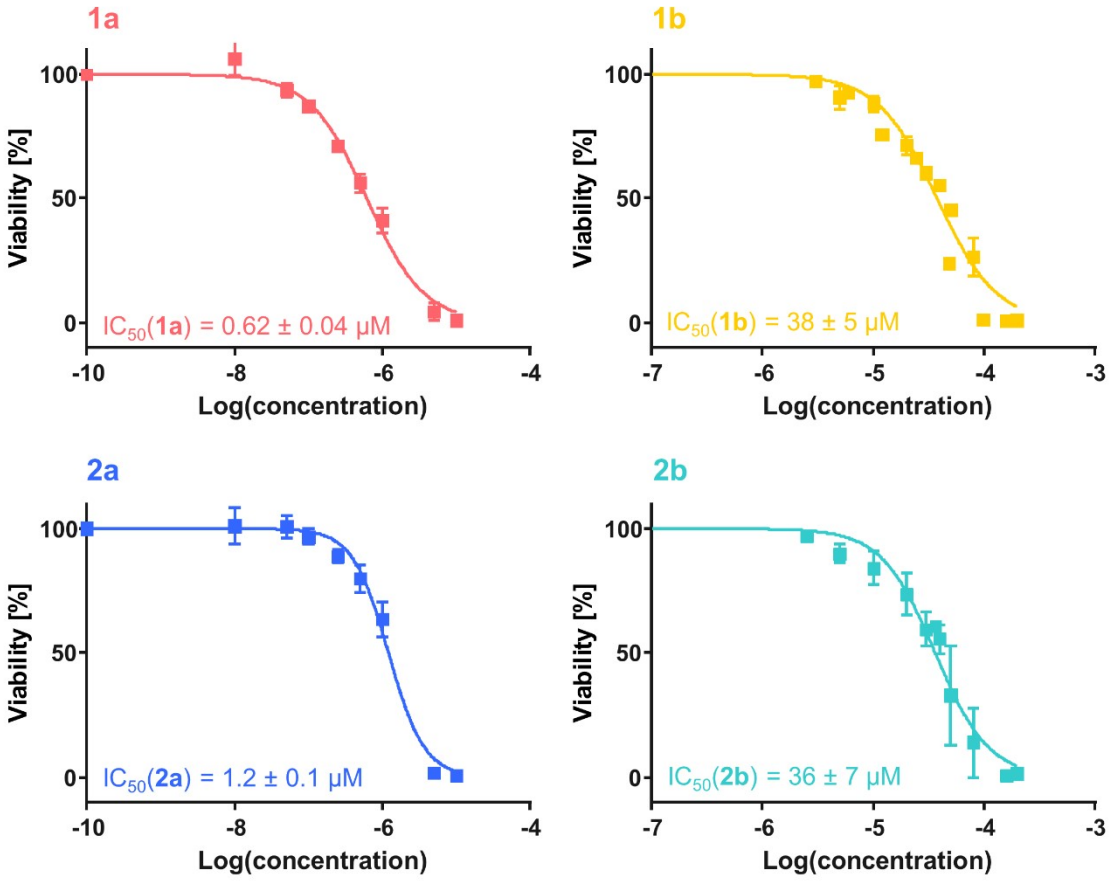

Suppl. Figure S15. Concentration-effect curves of **1a**, **1b**, **2a** and **2b** after a 24 h incubation of SW480 colon carcinoma cells. A total of 4000 cells were seeded per well for experiments with **1a** and **2a** and a total of 10'000 cells were seeded per well for experiments with **1b** and **2b**. The IC_{50} values are presented as the mean ± standard deviation of at least three independent experiments, each in at least three replicates.

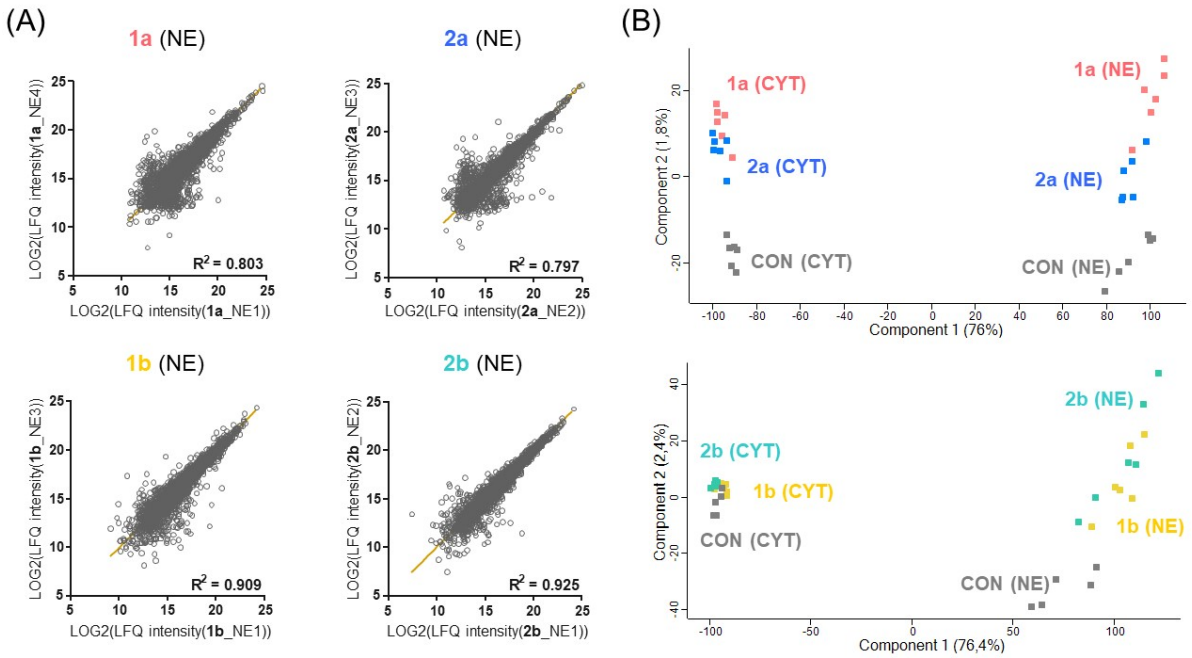

Suppl. Figure S16. Qualification of the proteomic profiling experiments. (**A**) Scatter plots show the precision of two representative replicates (out of six) of nuclear extracts (NE) representing the last step of fractionation. (**B**) Perturbations with **1a**/**2a** and **1b**/**2b** were carried out against their own solvent-treated controls (CON). The principle component analysis shows the pairs **1a**/**2a** and **1b**/**2b** against their respective controls. Each square represents a sample of either cytoplasmic (CYT) or NE fractions.

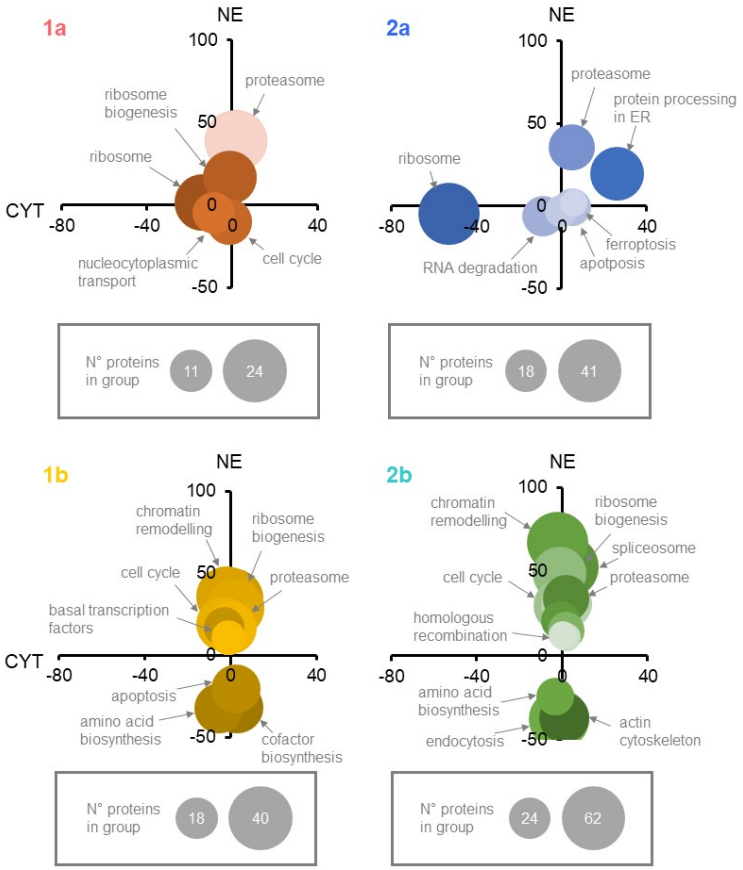

Suppl. Figure S17. (**A**) Regulomes showing KEGG pathways affected by the treatment of in SW480 cancer cells with the four compounds. The axes depict the cytoplasmic (CYT) and nuclear (NE) subcellular space.

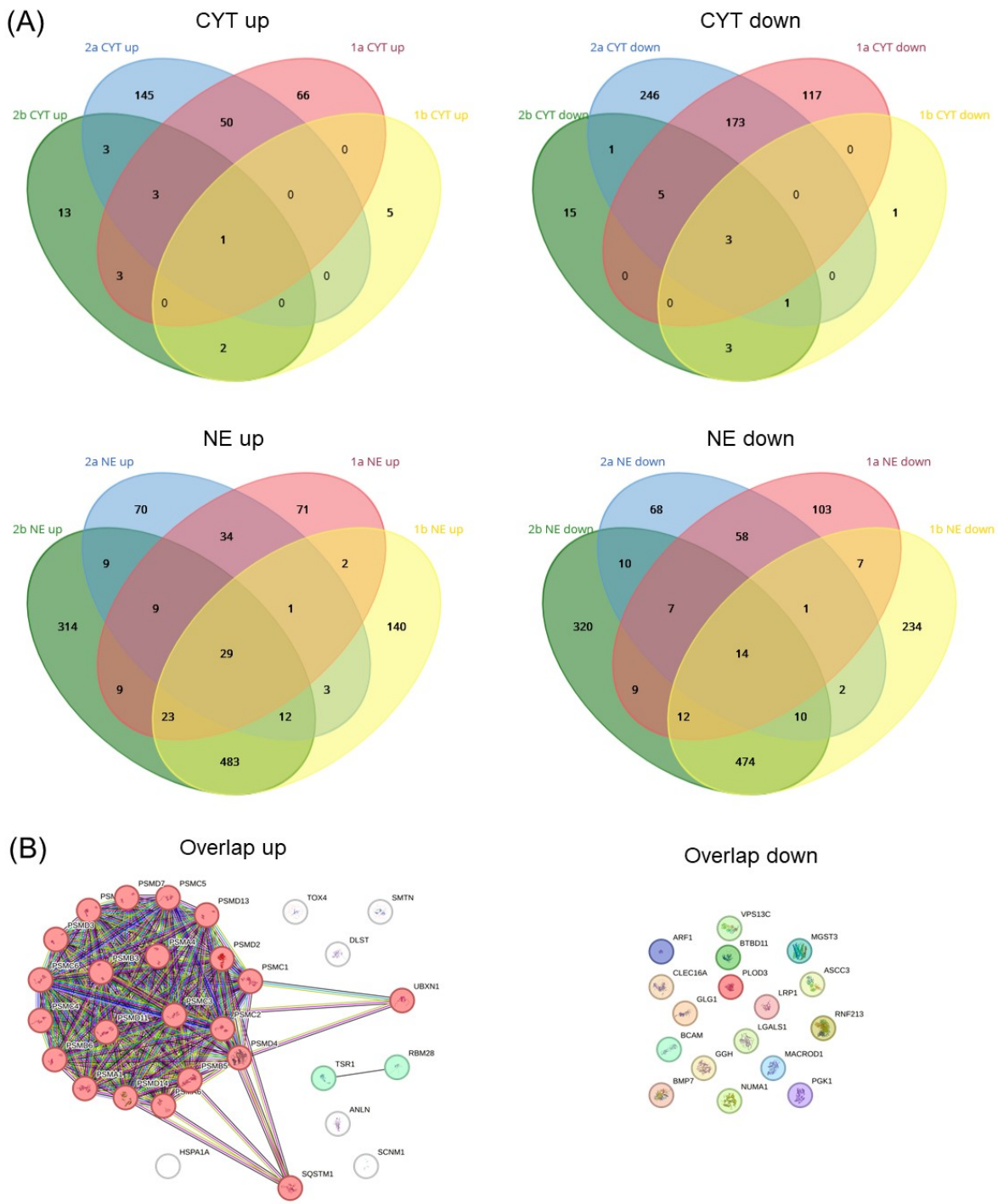

Suppl. Figure S18. (**A**) VENN diagrams showing the shared significantly proteins of each treatment according to cytoplasmic (CYT) and nuclear (NE) fractions and direction of regulation. up = up-regulated; down = down-regulated. (**B**) STRING network of the shared proteins of all four treatments according to upregulated (*left*) and down-regulated (*right*) proteins.

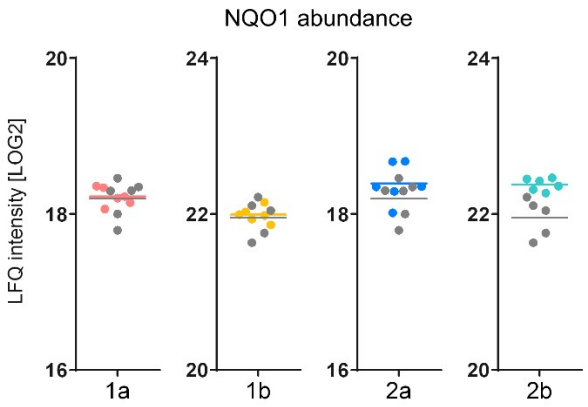

Suppl. Figure S19. Regulation of NQO1, the target of hydroxy-naphthoquinones, in SW480 cancer cells upon treatment with the compounds of this study after 24 h. Control samples are shown in grey and the treated samples are coloured.

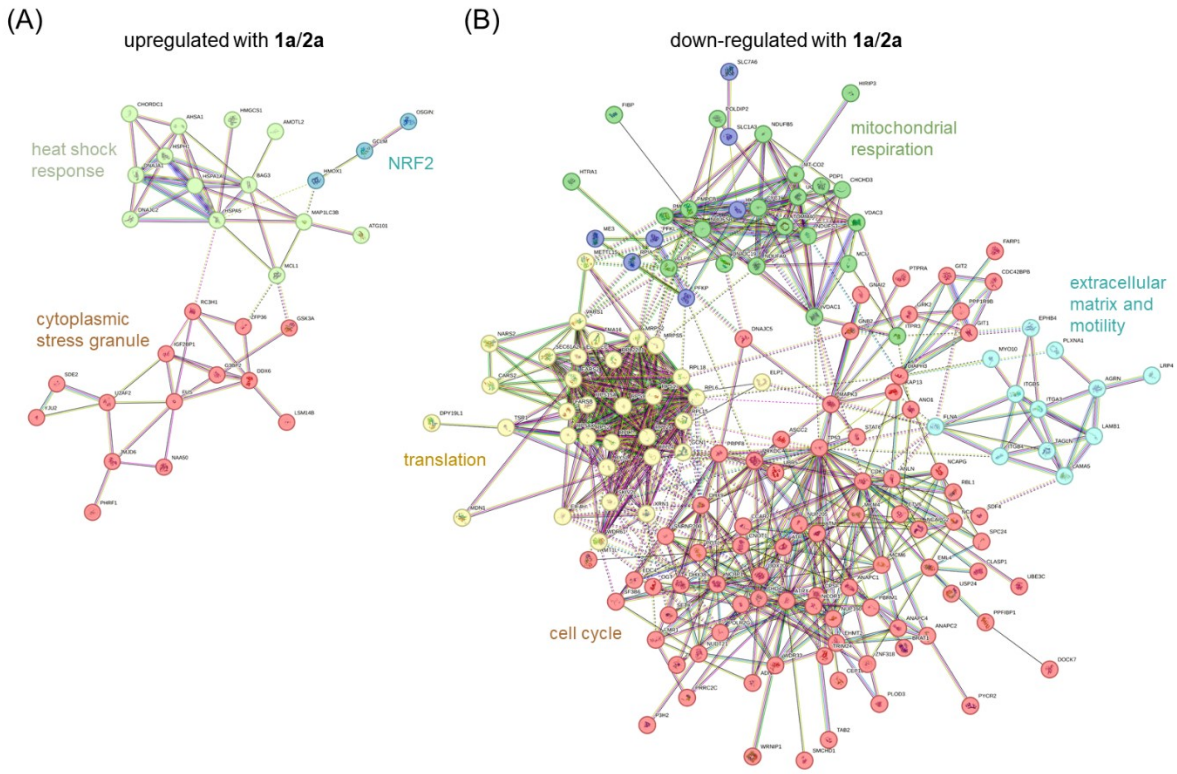

Suppl. Figure S20. (**A**) STRING network analysis of the shared upregulated proteins of **1a** and **2a** treated SW480 cancer cells in both the CYT and NE fractions. (**B**) STRING network analysis of the shared down-regulated proteins of **1a** and **2a** treated SW480 cancer cells in both the CYT and NE fractions.

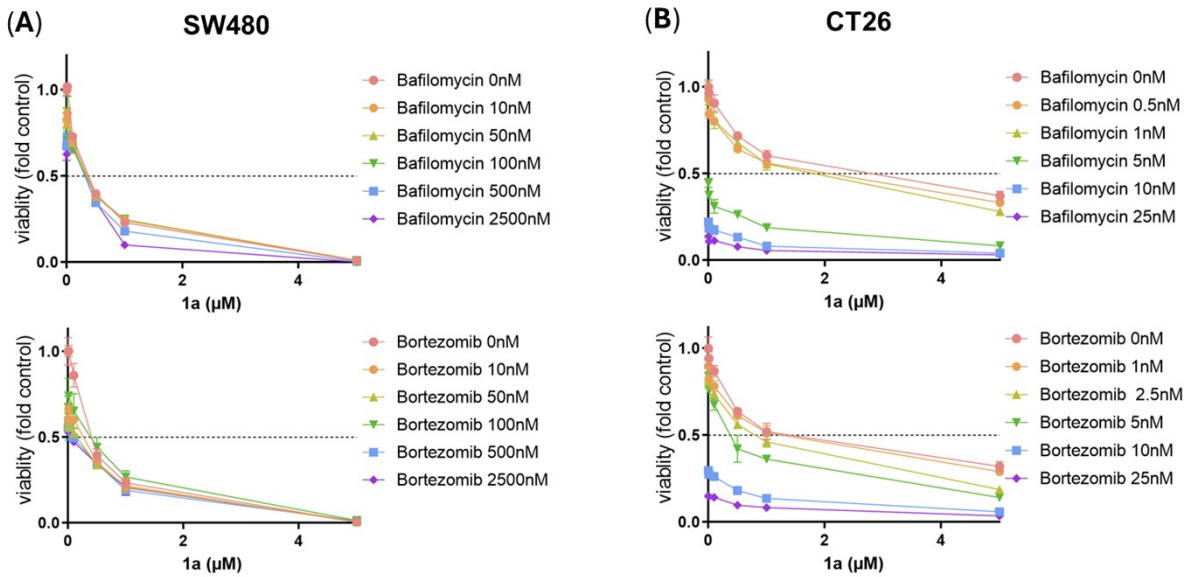

Suppl. Figure S21. Dose-response curves of **1a** in combination with bafilomycin or bortezomib after 24 h incubation of (**A**) SW480 or (**B**) CT26 cells. One representative of at least three independent experiments is shown.

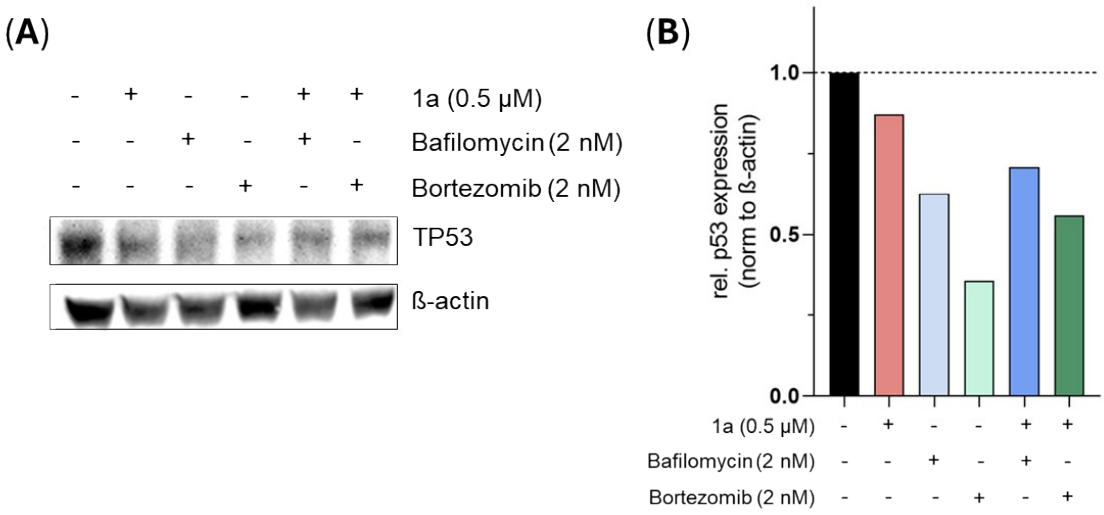

Suppl. Figure S22. (A) Protein expression levels of TP53 in whole cell lysates of CT26 cells treated with indicated compounds for 24 h and analysed by Western blotting. β-actin served as loading control. (**B**) TP53 protein expression relative to DMSO control, normalized to ß-actin quantified from (**A**) using Image J.

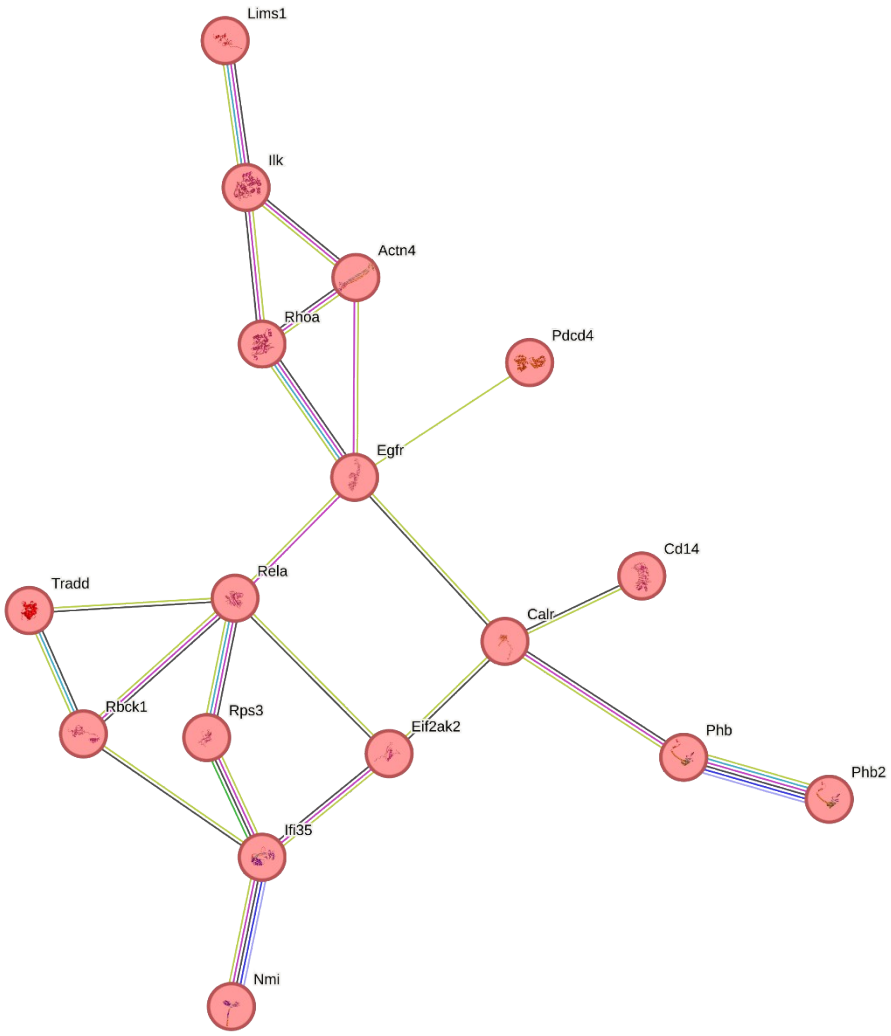

Suppl. Figure S23. STRING network analysis of the down-regulated proteins in tumour tissue of CT26-bearing mice after treatment with **1a** over five days at 10 mg·kg^{-1} i.p.

Supplementary Tables

Table S1. Concentrations to inhibit 50% of cell growth (IC_{50}) in micromolar concentrations. IC50-values are reported after a specific incubation time. IC_{50} values of incubation times of 96 h were obtained from Ref. 1. **a** = 3Et-NQ, **b** = 3Morph-NQ.

Compound	IC_{50} values [µM]		
	SW480 24h	**SW480 96h[1]**	**CH1/PA-1 96h[1]**
cisplatin	n.d.	2.3 ± 0.2	0.073± 0.001
a	n.d.	100 ± 10	173 ± 10
b	n.d.	160 ± 30	>200
[Ru(cym)(3Et-NQ)Cl]	n.d.	27 ± 1	70 ± 10
1a	0.62 ± 0.04	0.046 ± 0.007	62 ± 5
1b	38 ± 5	33 ± 2	150 ± 20
2a	1.2 ± 0.1	n.d.	n.d.
2b	36 ± 7	n.d.	n.d.

Table S2. Number of significantly regulated proteins in the cytoplasmic (CYT) and nuclear (NE) fractions of compound-treated SW480 cancer cells with respect to solvent-treated controls. Each condition was carried out in hexuplicates. A total of 5657 proteins were identified overall.

Compound	CYT		NE		Total
	N° proteins upregulated	N° proteins down-regulated	N° proteins upregulated	N° proteins down-regulated	
1a	**123**	**298**	**178**	**211**	**810**
2a	**202**	**429**	**167**	**170**	**968**
1b	**8**	**8**	**710**	**772**	**1498**
2b	**25**	**28**	**896**	**877**	**1826**

Table S3. Results of gene set variation analysis (GSVA) of in vivo proteomic data with respect to terms according to gene ontology biological processes (GO BP). Statistical significance of term enrichments was calculated using a Benjamini-Hochberg false discovery rate (adjusted P-Value). FC = Fold-change

Gene Set Name	N° Proteins in set	Log2(FC)	adj P-Value
Tumour			
GOBP REGULATION OF INTRINSIC APOPTOTIC SIGNALING PATHWAY IN RESPONSE TO OSMOTIC STRESS	3	0,70	2,7E-02
GOBP REGULATION OF SMOOTHENED SIGNALING PATHWAY	8	0,70	2,3E-02
GOBP CELLULAR RESPONSE TO ARSENIC CONTAINING SUBSTANCE	7	0,48	1,6E-02
GOBP SMOOTHENED SIGNALING PATHWAY	13	0,47	2,7E-02
GOBP POSITIVE REGULATION OF NIK NF KAPPAB SIGNALING	18	-0,47	1,2E-02
GOBP FATTY ACID DERIVATIVE CATABOLIC PROCESS	7	-0,56	2,7E-02
GOBP CELLULAR RESPONSE TO LIPOPROTEIN PARTICLE STIMULUS	10	-0,65	2,3E-02
Plasma			
GOBP REGULATION OF RESPONSE TO ENDOPLASMIC RETICULUM STRESS	2	1,14	1,1E-03
GOBP LYMPHOCYTE CHEMOTAXIS	2	1,13	1,4E-03
GOBP POSITIVE REGULATION OF INTERLEUKIN 1 PRODUCTION	3	1,03	4,5E-03
GOBP POSITIVE REGULATION OF ADAPTIVE IMMUNE RESPONSE	4	0,76	2,6E-02
Liver			
GOBP LEUKOCYTE MIGRATION INVOLVED IN INFLAMMATORY RESPONSE	2	1,02	3,2E-03
GOBP LEUKOCYTE AGGREGATION	3	0,91	2,4E-03
GOBP REGULATION OF MONOCYTE DIFFERENTIATION	2	0,70	4,5E-02
GOBP ENDOPLASMIC RETICULUM TUBULAR NETWORK ORGANIZATION	5	0,65	4,1E-02
GOBP POSITIVE REGULATION OF TOR SIGNALING	7	0,55	4,5E-02
GOBP REGULATION OF MITOCHONDRIAL FISSION	6	0,54	3,8E-02
GOBP MONOCYTE ACTIVATION	3	0,54	3,0E-02
GOBP RESPONSE TO AMINO ACID STARVATION	8	0,51	4,4E-02
GOBP RESPONSE TO INTERLEUKIN 1	15	0,43	1,4E-02
GOBP ENDOPLASMIC RETICULUM ORGANIZATION	35	0,39	4,3E-02
GOBP TRANSITION METAL ION TRANSPORT	22	0,38	4,8E-02
GOBP TOR SIGNALING	16	0,37	4,4E-02
GOBP NADH DEHYDROGENASE COMPLEX ASSEMBLY	30	-0,55	2,7E-03
GOBP OXIDATIVE PHOSPHORYLATION	70	-0,55	2,0E-03
GOBP AEROBIC RESPIRATION	94	-0,56	1,5E-03
GOBP ATP SYNTHESIS COUPLED ELECTRON TRANSPORT	47	-0,60	5,2E-04
GOBP MITOCHONDRIAL ELECTRON TRANSPORT NADH TO UBIQUINONE	32	-0,61	7,5E-04

References

1. H. Geisler, J. Westermayr, K. Cseh, D. Wenisch, V. Fuchs, S. Harringer, S. Plutzar, N. Gajic, M. Hejl, M. A. Jakupec, P. Marquetand and W. Kandioller, Tridentate 3-substituted naphthoquinone ruthenium arene complexes: Synthesis, characterization, aqueous behavior, and theoretical and biological studies, *Inorg. Chem.*, 2021, **60**, 9805-9819.
2. H. Geisler, S. Harringer, D. Wenisch, R. Urban, M. A. Jakupec, W. Kandioller and B. K. Keppler, Systematic study on the cytotoxic potency of commonly used dimeric metal precursors in human cancer cell lines, *ChemistryOpen*, 2022, **11**, e202200019.
3. B. Neuditschko, A. P. King, Z. Huang, L. Janker, A. Bileck, Y. Borutzki, S. C. Marker, C. Gerner, J. J. Wilson and S. M. Meier-Menches, An anticancer rhenium tricarbonyl targets Fe−S cluster biogenesis in ovarian cancer cells, *Angew. Chem., Int. Ed.*, 2022, **61**, e202209136.
4. A. Zougman, P. J. Selby and R. E. Banks, Suspension trapping (STrap) sample preparation method for bottom-up proteomics analysis, *Proteomics*, 2014, **14**, 1006-1000.
5. W. Berger, L. Elbling and M. Micksche, Expression of the major vault protein LRP in human non-small-cell lung cancer cells: activation by short-term exposure to antineoplastic drugs, *Int. J. Cancer*, 2000, **88**, 293-300.
6. A. T. Feldman and D. Wolfe, Tissue processing and hematoxylin and eosin staining, *Methods Mol. Biol.*, 2014, **1180**, 31-43.
7. P. Bortel, G. Hagn, L. Skos, A. Bileck, V. Paulitschke, P. Paulitschke, L. Gleiter, T. Mohr, C. Gerner and S. M. Meier-Menches, Memory effects of prior subculture may impact the quality of multiomic perturbation profiles, *Proc. Natl. Acad. Sci.*, 2024, **121**, e2313851121.
8. L. Skos, C. Schmidt, S. R. Thomas, M. Park, V. Geiger, D. Wenisch, R. Bonsignore, G. Del Favero, T. Mohr, A. Bileck, C. Gerner, A. Casini and S. M. Meier-Menches, Gold-templated covalent targeting of the CysSec-dyad of thioredoxin reductase 1 in cancer cells, *Cell Rep. Phys. Sci.*, 2024, **5**, 102072.
9. T. Weiss, S. Taschner-Mandl, L. Janker, A. Bileck, F. Rifatbegovic, F. Kromp, H. Sorger, M. O. Kauer, C. Frech, R. Windhager, C. Gerner, P. F. Ambros and I. M. Ambros, Schwann cell plasticity regulates neuroblastic tumor cell differentiation via epidermal growth factor-like protein 8, *Nat. Commun.*, 2021, **12**, 1624.
10. J. Cox and M. Mann, MaxQuant enables high peptide identification rates, individualized p.p.b.-range mass accuracies and proteome-wide protein quantification, *Nat. Biotechnol.*, 2008, **26**, 1367-1372.
11. A. Bateman, M.-J. Martin, S. Orchard, M. Magrane, R. Agivetova, S. Ahmad, E. Alpi, E. H. Bowler-Barnett, R. Britto, B. Bursteinas*, et al.*, UniProt: the universal protein knowledgebase in 2021, *Nucleic Acids Res.*, 2021, **49**, D480-D489.
12. S. Tyanova, T. Temu, P. Sinitcyn, A. Carlson, M. Y. Hein, T. Geiger, M. Mann and J. Cox, The Perseus computational platform for comprehensive analysis of (prote)omics data, *Nat. Methods*, 2016, **13**, 731-740.
13. B. T. Sherman, M. Hao, J. Qiu, X. Jiao, M. W. Baseler, H. C. Lane, T. Imamichi and W. Chang, DAVID: a web server for functional enrichment analysis and functional annotation of gene lists (2021 update), *Nucleic Acids Res.*, 2022, **50**, W216-W221.
14. D. Szklarczyk, R. Kirsch, M. Koutrouli, K. Nastou, F. Mehryary, R. Hachilif, A. L. Gable, T. Fang, Nadezhda T. Doncheva, S. Pyysalo, P. Bork, Lars J. Jensen and C. von Mering, The STRING database in 2023: protein–protein association networks and functional enrichment analyses for any sequenced genome of interest, *Nucleic Acids Res.*, 2023, **51**, D638-D646.
15. M. E. Ritchie, B. Phipson, D. Wu, Y. Hu, C. W. Law, W. Shi and G. K. Smyth, LIMMA powers differential expression analyses for RNA-sequencing and microarray studies, *Nucleic Acids Res.*, 2015, **43**, e47-e47.
16. Y. Hochberg and Y. Benjamini, More powerful procedures for multiple significance testing, *Stat. Med.*, 1990, **9**, 811-818.
17. S. Hänzelmann, R. Castelo and J. Guinney, GSVA: Gene set variation analysis for microarray and RNA-Seq data, *BMC Bioinformatics*, 2013, **14**, 7.
18. A. Liberzon, A. Subramanian, R. Pinchback, H. Thorvaldsdóttir, P. Tamayo and J. P. Mesirov, Molecular signatures database (MSigDB) 3.0, *Bioinformatics*, 2011, **27**, 1739-1740.

3.3 Methods to identify protein targets of metal-based drugs

Lukas Skos[1,2], Yasmin Borutzki[1,2,3], Christopher Gerner[1,4], Samuel M. Meier-Menches[1,3,4]

[1] Department of Analytical Chemistry, Faculty of Chemistry, University of Vienna, 1090 Vienna, Austria

[2] Doctoral School of Chemistry, University of Vienna, 1090 Vienna, Austria

[3] Institute of Inorganic Chemistry, Faculty of Chemistry, University of Vienna, 1090 Vienna, Austria

[4] Joint Metabolome Facility, University of Vienna and Medical University Vienna, 1090 Vienna, Austria

Current Opinion in Chemical Biology, 2023, Volume 73, 102257

DOI: 10.1016/j.cbpa.2022.102257

Contributions to this work:

- Literature search
- Writing and editing of the manuscript

Available online at www.sciencedirect.com

ScienceDirect

Current Opinion in Chemical Biology

Methods to identify protein targets of metal-based drugs

Lukas Skos[1,2], Yasmin Borutzki[1,2,3], Christopher Gerner[1,4] and Samuel M. Meier-Menches[1,3,4]

Abstract

Metal-based anticancer agents occupy a distinct chemical space due to their particular coordination geometry and reactivity. Despite the initial DNA-targeting paradigm for this class of compounds, it is now clear that they can also be tuned to target proteins in cells, depending on the metal and ligand scaffold. Since metallodrug discovery is dominated by phenotypic screenings, tailored proteomics strategies were crucial to identify and validate protein targets of several investigative and clinically advanced metal-based drugs. Here, such experimental approaches are discussed, which showed that metallodrugs based on ruthenium, gold, rhenium and even platinum, can selectively and specifically target proteins with clear-cut down-stream effects. Target identification strategies are expected to support significantly the mechanism-driven clinical translation of metal-based drugs.

Addresses

[1] Department of Analytical Chemistry, Faculty of Chemistry, University of Vienna, 1090 Vienna, Austria
[2] Doctoral School of Chemistry, University of Vienna, 1090 Vienna, Austria
[3] Institute of Inorganic Chemistry, Faculty of Chemistry, University of Vienna, 1090 Vienna, Austria
[4] Joint Metabolome Facility, University of Vienna and Medical University Vienna, 1090 Vienna, Austria

Corresponding author: Meier-Menches, Samuel M. (samuel.meier-menches@univie.ac.at)

Current Opinion in Chemical Biology 2023, **73**:102257

This review comes from a themed issue on **Next Generation Therapeutics (2023)**

Edited by **Justin Wilson** and **Timothy Johnstone**

For complete overview of the section, please refer to the article collection Next Generation Therapeutics (2023)

Available online 2 January 2023

https://doi.org/10.1016/j.cbpa.2022.102257

Keywords

Chemoproteomics, Drug discovery, Inorganic drug discovery, Metallodrug, Omics, Probes, Target identification.

Introduction

Metal-based drugs are frequently and successfully applied anticancer agents, especially the platinum derivatives cisplatin, carboplatin and oxaliplatin [1]. Their tremendous success established a long-standing DNA-targeting paradigm [2] in the field even beyond the platinum family. However, accumulating experimental evidence by the anti-rheumatic gold-based auranofin, by gold-based anticancer agents targeting thioredoxin reductase or the proteasome [3], as well as crystallographic models involving the nucleosome core particle [4] added support for the protein targeting capability of non-platinum drug families. Finally, it was found that even oxaliplatin most probably induces ribosomal biogenesis stress as its anticancer mode of action [5].

Due to their coordination geometry, metal-based drugs occupy a chemical space that is distinct from other drug classes [6]. They are not only particular because of their coordination geometry, but because they may engage with a target via coordinative interactions or metal-mediated transfer reactions in addition to non-covalent interactions (Figure 1). Indeed, protein metalation processes have been extensively characterized by several research groups in the past decade [7–10]. This property may be key towards mining this area of chemical space with respect to novel targets [11,12]. The appreciation that proteins play an important role in the modes of action of potentially numerous investigational and clinically advanced metal-based drugs led to the recent development of proteomic methods to identify protein targets [13], although target identification remains a significant bottleneck in drug discovery [14,15]. Here, we discuss strategies and methods for target identification of metal-based drugs in the cellular context, including recent discoveries in metal-mediated ligandability of biological nucleophiles.

Methods for target identification

A diverse spectrum of proteomic strategies for target identification was developed in recent years with the aim of profiling interactions between metal-based drugs and potential targets in complex matrices

Figure 1

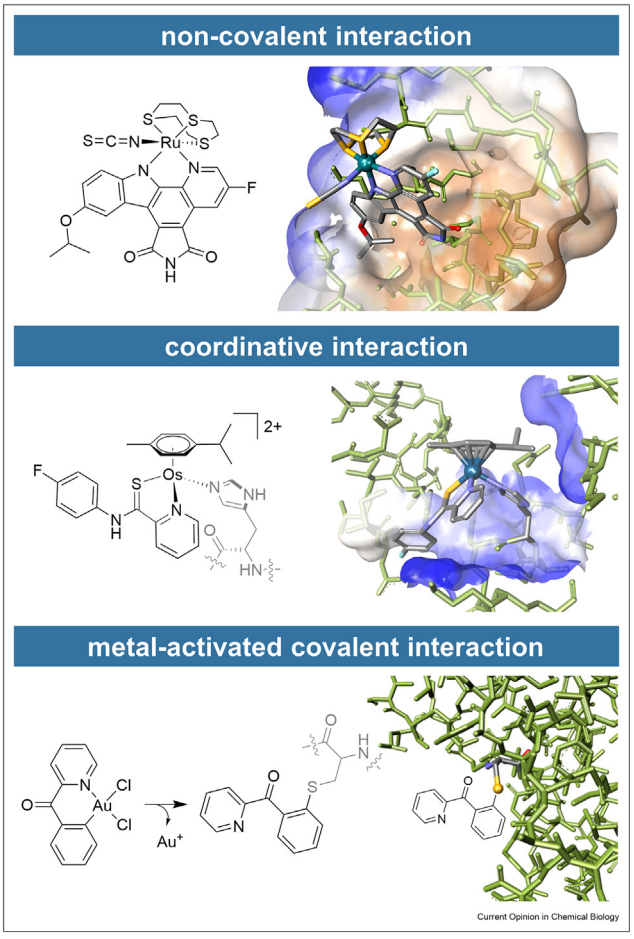

Inorganic drug candidates can engage with protein targets by means of different types of interaction: (*top*) Non-covalent interaction exemplified by death-associated protein kinase 1 in complex with ruthenium octasporine (*PDB 2YAK*). (*middle*) Coordinative interaction exemplified by an osmium analogue of plecstatin-1 binding specifically to histone 2A of the nucleosome core particle (*PDB 4J8W*). (*bottom*) Metal-activated covalent interaction schematically shown for the gold-mediated arylation of Cys151 of glyceraldehyde-3-phosphate dehydrogenase 1 in *Staphylococcus aureus* (*GapA1: PDB 5T73*).

[15–17]. To be amenable for protein target identification, the investigated metallodrug has ideally been shown to selectively target the proteome over the genome [18,19]. Moreover, information about hydrolysis kinetics and possible ligand exchange pathways of metallo-prodrugs is required to correctly attribute the interaction type and determine suitable incubation times [20]. Cell-free protein metalation studies may provide useful prior information [8,18]. Strong to moderate drug-target interactions may be profiled by affinity enrichment strategies and involve synthetic immobilization of metallodrug candidates (Figure 2a). More recently, approaches without the need of chemical modification were established to globally assess

Figure 2

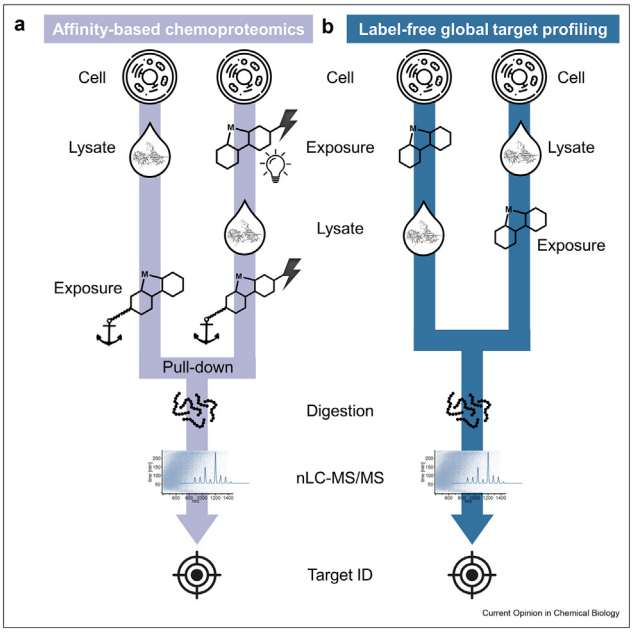

Schematic workflows of the strategies used to identify protein targets in inorganic drug discovery, based on (**a**) affinity-enrichment or (**b**) label-free global target profiling.

weaker drug-target interactions (Figure 2b). While chemoproteomics strategies were applied for metallo-prodrugs and purely structural complexes, label-free target profiling was performed for purely structural complexes only.

Affinity-based chemoproteomics

Affinity-based target identification typically involves chemical proteomic – or chemoproteomic – strategies, which are defined as a collection of biochemical and analytical techniques to interrogate cell-specific proteomes and enrich relevant proteins using small molecule probes [21,22]. Affinity-based chemoproteomics uses an immobilized probe to fish for interactors by affinity enrichment from native whole cell lysates or from intact cells (Figure 2a). The involved buffers and the requirement for extensive washing select preferentially strong interactions between a metal-probe and potential targets. A number of immobilization strategies exist among which biotin-streptavidin is most commonly reported, and which displays an exceptionally high enrichment efficiency [23–26]. Affinity-based chemoproteomics is typically performed in a differential approach to filter specific binding partners (Figure 3a) [20,27]. The target landscape can be visualized by plotting the identified interactors according to their fold-change and significance of enrichment (Figure 3b). Long and hydrophilic linkers are employed to reduce nonspecific interactions.

Figure 3

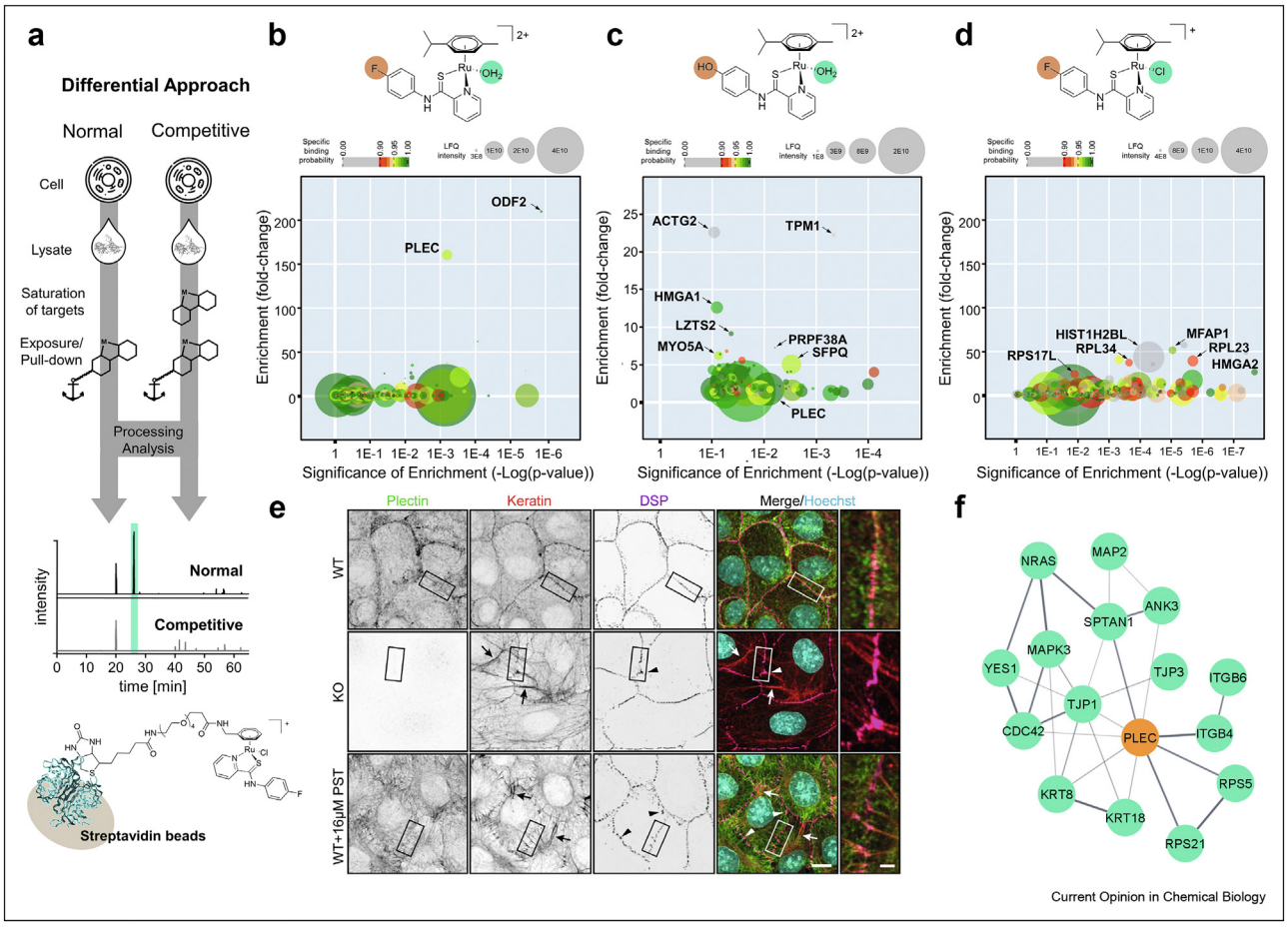

(**a**) Affinity-based chemoproteomics from cell lysates is performed in a differential approach. The structure of an immobilized probe is also shown. (**b**) Chemical structure of activated plecstatin-1 and the corresponding target landscape. The y-axis represents the fold-change of the differential approach and the x-axis the significance of this enrichment based on a p-value. (**c**) Derivatization of the 4-fluorophenyl to a 4-phenol abrogates the plectin selectivity. (**d**) The prodrug form of plecstatin-1 does not feature plectin as a target. (**e**) Plecstatin-1 treatment results in a similar phenotype in epithelial MCDK cell monolayers compared to plectin knock-out cells. Representative confocal images of wild type (WT), knock-outs (KO), and plecstatin-1 (PST)-treated MDKC cells (16 μM, 4 h) monolayers immunolabeled for plectin (green), keratin (red), and desmoplakin (DSP, magenta). Arrows, thick keratin bundles; arrowheads, misshaped desmosomes. Scale bars, 10 and 3 μm (boxed areas). (**f**) Target-response network of the target protein plectin with the surrounding significantly regulated proteins upon plecstatin-1 treatment (obtained using Cytoscape Version 3.8.1). Figures 3 b-d were adapted from ref. [20] under a Creative Commons CC-BY license. Figure 3e was licensed for re-use from ref. [29] under Creative Commons BY-NC-SA.

Cell lysates. Affinity-based chemoproteomics in cell lysates was used successfully to identify protein targets of several investigative and clinically evaluated metal-based anticancer agents. These approaches can sample non-covalent and coordinative bonding. The latter includes the clinically investigated ruthenium(III)-based BOLD-100 (formerly KP-1339), whose protein target landscape was obtained by exploiting the naturally formed stable ruthenium(III)-adduct with human serum albumin after hydrolysis of a metal-chlorido bond. The resulting drug-protein conjugate was immobilized using antibodies and revealed the ribosomal subunits RPL10 and RPL24 as potential interaction partners [24]. Polyribosome formation in BOLD-100-treated cancer cells corroborated this result.

Secondly, plectin was determined as the main target of the organoruthenium(II) compound plecstatin-1 [27]. In this case, the probe was generated by modifying the arene with a PEG4 linker attached to biotin, which was then immobilized on streptavidin beads. The impact of slight structural modifications of plecstatin-1 on the target landscape was studied. The 4-fluorophenyl substituent turned out to be an essential H-bond acceptor for an efficient target engagement with plectin (Figure 3b) since substitution by a phenol, *i.e.* H-bond donor, abrogated the selectivity for plectin (Figure 3c) [20]. Moreover, plecstatin-1 is a prodrug that is activated by hydrolysis of the metal-chlorido bond. This activation step is necessary for efficient target engagement with plectin (Figure 3d) [20]. Plectin is an important scaffold

protein and cytolinker [28]. Importantly, plectin modulation by plecstatin-1 treatment was shown to mimic genetic plectin knock-out phenotypes (Figure 3e) [29].

To narrow down a large collection of potential interactors to a few highly probable targets, it may be helpful to connect potential targets with the proteomic response of cells treated with the same drug in target-response networks, as exemplified for plecstatin-1 (Figure 3f) [27].

Recently, a concentration-dependent pull-down was reported as a further means to rank potential targets, based on the potency of interaction in addition to the enrichment factor. This approach was applied to TRIP, a structural rheniumtricarbonyl compound, and led to the identification of the cytosolic Fe-S cluster assembly factor NUBP2 as a highly probable target, which was targeted at sub-cytotoxic concentrations [30].

Intact Cells. Covalent capture of the drug-target interaction in cells can be used to identify moderately strong binding events by affinity-based chemoproteomics. A bifunctional probe is typically used for these purposes, which may be synthetically demanding (Figure 2a). One functional site consists of a photo-reactive crosslinker, typically diazirine or benzophenone, which upon light irradiation irreversibly binds to the closest interactors *via* radical mechanisms. The second functional moiety usually presents an alkyne, which may be modified via Click reaction to enable affinity enrichment or conjugation to a fluorescent marker for spectroscopic detection. Alkyne handles have minimal structural impact and are used preferentially together with the diazirine-based photoactive probes to determine targets of metal-based drug candidates [31,32]. Furthermore, the linker properties also affect target specificity [33].

The target landscape of a C^N^C-cyclometalated gold(III) N-heterocyclic carbene (NHC) complex was investigated using this approach [34]. Indeed, a bifunctional diazirine-alkyne analogue revealed protein targets by coupling to biotin or a fluorescent tag (Figure 4a). Multiple target proteins were identified including vimentin, HSP60, nucleophosmin, and YB-1, which were further verified. Vimentin is a non-enzymatic cytoskeletal protein and implicated in the epithelial-to-mesenchymal transition of cancer cells [35]. In a follow-up study, the (C^N^C)Au-moiety was exchanged for (C^N^N)Pt in the complex, which narrowed down the target range of the complex [36]. Employing thermal shift assays, including thermal proteome profiling (*vide infra*), it was shown that also the platinum(II) complex demonstrated a strong non-covalent interaction with vimentin and showed promising anticancer properties (Figure 4b). The (C^N^N)Pt represents one of the few examples of a platinum(II) compound that targets proteins over DNA.

A potential disadvantage of the photoactivation strategy using diazirines is the low efficiency of covalent adduct formation with the putative target. An iridium-based photocatalyst conjugated to the small molecule probe activated multiple diaziridines *via* Dexter energy transfer [37].

Label-free global target profiling

Label-free techniques are capable of mapping transient interactions of drug candidates with potential protein targets by globally assessing the drug-altered thermal, proteolytic or chemical protein stability and do not require synthetic modification of the drug (Figure 2b) [15]. Thermal proteome profiling (TPP) represents a label-free strategy [38] that was used to study targets of metallodrugs either by proteomic profiling [39,40] or by differential 2D gel electrophoresis [41]. TPP assesses the extent of drug-target interaction by monitoring the effect of drug treatment on protein denaturation and precipitation as a function of increasing temperature. The extent of protein stabilization by the small molecule parallels the potency of the interaction and can be evaluated by multiplexed mass spectrometric profiling [42]. Due to the experimental setup, TPP may preferentially select small, soluble proteins as potential interactors.

TPP has been successfully used to determine the protein targets of auranofin [39,43] or a bis-N-heterocyclic (NHC) platinum(II) complex containing a 1-(3-hydroxybenzo[*b*]thiophene-2-yl)ethanone derivative as leaving group [40]. The (bis-NHC)Pt-moiety was shown to target the proteins asparagine synthetase (ASNS), ferrochelatase and glutathione S-transferase Mu 1 by increasing their thermal stability. ASNS inhibition was further verified by immunoblotting and its effect on tumour growth was validated in cancer cells. The (bis-NHC)Pt-moiety was also shown to coordinate directly to an N-terminal cysteine that is required for the catalytic function of ASNS [40].

In an orthogonal label-free approach based on gel electrophoresis hyphenated to an inductively coupled plasma mass spectrometer, Wang et al. were able to uncover sensitive silver-binding proteins in *E. coli* that account for its antimicrobial effect. A total of 34 silver-binding proteins were identified, among which glyceraldehyde-3-phosphate dehydrogenase and phosphoglycerate kinase were validated as the main targets [44]. Similar approaches were developed by the same group to study other metals [45].

Metal-mediated ligand transfer to target proteins

Metal complexes typically interact with target proteins *via* non-covalent bonding or direct metal-coordination. Recent reports also discovered metal-mediated ligand

Figure 4

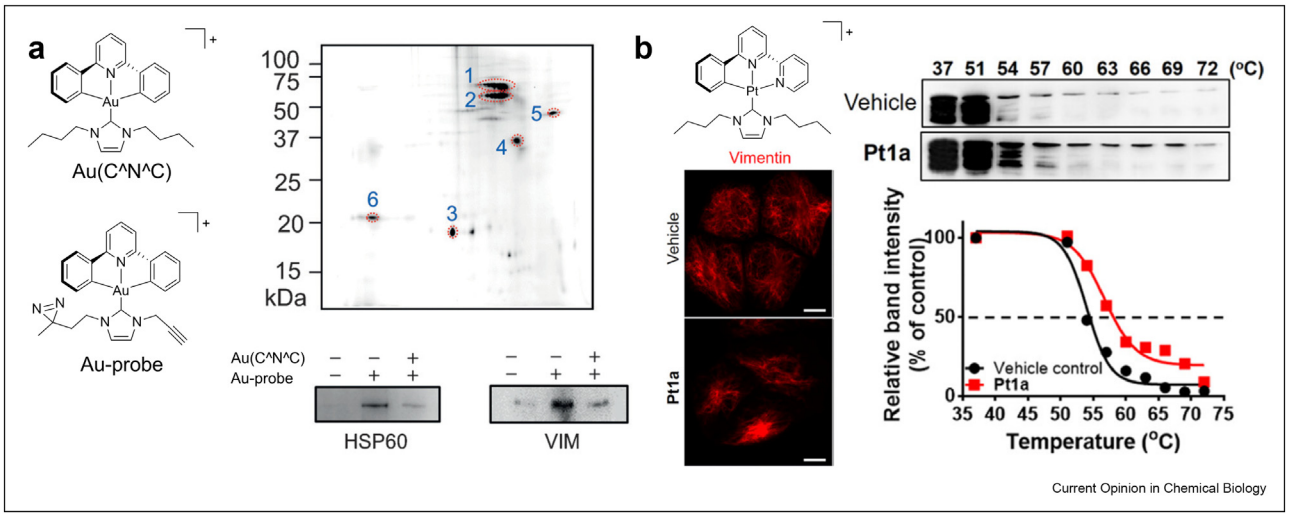

C^N^C-cyclometalated gold(III) and platinum(II) N-heterocyclic carbenes (NHCs) target vimentin amongst others based on the similar coordination geometry. (**a**) The C^N^C-cyclometalated gold(III) NHC compound [Au(C^N^C)] was derivatized by a diaziridine and an alkyne for photo-capture on the target and subsequent 2D gel electrophoresis using a fluorescent dye. The compound targets heat-shock protein 60 (HSP60, 1), vimentin (VIM, 2), NDKA (3), nucleophosmin (4), YB-1 (5) and PRDX1 (6). (**b**) The analogous platinum(II) derivative (Pt1a) also targets vimentin, as revealed by confocal microscopy and thermal shift assays. Figure 4a was adapted from ref. [34] with permission for reuse from John Wiley and Sons Inc. Figure 4b was adapted from ref. [36] with permission from PNAS.

activation, culminating in the covalent modification of target proteins by the ligand, and this reactivity differs from metal-based catalysis in cells [46,47]. Gold(III) complexes seem to be especially suited for the conjugation of ligands to cysteine thiols.

For instance, C^N-cyclometalated gold(III) complexes were found to promote cysteine arylation *via* reductive elimination (Figure 1). The derivative [Au^{III}(2-benzoylpyridine)Cl_2] was used to detect and quantify cysteine modifications in the bacterial proteome in *Staphylococcus aureus* [48]. An activity-based protein profiling approach based on isotopically labelled desthiobiotin azide-activity (isoDTB-ABPP) revealed more than 108 ligandable cysteines including 59 new cysteines, which have not been targeted by previous cysteine-directed covalent binders. Arylation of GCN5-like putative *N*-acetyltransferase was further verified by adduct formation with the isolated protein.

Furthermore, the electrophilic gold(III) centre of a gold-mesoporphyrin IX dimethyl ester (AuMesoIX) activates the *meso*-carbon of the porphyrin ring to selectively form adducts with cysteine thiols as well [49]. AuMesoIX was shown to covalently modify thioredoxin in cell-free approaches, as well as peroxiredoxin III and deubiquitinases in cells. The latter was corroborated by TPP and independent cellular thermal shift assays.

Conclusion

The ability to identify protein targets of metal-based drugs using tailored proteomics methods has enabled unprecedented insight into their target landscapes. Importantly, these target identification approaches have unequivocally revealed that metallo(-pro)drugs can selectively engage with protein targets in cells and in some cases with unexpectedly high specificity. The particular structural and chemical properties of metal-based drugs define a chemical space that seems to be promising to modulate so far hard-to-drug targets, including structural and scaffold proteins as highlighted by the discovery of first-in-class metal-based modulators of plectin and NUBP2. Additionally, promising metal-mediated ligand transfers were discovered that may be further developed to characterize the ligandability of additional biological nucleophiles. Implementing proteomic target identification strategies into drug discovery programs may enable mechanism-driven therapy development [50] and successfully contribute towards an enhanced understanding of the modes of action of metal-based drugs in general.

Author contributions

SMM, CG Conceptualization; SMM, CG Project administration; LS, YB, CG, SMM Writing of original draft; LS, YB, CG, SMM Writing review and editing.

Declaration of competing interest

The authors declare the following financial interests/personal relationships which may be considered as potential competing interests: Samuel M. Meier-Menches reports financial support was provided by Austrian Science Fund.

Data availability

Data will be made available on request.

Acknowledgment

The authors acknowledge financial support by the Austrian Science Fund (FWF, P33238-N). SMM and CG are grateful to the Core Facility of Mass Spectrometry (Faculty of Chemistry) and the Joint Metabolome Facility, members of the Vienna Life-Science Instruments (VLSI).

References

Papers of particular interest, published within the period of review, have been highlighted as:

- • of special interest
- •• of outstanding interest

1. *Metal-based anticancer agents*. London: Royal Society of Chemistry; 2019.
2. Wang D, Lippard SJ: **Cellular processing of platinum anticancer drugs**. *Nat Rev Drug Discov* 2005, **4**:307–320.
3. Casini A, Messori L: **Molecular mechanisms and proposed targets for selected anticancer gold compounds**. *Curr Top Med Chem* 2011, **11**:2647–2660.
4. Adhireksan Z, Davey GE, Campomanes P, Groessl M, Clavel CM, Yu H, Nazarov AA, Yeo CHF, Ang WH, Dröge P, Rothlisberger U, Dyson PJ, Davey CA: **Ligand substitutions between ruthenium–cymene compounds can control protein versus DNA targeting and anticancer activity**. *Nat Commun* 2014, **5**:3462.
5. Bruno PM, Liu Y, Park GY, Murai J, Koch CE, Eisen TJ, Pritchard JR, Pommier Y, Lippard SJ, Hemann MT: **A subset of platinum-containing chemotherapeutic agents kills cells by inducing ribosome biogenesis stress**. *Nat Med* 2017, **23**:461–471.
6. Lipinski C, Hopkins A: **Navigating chemical space for biology and medicine**. *Nature* 2004, **432**:855–861.
7. Merlino A: **Recent advances in protein metalation: structural studies**. *Chem Commun* 2021, **57**:1295–1307.
8. Kreutz D, Gerner C, Meier-Menches SM: **Enabling methods to elucidate the effects of metal-based anticancer agents**. In *Metal-based anticancer agents*. Edited by Casini A, Vessières A, Meier-Menches, SM: Royal Society of Chemistry; 2019:246–270.
9. Merlino A, Marzo T, Messori L: **Protein metalation by anticancer metallodrugs: a joint ESI MS and XRD investigative strategy**. *Chem Eur J* 2017, **23**:6942–6947.
10. Wenzel M, Casini A: **Mass spectrometry as a powerful tool to study therapeutic metallodrugs speciation mechanisms: current frontiers and perspectives**. *Coord Chem Rev* 2017, **352**:432–460.
11. Coleman N, Rodon J: **Taking aim at the undruggable**. *Am Soc Clin Oncol Educ Book* 2021, **41**:e145–e152.
12. Dang CV, Reddy EP, Shokat KM, Soucek L: **Drugging the 'undruggable' cancer targets**. *Nat Rev Cancer* 2017, **17**:502–508.
13. Wang Y, Li H, Sun H: **Metalloproteomics for unveiling the mechanism of action of metallodrugs**. *Inorg Chem* 2019, **58**:13673–13685.
14. Zhou Y, Li H, Sun H: **Metalloproteomics for biomedical research: methodology and applications**. *Annu Rev Biochem* 2022, **91**:449–473.
15. Ha J, Park H, Park J, Park SB: **Recent advances in identifying protein targets in drug discovery**. *Cell Chem Biol* 2021, **28**:394–423.
16. Huang JX, Coukos JS, Moellering RE: **Interaction profiling methods to map protein and pathway targets of bioactive ligands**. *Curr Opin Chem Biol* 2020, **54**:76–84.
17. Steel TR, Hartinger CG: **Metalloproteomics for molecular target identification of protein-binding anticancer metallodrugs**. *Metallomics* 2020, **12**:1627–1636.
18. Artner C, Holtkamp HU, Kandioller W, Hartinger CG, Meier-Menches SM, Keppler BK: **DNA or protein? Capillary zone electrophoresis-mass spectrometry rapidly elucidates metallodrug binding selectivity**. *Chem Commun* 2017, **53**:8002–8005.
19. Adhireksan Z, Davey GE, Campomanes P, Groessl M, Clavel CM, Yu H, Nazarov AA, Yeo CHF, Ang WH, Dröge P, Rothlisberger U, Dyson PJ, Davey CA: **Ligand substitutions between ruthenium–cymene compounds can control protein versus DNA targeting and anticancer activity**. *Nat Commun* 2014, **5**:3462.
20. Meier-Menches SM, Zappe K, Bileck A, Kreutz D, Tahir A, Cichna-Markl M, Gerner C: **Time-dependent shotgun proteomics revealed distinct effects of an organoruthenium prodrug and its activation product on colon carcinoma cells**. *Metallomics* 2019, **11**:118–127.
21. Lu KY: **Chemoproteomics: towards global drug target profiling**. *Chembiochem* 2020, **21**:3189–3191.
22. Jenmalm Jensen A, Cornella Taracido I: **Affinity-based chemoproteomics for target identification**. In *Target discovery and validation*. Edited by Plowright AT, Wiley VCH; 2019:25–49.
23. Anghel N, Müller J, Serricchio M, Jelk J, Bütikofer P, Boubaker G, Imhof D, Ramseier J, Desiatkina O, Păunescu E, Braga-Lagache S, Heller M, Furrer J, Hemphill A: **Cellular and molecular targets of nucleotide-tagged trithiolato-bridged arene ruthenium complexes in the protozoan parasites toxoplasma gondii and trypanosoma brucei**. *Int J Mol Sci* 2021, **22**, 10787.
24. Neuditschko B, Legin AA, Baier D, Schintlmeister A, Reipert S, Wagner M, Keppler BK, Berger W, Meier-Menches SM, Gerner C: **Interaction with ribosomal proteins accompanies stress induction of the anticancer metallodrug BOLD-100/KP1339 in the endoplasmic reticulum**. *Angew Chem Int Ed* 2021, **60**:5063–5068.
25. Yin HY, Gao JJ, Chen X, Ma B, Yang ZS, Tang J, Wang BW, Chen T, Wang C, Gao S, Zhang JL: **A gallium(III) complex that engages protein disulfide isomerase A3 (PDIA3) as an anticancer target**. *Angew Chem Int Ed* 2020, **59**:20147–20153.
26. Babak MV, Meier SM, Huber KVM, Reynisson J, Legin AA, Jakupec MA, Roller A, Stukalov A, Gridling M, Bennett KL, Colinge J, Berger W, Dyson PJ, Superti-Furga G, Keppler BK, Hartinger CG: **Target profiling of an antimetastatic RAPTA agent by chemical proteomics: relevance to the mode of action**. *Chem Sci* 2015, **6**:2449–2456.
27. •• Meier SM, Kreutz D, Winter L, Klose MHM, Cseh K, Weiss T, Bileck A, Alte B, Mader JC, Jana S, Chatterjee A, Bhattacharyya A, Hejl M, Jakupec MA, Heffeter P, Berger W, Hartinger CG, Keppler BK, Wiche G, Gerner C: **An organoruthenium anticancer agent shows unexpected target selectivity for plectin**. *Angew Chem Int Ed* 2017, **56**:8267–8271.
Successful affinity-based chemoproteomics approach for a ruthenium(II)-prodrug and validation of the scaffold protein plectin as a major target in the mode of action.
28. Wiche G, Castañón MJ: **Cytoskeleton | Intermediate filament linker proteins: plectin and BPAG1**. In *Encyclopedia of biological Chemistry III*. Edited by Jez J, Elsevier; 2021:200–219.
29. • Prechova M, Adamova Z, Schweizer AL, Maninova M, Bauer A, Kah D, Meier-Menches SM, Wiche G, Fabry B, Gregor M: **Plectin-mediated cytoskeletal crosstalk controls cell tension and cohesion in epithelial sheets**. *J Cell Biol* 2022, **221**, e202105146.

Biological validation of chemical plectin-modulation by a ruthenium(II)-prodrug to induce a genetic plectin knock-out phenotype mimic.

30. Neuditschko B, King AP, Huang Z, Janker L, Bileck A, Borutzki Y, Marker SC, Gerner C, Wilson JJ, Meier-Menches SM: **An anti-cancer rhenium tricarbonyl targets Fe-S cluster biogenesis in ovarian cancer cells**. *Angew Chem Int Ed* 2022, **61**, e202209136.

31. Hu D, Liu Y, Lai YT, Tong KC, Fung YM, Lok CN, Che CM: **Anticancer gold(III) porphyrins target mitochondrial chaperone Hsp60**. *Angew Chem Int Ed* 2016, **55**:1387–1391.

32. Xiong X, Huang KB, Wang Y, Cao B, Luo Y, Chen H, Yang Y, Long Y, Liu M, Chan ASC, Liang H, Zou T: **Target profiling of an iridium(III)-based immunogenic cell death inducer unveils the engagement of unfolded protein response regulator BiP**. *J Am Chem Soc* 2022, **144**:10407–10416.

33. Kitamura K, Itoh H, Sakurai K, Dan S, Inoue M: **Target identification of Yaku'amide B and its two distinct activities against mitochondrial FoF1-ATP synthase**. *J Am Chem Soc* 2018, **140**: 12189–12199.

34. Fung SK, Zou T, Cao B, Lee PY, Fung YME, Hu D, Lok CN, Che CM: **Cyclometalated gold(III) complexes containing N-heterocyclic carbene ligands engage multiple anti-cancer molecular targets**. *Angew Chem Int Ed* 2017, **56**:3892–3896.

35. Dongre A, Weinberg RA: **New insights into the mechanisms of epithelial–mesenchymal transition and implications for cancer**. *Nat Rev Mol Cell Biol* 2018, **20**:69–84.

36. •• Wan PK, Tong KC, Lok CN, Zhang C, Chang XY, Sze KH, Wong AST, Che CM: **Platinum(II) N-heterocyclic carbene complexes arrest metastatic tumor growth**. *Proc Natl Acad Sci USA* 2021, **118**, e2025806118.
Successful label-free global target profiling to identify and validate vimentin as a major target in the mode of action of a platinum(II)-based anticancer agent.

37. Trowbridge AD, Seath CP, Rodriguez-Rivera FP, Li BX, Dul BE, Schwaid AG, Buksh BF, Geri JB, Oakley JV, Fadeyi OO, Oslund RC, Ryu KA, White C, Reyes-Robles T, Tawa P, Parker DL, MacMillan DWC: **Small molecule photocatalysis enables drug target identification via energy transfer**. *Proc Natl Acad Sci USA* 2022, **119**, e2208077119.

38. Savitski MM, Reinhard FB, Franken H, Werner T, Savitski MF, Eberhard D, Martinez Molina D, Jafari R, Dovega RB, Klaeger S, Kuster B, Nordlund P, Bantscheff M, Drewes G: **Tracking cancer drugs in living cells by thermal profiling of the proteome**. *Science* 2014, **346**, 1255784.

39. Saei AA, Gullberg H, Sabatier P, Beusch CM, Johansson K, Lundgren B, Arvidsson PI, Arnér ESJ, Zubarev RA: **Comprehensive chemical proteomics for target deconvolution of the redox active drug auranofin**. *Redox Biol* 2020, **32**, 101491.

40. Hu D, Yang C, Lok CN, Xing F, Lee PY, Fung YME, Jiang H, Che CM: **An antitumor bis(N-heterocyclic carbene)platinum(II) complex that engages asparagine synthetase as an anticancer target**. *Angew Chem Int Ed* 2019, **58**: 10914–10918.

41. Yim J, Park SB: **Label-free target identification reveals the anticancer mechanism of a rhenium isonitrile complex**. *Front Chem* 2022, **10**, 850638.

42. Franken H, Mathieson T, Childs D, Sweetman GMA, Werner T, Tögel I, Doce C, Gade S, Bantscheff M, Drewes G, Reinhard FBM, Huber W, Savitski MM: **Thermal proteome profiling for unbiased identification of direct and indirect drug targets using multiplexed quantitative mass spectrometry**. *Nat Protoc* 2015, **10**:1567–1593.

43. Roder C, Thomson MJ: **Auranofin: repurposing an old drug for a golden new age**. *Drugs R* 2015, **15**:13–20.

44. Wang H, Yan A, Liu Z, Yang X, Xu Z, Wang Y, Wang R, Koohi-Moghadam M, Hu L, Xia W, Tang H, Wang Y, Li H, Sun H: **Deciphering molecular mechanism of silver by integrated omic approaches enables enhancing its antimicrobial efficacy in E. coli**. *PLoS Biol* 2019, **17**, e3000292.

45. Hu X, Li H, Ip TKY, Cheung YF, Koohi-Moghadam M, Wang H, Yang X, Tritton DN, Wang Y, Wang Y, Wang R, Ng KM, Naranmandura H, Tse EWC, Sun H: **Arsenic trioxide targets Hsp60, triggering degradation of p53 and survivin**. *Chem Sci* 2021, **12**:10893–10900.

46. Boros E, Dyson PJ, Gasser G: **Classification of metal-based drugs according to their mechanisms of action**. *Chem* 2020, **6**:41–60.

47. Fan Z, Huang J, Huang H, Banerjee S: **Metal-based catalytic drug development for next-generation cancer therapy**. *ChemMedChem* 2021, **16**:2480–2486.

48. •• Schmidt C, Zollo M, Bonsignore R, Casini A, Hacker SM: **Competitive profiling of ligandable cysteines in Staphylococcus aureus with an organogold compound**. *Chem Commun* 2022, **58**:5526–5529.
Demonstration that gold(III)-mediated ligand activation is possible to globally monitor nucleophile ligandability in cells.

49. Tong KC, Lok CN, Wan PK, Hu D, Fung YME, Chang XY, Huang S, Jiang H, Che CM: **An anticancer gold(III)-activated porphyrin scaffold that covalently modifies protein cysteine thiols**. *Proc Natl Acad Sci USA* 2020, **117**:1321–1329.

50. Wang H, Zhou Y, Xu X, Li H, Sun H: **Metalloproteomics in conjunction with other omics for uncovering the mechanism of action of metallodrugs: mechanism-driven new therapy development**. *Curr Opin Chem Biol* 2020, **55**: 171–179.

4 Conclusion

This thesis demonstrates the successful establishment of a mass spectrometry-based drug discovery platform to characterize the modes of action of phenotypically discovered metallodrug candidates. The projects also highlight the potential of proteomic combinations, *e.g.* chemoproteomics and perturbation profiling, to characterize in detail previously unknown biological effects of metallodrugs, accompanied by suitable cell culture model systems.

The first study focused on the investigation of a C^N cyclometalated gold(III) complex and its novel gold-assisted ligand transfer mechanism in SW480 colon carcinoma cells. Employing protein profiling, dose-dependent affinity pulldown experiments and cell free interaction studies, we were able to show a novel two step mechanism that includes the coordination of the Au-complex to the redox protective protein TXNRD1, followed by the arylation of its biological nucleophiles Cys and Sec, ultimately yielding the selective inhibition of the enzyme. The pulldown experiments were successfully performed by a novel immobilization strategy on agarose beads that enabled the efficient immobilization of the probe *via* a simple amide bond formation. Selective arylation of Cys and Sec residues was directly verified by cell-free mass spectrometry approaches. The treatment was further accompanied by the downregulation of other selenoproteins and the induction of the NRF2-Keap1 pathway, without ROS formation. In additional synergism studies, we determined that cancer cell survival heavily relies on inducing the NRF2-pathway after treatment with the gold compound. Overall, the presented metal-assisted arylation mechanism could be used to design improved organogold anticancer drug candidates or explore their ligandable space in covalent drug discovery.

In the second study, the mode of action of a highly cytotoxic N,O,O-tridentate ruthenium(arene) derivative was elucidated. Based on that lead compound three structurally similar candidates, differing in the ligand by using 3-ethyl naphthoquinone or 3-morpholine naphthoquinone, and the metal center by using Ru or Os were investigated. These complexes are kinetically more inert compared to bidentate analogues but retain their reactivity *via* slowly hydrolyzing a metal-oxygen bond in the naphthoquinone ligand. After confirming the complexes preferred binding to AA over nucleotides, it was shown that the type of ligand had a stronger impact on the antiproliferative activity and solubility of the complexes compared to the metal center. This feature was corroborated by structure-activity relationships on the proteome level. Especially, the 3-ethyl naphthoquinone analogues were found to affect the TP53 network, with the Ru lead structure showing a more pronounced perturbation compared to the Os analogue. Disruption of

the TP53-DDX3X-p21 signaling axis accompanied by loss of p21 expression was then verified for the Ru lead compound, which was most likely modulated *via* direct DDX3X interaction. The latter was revealed by implementing an orthogonal target identification assay based on Limited Proteolysis. *In vivo* investigations in a CT26 mouse model of the four complexes revealed again the Ru-ethyl analogue as most potent candidate with significant tumor size reduction and anticancer activity. Further, we were able to distinguish between direct and indirect drug effects by comparing local vs systemic responses, which revealed EGFR downregulation in tumor tissue as direct effect of the lead compound. As EGFR levels have previously been demonstrated to be mediated by the TP53-DDX3X-p21 axis these *in vivo* results support the *in vitro* findings of the 3-ethyl ruthenium(arene) directly impacting this signaling pathway. In summary, this study highlights a strategy to elucidate the MoA of metal-based anticancer candidates developed in a PDD setting by connecting their detected effects *in vitro* and *in vivo*.

The projects presented here highlight how proteomics-based discovery platforms, combining perturbation profiling with chemoproteomic techniques, can be used to investigate the effects of metal-based compounds selected from phenotypic models, thereby generating hypotheses about their MoA and also verifying those claims. This mechanism-based approach is broadly applicable, may guide lead compound maturation and facilitate the translation into clinical candidates.

5 References

(1) Swinney, D. C.; Anthony, J. How Were New Medicines Discovered? *Nat. Rev. Drug Discov.* **2011**, *10* (7), 507–519. https://doi.org/10.1038/nrd3480.

(2) Vincent, F.; Nueda, A.; Lee, J.; Schenone, M.; Prunotto, M.; Mercola, M. Phenotypic Drug Discovery: Recent Successes, Lessons Learned and New Directions. *Nat. Rev. Drug Discov.* **2022**, *21* (12), 899–914. https://doi.org/10.1038/s41573-022-00472-w.

(3) Berg, E. L. The Future of Phenotypic Drug Discovery. *Cell Chem. Biol.* **2021**, *28* (3), 424–430. https://doi.org/10.1016/j.chembiol.2021.01.010.

(4) Meissner, F.; Geddes-McAlister, J.; Mann, M.; Bantscheff, M. The Emerging Role of Mass Spectrometry-Based Proteomics in Drug Discovery. *Nat. Rev. Drug Discov.* **2022**, *21* (9), 637–654. https://doi.org/10.1038/s41573-022-00409-3.

(5) Ha, J.; Park, H.; Park, J.; Park, S. B. Recent Advances in Identifying Protein Targets in Drug Discovery. *Cell Chem. Biol.* **2021**, *28* (3), 394–423. https://doi.org/10.1016/j.chembiol.2020.12.001.

(6) Casini, A.; Pöthig, A. Metals in Cancer Research: Beyond Platinum Metallodrugs. *ACS Cent. Sci.* **2024**, *10* (2), 242–250. https://doi.org/10.1021/acscentsci.3c01340.

(7) Jones, A. W. Early Drug Discovery and the Rise of Pharmaceutical Chemistry. *Drug Test. Anal.* **2011**, *3* (6), 337–344. https://doi.org/10.1002/dta.301.

(8) Fricker, S. P. Metal Based Drugs: From Serendipity to Design. *Dalton Trans.* **2007**, No. 43, 4903–4917. https://doi.org/10.1039/b705551j.

(9) Polak, A. M.; Karska, K.; Drozd, M. The Discovery of Medicines: Drug Testing on Humans and the Development of Medical Ethics before the 20th Century. *Drug Discov. Today* **2025**, *30* (8), 104418. https://doi.org/10.1016/j.drudis.2025.104418.

(10) *Alexander Fleming Discovery and Development of Penicillin - Landmark*. American Chemical Society. https://www.acs.org/education/whatischemistry/landmarks/flemingpenicillin.html (accessed 2026-05-03).

(11) Jin, S.; Feng, C.; Wang, X. DNA or Not DNA —That Is the Question Determining the Design of Platinum Anticancer Drugs. *Eur. J. Med. Chem.* **2025**, *282*, 117077. https://doi.org/10.1016/j.ejmech.2024.117077.

(12) Sadri, A. Is Target-Based Drug Discovery Efficient? Discovery and "Off-Target" Mechanisms of All Drugs. *J. Med. Chem.* **2023**, *66* (18), 12651–12677. https://doi.org/10.1021/acs.jmedchem.2c01737.

(13) de Vienne, D. What Is a Phenotype? History and New Developments of the Concept. *Genetica* **2022**, *150* (3), 153–158. https://doi.org/10.1007/s10709-021-00134-6.

(14) Hajar, R. History of Medicine Timeline. *Heart Views Off. J. Gulf Heart Assoc.* **2015**, *16* (1), 43–45. https://doi.org/10.4103/1995-705x.153008.

(15) *The Top 10 Milestones in MS*. The Analytical Scientist. https://theanalyticalscientist.com/issues/2021/articles/nov/the-top-10-milestones-in-ms (accessed 2026-05-03).

(16) *Discovery of Highly Active Antiretroviral Therapy for HIV*. American Chemical Society. https://www.acs.org/education/whatischemistry/landmarks/highly-active-antiretroviral-therapy-hiv.html (accessed 2026-05-03).

(17) *Milestones in Cancer Research and Discovery*. National Cancer Institute. https://www.cancer.gov/research/progress/250-years-milestones (accessed 2026-05-03).

(18) *Human Genome Project Fact Sheet*. National Human Genome Research Institute. https://www.genome.gov/about-genomics/educational-resources/fact-sheets/human-genome-project (accessed 2026-05-03).

(19) *CRISPR Timeline*. Broad Institute. https://www.broadinstitute.org/what-broad/areas-focus/project-spotlight/crispr-timeline (accessed 2026-05-03).

(20) Nakajima, E. C.; Drezner, N.; Li, X.; Mishra-Kalyani, P. S.; Liu, Y.; Zhao, H.; Bi, Y.; Liu, J.; Rahman, A.; Wearne, E.; Ojofeitimi, I.; Hotaki, L. T.; Spillman, D.; Pazdur, R.; Beaver, J. A.; Singh, H. FDA Approval Summary: Sotorasib for KRAS G12C Mutated Metastatic NSCLC. *Clin. Cancer Res. Off. J. Am. Assoc. Cancer Res.* **2022**, *28* (8), 1482–1486. https://doi.org/10.1158/1078-0432.CCR-21-3074.

(21) Gilbert, I. H. Drug Discovery for Neglected Diseases: Molecular Target-Based and Phenotypic Approaches. *J. Med. Chem.* **2013**, *56* (20), 7719–7726. https://doi.org/10.1021/jm400362b.

(22) Vasaikar, S.; Bhatia, P.; Bhatia, P. G.; Chu Yaiw, K. Complementary Approaches to Existing Target Based Drug Discovery for Identifying Novel Drug Targets. *Biomedicines* **2016**, *4* (4), 27. https://doi.org/10.3390/biomedicines4040027.

(23) Kumar, V.; Chunchagatta Lakshman, P. K.; Prasad, T. K.; Manjunath, K.; Bairy, S.; Vasu, A. S.; Ganavi, B.; Jasti, S.; Kamariah, N. Target-Based Drug Discovery: Applications of Fluorescence Techniques in High Throughput and Fragment-Based Screening. *Heliyon* **2024**, *10* (1), e23864. https://doi.org/10.1016/j.heliyon.2023.e23864.

(24) Guidi, A.; Mansour, N. R.; Paveley, R. A.; Carruthers, I. M.; Besnard, J.; Hopkins, A. L.; Gilbert, I. H.; Bickle, Q. D. Application of RNAi to Genomic Drug Target Validation in Schistosomes. *PLoS Negl. Trop. Dis.* **2015**, *9* (5), e0003801. https://doi.org/10.1371/journal.pntd.0003801.

(25) Wang, Z.; Zhao, Y.; Zhang, L. Emerging Trends and Hot Topics in the Application of Multi-Omics in Drug Discovery: A Bibliometric and Visualized Study. *Curr. Pharm. Anal.* **2024**, *21* (1), 20–32. https://doi.org/10.1016/j.cpan.2024.12.001.

(26) *OpenAI | ChatGPT, Sam Altman, Microsoft, & History | Britannica Money*. Encyclopedia Britannica. https://www.britannica.com/money//money/OpenAI (accessed 2025-10-08).

(27) Zimmermann, G. R.; Lehár, J.; Keith, C. T. Multi-Target Therapeutics: When the Whole Is Greater than the Sum of the Parts. *Drug Discov. Today* **2007**, *12* (1), 34–42. https://doi.org/10.1016/j.drudis.2006.11.008.

(28) Deininger, M.; Buchdunger, E.; Druker, B. J. The Development of Imatinib as a Therapeutic Agent for Chronic Myeloid Leukemia. *Blood* **2005**, *105* (7), 2640–2653. https://doi.org/10.1182/blood-2004-08-3097.

(29) Harries, M.; Smith, I. The Development and Clinical Use of Trastuzumab (Herceptin). *Endocr. Relat. Cancer* **2002**, *9* (2), 75–85.

(30) Portsmouth, S. D.; Scott, C. J. The Renaissance of Fixed Dose Combinations: Combivir. *Ther. Clin. Risk Manag.* **2007**, *3* (4), 579–583.

(31) Summa, V.; Petrocchi, A.; Bonelli, F.; Crescenzi, B.; Donghi, M.; Ferrara, M.; Fiore, F.; Gardelli, C.; Gonzalez Paz, O.; Hazuda, D. J.; Jones, P.; Kinzel, O.; Laufer, R.; Monteagudo, E.; Muraglia, E.; Nizi, E.; Orvieto, F.; Pace, P.; Pescatore, G.; Scarpelli, R.; Stillmock, K.; Witmer, M. V.; Rowley, M. Discovery of Raltegravir, a Potent, Selective Orally Bioavailable HIV-Integrase Inhibitor for the Treatment of HIV-AIDS Infection. *J. Med. Chem.* **2008**, *51* (18), 5843–5855. https://doi.org/10.1021/jm800245z.

(32) El-Tanani, M.; Rabbani, S. A.; El-Tanani, Y.; Matalka, I. I.; Khalil, I. A. Bridging the Gap: From Petri Dish to Patient - Advancements in Translational Drug Discovery. *Heliyon* **2025**, *11* (1), e41317. https://doi.org/10.1016/j.heliyon.2024.e41317.

(33) Mendiratta, G.; Ke, E.; Aziz, M.; Liarakos, D.; Tong, M.; Stites, E. C. Cancer Gene Mutation Frequencies for the U.S. Population. *Nat. Commun.* **2021**, *12* (1), 5961. https://doi.org/10.1038/s41467-021-26213-y.

(34) Sinkala, M. Mutational Landscape of Cancer-Driver Genes across Human Cancers. *Sci. Rep.* **2023**, *13* (1), 12742. https://doi.org/10.1038/s41598-023-39608-2.

(35) He, Z.; Song, B.; Zhu, M.; Liu, J. Comprehensive Pan-Cancer Analysis of STAT3 as a Prognostic and Immunological Biomarker. *Sci. Rep.* **2023**, *13* (1), 5069. https://doi.org/10.1038/s41598-023-31226-2.

(36) Xie, X.; Yu, T.; Li, X.; Zhang, N.; Foster, L. J.; Peng, C.; Huang, W.; He, G. Recent Advances in Targeting the "Undruggable" Proteins: From Drug Discovery to Clinical Trials. *Signal Transduct. Target. Ther.* **2023**, *8* (1), 335. https://doi.org/10.1038/s41392-023-01589-z.

(37) Heilker, R.; Lessel, U.; Bischoff, D. The Power of Combining Phenotypic and Target-Focused Drug Discovery. *Drug Discov. Today* **2019**, *24* (2), 526–532. https://doi.org/10.1016/j.drudis.2018.10.009.

(38) Hughes, R. E.; Elliott, R. J. R.; Dawson, J. C.; Carragher, N. O. High-Content Phenotypic and Pathway Profiling to Advance Drug Discovery in Diseases of Unmet Need. *Cell Chem. Biol.* **2021**, *28* (3), 338–355. https://doi.org/10.1016/j.chembiol.2021.02.015.

(39) Schneider, P.; Walters, W. P.; Plowright, A. T.; Sieroka, N.; Listgarten, J.; Goodnow, R. A.; Fisher, J.; Jansen, J. M.; Duca, J. S.; Rush, T. S.; Zentgraf, M.; Hill, J. E.; Krutoholow, E.; Kohler, M.; Blaney, J.; Funatsu, K.; Luebkemann, C.; Schneider, G. Rethinking Drug Design in the Artificial Intelligence Era. *Nat. Rev. Drug Discov.* **2020**, *19* (5), 353–364. https://doi.org/10.1038/s41573-019-0050-3.

(40) Liu, J.; Bao, C.; Zhang, J.; Han, Z.; Fang, H.; Lu, H. Artificial Intelligence with Mass Spectrometry-Based Multimodal Molecular Profiling Methods for Advancing Therapeutic Discovery of Infectious Diseases. *Pharmacol. Ther.* **2024**, *263*, 108712. https://doi.org/10.1016/j.pharmthera.2024.108712.

(41) Pun, F. W.; Podolskiy, D.; Izumchenko, E.; Mortlock, A.; Oprea, T. I.; Scheibye-Knudsen, M.; Fortney, K.; Morgen, E.; Ren, F.; Zhavoronkov, A. Target Identification and Assessment in the Era of AI. *Nat. Rev. Drug Discov.* **2026**, 1–19. https://doi.org/10.1038/s41573-026-01412-8.

(42) Corsello, S. M.; Bittker, J. A.; Liu, Z.; Gould, J.; McCarren, P.; Hirschman, J. E.; Johnston, S. E.; Vrcic, A.; Wong, B.; Khan, M.; Asiedu, J.; Narayan, R.; Mader, C. C.; Subramanian, A.; Golub, T. R. The Drug Repurposing Hub: A next-Generation Drug Library and Information Resource. *Nat. Med.* **2017**, *23* (4), 405–408. https://doi.org/10.1038/nm.4306.

(43) Wan, Z.; Sun, X.; Li, Y.; Chu, T.; Hao, X.; Cao, Y.; Zhang, P. Applications of Artificial Intelligence in Drug Repurposing. *Adv. Sci.* **2025**, *12* (14), 2411325. https://doi.org/10.1002/advs.202411325.

(44) Keenan, A. B.; Jenkins, S. L.; Jagodnik, K. M.; Koplev, S.; He, E.; Torre, D.; Wang, Z.; Dohlman, A. B.; Silverstein, M. C.; Lachmann, A.; Kuleshov, M. V.; Ma'ayan, A.; Stathias, V.; Terryn, R.; Cooper, D.; Forlin, M.; Koleti, A.; Vidovic, D.; Chung, C.; Schürer, S. C.; Vasiliauskas, J.; Pilarczyk, M.; Shamsaei, B.; Fazel, M.; Ren, Y.; Niu, W.; Clark, N. A.; White, S.; Mahi, N.; Zhang, L.; Kouril, M.; Reichard, J. F.; Sivaganesan, S.; Medvedovic, M.; Meller, J.; Koch, R. J.; Birtwistle, M. R.; Iyengar, R.; Sobie, E. A.; Azeloglu, E. U.; Kaye, J.; Osterloh, J.; Haston, K.; Kalra, J.; Finkbiener, S.; Li, J.; Milani, P.; Adam, M.; Escalante-Chong, R.; Sachs, K.; Lenail, A.; Ramamoorthy, D.; Fraenkel, E.; Daigle, G.; Hussain, U.; Coye, A.; Rothstein, J.; Sareen, D.; Ornelas, L.; Banuelos, M.; Mandefro, B.; Ho, R.; Svendsen, C. N.; Lim, R. G.; Stocksdale, J.; Casale, M. S.; Thompson, T. G.; Wu, J.; Thompson, L. M.; Dardov, V.; Venkatraman, V.; Matlock, A.; Eyk, J. E. V.; Jaffe, J. D.; Papanastasiou, M.; Subramanian, A.; Golub, T. R.; Erickson, S. D.; Fallahi-Sichani, M.; Hafner, M.; Gray, N. S.; Lin, J.-R.; Mills, C. E.; Muhlich, J. L.; Niepel, M.; Shamu, C. E.; Williams, E. H.; Wrobel, D.; Sorger, P. K.; Heiser, L. M.; Gray, J. W.; Korkola, J. E.; Mills, G. B.; LaBarge, M.; Feiler, H. S.; Dane, M. A.; Bucher, E.; Nederlof, M.; Sudar, D.; Gross, S.; Kilburn, D. F.; Smith, R.; Devlin, K.; Margolis, R.; Derr, L.; Lee, A.; Pillai, A. The Library of Integrated Network-Based Cellular Signatures NIH Program: System-Level Cataloging of Human Cells Response to Perturbations. *Cell Syst.* **2018**, *6* (1), 13–24. https://doi.org/10.1016/j.cels.2017.11.001.

(45) Bray, M.-A.; Singh, S.; Han, H.; Davis, C. T.; Borgeson, B.; Hartland, C.; Kost-Alimova, M.; Gustafsdottir, S. M.; Gibson, C. C.; Carpenter, A. E. Cell Painting, a High-Content Image-Based Assay for Morphological Profiling Using Multiplexed Fluorescent Dyes. *Nat. Protoc.* **2016**, *11* (9), 1757–1774. https://doi.org/10.1038/nprot.2016.105.
(46) Vulliard, L.; Menche, J. Complex Networks in Health and Disease. *Syst. Med.* **2021**, 26–33. https://doi.org/10.1016/B978-0-12-801238-3.11640-X.
(47) Yilmaz, M.; Kantarjian, H.; Ravandi, F. Acute Promyelocytic Leukemia Current Treatment Algorithms. *Blood Cancer J.* **2021**, *11* (6), 123. https://doi.org/10.1038/s41408-021-00514-3.
(48) Naryshkin, N. A.; Weetall, M.; Dakka, A.; Narasimhan, J.; Zhao, X.; Feng, Z.; Ling, K. K. Y.; Karp, G. M.; Qi, H.; Woll, M. G.; Chen, G.; Zhang, N.; Gabbeta, V.; Vazirani, P.; Bhattacharyya, A.; Furia, B.; Risher, N.; Sheedy, J.; Kong, R.; Ma, J.; Turpoff, A.; Lee, C.-S.; Zhang, X.; Moon, Y.-C.; Trifillis, P.; Welch, E. M.; Colacino, J. M.; Babiak, J.; Almstead, N. G.; Peltz, S. W.; Eng, L. A.; Chen, K. S.; Mull, J. L.; Lynes, M. S.; Rubin, L. L.; Fontoura, P.; Santarelli, L.; Haehnke, D.; McCarthy, K. D.; Schmucki, R.; Ebeling, M.; Sivaramakrishnan, M.; Ko, C.-P.; Paushkin, S. V.; Ratni, H.; Gerlach, I.; Ghosh, A.; Metzger, F. SMN2 Splicing Modifiers Improve Motor Function and Longevity in Mice with Spinal Muscular Atrophy. *Science* **2014**, *345* (6197), 688–693. https://doi.org/10.1126/science.1250127.
(49) Ratni, H.; Scalco, R. S.; Stephan, A. H. Risdiplam, the First Approved Small Molecule Splicing Modifier Drug as a Blueprint for Future Transformative Medicines. *ACS Med. Chem. Lett.* **2021**, *12* (6), 874–877. https://doi.org/10.1021/acsmedchemlett.0c00659.
(50) Belema, M.; Meanwell, N. A. Discovery of Daclatasvir, a Pan-Genotypic Hepatitis C Virus NS5A Replication Complex Inhibitor with Potent Clinical Effect. *J. Med. Chem.* **2014**, *57* (12), 5057–5071. https://doi.org/10.1021/jm500335h.
(51) Connett, G. J. Lumacaftor-Ivacaftor in the Treatment of Cystic Fibrosis: Design, Development and Place in Therapy. *Drug Des. Devel. Ther.* **2019**, *13*, 2405–2412. https://doi.org/10.2147/DDDT.S153719.
(52) Wang, X.; Tse, C.; Singh, A. Discovery and Development of CFTR Modulators for the Treatment of Cystic Fibrosis. *J. Med. Chem.* **2025**, *68* (3), 2255–2300. https://doi.org/10.1021/acs.jmedchem.4c02547.
(53) Grant, S.; Easley, C.; Kirkpatrick, P. Vorinostat. *Nat. Rev. Drug Discov.* **2007**, *6* (1), 21–22. https://doi.org/10.1038/nrd2227.
(54) Richon, V. M.; Webb, Y.; Merger, R.; Sheppard, T.; Jursic, B.; Ngo, L.; Civoli, F.; Breslow, R.; Rifkind, R. A.; Marks, P. A. Second Generation Hybrid Polar Compounds Are Potent Inducers of Transformed Cell Differentiation. *Proc. Natl. Acad. Sci.* **1996**, *93* (12), 5705–5708. https://doi.org/10.1073/pnas.93.12.5705.
(55) Moffat, J. G.; Vincent, F.; Lee, J. A.; Eder, J.; Prunotto, M. Opportunities and Challenges in Phenotypic Drug Discovery: An Industry Perspective. *Nat. Rev. Drug Discov.* **2017**, *16* (8), 531–543. https://doi.org/10.1038/nrd.2017.111.
(56) Kunnumakkara, A. B.; Bordoloi, D.; Sailo, B. L.; Roy, N. K.; Thakur, K. K.; Banik, K.; Shakibaei, M.; Gupta, S. C.; Aggarwal, B. B. Cancer Drug Development: The Missing Links. *Exp. Biol. Med.* **2019**, *244* (8), 663–689. https://doi.org/10.1177/1535370219839163.
(57) Loewa, A.; Feng, J. J.; Hedtrich, S. Human Disease Models in Drug Development. *Nat. Rev. Bioeng.* **2023**, *1* (8), 545–559. https://doi.org/10.1038/s44222-023-00063-3.
(58) Gupta, R.; Radhakrishnan, R.; Kabekkodu, S. P.; Chakrabarty, S. Application of in Vitro and in Vivo Cancer Models to Study the Impact of the Tumor Immune Microenvironment on Anticancer Therapy. *Biochim. Biophys. Acta BBA - Rev. Cancer* **2026**, *1881* (1), 189504. https://doi.org/10.1016/j.bbcan.2025.189504.
(59) *SMART*. Servier Medical Art. https://smart.servier.com/ (accessed 2026-05-05).

(60) Cardoso, B. D.; Castanheira, E. M. S.; Lanceros-Méndez, S.; Cardoso, V. F. Recent Advances on Cell Culture Platforms for In Vitro Drug Screening and Cell Therapies: From Conventional to Microfluidic Strategies. *Adv. Healthc. Mater.* **2023**, *12* (18), 2202936. https://doi.org/10.1002/adhm.202202936.
(61) Justus, C. R.; Marie, M. A.; Sanderlin, E. J.; Yang, L. V. Transwell In Vitro Cell Migration and Invasion Assays. *Methods Mol. Biol. Clifton NJ* **2023**, *2644*, 349–359. https://doi.org/10.1007/978-1-0716-3052-5_22.
(62) Williams, S. T.; Wells, G.; Conroy, S.; Gagg, H.; Allen, R.; Rominiyi, O.; Helleday, T.; Hullock, K.; Pennington, C. E. W.; Rantala, J.; Collis, S. J.; Danson, S. J. Precision Oncology Using Ex Vivo Technology: A Step towards Individualised Cancer Care? *Expert Rev. Mol. Med.* **2022**, *24*, e39. https://doi.org/10.1017/erm.2022.32.
(63) Bortel, P.; Hagn, G.; Skos, L.; Bileck, A.; Paulitschke, V.; Paulitschke, P.; Gleiter, L.; Mohr, T.; Gerner, C.; Meier-Menches, S. M. Memory Effects of Prior Subculture May Impact the Quality of Multiomic Perturbation Profiles. *Proc. Natl. Acad. Sci.* **2024**, *121* (29), e2313851121. https://doi.org/10.1073/pnas.2313851121.
(64) Wei, F.; Wang, S.; Gou, X. A Review for Cell-Based Screening Methods in Drug Discovery. *Biophys. Rep.* **2021**, *7* (6), 504–516. https://doi.org/10.52601/bpr.2021.210042.
(65) Lai, Y.; Chu, X.; Di, L.; Gao, W.; Guo, Y.; Liu, X.; Lu, C.; Mao, J.; Shen, H.; Tang, H.; Xia, C. Q.; Zhang, L.; Ding, X. Recent Advances in the Translation of Drug Metabolism and Pharmacokinetics Science for Drug Discovery and Development. *Acta Pharm. Sin. B* **2022**, *12* (6), 2751–2777. https://doi.org/10.1016/j.apsb.2022.03.009.
(66) Di Meo, A.; Sohaei, D.; Batruch, I.; Alexandrou, P.; Prassas, I.; Diamandis, E. P. Proteomic Profiling of the Human Tissue and Biological Fluid Proteome. *J. Proteome Res.* **2021**, *20* (1), 444–452. https://doi.org/10.1021/acs.jproteome.0c00502.
(67) Gheybi, E.; Hosseinzadeh, P.; Tayebi-Khorrami, V.; Rostami, M.; Soukhtanloo, M. Proteomics in Decoding Cancer: A Review. *Clin. Chim. Acta* **2025**, *574*, 120302. https://doi.org/10.1016/j.cca.2025.120302.
(68) Nagy, P.; Thorgeirsson, S. S.; Grisham, J. W. Organizational Principles of the Liver. In *The Liver*; Arias, I. M., Alter, H. J., Boyer, J. L., Cohen, D. E., Shafritz, D. A., Thorgeirsson, S. S., Wolkoff, A. W., Eds.; Wiley, 2020; pp 1–13. https://doi.org/10.1002/9781119436812.ch1.
(69) Geyer, P. E.; Voytik, E.; Treit, P. V.; Doll, S.; Kleinhempel, A.; Niu, L.; Müller, J. B.; Buchholtz, M.; Bader, J. M.; Teupser, D.; Holdt, L. M.; Mann, M. Plasma Proteome Profiling to Detect and Avoid Sample-related Biases in Biomarker Studies. *EMBO Mol. Med.* **2019**, *11* (11), e10427. https://doi.org/10.15252/emmm.201910427.
(70) Liu, Y.; Wu, W.; Cai, C.; Zhang, H.; Shen, H.; Han, Y. Patient-Derived Xenograft Models in Cancer Therapy: Technologies and Applications. *Signal Transduct. Target. Ther.* **2023**, *8* (1), 160. https://doi.org/10.1038/s41392-023-01419-2.
(71) Yang, Y.; Yang, H. H.; Hu, Y.; Watson, P. H.; Liu, H.; Geiger, T. R.; Anver, M. R.; Haines, D. C.; Martin, P.; Green, J. E.; Lee, M. P.; Hunter, K. W.; Wakefield, L. M. Immunocompetent Mouse Allograft Models for Development of Therapies to Target Breast Cancer Metastasis. *Oncotarget* **2017**, *8* (19), 30621–30643. https://doi.org/10.18632/oncotarget.15695.
(72) Stribbling, S. M.; Beach, C.; Ryan, A. J. Orthotopic and Metastatic Tumour Models in Preclinical Cancer Research. *Pharmacol. Ther.* **2024**, *257*, 108631. https://doi.org/10.1016/j.pharmthera.2024.108631.
(73) Kadam, J. D.; Kulkarni, Y. A. Experimental Animal Models of Chemically Induced Breast Cancer: An Update. *Rev. Senol. Patol. Mamar.* **2026**, *39* (1), 100730. https://doi.org/10.1016/j.senol.2025.100730.

(74) Al Shoyaib, A.; Archie, S. R.; Karamyan, V. T. Intraperitoneal Route of Drug Administration: Should It Be Used in Experimental Animal Studies? *Pharm. Res.* **2019**, *37* (1), 12. https://doi.org/10.1007/s11095-019-2745-x.
(75) Boike, L.; Henning, N. J.; Nomura, D. K. Advances in Covalent Drug Discovery. *Nat. Rev. Drug Discov.* **2022**, *21* (12), 881–898. https://doi.org/10.1038/s41573-022-00542-z.
(76) Faridoon; Ng, R.; Zhang, G.; Li, J. J. An Update on the Discovery and Development of Reversible Covalent Inhibitors. *Med. Chem. Res.* **2023**, *32* (6), 1039–1062. https://doi.org/10.1007/s00044-023-03065-3.
(77) Yip, D. W.; Gerriets, V. Penicillin. In *StatPearls [Online]*; StatPearls Publishing: Treasure Island (FL), 2026.
(78) Tuley, A.; Fast, W. The Taxonomy of Covalent Inhibitors. *Biochemistry* **2018**, *57* (24), 3326–3337. https://doi.org/10.1021/acs.biochem.8b00315.
(79) Vajda, S.; Beglov, D.; Wakefield, A. E.; Egbert, M.; Whitty, A. Cryptic Binding Sites on Proteins: Definition, Detection, and Druggability. *Curr. Opin. Chem. Biol.* **2018**, *44*, 1–8. https://doi.org/10.1016/j.cbpa.2018.05.003.
(80) Bhole, R. P.; Joshi, G. O.; Kapare, H. S.; Chikhale, R. V.; Chaudhari, S. Covalent Drug – An Emerging Framework for Targeted Drug Development. *Results Chem.* **2024**, *8*, 101615. https://doi.org/10.1016/j.rechem.2024.101615.
(81) Ertl, P.; Altmann, E.; McKenna, J. M. The Most Common Functional Groups in Bioactive Molecules and How Their Popularity Has Evolved over Time. *J. Med. Chem.* **2020**, *63* (15), 8408–8418. https://doi.org/10.1021/acs.jmedchem.0c00754.
(82) Mehta, N. V.; Degani, M. S. The Expanding Repertoire of Covalent Warheads for Drug Discovery. *Drug Discov. Today* **2023**, *28* (12), 103799. https://doi.org/10.1016/j.drudis.2023.103799.
(83) Hillebrand, L.; Liang, X. J.; Serafim, R. A. M.; Gehringer, M. Emerging and Re-Emerging Warheads for Targeted Covalent Inhibitors: An Update. *J. Med. Chem.* **2024**, *67* (10), 7668–7758. https://doi.org/10.1021/acs.jmedchem.3c01825.
(84) Kim, G.; Grams, R. J.; Hsu, K.-L. Advancing Covalent Ligand and Drug Discovery beyond Cysteine. *Chem. Rev.* **2025**, *125* (14), 6653–6684. https://doi.org/10.1021/acs.chemrev.5c00001.
(85) Butterworth, S.; Cross, D. A. E.; Finlay, M. R. V.; Ward, R. A.; Waring, M. J. The Structure-Guided Discovery of Osimertinib: The First U.S. FDA Approved Mutant Selective Inhibitor of EGFR T790M. *MedChemComm* **2017**, *8* (5), 820–822. https://doi.org/10.1039/c7md90012k.
(86) da Cunha-Bang, C.; Niemann, C. U. Targeting Bruton's Tyrosine Kinase Across B-Cell Malignancies. *Drugs* **2018**, *78* (16), 1653–1663. https://doi.org/10.1007/s40265-018-1003-6.
(87) Galli, M.; Migliano, F.; Fasano, V.; Silvani, A.; Passarella, D.; Citarella, A. Nirmatrelvir: From Discovery to Modern and Alternative Synthetic Approaches. *Processes* **2024**, *12* (6), 1242. https://doi.org/10.3390/pr12061242.
(88) Lanman, B. A.; Allen, J. R.; Allen, J. G.; Amegadzie, A. K.; Ashton, K. S.; Booker, S. K.; Chen, J. J.; Chen, N.; Frohn, M. J.; Goodman, G.; Kopecky, D. J.; Liu, L.; Lopez, P.; Low, J. D.; Ma, V.; Minatti, A. E.; Nguyen, T. T.; Nishimura, N.; Pickrell, A. J.; Reed, A. B.; Shin, Y.; Siegmund, A. C.; Tamayo, N. A.; Tegley, C. M.; Walton, M. C.; Wang, H.-L.; Wurz, R. P.; Xue, M.; Yang, K. C.; Achanta, P.; Bartberger, M. D.; Canon, J.; Hollis, L. S.; McCarter, J. D.; Mohr, C.; Rex, K.; Saiki, A. Y.; San Miguel, T.; Volak, L. P.; Wang, K. H.; Whittington, D. A.; Zech, S. G.; Lipford, J. R.; Cee, V. J. Discovery of a Covalent Inhibitor of KRASG12C (AMG 510) for the Treatment of Solid Tumors. *J. Med. Chem.* **2020**, *63* (1), 52–65. https://doi.org/10.1021/acs.jmedchem.9b01180.

(89) Binda, C.; Wang, J.; Li, M.; Hubalek, F.; Mattevi, A.; Edmondson, D. E. Structural and Mechanistic Studies of Arylalkylhydrazine Inhibition of Human Monoamine Oxidases A and B. *Biochemistry* **2008**, *47* (20), 5616–5625. https://doi.org/10.1021/bi8002814.
(90) Lu, W.; Kostic, M.; Zhang, T.; Che, J.; Patricelli, M. P.; Jones, L. H.; Chouchani, E. T.; Gray, N. S. Fragment-Based Covalent Ligand Discovery. *RSC Chem. Biol.* **2021**, *2* (2), 354–367. https://doi.org/10.1039/D0CB00222D.
(91) Bon, M.; Bilsland, A.; Bower, J.; McAulay, K. Fragment-based Drug Discovery—the Importance of High-quality Molecule Libraries. *Mol. Oncol.* **2022**, *16* (21), 3761–3777. https://doi.org/10.1002/1878-0261.13277.
(92) Harris, C. J.; Hill, R. D.; Sheppard, D. W.; Slater, M. J.; Stouten, P. F. W. The Design and Application of Target-Focused Compound Libraries. *Comb. Chem. High Throughput Screen.* **2011**, *14* (6), 521–531. https://doi.org/10.2174/138620711795767802.
(93) Carbery, A.; Skyner, R.; von Delft, F.; Deane, C. M. Fragment Libraries Designed to Be Functionally Diverse Recover Protein Binding Information More Efficiently Than Standard Structurally Diverse Libraries. *J. Med. Chem.* **2022**, *65* (16), 11404–11413. https://doi.org/10.1021/acs.jmedchem.2c01004.
(94) Imbernon, J. R.; Jacquemard, C.; Bret, G.; Marcou, G.; Kellenberger, E. Comprehensive Analysis of Commercial Fragment Libraries. *RSC Med. Chem.* **2022**, *13* (3), 300–310. https://doi.org/10.1039/D1MD00363A.
(95) *Chemicals for Drug Discovery*. Thermo Fisher Scientific - AT. https://www.thermofisher.com/uk/en/home/chemicals/applications/drug-discovery.html (accessed 2026-05-09).
(96) Chan, A. I.; McGregor, L. M.; Jain, T.; Liu, D. R. Discovery of a Covalent Kinase Inhibitor from a DNA-Encoded Small-Molecule Library × Protein Library Selection. *J. Am. Chem. Soc.* **2017**, *139* (30), 10192–10195. https://doi.org/10.1021/jacs.7b04880.
(97) Drewes, G.; Knapp, S. Chemoproteomics and Chemical Probes for Target Discovery. *Trends Biotechnol.* **2018**, *36* (12), 1275–1286. https://doi.org/10.1016/j.tibtech.2018.06.008.
(98) Fang, H.; Peng, B.; Ong, S. Y.; Wu, Q.; Li, L.; Yao, S. Q. Recent Advances in Activity-Based Probes (ABPs) and Affinity-Based Probes (AfBPs) for Profiling of Enzymes. *Chem. Sci.* **2021**, *12* (24), 8288–8310. https://doi.org/10.1039/D1SC01359A.
(99) Ma, N.; Zhang, Z.-M.; Lee, J.-S.; Cheng, K.; Lin, L.; Zhang, D.-M.; Hao, P.; Ding, K.; Ye, W.-C.; Li, Z. Affinity-Based Protein Profiling Reveals Cellular Targets of Photoreactive Anticancer Inhibitors. *ACS Chem. Biol.* **2019**, *14* (12), 2546–2552. https://doi.org/10.1021/acschembio.9b00784.
(100) Zhou, Y.-F.; Zhang, L.; Niu, Z. L.; Wang, Z. A. Targeting the Reactive Proteome: Recent Advances in Activity-Based Protein Profiling and Probe Design. *Biomolecules* **2025**, *15* (12), 1699. https://doi.org/10.3390/biom15121699.
(101) Wang, H.; Liu, L.; Zhang, Z.; Li, C.; Wang, K.; Gao, J.; Hu, Q.; Wang, W.; Li, H. Insights of Affinity-Based Probes for Target Identification in Drug Discovery. *Eur. J. Med. Chem.* **2025**, *293*, 117711. https://doi.org/10.1016/j.ejmech.2025.117711.
(102) Wang, S.; Zhang, Y.; Yu, R.; Chai, Y.; Liu, R.; Yu, J.; Qu, Z.; Zhang, W.; Zhuang, C. Labeled and Label-Free Target Identifications of Natural Products. *J. Med. Chem.* **2024**, *67* (20), 17980–17996. https://doi.org/10.1021/acs.jmedchem.4c01576.
(103) Chen, H.; Liu, H.; Tian, Y.; Liu, Y.; Tang, F.; Huang, J.; Peng, W.; Yang, J. Limited Proteolysis-Coupled Mass Spectrometry (LiP-MS): A Cutting-Edge Tool for De Novo Drug Target Discovery. *J. Proteome Res.* **2026**, *25* (1), 41–54. https://doi.org/10.1021/acs.jproteome.5c00565.
(104) Ren, Y.-S.; Li, H.-L.; Piao, X.-H.; Yang, Z.-Y.; Wang, S.-M.; Ge, Y.-W. Drug Affinity Responsive Target Stability (DARTS) Accelerated Small Molecules Target Discovery:

Principles and Application. *Biochem. Pharmacol.* **2021**, *194*, 114798. https://doi.org/10.1016/j.bcp.2021.114798.
(105) Li, K.; Chen, S.; Wang, K.; Wang, Y.; Xue, L.; Ye, Y.; Fang, Z.; Lyu, J.; Zhu, H.; Li, Y.; Yu, T.; Yang, F.; Zhang, X.; Guo, S.; Ruan, C.; Zhou, J.; Wang, Q.; Dong, M.; Luo, C.; Ye, M. A Peptide-Centric Local Stability Assay Enables Proteome-Scale Identification of the Protein Targets and Binding Regions of Diverse Ligands. *Nat. Methods* **2025**, *22* (2), 278–282. https://doi.org/10.1038/s41592-024-02553-7.
(106) Zou, Y.; Huang, C.-F.; Sturrock, G. R.; Kelleher, N. L.; Fitzgerald, M. C. Top-Down Stability of Proteins from Rates of Oxidation (TD-SPROX) Approach for Measuring Proteoform-Specific Folding Stability. *Anal. Chem.* **2024**, *96* (49), 19597–19604. https://doi.org/10.1021/acs.analchem.4c04469.
(107) Jafari, R.; Almqvist, H.; Axelsson, H.; Ignatushchenko, M.; Lundbäck, T.; Nordlund, P.; Molina, D. M. The Cellular Thermal Shift Assay for Evaluating Drug Target Interactions in Cells. *Nat. Protoc.* **2014**, *9* (9), 2100–2122. https://doi.org/10.1038/nprot.2014.138.
(108) Mateus, A.; Kurzawa, N.; Becher, I.; Sridharan, S.; Helm, D.; Stein, F.; Typas, A.; Savitski, M. M. Thermal Proteome Profiling for Interrogating Protein Interactions. *Mol. Syst. Biol.* **2020**, *16* (3), MSB199232. https://doi.org/10.15252/msb.20199232.
(109) Zecha, J.; Satpathy, S.; Kanashova, T.; Avanessian, S. C.; Kane, M. H.; Clauser, K. R.; Mertins, P.; Carr, S. A.; Kuster, B. TMT Labeling for the Masses: A Robust and Cost-Efficient, In-Solution Labeling Approach. *Mol. Cell. Proteomics* **2019**, *18* (7), 1468–1478. https://doi.org/10.1074/mcp.TIR119.001385.
(110) Restrepo-Pérez, L.; Wong, C. H.; Maglia, G.; Dekker, C.; Joo, C. Label-Free Detection of Post-Translational Modifications with a Nanopore. *Nano Lett.* **2019**, *19* (11), 7957–7964. https://doi.org/10.1021/acs.nanolett.9b03134.
(111) Li, W.; Wei, Q.; Llanos, M.; Gathmann, C.; Governa, P.; Chiu, T.-Y.; Wozniak, J. M.; Jadhav, A. M.; Holcomb, M.; Cravatt, J.; Dongre, A.; Huang, M. L.; Forli, S.; Parker, C. G. Posttranslational Modifications Remodel Proteome-Wide Ligandability. *Nat. Chem. Biol.* **2026**, 1–13. https://doi.org/10.1038/s41589-026-02216-y.
(112) Adelusi, T. I.; Oyedele, A.-Q. K.; Boyenle, I. D.; Ogunlana, A. T.; Adeyemi, R. O.; Ukachi, C. D.; Idris, M. O.; Olaoba, O. T.; Adedotun, I. O.; Kolawole, O. E.; Xiaoxing, Y.; Abdul-Hammed, M. Molecular Modeling in Drug Discovery. *Inform. Med. Unlocked* **2022**, *29*, 100880. https://doi.org/10.1016/j.imu.2022.100880.
(113) Ferenczy, G. G.; Keserű, G. M. Covalent Ligand Efficiency. *Drug Discov. Today* **2025**, *30* (9), 104454. https://doi.org/10.1016/j.drudis.2025.104454.
(114) Damghani, T.; Chitnis, S. P.; Abidakun, O. A.; Patel, K. B.; Lin, K. S.; Ouellette, E. A.; Lantry, A. M.; Heppner, D. E. Profiling and Optimizing Targeted Covalent Inhibitors through EGFR-Guided Studies. *J. Med. Chem.* **2025**, *68* (16), 17917–17932. https://doi.org/10.1021/acs.jmedchem.5c01661.
(115) Schaefer, D.; Cheng, X. Recent Advances in Covalent Drug Discovery. *Pharmaceuticals* **2023**, *16* (5), 663. https://doi.org/10.3390/ph16050663.
(116) Hameed, M. S.; Cao, H.; Guo, L.; Zeng, L.; Ren, Y. Advancements, Challenges, and Future Frontiers in Covalent Inhibitors and Covalent Drugs: A Review. *Eur. J. Med. Chem. Rep.* **2024**, *12*, 100217. https://doi.org/10.1016/j.ejmcr.2024.100217.
(117) Popow, J.; Farnaby, W.; Gollner, A.; Kofink, C.; Fischer, G.; Wurm, M.; Zollman, D.; Wijaya, A.; Mischerikow, N.; Hasenoehrl, C.; Prokofeva, P.; Arnhof, H.; Arce-Solano, S.; Bell, S.; Boeck, G.; Diers, E.; Frost, A. B.; Goodwin-Tindall, J.; Karolyi-Oezguer, J.; Khan, S.; Klawatsch, T.; Koegl, M.; Kousek, R.; Kratochvil, B.; Kropatsch, K.; Lauber, A. A.; McLennan, R.; Olt, S.; Peter, D.; Petermann, O.; Roessler, V.; Stolt-Bergner, P.; Strack, P.; Strauss, E.; Trainor, N.; Vetma, V.; Whitworth, C.; Zhong, S.; Quant, J.; Weinstabl, H.; Kuster, B.; Ettmayer, P.; Ciulli, A. Targeting Cancer with Small-Molecule

Pan-KRAS Degraders. *Science* **2024**, *385* (6715), 1338–1347. https://doi.org/10.1126/science.adm8684.
(118) Guo, T.; Steen, J. A.; Mann, M. Mass-Spectrometry-Based Proteomics: From Single Cells to Clinical Applications. *Nature* **2025**, *638* (8052), 901–911. https://doi.org/10.1038/s41586-025-08584-0.
(119) Legrain, P.; Aebersold, R.; Archakov, A.; Bairoch, A.; Bala, K.; Beretta, L.; Bergeron, J.; Borchers, C. H.; Corthals, G. L.; Costello, C. E.; Deutsch, E. W.; Domon, B.; Hancock, W.; He, F.; Hochstrasser, D.; Marko-Varga, G.; Salekdeh, G. H.; Sechi, S.; Snyder, M.; Srivastava, S.; Uhlén, M.; Wu, C. H.; Yamamoto, T.; Paik, Y.-K.; Omenn, G. S. The Human Proteome Project: Current State and Future Direction. *Mol. Cell. Proteomics* **2011**, *10* (7), 1–5. https://doi.org/10.1074/mcp.M111.009993.
(120) Morris, R.; Black, K. A.; Stollar, E. J. Uncovering Protein Function: From Classification to Complexes. *Essays Biochem.* **2022**, *66* (3), 255–285. https://doi.org/10.1042/EBC20200108.
(121) Castellano, S.; Andrés, A. M.; Bosch, E.; Bayes, M.; Guigó, R.; Clark, A. G. Low Exchangeability of Selenocysteine, the 21st Amino Acid, in Vertebrate Proteins. *Mol. Biol. Evol.* **2009**, *26* (9), 2031–2040. https://doi.org/10.1093/molbev/msp109.
(122) Craveur, P.; Narwani, T. J.; Rebehmed, J.; de Brevern, A. G. Investigation of the Impact of PTMs on the Protein Backbone Conformation. *Amino Acids* **2019**, *51* (7), 1065–1079. https://doi.org/10.1007/s00726-019-02747-w.
(123) Bagwan, N.; El Ali, H. H.; Lundby, A. Proteome-Wide Profiling and Mapping of Post Translational Modifications in Human Hearts. *Sci. Rep.* **2021**, *11* (1), 2184. https://doi.org/10.1038/s41598-021-81986-y.
(124) Bortel, P.; Piga, I.; Koenig, C.; Gerner, C.; Martinez-Val, A.; Olsen, J. V. Systematic Optimization of Automated Phosphopeptide Enrichment for High-Sensitivity Phosphoproteomics. *Mol. Cell. Proteomics* **2024**, *23* (5), 100754. https://doi.org/10.1016/j.mcpro.2024.100754.
(125) Jiang, Y.; Rex, D. A. B.; Schuster, D.; Neely, B. A.; Rosano, G. L.; Volkmar, N.; Momenzadeh, A.; Peters-Clarke, T. M.; Egbert, S. B.; Kreimer, S.; Doud, E. H.; Crook, O. M.; Yadav, A. K.; Vanuopadath, M.; Hegeman, A. D.; Mayta, M. L.; Duboff, A. G.; Riley, N. M.; Moritz, R. L.; Meyer, J. G. Comprehensive Overview of Bottom-Up Proteomics Using Mass Spectrometry. *ACS Meas. Sci. Au* **2024**, *4* (4), 338–417. https://doi.org/10.1021/acsmeasuresciau.3c00068.
(126) Rothenberg, D. A.; Taliaferro, J. M.; Huber, S. M.; Begley, T. J.; Dedon, P. C.; White, F. M. A Proteomics Approach to Profiling the Temporal Translational Response to Stress and Growth. *iScience* **2018**, *9*, 367–381. https://doi.org/10.1016/j.isci.2018.11.004.
(127) Eckert, S.; Berner, N.; Kramer, K.; Schneider, A.; Müller, J.; Lechner, S.; Brajkovic, S.; Sakhteman, A.; Graetz, C.; Fackler, J.; Dudek, M.; Pfaffl, M. W.; Knolle, P.; Wilhelm, S.; Kuster, B. Decrypting the Molecular Basis of Cellular Drug Phenotypes by Dose-Resolved Expression Proteomics. *Nat. Biotechnol.* **2025**, *43* (3), 406–415. https://doi.org/10.1038/s41587-024-02218-y.
(128) Gao, Y.; Ma, M.; Li, W.; Lei, X. Chemoproteomics, A Broad Avenue to Target Deconvolution. *Adv. Sci.* **2024**, *11* (8), 2305608. https://doi.org/10.1002/advs.202305608.
(129) Kozoriz, K.; Lee, J.-S. Chemical Proteomics for a Comprehensive Understanding of Functional Activity and the Interactome. *Chem. Soc. Rev.* **2025**, *54* (13), 6186–6207. https://doi.org/10.1039/D5CS00381D.
(130) Cupp-Sutton, K. A.; Wu, S. High-Throughput Quantitative Top-down Proteomics. *Mol. Omics* **2020**, *16* (2), 91–99. https://doi.org/10.1039/C9MO00154A.
(131) Neuditschko, B.; King, A. P.; Huang, Z.; Janker, L.; Bileck, A.; Borutzki, Y.; Marker, S. C.; Gerner, C.; Wilson, J. J.; Meier-Menches, S. M. An Anticancer Rhenium Tricarbonyl

Targets Fe−S Cluster Biogenesis in Ovarian Cancer Cells. *Angew. Chem. Int. Ed.* **2022**, *61* (43), e202209136. https://doi.org/10.1002/anie.202209136.
(132) Chen, B.; Brown, K. A.; Lin, Z.; Ge, Y. Top-Down Proteomics: Ready for Prime Time? *Anal. Chem.* **2018**, *90* (1), 110–127. https://doi.org/10.1021/acs.analchem.7b04747.
(133) Alanazi, S. Recent Advances in Liquid Chromatography–Mass Spectrometry (LC–MS) Applications in Biological and Applied Sciences. *Anal. Sci. Adv.* **2025**, *6* (1), e70024. https://doi.org/10.1002/ansa.70024.
(134) Chen, C.; Hou, J.; Tanner, J. J.; Cheng, J. Bioinformatics Methods for Mass Spectrometry-Based Proteomics Data Analysis. *Int. J. Mol. Sci.* **2020**, *21* (8), 2873. https://doi.org/10.3390/ijms21082873.
(135) D'Atri, V.; Barrientos, R. C.; Losacco, G. L.; Rudaz, S.; Delobel, A.; Regalado, E. L.; Guillarme, D. Trends in Pharmaceutical Analysis: The Evolving Role of Liquid Chromatography. *Anal. Chem.* **2025**, *97* (9), 4706–4727. https://doi.org/10.1021/acs.analchem.4c06662.
(136) Mitulović, G. New HPLC Techniques for Proteomics Analysis: A Short Overview of Latest Developments. *J. Liq. Chromatogr. Relat. Technol.* **2015**, *38* (3), 390–403. https://doi.org/10.1080/10826076.2014.941266.
(137) Lenčo, J.; Jadeja, S.; Naplekov, D. K.; Krokhin, O. V.; Khalikova, M. A.; Chocholouš, P.; Urban, J.; Broeckhoven, K.; Nováková, L.; Švec, F. Reversed-Phase Liquid Chromatography of Peptides for Bottom-Up Proteomics: A Tutorial. *J. Proteome Res.* **2022**, *21* (12), 2846–2892. https://doi.org/10.1021/acs.jproteome.2c00407.
(138) Poole, C. F.; Lenca, N. Reversed-Phase Liquid Chromatography. In *Liquid Chromatography*; Elsevier, 2017; pp 91–123. https://doi.org/10.1016/B978-0-12-805393-5.00004-X.
(139) Hung, M.-M.; Elpa, D. P.; Ochirov, O.; Urban, P. L. Critical Role of Voltage Application Points in "Analog" and "Digital" Electrospray Ionization Mass Spectrometry. *J. Am. Soc. Mass Spectrom.* **2025**, *36* (5), 1191–1199. https://doi.org/10.1021/jasms.5c00082.
(140) Ho, C.; Lam, C.; Chan, M.; Cheung, R.; Law, L.; Lit, L.; Ng, K.; Suen, M.; Tai, H. Electrospray Ionisation Mass Spectrometry: Principles and Clinical Applications. *Clin. Biochem. Rev.* **2003**, *24* (1), 3–12.
(141) Banerjee, S.; Mazumdar, S. Electrospray Ionization Mass Spectrometry: A Technique to Access the Information beyond the Molecular Weight of the Analyte. *Int. J. Anal. Chem.* **2012**, *2012* (1), 282574. https://doi.org/10.1155/2012/282574.
(142) Geue, N. Modern Electrospray Ionization Mass Spectrometry Techniques for the Characterization of Supramolecules and Coordination Compounds. *Anal. Chem.* **2024**, *96* (19), 7332–7341. https://doi.org/10.1021/acs.analchem.4c01028.
(143) Shan, L.; Jones, B. R. Nano-LC: An Updated Review. *Biomed. Chromatogr.* **2022**, *36* (5), e5317. https://doi.org/10.1002/bmc.5317.
(144) Chen, S.; Zeng, J.; Zhang, Z.; Xu, B.; Zhang, B. Recent Advancements in Nanoelectrospray Ionization Interface and Coupled Devices. *J. Chromatogr. Open* **2022**, *2*, 100064. https://doi.org/10.1016/j.jcoa.2022.100064.
(145) Asensio-Ramos, M.; Fanali, C.; D'Orazio, G.; Fanali, S. Nano-Liquid Chromatography. In *Liquid Chromatography*; Elsevier, 2017; pp 637–695. https://doi.org/10.1016/B978-0-12-805393-5.00027-0.
(146) Chetwynd, A. J.; David, A. A Review of Nanoscale LC-ESI for Metabolomics and Its Potential to Enhance the Metabolome Coverage. *Talanta* **2018**, *182*, 380–390. https://doi.org/10.1016/j.talanta.2018.01.084.
(147) Li, C.; Chu, S.; Tan, S.; Yin, X.; Jiang, Y.; Dai, X.; Gong, X.; Fang, X.; Tian, D. Towards Higher Sensitivity of Mass Spectrometry: A Perspective From the Mass Analyzers. *Front. Chem.* **2021**, *9*, 813359. https://doi.org/10.3389/fchem.2021.813359.

(148) Yang, L.; Gu, Y.; Gong, H.; Liu, Z.; Xiong, X.; Fang, X. Development and Research of the Quadrupole Mass Spectrometry Simulation Model with the Entire Ion Optics System. *Sci. Rep.* **2025**, *15* (1), 7510. https://doi.org/10.1038/s41598-025-91747-w.
(149) Tsakalof, A.; Sysoev, A. A.; Vyatkina, K. V.; Eganov, A. A.; Eroshchenko, N. N.; Kiryushin, A. N.; Adamov, A. Y.; Danilova, E. Y.; Nosyrev, A. E. Current Role and Potential of Triple Quadrupole Mass Spectrometry in Biomedical Research and Clinical Applications. *Molecules* **2024**, *29* (23), 5808. https://doi.org/10.3390/molecules29235808.
(150) Doerr, A. Mass Spectrometry–Based Targeted Proteomics. *Nat. Methods* **2013**, *10* (1), 23–23. https://doi.org/10.1038/nmeth.2286.
(151) Nolting, D.; Malek, R.; Makarov, A. Ion Traps in Modern Mass Spectrometry. *Mass Spectrom. Rev.* **2019**, *38* (2), 150–168. https://doi.org/10.1002/mas.21549.
(152) Zhang, X.; Wang, Y.; Hu, L.; Guo, D.; Fang, X.; Zhou, M.; Xu, W. Reducing Space Charge Effects in a Linear Ion Trap by Rhombic Ion Excitation and Ejection. *J. Am. Soc. Mass Spectrom.* **2016**, *27* (7), 1256–1262. https://doi.org/10.1007/s13361-016-1393-1.
(153) Scigelova, M.; Makarov, A. Orbitrap Mass Analyzer – Overview and Applications in Proteomics. *PROTEOMICS* **2006**, *6* (S2), 16–21. https://doi.org/10.1002/pmic.200600528.
(154) Eliuk, S.; Makarov, A. Evolution of Orbitrap Mass Spectrometry Instrumentation. *Annu. Rev. Anal. Chem.* **2015**, *8* (1), 61–80. https://doi.org/10.1146/annurev-anchem-071114-040325.
(155) Brais, C. J.; Ibañez, J. O.; Schwartz, A. J.; Ray, S. J. Recent Advances in Instrumental Approaches to Time-of-Flight Mass Spectrometry. *Mass Spectrom. Rev.* **2021**, *40* (5), 647–669. https://doi.org/10.1002/mas.21650.
(156) Jeanne Dit Fouque, K.; Fernandez-Lima, F. Recent Advances in Biological Separations Using Trapped Ion Mobility Spectrometry – Mass Spectrometry. *TrAC Trends Anal. Chem.* **2019**, *116*, 308–315. https://doi.org/10.1016/j.trac.2019.04.010.
(157) *PASEF*. Bruker. https://www.bruker.com/en/products-and-solutions/mass-spectrometry/timstof/pasef.html (accessed 2026-02-19).
(158) Guo, J.; Huan, T. Comparison of Full-Scan, Data-Dependent, and Data-Independent Acquisition Modes in Liquid Chromatography–Mass Spectrometry Based Untargeted Metabolomics. *Anal. Chem.* **2020**, *92* (12), 8072–8080. https://doi.org/10.1021/acs.analchem.9b05135.
(159) Aebersold, R.; Mann, M. Mass-Spectrometric Exploration of Proteome Structure and Function. *Nature* **2016**, *537* (7620), 347–355. https://doi.org/10.1038/nature19949.
(160) Wu, C.; Lei, J.; Meng, F.; Wang, X.; Wong, C. J.; Peng, J.; Lin, G.; Gingras, A.-C.; Ma, J.; Zhang, S. Trace Sample Proteome Quantification by Data-Dependent Acquisition without Dynamic Exclusion. *Anal. Chem.* **2023**, *95* (49), 17981–17987. https://doi.org/10.1021/acs.analchem.3c03357.
(161) Kitata, R. B.; Yang, J.-C.; Chen, Y.-J. Advances in Data-Independent Acquisition Mass Spectrometry towards Comprehensive Digital Proteome Landscape. *Mass Spectrom. Rev.* **2023**, *42* (6), 2324–2348. https://doi.org/10.1002/mas.21781.
(162) *MaxQuant*. MaxQuant. https://maxquant.org/ (accessed 2026-05-18).
(163) *Proteome Discoverer Software*. Thermo Fisher Scientific - AT. https://www.thermofisher.com/uk/en/home/industrial/mass-spectrometry/liquid-chromatography-mass-spectrometry-lc-ms/lc-ms-software/multi-omics-data-analysis/proteome-discoverer-software.html (accessed 2026-03-21).
(164) *FragPipe*. FragPipe. https://fragpipe.nesvilab.org/ (accessed 2026-03-21).
(165) *UniProt*. UniProt. https://www.uniprot.org (accessed 2026-03-21).

(166) Chen, C.; Hou, J.; Tanner, J. J.; Cheng, J. Bioinformatics Methods for Mass Spectrometry-Based Proteomics Data Analysis. *Int. J. Mol. Sci.* **2020**, *21* (8), 2873. https://doi.org/10.3390/ijms21082873.
(167) Benjamini, Y.; Hochberg, Y. Controlling the False Discovery Rate: A Practical and Powerful Approach to Multiple Testing. *J. R. Stat. Soc. Ser. B Methodol.* **1995**, *57* (1), 289–300. https://doi.org/10.1111/j.2517-6161.1995.tb02031.x.
(168) Searle, B. C.; Swearingen, K. E.; Barnes, C. A.; Schmidt, T.; Gessulat, S.; Küster, B.; Wilhelm, M. Generating High Quality Libraries for DIA MS with Empirically Corrected Peptide Predictions. *Nat. Commun.* **2020**, *11* (1), 1548. https://doi.org/10.1038/s41467-020-15346-1.
(169) Sinitcyn, P.; Hamzeiy, H.; Salinas Soto, F.; Itzhak, D.; McCarthy, F.; Wichmann, C.; Steger, M.; Ohmayer, U.; Distler, U.; Kaspar-Schoenefeld, S.; Prianichnikov, N.; Yılmaz, Ş.; Rudolph, J. D.; Tenzer, S.; Perez-Riverol, Y.; Nagaraj, N.; Humphrey, S. J.; Cox, J. MaxDIA Enables Library-Based and Library-Free Data-Independent Acquisition Proteomics. *Nat. Biotechnol.* **2021**, *39* (12), 1563–1573. https://doi.org/10.1038/s41587-021-00968-7.
(170) Zhang, F.; Ge, W.; Huang, L.; Li, D.; Liu, L.; Dong, Z.; Xu, L.; Ding, X.; Zhang, C.; Sun, Y.; A, J.; Gao, J.; Guo, T. A Comparative Analysis of Data Analysis Tools for Data-Independent Acquisition Mass Spectrometry. *Mol. Cell. Proteomics* **2023**, *22* (9), 100623. https://doi.org/10.1016/j.mcpro.2023.100623.
(171) Calderón-Celis, F.; Encinar, J. R.; Sanz-Medel, A. Standardization Approaches in Absolute Quantitative Proteomics with Mass Spectrometry. *Mass Spectrom. Rev.* **2018**, *37* (6), 715–737. https://doi.org/10.1002/mas.21542.
(172) Hutchinson-Bunch, C.; Sanford, J. A.; Hansen, J. R.; Gritsenko, M. A.; Rodland, K. D.; Piehowski, P. D.; Qian, W.-J.; Adkins, J. N. Assessment of TMT Labeling Efficiency in Large-Scale Quantitative Proteomics: The Critical Effect of Sample pH. *ACS Omega* **2021**, *6* (19), 12660–12666. https://doi.org/10.1021/acsomega.1c00776.
(173) Griffin, T. J.; Xie, H.; Bandhakavi, S.; Popko, J.; Mohan, A.; Carlis, J. V.; Higgins, L. iTRAQ Reagent-Based Quantitative Proteomic Analysis on a Linear Ion Trap Mass Spectrometer. *J. Proteome Res.* **2007**, *6* (11), 4200–4209. https://doi.org/10.1021/pr070291b.
(174) Savitski, M. M.; Mathieson, T.; Zinn, N.; Sweetman, G.; Doce, C.; Becher, I.; Pachl, F.; Kuster, B.; Bantscheff, M. Measuring and Managing Ratio Compression for Accurate iTRAQ/TMT Quantification. *J. Proteome Res.* **2013**, *12* (8), 3586–3598. https://doi.org/10.1021/pr400098r.
(175) Ong, S.-E.; Blagoev, B.; Kratchmarova, I.; Kristensen, D. B.; Steen, H.; Pandey, A.; Mann, M. Stable Isotope Labeling by Amino Acids in Cell Culture, SILAC, as a Simple and Accurate Approach to Expression Proteomics. *Mol. Cell. Proteomics* **2002**, *1* (5), 376–386. https://doi.org/10.1074/mcp.M200025-MCP200.
(176) Gao, B.-B.; Stuart, L.; Feener, E. P. Label-Free Quantitative Analysis of One-Dimensional PAGE LC/MS/MS Proteome: Application on Angiotensin II-Stimulated Smooth Muscle Cells Secretome. *Mol. Cell. Proteomics* **2008**, *7* (12), 2399–2409. https://doi.org/10.1074/mcp.M800104-MCP200.
(177) Blein-Nicolas, M.; Zivy, M. Thousand and One Ways to Quantify and Compare Protein Abundances in Label-Free Bottom-up Proteomics. *Biochim. Biophys. Acta BBA - Proteins Proteomics* **2016**, *1864* (8), 883–895. https://doi.org/10.1016/j.bbapap.2016.02.019.
(178) Goeminne, L. J. E.; Gevaert, K.; Clement, L. Experimental Design and Data-Analysis in Label-Free Quantitative LC/MS Proteomics: A Tutorial with MSqRob. *J. Proteomics* **2018**, *171*, 23–36. https://doi.org/10.1016/j.jprot.2017.04.004.

(179) Dowell, J. A.; Wright, L. J.; Armstrong, E. A.; Denu, J. M. Benchmarking Quantitative Performance in Label-Free Proteomics. *ACS Omega* **2021**, *6* (4), 2494–2504. https://doi.org/10.1021/acsomega.0c04030.
(180) Callister, S. J.; Barry, R. C.; Adkins, J. N.; Johnson, E. T.; Qian, W.; Webb-Robertson, B.-J. M.; Smith, R. D.; Lipton, M. S. Normalization Approaches for Removing Systematic Biases Associated with Mass Spectrometry and Label-Free Proteomics. *J. Proteome Res.* **2006**, *5* (2), 277–286. https://doi.org/10.1021/pr050300l.
(181) Megger, D. A.; Pott, L. L.; Ahrens, M.; Padden, J.; Bracht, T.; Kuhlmann, K.; Eisenacher, M.; Meyer, H. E.; Sitek, B. Comparison of Label-Free and Label-Based Strategies for Proteome Analysis of Hepatoma Cell Lines. *Biochim. Biophys. Acta BBA - Proteins Proteomics* **2014**, *1844* (5), 967–976. https://doi.org/10.1016/j.bbapap.2013.07.017.
(182) *Perseus*. MaxQuant. https://maxquant.org/perseus/ (accessed 2026-05-18).
(183) *Spectronaut®*. Biognosys. https://biognosys.com/software/spectronaut/ (accessed 2026-05-18).
(184) Marsh, A. N.; Sharma, V.; Mani, S. K.; Vitek, O.; MacCoss, M. J.; MacLean, B. X. Skyline Batch: An Intuitive User Interface for Batch Processing with Skyline. *J. Proteome Res.* **2022**, *21* (1), 289–294. https://doi.org/10.1021/acs.jproteome.1c00749.
(185) Jones, J.; MacKrell, E. J.; Wang, T.-Y.; Lomenick, B.; Roukes, M. L.; Chou, T.-F. Tidyproteomics: An Open-Source R Package and Data Object for Quantitative Proteomics Post Analysis and Visualization. *BMC Bioinformatics* **2023**, *24* (1), 239. https://doi.org/10.1186/s12859-023-05360-7.
(186) Strauss, M. T.; Bludau, I.; Zeng, W.-F.; Voytik, E.; Ammar, C.; Schessner, J. P.; Ilango, R.; Gill, M.; Meier, F.; Willems, S.; Mann, M. AlphaPept: A Modern and Open Framework for MS-Based Proteomics. *Nat. Commun.* **2024**, *15* (1), 2168. https://doi.org/10.1038/s41467-024-46485-4.
(187) Neuditschko, B.; Legin, A. A.; Baier, D.; Schintlmeister, A.; Reipert, S.; Wagner, M.; Keppler, B. K.; Berger, W.; Meier-Menches, S. M.; Gerner, C. Interaction with Ribosomal Proteins Accompanies Stress Induction of the Anticancer Metallodrug BOLD-100/KP1339 in the Endoplasmic Reticulum. *Angew. Chem. Int. Ed.* **2021**, *60* (10), 5063–5068. https://doi.org/10.1002/anie.202015962.
(188) Meier, S. M.; Kreutz, D.; Winter, L.; Klose, M. H. M.; Cseh, K.; Weiss, T.; Bileck, A.; Alte, B.; Mader, J. C.; Jana, S.; Chatterjee, A.; Bhattacharyya, A.; Hejl, M.; Jakupec, M. A.; Heffeter, P.; Berger, W.; Hartinger, C. G.; Keppler, B. K.; Wiche, G.; Gerner, C. An Organoruthenium Anticancer Agent Shows Unexpected Target Selectivity For Plectin. *Angew. Chem. Int. Ed.* **2017**, *56* (28), 8267–8271. https://doi.org/10.1002/anie.201702242.
(189) *STRING: functional protein association networks*. STRING Consortium. https://string-db.org/ (accessed 2026-03-10).
(190) *DAVID Functional Annotation Bioinformatics Microarray Analysis*. National Institutes of Health. https://davidbioinformatics.nih.gov/ (accessed 2026-03-10).
(191) *Gene Ontology overview*. Gene Ontology Resource. http://geneontology.org/docs/ontology-documentation/ (accessed 2026-03-10).
(192) Li, Z.; Weller, C. A.; Shah, S.; Johnson, N. L.; Hao, Y.; Jarreau, P. B.; Roberts, J.; Guha, D.; Bereda, C.; Klaisner, S.; Machado, P.; Zanovello, M.; Prudencio, M.; Oskarsson, B.; Staff, N. P.; Dickson, D. W.; Fratta, P.; Petrucelli, L.; Narayan, P.; Cookson, M. R.; Ward, M. E.; Singleton, A. B.; Nalls, M. A.; Qi, Y. A. ProtPipe: A Multifunctional Data Analysis Pipeline for Proteomics and Peptidomics. *Genomics Proteomics Bioinformatics* **2024**, *22* (6), qzae083. https://doi.org/10.1093/gpbjnl/qzae083.
(193) Mjos, K. D.; Orvig, C. Metallodrugs in Medicinal Inorganic Chemistry. *Chem. Rev.* **2014**, *114* (8), 4540–4563. https://doi.org/10.1021/cr400460s.

(194) Boros, E.; Dyson, P. J.; Gasser, G. Classification of Metal-Based Drugs According to Their Mechanisms of Action. *Chem* **2020**, *6* (1), 41–60. https://doi.org/10.1016/j.chempr.2019.10.013.
(195) Varghese, T. P.; John, A.; Mathew, J. Revolutionizing Cancer Treatment: The Role of Radiopharmaceuticals in Modern Cancer Therapy. *Precis. Radiat. Oncol.* **2024**, *8* (3), 145–152. https://doi.org/10.1002/pro6.1239.
(196) O'Dowd, P. D.; Sutcliffe, D. F.; Griffith, D. M. Oxaliplatin and Its Derivatives – An Overview. *Coord. Chem. Rev.* **2023**, *497*, 215439. https://doi.org/10.1016/j.ccr.2023.215439.
(197) Johnstone, T. C.; Suntharalingam, K.; Lippard, S. J. The Next Generation of Platinum Drugs: Targeted Pt(II) Agents, Nanoparticle Delivery, and Pt(IV) Prodrugs. *Chem. Rev.* **2016**, *116* (5), 3436–3486. https://doi.org/10.1021/acs.chemrev.5b00597.
(198) Jin, S.; Feng, C.; Wang, X. DNA or Not DNA —That Is the Question Determining the Design of Platinum Anticancer Drugs. *Eur. J. Med. Chem.* **2025**, *282*, 117077. https://doi.org/10.1016/j.ejmech.2024.117077.
(199) Lee, J. A.; Berg, E. L. Neoclassic Drug Discovery: The Case for Lead Generation Using Phenotypic and Functional Approaches. *SLAS Discov.* **2013**, *18* (10), 1143–1155. https://doi.org/10.1177/1087057113506118.
(200) Bold Therapeutics, Inc. *A Phase 1b&2a Dose Escalation Study of BOLD-100 in Combination With FOLFOX Chemotherapy in Patients With Advanced Solid Tumours*; Clinical trial registration NCT04421820; clinicaltrials.gov, 2026. https://clinicaltrials.gov/study/NCT04421820 (accessed 2026-04-12).
(201) Baier, D.; Mendrina, T.; Schoenhacker-Alte, B.; Pirker, C.; Mohr, T.; Rusz, M.; Regner, B.; Schaier, M.; Sgarioto, N.; Raynal, N. J.-M.; Nowikovsky, K.; Schmidt, W. M.; Heffeter, P.; Meier-Menches, S. M.; Koellensperger, G.; Keppler, B. K.; Berger, W. The Lipid Metabolism as Target and Modulator of BOLD-100 Anticancer Activity: Crosstalk with Histone Acetylation. *Adv. Sci.* **2023**, *10* (32), 2301939. https://doi.org/10.1002/advs.202301939.
(202) Theralase® Technologies Inc. *Intravesical Photodynamic Therapy ("PDT") in BCG-Unresponsive/Intolerant Non-Muscle Invasive Bladder Cancer ("NMIBC") Patients*; Clinical trial registration NCT03945162; clinicaltrials.gov, 2025. https://clinicaltrials.gov/study/NCT03945162 (accessed 2026-04-12).
(203) Kaspler, P.; Lazic, S.; Forward, S.; Arenas, Y.; Mandel, A.; Lilge, L. A Ruthenium(II) Based Photosensitizer and Transferrin Complexes Enhance Photo-Physical Properties, Cell Uptake, and Photodynamic Therapy Safety and Efficacy. *Photochem. Photobiol. Sci.* **2016**, *15* (4), 481–495. https://doi.org/10.1039/C5PP00450K.
(204) Shen, S.; Shen, J.; Luo, Z.; Wang, F.; Min, J. Molecular Mechanisms and Clinical Implications of the Gold Drug Auranofin. *Coord. Chem. Rev.* **2023**, *493*, 215323. https://doi.org/10.1016/j.ccr.2023.215323.
(205) Giorgini, D.; Chiaverini, L.; Viviano, M.; Belvedere, R.; Salerno, S.; Baglini, E.; Da Settimo, F.; Marzo, T.; Taliani, S.; Barresi, E. Repurposing Auranofin for Oncology and Beyond: A Brief Overview of Clinical Trials as Mono- and Combination Therapy. *Pharmaceuticals* **2025**, *18* (11), 1628. https://doi.org/10.3390/ph18111628.
(206) Mayo Clinic. *A Pilot Trial to Evaluate the Feasibility Auranofin (Ridaura®) for Asymptomatic Patients With First-Recurrence Epithelial Ovarian Cancer*; Clinical trial registration NCT01747798; clinicaltrials.gov, 2019. https://clinicaltrials.gov/study/NCT01747798 (accessed 2026-05-11).
(207) Diaz, R. S. *Multi Interventional Approaches to Mitigate HIV Reservoirs Aiming the Sustained HIV Remission Without Use of Antiretrovirals*; Clinical trial registration NCT06805656; clinicaltrials.gov, 2025. https://clinicaltrials.gov/study/NCT06805656 (accessed 2026-05-11).

(208) The Aurum Institute NPC. *A Ph2 Randomized Trial to Evaluate the Safety Preliminary Efficacy and Biomarker Response of Host Directed Therapies Added to Rifabutin-Modified Standard Therapy in Adults With Drug-Sensitive Smear-Positive Pulmonary TB*; Clinical trial registration NCT02968927; clinicaltrials.gov, 2019. https://clinicaltrials.gov/study/NCT02968927 (accessed 2026-05-12).
(209) Hennrich, U.; Eder, M. [177Lu]Lu-PSMA-617 (PluvictoTM): The First FDA-Approved Radiotherapeutical for Treatment of Prostate Cancer. *Pharmaceuticals* **2022**, *15* (10), 1292. https://doi.org/10.3390/ph15101292.
(210) Kim, W. K.; An, J. M.; Lim, Y. J.; Kim, K.; Kim, Y. H.; Kim, D. Recent Advances in Metallodrug: Coordination-Induced Synergy between Clinically Approved Drugs and Metal Ions. *Mater. Today Adv.* **2025**, *25*, 100569. https://doi.org/10.1016/j.mtadv.2025.100569.
(211) Englinger, B.; Pirker, C.; Heffeter, P.; Terenzi, A.; Kowol, C. R.; Keppler, B. K.; Berger, W. Metal Drugs and the Anticancer Immune Response. *Chem. Rev.* **2019**, *119* (2), 1519–1624. https://doi.org/10.1021/acs.chemrev.8b00396.
(212) Meier-Menches, S. M.; Zappe, K.; Bileck, A.; Kreutz, D.; Tahir, A.; Cichna-Markl, M.; Gerner, C. Time-Dependent Shotgun Proteomics Revealed Distinct Effects of an Organoruthenium Prodrug and Its Activation Product on Colon Carcinoma Cells. *Metallomics* **2019**, *11* (1), 118–127. https://doi.org/10.1039/C8MT00152A.
(213) Wernitznig, D.; Meier-Menches, S. M.; Cseh, K.; Theiner, S.; Wenisch, D.; Schweikert, A.; Jakupec, M. A.; Koellensperger, G.; Wernitznig, A.; Sommergruber, W.; Keppler, B. K. Plecstatin-1 Induces an Immunogenic Cell Death Signature in Colorectal Tumour Spheroids. *Metallomics* **2020**, *12* (12), 2121–2133. https://doi.org/10.1039/d0mt00227e.
(214) Prechova, M.; Adamova, Z.; Schweizer, A.-L.; Maninova, M.; Bauer, A.; Kah, D.; Meier-Menches, S. M.; Wiche, G.; Fabry, B.; Gregor, M. Plectin-Mediated Cytoskeletal Crosstalk Controls Cell Tension and Cohesion in Epithelial Sheets. *J. Cell Biol.* **2022**, *221* (3), e202105146. https://doi.org/10.1083/jcb.202105146.
(215) Bhattacharya, S.; Adon, T.; Dsouza, K.; Kumar, H. Y. Exploring the Future of Metal-Based Anticancer Agents: A Comprehensive Review of Ruthenium-Based Complexes. *ChemistrySelect* **2025**, *10* (9), e202404147. https://doi.org/10.1002/slct.202404147.
(216) Rilak Simović, A.; Masnikosa, R.; Bratsos, I.; Alessio, E. Chemistry and Reactivity of Ruthenium(II) Complexes: DNA/Protein Binding Mode and Anticancer Activity Are Related to the Complex Structure. *Coord. Chem. Rev.* **2019**, *398*, 113011. https://doi.org/10.1016/j.ccr.2019.07.008.
(217) Adhireksan, Z.; Davey, G. E.; Campomanes, P.; Groessl, M.; Clavel, C. M.; Yu, H.; Nazarov, A. A.; Yeo, C. H. F.; Ang, W. H.; Dröge, P.; Rothlisberger, U.; Dyson, P. J.; Davey, C. A. Ligand Substitutions between Ruthenium–Cymene Compounds Can Control Protein versus DNA Targeting and Anticancer Activity. *Nat. Commun.* **2014**, *5* (1), 3462. https://doi.org/10.1038/ncomms4462.
(218) Meier-Menches, S. M.; Gerner, C.; Berger, W.; Hartinger, C. G.; Keppler, B. K. Structure–Activity Relationships for Ruthenium and Osmium Anticancer Agents – towards Clinical Development. *Chem. Soc. Rev.* **2018**, *47* (3), 909–928. https://doi.org/10.1039/C7CS00332C.
(219) Jürgens, S.; Scalcon, V.; Estrada-Ortiz, N.; Folda, A.; Tonolo, F.; Jandl, C.; Browne, D. L.; Rigobello, M. P.; Kühn, F. E.; Casini, A. Exploring the C^N^C Theme: Synthesis and Biological Properties of Tridentate Cyclometalated Gold(III) Complexes. *Bioorg. Med. Chem.* **2017**, *25* (20), 5452–5460. https://doi.org/10.1016/j.bmc.2017.08.001.
(220) Meier, S. M.; Gerner, C.; Keppler, B. K.; Cinellu, M. A.; Casini, A. Mass Spectrometry Uncovers Molecular Reactivities of Coordination and Organometallic Gold(III) Drug Candidates in Competitive Experiments That Correlate with Their Biological Effects. *Inorg. Chem.* **2016**, *55* (9), 4248–4259. https://doi.org/10.1021/acs.inorgchem.5b03000.

(221) Thomas, S. R.; Bonsignore, R.; Sánchez Escudero, J.; Meier-Menches, S. M.; Brown, C. M.; Wolf, M. O.; Barone, G.; Luk, L. Y. P.; Casini, A. Exploring the Chemoselectivity towards Cysteine Arylation by Cyclometallated Au^{III} Compounds: New Mechanistic Insights. *ChemBioChem* **2020**, *21* (21), 3071–3076. https://doi.org/10.1002/cbic.202000262.
(222) de Paiva, R. E. F.; Du, Z.; Nakahata, D. H.; Lima, F. A.; Corbi, P. P.; Farrell, N. P. Gold-Catalyzed C–S Aryl-Group Transfer in Zinc Finger Proteins. *Angew. Chem. Int. Ed.* **2018**, *57* (30), 9305–9309. https://doi.org/10.1002/anie.201803082.
(223) Kung, K. K.-Y.; Ko, H.-M.; Cui, J.-F.; Chong, H.-C.; Leung, Y.-C.; Wong, M.-K. Cyclometalated Gold(III) Complexes for Chemoselective Cysteine Modification via Ligand Controlled C–S Bond-Forming Reductive Elimination. *Chem. Commun.* **2014**, *50* (80), 11899–11902. https://doi.org/10.1039/C4CC04467C.
(224) Patwardhan, R. S.; Rai, A.; Sharma, D.; Sandur, S. K.; Patwardhan, S. Txnrd1 as a Prognosticator for Recurrence, Metastasis and Response to Neoadjuvant Chemotherapy and Radiotherapy in Breast Cancer Patients. *Heliyon* **2024**, *10* (6), e27011. https://doi.org/10.1016/j.heliyon.2024.e27011.
(225) Hsieh, M.-S.; Ling, H. H.; Setiawan, S. A.; Hardianti, M. S.; Fong, I.-H.; Yeh, C.-T.; Chen, J.-H. Therapeutic Targeting of Thioredoxin Reductase 1 Causes Ferroptosis While Potentiating Anti-PD-1 Efficacy in Head and Neck Cancer. *Chem. Biol. Interact.* **2024**, *395*, 111004. https://doi.org/10.1016/j.cbi.2024.111004.
(226) Lu, Y.; Liu, Y.; Yang, C. Evaluating In Vitro DNA Damage Using Comet Assay. *J. Vis. Exp. JoVE* **2017**, No. 128, e56450. https://doi.org/10.3791/56450.
(227) Kellett, A.; Molphy, Z.; Slator, C.; McKee, V.; Farrell, N. P. Molecular Methods for Assessment of Non-Covalent Metallodrug–DNA Interactions. *Chem. Soc. Rev.* **2019**, *48* (4), 971–988. https://doi.org/10.1039/C8CS00157J.
(228) Foteeva, L. S.; Matczuk, M.; Timerbaev, A. R. Analytical Methodology for Determination of Interactions between Metallodrugs and DNA: A Critical Examination. *TrAC Trends Anal. Chem.* **2017**, *90*, 107–113. https://doi.org/10.1016/j.trac.2017.03.003.
(229) Iacobucci, I.; La Manna, S.; Cipollone, I.; Monaco, V.; Canè, L.; Cozzolino, F. From the Discovery of Targets to Delivery Systems: How to Decipher and Improve the Metallodrugs' Actions at a Molecular Level. *Pharmaceutics* **2023**, *15* (7), 1997. https://doi.org/10.3390/pharmaceutics15071997.
(230) Fung, S. K.; Zou, T.; Cao, B.; Lee, P.-Y.; Fung, Y. M. E.; Hu, D.; Lok, C.-N.; Che, C.-M. Cyclometalated Gold(III) Complexes Containing N-Heterocyclic Carbene Ligands Engage Multiple Anti-Cancer Molecular Targets. *Angew. Chem. Int. Ed.* **2017**, *56* (14), 3892–3896. https://doi.org/10.1002/anie.201612583.
(231) Wan, P.-K.; Tong, K.-C.; Lok, C.-N.; Zhang, C.; Chang, X.-Y.; Sze, K.-H.; Wong, A. S. T.; Che, C.-M. Platinum(II) N-Heterocyclic Carbene Complexes Arrest Metastatic Tumor Growth. *Proc. Natl. Acad. Sci.* **2021**, *118* (17), e2025806118. https://doi.org/10.1073/pnas.2025806118.
(232) Saei, A. A.; Gullberg, H.; Sabatier, P.; Beusch, C. M.; Johansson, K.; Lundgren, B.; Arvidsson, P. I.; Arnér, E. S. J.; Zubarev, R. A. Comprehensive Chemical Proteomics for Target Deconvolution of the Redox Active Drug Auranofin. *Redox Biol.* **2020**, *32*, 101491. https://doi.org/10.1016/j.redox.2020.101491.
(233) Hu, D.; Yang, C.; Lok, C.-N.; Xing, F.; Lee, P.-Y.; Fung, Y. M. E.; Jiang, H.; Che, C.-M. An Antitumor Bis(N-Heterocyclic Carbene)Platinum(II) Complex That Engages Asparagine Synthetase as an Anticancer Target. *Angew. Chem. Int. Ed.* **2019**, *58* (32), 10914–10918. https://doi.org/10.1002/anie.201904131.
(234) Wang, H.; Yan, A.; Liu, Z.; Yang, X.; Xu, Z.; Wang, Y.; Wang, R.; Koohi-Moghadam, M.; Hu, L.; Xia, W.; Tang, H.; Wang, Y.; Li, H.; Sun, H. Deciphering Molecular Mechanism of Silver by Integrated Omic Approaches Enables Enhancing Its

Antimicrobial Efficacy in E. Coli. *PLOS Biol.* **2019**, *17* (6), e3000292. https://doi.org/10.1371/journal.pbio.3000292.
(235) Schmidt, C.; Zollo, M.; Bonsignore, R.; Casini, A.; Hacker, S. M. Competitive Profiling of Ligandable Cysteines in Staphylococcus Aureus with an Organogold Compound. *Chem. Commun.* **2022**, *58* (36), 5526–5529. https://doi.org/10.1039/D2CC01259F.
(236) Xiong, X.; Liu, L.-Y.; Mao, Z.-W.; Zou, T. Approaches towards Understanding the Mechanism-of-Action of Metallodrugs. *Coord. Chem. Rev.* **2022**, *453*, 214311. https://doi.org/10.1016/j.ccr.2021.214311.
(237) Rodrigues, J. A. O.; Kiran, N. S.; Chatterjee, A.; Prajapati, B. G.; Dhas, N.; dos Santos, A. O.; de Sousa, F. F.; Souto, E. B. Metallodrugs: Synthesis, Mechanism of Action and Nanoencapsulation for Targeted Chemotherapy. *Biochem. Pharmacol.* **2025**, *231*, 116644. https://doi.org/10.1016/j.bcp.2024.116644.
(238) Guengerich, F. P. A History of the Roles of Cytochrome P450 Enzymes in the Toxicity of Drugs. *Toxicol. Res.* **2021**, *37* (1), 1–23. https://doi.org/10.1007/s43188-020-00056-z.
(239) Kabir, E.; Noyon, M. R. O. K.; Hossain, Md. A. Synthesis, Biological and Medicinal Impacts of Metallodrugs: A Study. *Results Chem.* **2023**, *5*, 100935. https://doi.org/10.1016/j.rechem.2023.100935.
(240) Dörr, M.; Meggers, E. Metal Complexes as Structural Templates for Targeting Proteins. *Curr. Opin. Chem. Biol.* **2014**, *19*, 76–81. https://doi.org/10.1016/j.cbpa.2014.01.005.
(241) Feng, L.; Geisselbrecht, Y.; Blanck, S.; Wilbuer, A.; Atilla-Gokcumen, G. E.; Filippakopoulos, P.; Kräling, K.; Celik, M. A.; Harms, K.; Maksimoska, J.; Marmorstein, R.; Frenking, G.; Knapp, S.; Essen, L.-O.; Meggers, E. Structurally Sophisticated Octahedral Metal Complexes as Highly Selective Protein Kinase Inhibitors. *J. Am. Chem. Soc.* **2011**, *133* (15), 5976–5986. https://doi.org/10.1021/ja1112996.

6 List of Figures

7 List of Tables

8 Scientific Contributions

Structure activity relationships of silver(I)- and gold(I)-NHC compounds and striking differences in the response of cisplatin-resistant ovarian cancer to bis-NHC gold(I) derivatives

Bormio Nunes, J. H., Hacker, C., Caban, M., … Kowol, C., Heffeter, P.

Journal of Medicinal Chemistry, 2026, 69, 3, 2462–2480

DOI: 10.1021/acs.jmedchem.5c02355

Selectivity for TP53 signalling drives the mode of action of a highly potent N,O,O-tridentate naphthoquinone-based organo-ruthenium anticancer drug candidate

Rosner, A., Skos, L., Mendrina, T., … Kandioller, W., Meier-Menches, S.M.

Chemical Science, 2025, 16, 15652-15665

DOI: 10.1039/d5sc00735f

Phosphoproteomics highlights complex resource management upon inflammatory stimulation of fibroblasts

Janker-Bortel, P., Martinez-Val, A., Hagn, G., Skos, L., Olsen, J. V., Gerner C.

bioRxiv, 2024.10.11.617591

DOI: 10.1101/2024.10.11.617591

Gold-templated covalent targeting of the CysSec-dyad of thioredoxin reductase 1 in cancer cells

Skos, L., Schmidt, C., Thomas, S.R., ... Casini, A., Meier-Menches, S.M.

Cell Reports Physical Science, 2024, 5(7), 102072

DOI: 10.1016/j.xcrp.2024.102072

Memory effects of prior subculture may impact the quality of multiomic perturbation profiles

Bortel, P., Hagn, G., Skos, L., ... Gerner, C., Meier-Menches, S.M.

Proceedings of the National Academy of Sciences of the United States of America, 2024, 121(29), e2313851121

DOI: 10.1073/pnas.231385112

Single-cell transcriptomics and epigenomics unravel the role of monocytes in neuroblastoma bone marrow metastasis

Fetahu, I.S., Esser-Skala, W., Dnyansagar, R., ... Fortelny, N., Taschner-Mandl, S.

Nature Communications, 2023, 14(1), 3620

DOI: 10.1038/s41467-023-39210-0

Exploring the Potential of Metal-Based Candidate Drugs as Modulators of the Cytoskeleton

Borutzki, Y., Skos, L., Gerner, C., Meier-Menches, S.M.

ChemBioChem, 2023, 24(17), e202300178

DOI: 10.1002/cbic.202300178

Methods to identify protein targets of metal-based drugs

Skos, L., Borutzki, Y., Gerner, C., Meier-Menches, S.M.

Current Opinion in Chemical Biology, 2023, 73, 102257

DOI: 10.1016/j.cbpa.2022.102257

A multi-omics based anti-inflammatory immune signature characterizes long COVID-19 syndrome

Kovarik, J.J., Bileck, A., Hagn, G., ... Schmetterer, K.G., Gerner, C.

iScience, 2023, 26(1), 105717

DOI: 10.1016/j.isci.2022.105717

Epithelial cell line derived from endometriotic lesion mimics macrophage nervous mechanism of pain generation on proteome and metabolome levels

Neuditschko, B., Leibetseder, M., Brunmair, J., ... Yotova, I., Gerner, C.

Biomolecules, 2021, 11(8), 1230

DOI: 10.3390/biom11081230

List of Oral Contributions

"Multi-Omics Readouts of Perturbation Studies are Determined by Memory Effects from Subculture"

Leoben, Austria – 18th ASAC Junganalytiker*innen Forum 2023

"Establishment of an affinity enrichment assay for the proteomic investigation of the human selenoproteome"

Linz, Austria – 2nd DoSChem Panel B Retreat 2022

"Enrichment of the selenoproteome"

Illmitz, Austria – 1st DoSChem Panel B Retreat 2021

List of Poster Contributions

"Towards in-vivo mode of action deconvolution: Investigation of a ruthenium(arene) tridentate naphthoquinone complex"

Andover, NH, USA – Gordon Research Conference Metals in Medicine 2024

Andover, NH, USA – Gordon Research Seminar Metals in Medicine 2024

"Selective Metal-Templated Arylation of Selenocysteine of Thioredoxin Reductase 1 by an Organogold Compound"

Braunschweig, Germany – International Symposium on Bioorganometallic Chemistry 2023

"Cell Culture Conditions Influence the Information Density of Treatment-Induced Omics-Readouts"

Fürstenfeld, Austria – 3rd DoSChem Panel B Retreat 2023

"Cell Culture Conditions Influence the Information Density of Treatment-Induced Omics-Readouts"

Andover, NH, USA – Gordon Research Conference Metals in Medicine 2022

Copyright Statement

Ich habe mich bemüht, sämtliche Inhaber der Bildrechte ausfindig zu machen und ihre Zustimmung zur Verwendung der Bilder in dieser Arbeit eingeholt. Sollte dennoch eine Urheberrechtsverletzung bekannt werden, ersuche ich um Meldung bei mir.

Nutzung von KI: Perplexity AI wurde bei der initialen Literaturrecherche verwendet und DeepL teilweise für die Verbesserung von Sprache, Formulierung und Grammatik.

Lukas Skos, Juni 2026